

Diss. ETH No. 18260

Generation and spectroscopy of atoms and molecules in metastable states

A dissertation submitted to

ETH ZURICH

for the degree of

Doctor of Sciences

presented by

Matthias Raunhardt

Dipl. Phys. ETH

born February 2, 1979

citizen of Zurich

Accepted on the recommendation of:

Prof. Dr. F. Merkt, examiner

Prof. Dr. A. Wokaun, co-examiner

2009

Meinen Eltern und meinem Bruder

Innre der Natur
Dringt kein erschaffner Geist.
Glücklich, wem sie nur
Die äussre Schale weist.

Albrecht von Haller

Abstract

A new spectrometer for the study of metastable states of atoms and molecules by high-resolution photoionization spectroscopy, pulsed-field-ionization zero-kinetic-energy (PFI-ZEKE) photoelectron spectroscopy, and mass spectrometry has been designed, built and tested. The apparatus consists of 1) a versatile pulsed laser system that enables investigations by single-photon excitation using coherent ultraviolet and vacuum-ultraviolet (VUV) radiation, and by multiphoton excitation, 2) a photoionization/photoelectron spectrometer especially designed for experiments on very high Rydberg states such as those probed by PFI-ZEKE photoelectron spectroscopy, 3) a probe gas source chamber in which metastable states of atoms and molecules can be generated using pulsed discharges, photolysis, and single- and multiphoton optical excitation of forbidden transitions, and 4) a source of narrow-bandwidth tunable millimeter-wave radiation for high-resolution spectroscopy of high Rydberg states. The spectrometer has been used to study the threshold ionization dynamics of ND_3 , the photolysis of ammonia cluster and the threshold ionization of ammoniated ammonium radical clusters, the hyperfine structure of long-lived high Rydberg states of ^{129}Xe and ^{131}Xe , the formation of metastable He and He_2 in supersonic expansions, the structure of He_2^+ , and the rotational autoionization dynamics of high Rydberg states of He_2 .

The PFI-ZEKE photoelectron spectrum of ND_3 was recorded following single-photon VUV excitation from the $\tilde{X}^+ 1A'_1$ ground state at a resolution and sensitivity sufficient to observe the rotational structure of the first three out-of-plane bending vibrational levels of ND_3^+ . The analysis of the photoelectron spectrum enabled the determination of the first adiabatic ionization energy of ND_3 ($82\,261.7 \pm 1.5 \text{ cm}^{-1}$) and of a set of molecular constants describing the rovibrational energy level structure of the $\tilde{X}^+ 2A''_2$ ground electronic state of ND_3^+ up to 1400 cm^{-1} of internal energy. The intensity distribution of the photoelectron spectrum was analyzed in terms of rovibronic photoionization selection rules, a simple orbital ionization model, and rovibronic channel interactions. The dominant ionization channels were found to be associated with photoelectron partial waves of even orbital angular momentum quantum number ℓ . Intensity perturbations resulting from vibrational channel interactions were identified and found to significantly modify the photoelectron partial wave composition near the position of strong autoionization resonances in the photoionization spectrum.

The formation of metastable undeuterated and perdeuterated ammonium radicals and ammoniated ammonium radicals by UV photolysis of ammonia clusters in supersonic expansions was studied by photoionization mass spectrometry and PFI-ZEKE photo-

electron spectroscopy. The $3s\ ^2A_1$ state of the perdeuterated ammonium radical was found to have a lifetime of about $20\ \mu\text{s}$, more than four orders of magnitude longer than the lifetime of the $3s\ ^2A_1$ state of the NH_4 radical. Very pronounced isotopic effects were also observed in the photolysis of ammonia trimers ($(\text{NH}_3)_3$ and $(\text{ND}_3)_3$) at $204\ \text{nm}$: Whereas the metastable NH_3NH_4 radical was identified as the dominant product in the case of the undeuterated clusters, ND_2ND_4 represented the main product in the case of the perdeuterated clusters. The PFI-ZEKE photoelectron and photoionization spectra enabled the determination of the adiabatic ionization energy of NH_3NH_4 ($31\,310(25)\ \text{cm}^{-1}$) and ND_3ND_4 ($31\,220(25)\ \text{cm}^{-1}$) and of a very pronounced ionization threshold at $30\,780\ \text{cm}^{-1}$ in ND_2ND_4 . The PFI-ZEKE photoelectron spectrum also provided information on low-lying vibrational levels of the N_2H_7^+ cation. Two low-lying vibrational levels were observed at $345\ \text{cm}^{-1}$ and $690\ \text{cm}^{-1}$ above the origin that were tentatively assigned to the fundamental and first overtone of the symmetric stretching vibrational mode involving the two NH_3 molecules on both side of the proton on the basis of a comparison with the IR spectrum of N_2H_7^+ and *ab initio* calculations [Yang *et al.*, J. Chem. Phys. **129**, 224302 (2008), García-Fernández *et al.*, J. Chem. Phys. **129**, 124313 (2008)].

Millimeter-wave spectra of transitions between metastable high ns , np , nd , and nf Rydberg states of Xe were recorded at a resolution sufficiently high ($\sim 500\ \text{kHz}$) to observe the hyperfine structure in the spectra of ^{129}Xe and ^{131}Xe . These spectra were analyzed using multichannel quantum defect theory (MQDT) and led to the first determination of the hyperfine structure of the $^2P_{3/2}$ ground state of $^{129}\text{Xe}^+$ and $^{131}\text{Xe}^+$. A set of MQDT parameters was derived for the ns and nd Rydberg states that accurately describes the photoionization dynamics of Xe and all spectroscopic data obtained up to date on neutral Xe.

A new method to generate the $1s2s\ ^3S_1$ metastable state of He and the $a\ ^3\Sigma_u^+$ metastable state of He_2 in supersonic expansions has been developed. Photoionization and PFI-ZEKE photoelectron spectra of $^4\text{He}_2$ and $^3\text{He}_2$ have been recorded and analyzed and a set of accurate molecular constants for the lowest three vibrational levels of the ground electronic state of He_2^+ has been derived. The use of Rydberg-state-resolved threshold-ionization spectroscopy in combination with photoionization spectroscopy and multichannel quantum defect theory has provided a detailed description of the rotational autoionization dynamics of the triplet np Rydberg states of $^4\text{He}_2$ has been derived. Series of metastable Rydberg states embedded in the ionization continua were observed, and the origin of their metastability explained by a simple MQDT model. The application of weak electric fields was found to induce rotational autoionization of these long-lived Rydberg states, inducing changes of the rotational angular momentum quantum number of the $^4\text{He}_2^+$ ion core by up to six units.

Zusammenfassung

Für die Untersuchung von Atomen und Molekülen in metastabilen Zuständen mittels hochauflösender Photoionisationspektroskopie, pulsed-field-ionization zero-kinetic energy (PFI-ZEKE) Photoelektronenspektroskopie und Massenspektrometrie wurde ein neues Spektrometer entwickelt, gebaut und getestet. Das Spektrometer besteht aus 1) einem gepulsten Lasersystem, das Untersuchungen von Einphotonen- und Mehrphotonenanregungen mittels kohärenter ultravioletter und vakuumultravioletter (VUV) Strahlung ermöglichte, 2) einem Photoionisations-/Photoelektronenspektrometer, das speziell für Experimente an sehr hohen Rydbergzuständen entwickelt wurde, 3) einer Probengaskammer, die zur Erzeugung von metastabilen Zuständen von Atomen und Molekülen mittels gepulster elektrischer Entladungen, Photolyse und Einphotonen- und Mehrphotonenanregungen verbotener Übergänge genutzt wurde, und 4) einer schmalbandigen, abstimmbaren Millimeterwellenquelle, mit der hohe Rydbergzustände bei sehr hoher Auflösung untersucht wurden. Das Spektrometer wurde für die Untersuchung der Schwellenionisationsdynamik von ND_3 , der Photolyse von NH_3 -Aggregaten, der Ionisation von NH_3NH_4 -Radikalaggregaten, der Hyperfeinstruktur von langlebigen, hohen Rydbergzuständen von ^{129}Xe und ^{131}Xe , der Erzeugung von metastabilem He und He_2 in Überschallstrahlexpansionen, der Struktur von He_2^+ , sowie der Rotationsautoionisationsdynamik hoher Rydbergzustände von He_2 verwendet.

Das PFI-ZEKE Photoelektronenspektrum von ND_3 wurde durch Einphotonenanregung aus dem $\tilde{X}^1A'_1$ Grundzustand gemessen, wobei die Auflösung und Empfindlichkeit es erlaubten, die Rotationsstruktur der ersten drei "out-of-plane" Biegeschwingungsniveaus von ND_3^+ zu beobachten. Die Auswertung des Photoelektronenspektrums ermöglichte die Bestimmung der ersten adiabatischen Ionisationsenergie von ND_3 ($82\,2261.7 \pm 1.5 \text{ cm}^{-1}$) und eines Satzes molekularer Konstanten, welche die rovibrationalen Energieniveaustruktur des $\tilde{X}^+ 2A''_2$ elektronischen Grundzustandes von ND_3^+ bis zu einer internen Energie von 1400 cm^{-1} beschreibt. Die Intensitätsverteilung des Photoelektronenspektrums wurde mit Hilfe von rovibrationalen Photoionisationsauswahlregeln, einem einfachen Orbitalionisationsmodell und rovibrationalen Kanalwechselwirkungen analysiert. Aus den beobachteten Übergängen konnte geschlossen werden, dass die dominierenden Ionisationskanäle Photoelektronenpartialwellen gerader Bahndrehimpulsquantenzahl ℓ entsprechen. Dabei wurde beobachtet, dass Intensitätsstörungen, welche von vibrationellen Kanalwechselwirkungen stammen, die Zusammensetzung der Photoelektronenpartialwellen in der Nähe von starken Autoionisationsresonanzen im Photoionisationsspektrum deutlich veränderten.

Durch Photoionisationsmassenspektrometrie und PFI-ZEKE Photoelektronenspektro-

skopie wurde die Bildung von metastabilen undeuterten und komplett deuterierten Ammoniumradikalen sowie von metastabilen Aggregaten aus Ammoniak und Ammoniumradikalen durch UV Photolyse von Ammoniakaggregaten in einem Überschallstrahl untersucht. Es wurde eine Lebenszeit von ca. $20 \mu\text{s}$ für den $3s \ ^2A_1$ Zustand von ND_4 ermittelt, die mehr als vier Größenordnungen länger ist als die Lebenszeit des entsprechenden $3s \ ^2A_1$ Zustandes des NH_4 -Radikals. Auch bei der Photolyse des Ammoniaktrimers ($(\text{NH}_3)_3$ and $(\text{ND}_3)_3$) bei 204 nm wurde ein ausgeprägter Isotopeneffekt beobachtet: während im Falle der undeuterten Aggregate metastabile NH_3NH_4 Moleküle als vorherrschendes Produkt identifiziert wurden, stellte im Falle der volldeuterten Aggregate ND_2ND_4 das Hauptprodukt dar. Die PFI-ZEKE Photoelektronen- und Photoionisationsspektren ermöglichten die Bestimmung der adiabatischen Ionisierungsenergien von NH_3NH_4 ($31\,310(25) \text{ cm}^{-1}$), ND_3ND_4 ($31\,220(25) \text{ cm}^{-1}$) und einer ausgeprägten Ionisationsschwelle bei $30\,780 \text{ cm}^{-1}$ in ND_2ND_4 . Das PFI-ZEKE Photoelektronenspektrum enthielt auch Informationen über tiefliegende Vibrationszustände des N_2H_7^+ Kations. Zwei tiefliegende Vibrationszustände wurden bei 345 cm^{-1} und 690 cm^{-1} oberhalb der Ursprungsbande beobachtet. Auf Grund eines Vergleiches mit dem IR Spektrum von N_2H_7^+ und mit *ab initio* Rechnungen wird eine Zuordnung dieser zwei Zustände zur Grundschiwingung und zum ersten Oberton der Streckschwingungsmode der beiden NH_3 Moleküle auf beiden Seiten des Protons hin vorgeschlagen, die allerdings noch bestätigt werden muss [Yang *et al.*, J. Chem. Phys. **129**, 224302 (2008), García-Fernández *et al.*, J. Chem. Phys. **129**, 124313 (2008)].

Zusätzlich wurden Millimeterwellenspektren von Übergängen zwischen metastabilen hohen *ns*, *nd*, *np* and *nf* Rydbergzuständen von Xenon gemessen. Die Auflösung dieser Spektren war hoch genug ($\sim 500 \text{ kHz}$), um die Hyperfeinstruktur in den Spektren von ^{129}Xe und ^{131}Xe zu beobachten. Die Analyse der Spektren mittels der Vielkanal-Quantendefekt-Theorie (MQDT) führte zur ersten Bestimmung der Hyperfeinstruktur des $^2P_{3/2}$ Grundzustandes von $^{129}\text{Xe}^+$ und $^{131}\text{Xe}^+$. Dabei wurde ein Satz von MQDT Parametern für die *ns* und *nd* Rydbergzustände ermittelt, der die Photoionisationsdynamik von Xenon und alle spektroskopischen Information, welche bis heute erhalten wurden, beschreibt.

Durch eine neuentwickelte Methode konnte der $1s2s \ ^3S_1$ metastabile Zustand von He und der $a \ ^3\Sigma_u^+$ metastabile Zustand von He_2 in einer Überschallstrahlexpansion erzeugt werden. Die Analyse gemessener Photoionisations- und PFI-ZEKE Photoelektronenspektren von $^4\text{He}_2$ und $^3\text{He}_2$ ermöglichte die Bestimmung eines Satzes von molekularen Konstanten für die drei tiefsten Vibrationsniveaus des elektronischen Grundzustandes von He_2^+ . Die Kombination von Rydbergzustandsaufgelöster-Schwellenionisationsspektroskopie (Rydberg-state-resolved threshold-ionization spectroscopy), Photoionisationsspektroskopie und MQDT Analyse führte zu einer detaillierten Beschreibung der Autoionisationsdynamik der $S = 1 \ np$ Rydbergzustände von $^4\text{He}_2$. Es wurden Serien metastabiler

Rydbergzustände oberhalb der tiefsten Ionisationsschwelle beobachtet und der Ursprung ihrer Metastabilität durch ein einfaches MQDT Modell erklärt. Die rotationelle Autoionisation dieser metastabilen Zustände konnte durch das Anlegen von schwachen elektrischen Feldern induziert werden, die zu einer Änderung der Rotationsquantenzahl im ${}^4\text{He}_2^+$ Ionenrumpf von bis zu sechs Einheiten in führte.

Contents

Abstract	vii
Zusammenfassung	ix
1 Introduction	1
1.1 Metastable states of atoms and molecules	1
1.2 Outline of the thesis	2
1.3 Rydberg states – a brief introduction	4
2 Experimental setup and methods	7
2.1 Spectrometer	7
2.2 The laser systems	10
2.2.1 Experiments using VUV radiation	11
2.2.2 Experiments using single-photon excitation with UV radiation . . .	12
2.2.3 Experiments using multiphoton excitation	13
2.2.4 Calibration	14
2.3 Millimeter-wave source	14
2.4 Probe gas samples	15
2.4.1 Studies of molecular cations using seeded supersonic expansion . . .	16
2.4.2 Discharge source of metastable He and He ₂ in supersonic expansions	17
2.4.3 Optical preparation of metastable states	20
2.4.4 Photolysis source of metastable radicals in supersonic expansions .	22
2.5 Spectroscopic methods	23
2.5.1 Photoionization spectroscopy	23
2.5.2 PFI-ZEKE photoelectron spectroscopy	26
2.5.3 Millimeter-wave spectroscopy of high Rydberg states	28
3 The PFI-ZEKE photoelectron spectrum of ND₃	31
3.1 Introduction	31
3.2 Rovibronic photoionization selection rules of ND ₃	34
3.3 Experiment	36

3.4	Results	37
3.5	Discussion and conclusions	43
4	Threshold photoionization of ammoniated ammonium clusters	45
4.1	Introduction	45
4.2	Experiment	47
4.3	Results and discussion	48
4.3.1	Formation and threshold ionization of the deuterated ammonium radical	48
4.3.2	Formation and threshold ionization of the ammoniated ammonium dimers	50
4.3.2.1	Experiments on $(\text{NH}_3)_3$ clusters	50
4.3.2.2	Experiments on $(\text{ND}_3)_3$ clusters	53
4.4	Conclusions	55
5	Spectroscopy and MQDT analysis of high Rydberg states of Xe	57
5.1	Introduction	57
5.2	Experiments	61
5.3	MQDT calculations	62
5.4	Results	66
5.5	Discussion and conclusions	78
6	PFI-ZEKE photoelectron spectroscopy of metastable He and He₂	83
6.1	Introduction	83
6.2	Experiment	85
6.3	Results	86
6.3.1	Performance of the pulsed discharge	86
6.3.2	The photoionization and PFI-ZEKE photoelectron spectra of He*	89
6.3.3	The PFI-ZEKE spectra of He ₂ * and their assignment	91
6.3.4	The photoionization spectrum He ₂ * and its analysis by MQDT	97
6.3.5	Probing the autoionization dynamics of He ₂ Rydberg states by Rydberg-state-resolved threshold-ionization	102
6.4	Discussion	106
6.4.1	Energy level structure of the He ₂ ⁺ cation	106
6.4.2	The field ionization and rotational autoionization dynamics of Rydberg states of He ₂	108
6.5	Conclusions	115
7	Conclusions	117

A Physical constants	119
B Spectral positions of the observed Rydberg levels of He₂	121
List of figures	143
List of tables	153
Bibliography	157
Curriculum Vitae	183
Publications	185
Danksagung	187

Chapter 1

Introduction

1.1 Metastable states of atoms and molecules

Metastable states of atoms and molecules are excited states that are energetically unstable with respect to decay processes such as dissociation, ionization or the emission of a photon, but do not decay on the μs time scale because the decay processes are hindered by selection rules or by the nature of the potential energy landscape [1, 2].

The most common form of metastability is encountered in the lowest electronically excited state of atoms and molecules that possesses another spin multiplicity than the ground electronic state and could be called “radiative metastability”. Radiative decay to the ground state is inhibited by the $\Delta S = 0$ selection rule that holds in systems in which spin-orbit interactions are not significant. Numerous examples are known, such as, for instance the $1s2s\ ^3S_1$ state of He, the lowest 3P state of Hg, the $a\ ^1\Delta_g$ and $b\ ^1\Sigma_g^+$ states of O_2 , the $a\ ^3\Sigma_g^+$ state of H_2 , the $a\ ^3\Pi$ state of CO, etc. [3–5]. A related form of metastability can be found in systems in which an electronically excited state cannot radiatively decay to the ground, or a lower-lying electronic state because of restrictions imposed by electric dipole selection rules, such as $\Delta\ell = \pm 1$ and $\Delta J = 0, \pm 1$ ($0 \leftrightarrow 0$) in atoms (the most prominent example is the $2s\ ^2S_{1/2}$ state of the H atom) and the $\Delta\Lambda = 0, \pm 1$ or $\Delta\Omega = 0, \pm 1$ in linear molecules.

Metastability with respect to decay by dissociation or predissociation is encountered whenever the vibrational energy levels of a radiatively metastable electronic state of a molecule are located energetically above the first dissociation limit but the dissociation is hindered either by a barrier in the potential energy surface along the dissociation coordinate, or by vanishing rovibronic couplings to all energetically accessible dissociation continua. Similarly, metastability with respect to decay by ionization or autoionization results either from photoionization symmetry selection rules or from vanishing rovibronic coupling to all energetically accessible ionization continua.

Further forms of metastability, in particular the metastability of rotationally excited

levels of the ground electronic state of molecules, result from the conservation of nuclear spin symmetry and/or parity and/or the absence of a permanent dipole moment.

For a given state of an atom or a molecule to be metastable it is necessary that all radiative and nonradiative processes such as predissociation, autoionization and internal conversions be suppressed. This suppression inevitably occurs in Rydberg states of atoms and molecules of high principal quantum number n belonging to series converging to the lowest-lying quantum state of a positively charged ion. Indeed, when n tends towards infinity, the Rydberg electron wavefunction has a vanishingly small amplitude close to the ion core, and the motion of the electron gets entirely decoupled from that of the ion core; under these conditions, neither radiative nor nonradiative decay processes can take place.

Atoms and molecules in metastable states are important carriers of energy in chemical reactions, the a $^1\Delta_g$ and b $^1\Sigma_g^+$ states of O_2 and the lowest 3P state of Hg being among the most prominent examples. Metastability of an isolated atom or molecule is thus closely linked to, and almost inevitably results in a high reactivity.

Metastable states of atoms and molecules are also attractive systems for studies by high-resolution spectroscopy. Their long lifetimes allow long measurement times and, by virtue of the energy-time uncertainty principle, high spectral resolution. Because their electronic or nuclear configurations usually differ from those of the ground state, metastable states offer the possibility to study, by spectroscopy, states that are not accessible from the ground state. Finally, metastability is closely connected to unusual properties of potential energy surfaces, or unusual nuclear or electronic configurations, and consequently metastable atoms and molecules are per se interesting objects of scientific investigations.

This dissertation is devoted to spectroscopic studies of atoms and molecules in metastable states in the gas phase. Three aspects have been at the foreground: 1) The implementation of efficient methods to generate dense samples of metastable atoms and molecules, 2) The use or development of very sensitive spectroscopic methods to study these metastable atoms and molecules, and 3) The exploration of as diverse forms of metastability as possible.

1.2 Outline of the thesis

This introductory chapter will give in the next subsection a brief introduction to Rydberg states that have been central to this dissertation not only as an important class of metastable states, but also because the methods used to detect metastable atoms and molecules such as pulsed-field-ionization zero-kinetic-energy (PFI-ZEKE) photoelectron spectroscopy and Rydberg-state-resolved threshold-ionization (RSR-TI) spectroscopy rely

on the unusual physical properties of these states.

Chapter 2 focuses on the description of the apparatus that has been built and the methods that have been implemented to generate dense samples of metastable molecules and to study them. Metastable states of He, He₂, Xe, CO, ND₄, ND₂-ND₄, N₂H₇, N₂D₇ were populated using specific methods including optical excitation from the ground state by driving forbidden transitions with intense laser pulses, photolysis of suitable precursors in supersonic expansions, multiphoton excitation from the ground state, and electric discharges. They have been studied by photoionization spectroscopy, photoelectron spectroscopy (mostly PFI-ZEKE and RSR-TI spectroscopy), millimeter-wave spectroscopy and time-of-flight mass spectrometry.

Chapter 3 is devoted to a study of the photoionization and PFI-ZEKE photoelectron spectrum the ND₃⁺ $\tilde{X}^+ 2A_2'' \leftarrow ND_3 \tilde{X} 1A_1'$ transition. Though neither the ground electronic state of ND₃ nor that of ND₃⁺ classify as metastable states, the high Rydberg states of ND₃ used to record the photoelectron spectra are metastable. Particular emphasis was placed on the characterization of the photoionization dynamics, and of the high Rydberg states and ionization channels accessible from the ground neutral state.

Chapter 4 investigates the metastability with respect to dissociation of the ammonium radical and ammoniated ammonium radicals and their cations. Metastability in these molecules is strongly influenced by isotopic substitution, and the very pronounced differences in the behavior of undeuterated and perdeuterated samples proved very useful to characterize the origin of the metastability of these systems.

The fifth chapter summarizes the study of long-lived s, p, d and f high Rydberg states of atomic xenon by high-resolution millimeter-wave spectroscopy and multichannel quantum defect theory, a collision theory. The metastability of high Rydberg states originates from the decoupling of the motions of the Rydberg electron and of the ionic core. One of the main goals of this study was to resolve the hyperfine structure in high Rydberg states of ¹²⁹Xe and ¹³¹Xe to see whether the interaction of the Rydberg electron with the nuclear spin of the ion core can be observed in these metastable states despite the fact that the electron and ion core motions are decoupled and to study how nuclear spin influence the photoionization dynamics.

Chapter 6 presents the results of an investigation of the photoionization and photoelectron spectra of helium atoms in the metastable 1s2s ³S₁ He state and of He₂ molecules in the a ³Σ_u⁺ metastable state. The challenge was to derive a method of generating the metastable species in a supersonic expansion under conditions compatible with the recording of photoionization and photoelectron spectra. This study resulted in the spectroscopic characterization of the ground state of the He₂⁺ cation and in an investigation of the rotational autoionization dynamics of high Rydberg states of He₂. The emphasis was on the search, identification and characterization of states that are metastable with respect

to ionization. Many such states could be identified. However, weak electric fields were found to induce rapid ionization of the metastable states.

The thesis ends in Chapter 7 with a brief summary and an outlook.

1.3 Rydberg states – a brief introduction

Rydberg states represent an important class of metastable states in atoms and molecules. Their metastability is at the heart of important spectroscopic techniques such as PFI-ZEKE photoelectron spectroscopy [6,7], mass-analyzed-threshold-ionization (MATI) spectroscopy [8], photoinduced Rydberg ionization (PIRI) spectroscopy [9,10], and Rydberg-tagging photofragment translational spectroscopy [11–13].

Rydberg states are electronically excited states of neutral or positively charged atoms and molecules the spectral positions $\tilde{\nu}_{n,\ell}$ of which can be described by Rydberg's formula

$$\tilde{\nu}_{n,\ell} = \frac{E_I}{hc} - \frac{R_M}{(n - \delta_\ell)^2}, \quad (1.1)$$

in which E_I , the ionization energy, represents the convergence limit of the infinite series of levels with principal quantum number n ($n = 1, 2, 3, \dots$) and orbital angular momentum quantum number ℓ . R_M is the mass-dependent Rydberg constant which can be expressed in terms of the Rydberg constant for an atom of infinite mass R_∞ as (M^+ is the mass of the positively charged ionic core)

$$R_M = R_\infty \frac{M^+}{M^+ + m_e}. \quad (1.2)$$

In Eq. (1.1) δ_ℓ represents the quantum defect which is zero for all series of atomic hydrogen and one-electron atoms, and for all nonpenetrating series (i.e., series with ℓ typically larger than 3) but nonzero for core-penetrating series (typically $\ell \leq 3$) of atoms and molecules having more than one electron.

Most physical properties of Rydberg states scale as integer power of the principal quantum number, and Table 1.1 provides an overview of the n -scaling laws of selected properties with numerical values at $n = 1, 10$ and 100 . The n -scaling law can easily be derived by considering the wavefunctions $|n\ell m\rangle$ of the hydrogen atom. Of particular significance in the realm of the present dissertation are the following properties: 1) The lifetimes of Rydberg states of a given series increase with n^3 . Therefore high- n Rydberg states are metastable. The n^3 scaling of the lifetime can be understood from the fact that the decay of a Rydberg state, be it radiative, by autoionization or predissociation, is proportional to the probability of finding the electron in close vicinity of the ion core, i.e., to the square of the Rydberg electron wavefunction in this region. 2) The spacing

Table 1.1: Properties of Rydberg states. Values are calculated for the hydrogen atom if not mentioned otherwise

Property	n -scaling	Value at		
		$n = 1$	$n = 10$	$n = 100$
Radius / Å	$a_0 n^2$	0.53	53	5300
Binding energy / cm^{-1}	Rn^{-2}	$\sim 109\,667$	~ 1097	~ 0.1
Lifetime ^a / μs	$\propto n^3$			
Orbital period / s	$\tau_1 n^3$	$1.5 \cdot 10^{-16}$	$1.5 \cdot 10^{-13}$	$1.5 \cdot 10^{-10}$
Spacing between neighboring states / cm^{-1}	$2Rn^{-3}$	$\sim 82\,000$	220	~ 0.22
Polarizability ^b / $\text{MHz}/(\text{V}/\text{cm})^2$	$\propto n^7$	$2.1 \cdot 10^{-8}$	0.21	$2.1 \cdot 10^7$
Threshold ionization field / (V/cm)	$\propto n^{-4}$	$\geq 10^8$	$3.2 \cdot 10^4$	3.2

^aThe numerical values strongly depend on the series and on the atom or molecule

^bValues for the nd series of Na extrapolated from the measured value of the 10d state [14]

between adjacent members of a given series scales as $\frac{2R}{n^3}$ as can easily be derived by taking the derivative of Eq. (1.1). High-resolution spectroscopic methods are thus mandatory if one wants to resolve individual members of a Rydberg series at high n . 3) The electric field that is necessary to ionize a Rydberg state scales as n^{-4} and decreases very rapidly with n . This property renders the detection of high Rydberg states easy and efficient. A dc electric field lowers the ionization limit by ΔE_I

$$\frac{\Delta E_I}{hc \text{ cm}^{-1}} = 6.12 \sqrt{\frac{\mathcal{E}}{\text{V}/\text{cm}}} \quad (1.3)$$

and a pulsed electric field causes ionization of Rydberg states located within

$$\frac{\Delta E_I}{hc \text{ cm}^{-1}} = C \sqrt{\frac{\mathcal{E}}{\text{V}/\text{cm}}} \quad (1.4)$$

of the ionization limit, where C can take values ranging from 3 to 6.12 depending on the field ionization mechanism [14–16]. 4) The polarizability of Rydberg states scales as n^7 . In order to study Rydberg states at high n values it is thus imperative to minimize stray electric fields.

The rapid variation of the physical properties of Rydberg states with n implies that the properties of high Rydberg states are exaggerated which can be exploited in a variety of applications such as the spectroscopic methods mentioned at the beginning of this subsection, the measurement of stray fields and ion concentrations [17], the electrostatic acceleration and deceleration of beams of Rydberg atoms and molecules [18, 19], and the electrostatic trapping of translationally cold samples of Rydberg atoms [20].

Chapter 2

Experimental setup and methods

This chapter describes the spectrometer and spectroscopic methods that have been used in the realm of the present dissertation. The laser system, the vacuum chambers, and the source of metastable molecules have been specially designed, constructed and tested to carry out spectroscopic measurements on unstable, reactive or metastable molecules by exciting them to high Rydberg states close to their ionization thresholds. These species include molecular cations, electronically excited long-lived atoms and molecules and radicals. Several different photoexcitation schemes have been employed, including single-photon excitation or ionization with narrow-band VUV radiation (study of ND_3^+ in Chapter 3) or UV radiation (studies of He and He_2 and He_2^+ in Chapter 6 and of ND_4 and ammonium clusters in Chapter 4), and resonance-enhanced multiphoton excitation ionization (study of Xe Rydberg states in Chapter 5). This chapter begins in Section 2.1 with a description of the photoionization and photoelectron spectrometer, which was common to all experiments. This section is followed by a description of the laser and millimeter-wave radiation sources in Sections 2.2 and 2.3, respectively, and of the different methods used to generate metastable molecules in Section 2.4. Finally, the last section provides an introduction to the three spectroscopic methods employed: photoionization spectroscopy, pulsed-field-ionization zero-kinetic-energy (PFI-ZEKE) photoelectron spectroscopy and millimeter-wave spectroscopy.

2.1 Spectrometer

The spectrometer developed and used in the realm of this dissertation is depicted schematically in Fig. 2.1. It consists of a laser system, a probe gas chamber and a photoexcitation/photoionization chamber. The different configurations of the laser system used for the different experiments summarized in this thesis will be described in more detail in Section 2.2. This section presents the probe gas chamber and the photoexcitation/photoionization chamber that were common to all experiments. An enlarged view

of these chambers is shown in Fig. 2.2.

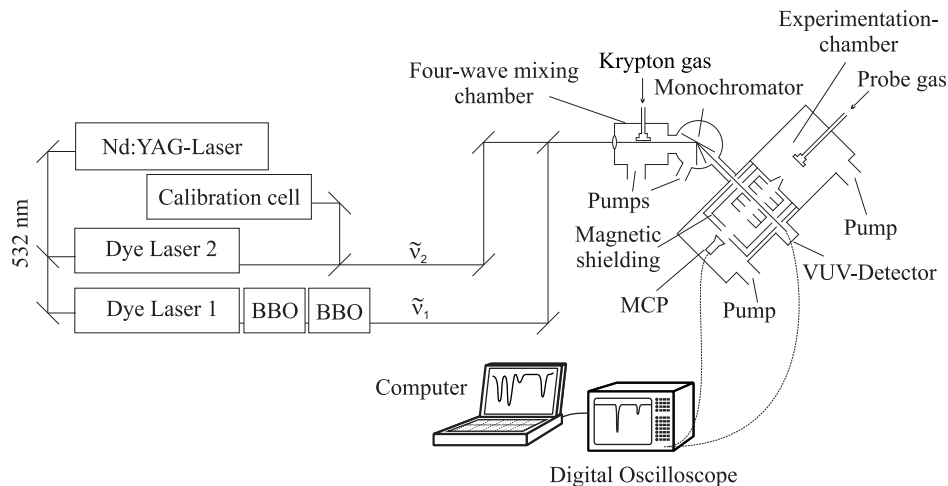


Figure 2.1: Schematic view of the experimental setup for experiments on metastable molecules, radicals and ions. The lasers with wave number $\tilde{\nu}_1$ and $\tilde{\nu}_2$ were used to generate VUV radiation of wave number $\tilde{\nu}_{\text{VUV}}$. Alternatively they could be used to induce two-color multiphoton excitation processes, in which case the four-wave mixing chamber and the monochromator were not used. The vacuum chambers where the photoexcitation and photoionization experiments were carried out are displayed on the right and the detection and measurement systems at the bottom of the figure.

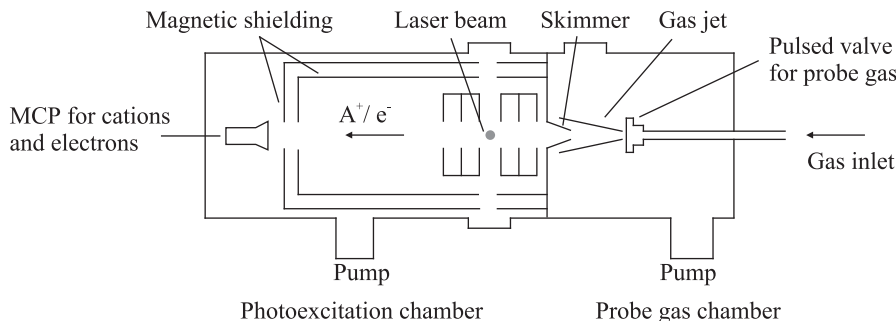


Figure 2.2: Schematic view of the photoelectron/photoion time-of-flight mass spectrometer. Depending on the sign of the voltages applied to the set of six extraction plates (middle of the figure) and the microchannel plate detectors, either ions or electrons can be detected using the same spectrometer. The electron or ion time-of-flight tube and the photoexcitation region are surrounded by a magnetic shield consisting of two concentric mumetal cylinders.

Photoionization and photoelectron spectroscopic experiments must be carried out under high vacuum. Pulsed skimmed supersonic expansions in which the species of interest is diluted in a carrier gas (typically a noble gas) were chosen as gas samples for the following reasons: 1) They offer a collision-free environment which is a prerequisite in experiments including reactive species. 2) They enable one to easily maintain a very low pressure (typically less than 10^{-6} mbar) in the regions of the spectrometer where the

charged particles are detected – higher pressures tend to lead to undesirable electric discharges in the vicinity of electron and ion detectors which are kept at high voltages. 3) The efficient cooling of vibrational and rotational degrees of freedom in supersonic beams greatly reduce the number of populated quantum states and permit the optimization of the population of the lowest rotational states of the molecular species. 4) The use of a skimmer to separate the probe gas chamber from the photoionization chamber enables one to carry out the experiments on highly directional atomic or molecular beams and thus to completely suppress Doppler broadening. It also offers the possibility of exploiting differential pumping between the probe gas chamber, which is exposed to a high gas load (pressure of 10^{-4} mbar were typical for the experiments described in this thesis), and the photoionization region, which is exposed to a much lower gas load and in which pressures below 10^{-6} mbar are mandatory as explained above. To reach these pressures, the probe gas chamber and the photoionization chamber were pumped by turbomolecular pumps of 520 l s^{-1} (Pfeiffer TMH 521) and 260 l s^{-1} (Pfeiffer TMH 261) pumping power, respectively.

The probe gas samples were introduced into the gas chamber using a pulsed solenoid valve (General Valve, Series 9, with IOTA One driver; nozzle orifice diameter of 0.5 mm). The repetition rate of the nozzle opening (25 Hz) matched the repetition rate of the laser system. The time difference between the opening times of the nozzle and the laser pulses was adjusted using a high-precision delay generator (Stanford Digital Delay/Pulse Generator Model DG535) to optimize the signal of the desired species and/or to minimize the rotational temperature of the sample. For selected experiments, a pulsed discharge setup or a quartz capillary crossed by a photolysis laser beam were mounted at the exit of the pulsed valve in order to generate reactive or metastable species just before the supersonic expansion (see Section 2.4).

Because most experiments reported in this thesis involved the photoexcitation to high Rydberg states and their subsequent field-ionization by pulsed electric fields, great care was taken in the design of the spectrometer to minimize stray electric and magnetic fields and ion concentrations to which high Rydberg states are extremely sensitive [14, 15, 21]: 1) To minimize magnetic fields in the photoexcitation region the extraction plates and the attached flight tube were surrounded by two cylindrical mumetal tubes in a geometry ensuring an attenuation of magnetic fields by at least three orders of magnitude. 2) The metallic plates used to apply the pulsed electric fields were carefully polished and made of demagnetized stainless steel. Their geometric arrangement (stack of six equidistant cylindrical parallel plates of total length of 7.8 cm length, each plate with a large central opening of 1.8 cm) was designed so that the minimal distance of any metallic surface from the photoexcitation region was at least 1 cm. In this way, the effects of stray fields arising at defects of the metal surfaces could be minimized and the applied electric fields

were very homogeneous across the photoexcitation region. 3) The cylindrical plates were carefully coupled by resistors and capacitors to ensure excellent impedance matching with the voltage pulse supplies. Large voltage pulses up to 6000 V could be applied with rise times of less than 50 ns, and ripples in the high voltages following the voltage rise time could be suppressed [22]. 4) The cylindrical symmetry of the spectrometer ensured minimal stray fields perpendicular to the symmetry axis, and the electrode stack permitted the accurate compensation of stray electric fields along the symmetry axis. 5) Finally, the gas inlet and pumping systems with a skimmer separating the probe gas chamber from the photoexcitation region, the optical access, and the laser intensities were carefully optimized to avoid undesirable effects arising from interactions of the Rydberg states with atoms and molecules in the background gas and with ions generated in the photoexcitation volume.

The necessity for these measures had been recognized prior to this thesis [17,22,23] but the photoexcitation region designed and built in the realm of this dissertation represented the first attempt to consider, in the design of a spectrometer in our group, all factors known to be important in studies of high Rydberg states by high-resolution spectroscopy.

The charged particles produced by photoionization or by pulsed-field-ionization following photoexcitation to a long-lived Rydberg state and extracted by the pulsed field were detected at the end of a field-free flight tube with a dual microchannel plate detector in chevron configuration. The ion or electron signal was transferred at each experimental cycle to a 500 MHz digital oscilloscope (LeCroy, WaveRunner 6050) where they were averaged over a predefined number of cycles. Temporal gates were placed at the position of the times of flight of the different charged fragments and the signal was integrated over these gates. The integrated signal was then transferred to a PC and stored on a disc together with various other signals (laser intensities, calibration signals, étalon signal, etc.).

2.2 The laser systems

The experiments were carried using a laser system consisting of a Nd:YAG pump laser (Continuum, Powerlite Precision 9030) operated at a repetition rate of 25 Hz and two dye lasers (Lambda-Physik, ScanMate 2E and Sirah, Cobra Stretch). Depending on the wave length needed for the experiments, either the second (532 nm) or the third (355 nm) harmonic output of the Nd:YAG laser was used to pump the dye lasers. Moreover, the frequency of the dye lasers could optionally be doubled using a β -Barium-Borate (BBO) crystal or tripled using two BBO crystals in series, the first to double the fundamental frequency, the second to generate a beam of a frequency corresponding to the sum of the frequencies of the fundamental and the frequency-doubled beams.

2.2.1 Experiments using VUV radiation

The investigations of the single-photon photoelectron spectrum of ND_3 and ND_3^+ presented in Chapter 3 relied on the use of VUV radiation tunable in the range of $80\,000\text{ cm}^{-1}$ and $84\,000\text{ cm}^{-1}$. Since no commercial tunable laser systems are available in the VUV region of the electromagnetic spectrum, this radiation was generated by resonance-enhanced four-wave mixing in a pulsed beam of atomic krypton used as nonlinear optical medium [24–28]. In these experiments, two additional vacuum chambers, the four-wave mixing chamber and the monochromator chamber, were used as depicted on the right-hand side of Fig. 2.1. In the four-wave mixing chamber, the nonlinear gas is introduced by means of a pulsed gas nozzle (General Valve, Series 9, with IOTA One driver; nozzle orifice diameter of 1 mm).

The VUV radiation generated by the interaction between the focused dye laser radiation and the nonlinear gas was then separated from laser beams of different wave lengths (e.g., the fundamental beams and beams generated by other nonlinear processes) using a home-built vacuum monochromator of the Seya-Namioka type, equipped with an adjustable toroidal platinum-coated diffraction grating and operated in first order. The toroidal geometry of the grating served the purpose of refocusing the initially divergent VUV radiation at the exit hole of the monochromator, enabling a clean separation of the desired beam. The VUV spot size amounted to approximately 1 mm in the photoexcitation region. The four-wave mixing chamber, which is exposed to a higher gas load, was evacuated with a turbomolecular pump of 520 l s^{-1} pumping power (Pfeiffer, TMH 521) and the monochromator, which is only connected to the other chambers by small holes, by a 260 l s^{-1} turbomolecular pump (Varian, Turbo V-300 ICE MacroTorr). In this way, the pressure in the four-wave mixing and the monochromator chambers could be maintained below 10^{-3} mbar and 10^{-6} mbar , respectively, during operation of the pulsed valves.

Two laser beams with wave numbers $\tilde{\nu}_1$ and $\tilde{\nu}_2$ were used to generate the VUV radiation by resonance-enhanced difference-frequency mixing in a pulsed atomic beam of krypton. They were recombined with a dichroic mirror and focused with a spherical lens of 25 cm focal length at the exit of the pulsed valve delivering the krypton gas beam in the four-wave mixing chamber. The beam of wave number $\tilde{\nu}_1$ corresponded to the tripled output of the first dye laser and was kept at the position of the $4\text{p}^5\ (^2\text{P}_{1/2})\ 5\text{p}'[1/2]_0 \leftarrow 4\text{p}^6\ (^1\text{S}_0)$ two-photon resonance of krypton ($2\tilde{\nu}_1 = 98\,855.0707\text{ cm}^{-1}$ [29]).

Resonance-enhanced sum- or difference-frequency mixing with a second laser beam of wave number $\tilde{\nu}_2$ leads to coherent radiation with a wave number $\tilde{\nu}_{\text{VUV}} = 2\tilde{\nu}_1 \pm \tilde{\nu}_2$ as schematically depicted in Fig. 2.3. The VUV wave number was scanned by scanning $\tilde{\nu}_2$, thus ensuring resonance enhancement of the four-wave mixing process at all VUV wave number. The bandwidth of the VUV radiation was typically 0.3 cm^{-1} , primarily limited by the bandwidth of the two dye lasers used for its generation. The VUV intensity was

monitored using a solar-blind electron multiplier (Hamamatsu). More than 10^8 photons per pulse were obtained after the monochromator which turned out to be sufficient to record PFI-ZEKE photoelectron spectra of ND_3 around $82\,000\text{ cm}^{-1}$ (see Chapter 3).

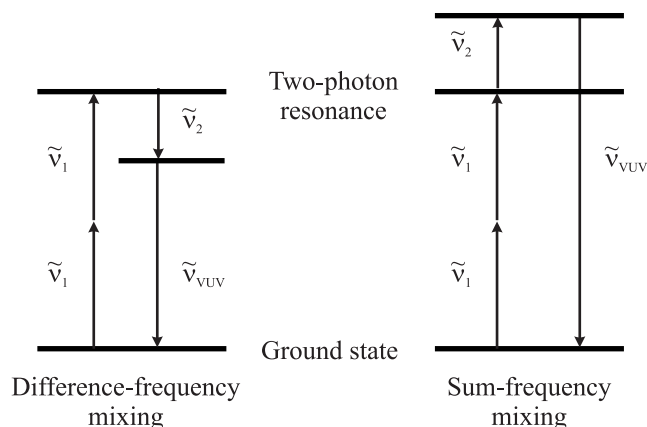


Figure 2.3: Schematic view of VUV generation using resonance-enhanced four-wave mixing in rare gases.

2.2.2 Experiments using single-photon excitation with UV radiation

The experiments carried out on metastable He and He_2 (Chapter 6), ND_4 , ammoniated ammonium clusters (Chapter 4) and metastable CO (Section 2.4.3) did not necessitate VUV radiation. The setup used in these experiments is displayed in Fig. 2.4.

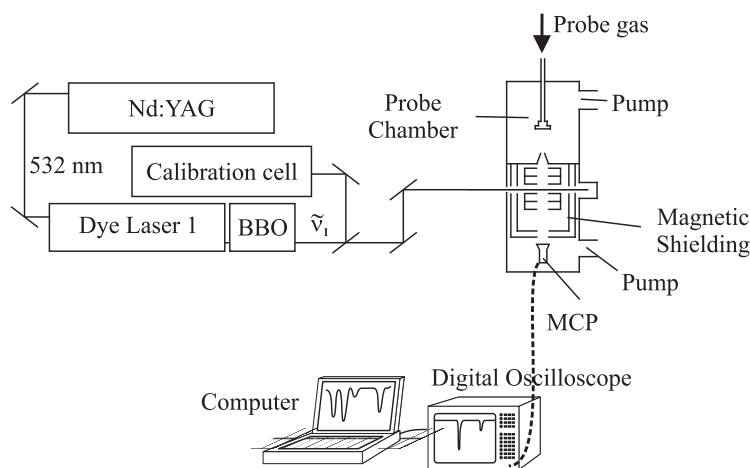


Figure 2.4: Schematic view of the experimental setup used in experiments requiring a single UV laser.

A single dye laser, the output of which was frequency doubled in a BBO crystal, was employed to excite these species to the region of the ionization thresholds. To avoid

the production of too high concentrations of ions in the photoexcitation volume, the UV radiation was not focused and its intensity was kept below $100 \mu\text{J}/\text{mm}^2$ per 8 ns long pulse.

2.2.3 Experiments using multiphoton excitation

The studies of high Rydberg states of xenon (see Chapter 5) were carried by $(2 + 1')$ resonance-enhanced three-photon excitation with the experimental setup depicted schematically in Fig. 2.5. The frequency-doubled output of a 355 nm Nd:YAG-pumped dye laser was employed to induce the $5p^5(^2P_{3/2})6p[1/2]_0 \leftarrow 5p^6(^1S_0)$ two-photon transition at $2\tilde{\nu}_1 = 80\,119.984 \text{ cm}^{-1}$ and the high ns and nd Rydberg states located below the $\text{Xe}^+ \ ^2P_{3/2}$ ionization limit were accessed from the $5p^5(^2P_{3/2})6p[1/2]_0$ intermediate level using the output (wave number $\tilde{\nu}_2$) of the second dye laser. The two lasers were recombined using a dichroic mirror and directed in a copropagating arrangement into the photoexcitation region where they intersected the xenon gas beam at right angles. In these experiments, care had to be taken to optimize the laser spot sizes in the photoexcitation region, particularly the spot size of the first laser: Indeed, whereas the efficient driving of two-photon transitions required a high intensity and some focusing, too tight a focus led to the production of high concentrations of undesirable Xe^+ ions by one-color $(2 + 1)$ resonance-enhanced three-photon ionization. In these experiments, the nonlinearity of the multiphoton excitation process and the necessity to work far below the saturation threshold for the two-photon transition led to unavoidable large signal fluctuations. The long lifetime of the intermediate state made it possible to delay the second laser pulse with respect to the first laser pulse using a delay line and thus avoid ac Stark shifts and broadenings of the transitions from the intermediate level to the Rydberg states.

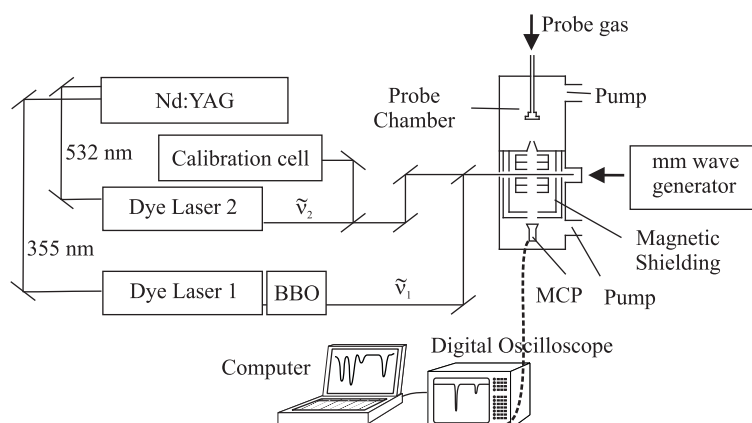


Figure 2.5: Schematic view of the experimental setup for the xenon experiment. The photon with wave number $\tilde{\nu}_1$ was used for the two-photon resonance of $80\,118.9839 \text{ cm}^{-1}$ in xenon. The photon with $\tilde{\nu}_2$ was used to prepare the Rydberg state. The millimeter-wave (mm-wave) radiation was used to induce transitions between two Rydberg states.

2.2.4 Calibration

Calibration of the dye laser wave numbers was achieved by splitting off small fractions of their fundamental outputs and directing them towards either an optogalvanic (OG) cell filled with neon or argon gas or an iodine cell where optogalvanic spectra or laser-induced fluorescence spectra were recorded, respectively. The fundamental frequency was then determined by comparing the lines in these spectra with tabulated transitions of neon or argon [30,31] or transitions listed in the I_2 atlas [32–34]. In addition, a monitor étalon spectrum of the fundamental output of the scanning laser (laser 2 in Fig. 2.1) was recorded with every measurement in order to detect and correct possible nonlinearities in the laser scans. The accuracy of the calibration procedure is estimated to be better than 0.2 cm^{-1} (OG cell) or 0.05 cm^{-1} (iodine cell) for the fundamental outputs of the dye lasers. In experiments where VUV radiation was used, the absolute accuracy of the VUV wave number is estimated to be better than 1 cm^{-1} , a conservative estimate corresponding to the sum of the uncertainties of all fundamental laser beams involved in the nonlinear frequency upconversion process.

2.3 Millimeter-wave source

The high-resolution millimeter-wave spectra of high- n Rydberg states of xenon presented in Chapter 5 were recorded with the experimental setup depicted in Fig. 2.5 which is similar to that described in Ref. [35]. The millimeter-wave source we used is a frequency- and phase-stabilized backward wave oscillator (BWO) operating in the frequency range of 240 - 380 GHz. This millimeter-wave source has been described in detail in Ref. [36] and the experimental procedure followed to record the millimeter-wave spectra was identical to that first described in Ref. [35] and subsequently reviewed in Ref. [23]. Only a brief description of the millimeter-wave source and the measurement procedure is described here and in Subection 2.5.3, and the reader is referred to the references mentioned above for a more complete description.

The millimetre-wave source is a heterodyne stabilized synthesizer (see Ref. [37], p. 198). The voltage controlled oscillator is a backward wave oscillator (BWO OB-65, from ISTOK, Fryazino, Moscow Region, Russian Federation) mounted and aligned in the 30 mm gap of a 0.7 T Nd-Fe-B alloy permanent magnet (IAPRAS, Nizhnii Novgorod, Russian Federation). The tube delivers continuous output power up to 40 mW at frequencies between 240 GHz and 380 GHz. Its operation requires a negative high voltage V_0 between -1500 V and -3800 V at an operating current in the range $10\text{--}35\text{ mA}$ for the cathode and an ac voltage of approximately 6.2 V at 1.4 A for the indirect cathode heating. The heating voltage is derived from the main power line at a frequency of 50 Hz and is connected to the cathode potential.

The BWO is driven by a commercially available controllable power supply (HCV 375M-6500, F.u.G. Elektronik GmbH, Rosenheim, Germany), which relies on all-solid-state technology, giving high reliability, a stability of $< 5 \cdot 10^{-5}$ and a repeatability of $< 10^{-3}$. Its ripple (peak to peak) is specified to be $< (10^{-5} \cdot |V_0| + 20 \text{ mV})$, which is to be expected from a switching topology.

Computer controlled sweeping of the millimeter-wave source is accomplished by varying the acceleration voltage and local oscillator frequency on the corresponding instruments over GPIB interfaces. The cathode potential is preset according to a tuning curve fitted to points measured manually:

$$V_{\text{cathode}}/V = 1387 - 19.682(f/\text{GHz}) + 0.12039(f/\text{GHz})^2 - 2.4599 \cdot 10^{-4}(f/\text{GHz})^3 + 2.9164 \cdot 10^{-7}(f/\text{GHz})^4. \quad (2.1)$$

The effective tuning curve deviates from the calculated one by offsets up to $\pm 3 \text{ V}$, which are compensated for by a phase-lock loop [36].

The frequency stability of this millimeter-wave source and the absolute accuracy of the frequency calibration are both better than 1 kHz which is negligible compared to the width of 250 kHz of the narrowest lines observed experimentally so that contributions of the millimeter-wave source to the uncertainty of the measured millimeter-wave transition frequencies can be ignored in excellent approximation.

Occasionally, the frequency dependence of the output power of the millimeter-wave source brought the source out of its lock position, leading to unusable spectra. In order to be able to identify such problematic regions in the spectra, the lock signal was continuously monitored during scans of the millimeter-wave spectra.

2.4 Probe gas samples

The study of metastable atoms and molecules, of high Rydberg states and of highly reactive species such as free radicals and molecular ions by high-resolution spectroscopy requires the development of adequate methods to produce them. Often, the best method to generate a given species in a given state is not known *a priori* and a substantial part of the experiments is invested in the search of a production method yielding concentrations of the desired species large enough for spectra of sufficient signal-to-noise ratios (i.e., at least 2) to be obtained during the typical time of four hours of a given measurement session. Longer measurements times turned out to be impractical because of the unavoidable drifts of the experimental conditions (stray fields, nozzle operation conditions, laser frequencies, temperature, etc.).

In the following subsections, the methods used to produce adequate samples for the spectroscopic investigations of the ammonium radical and ammoniated ammonium clus-

ters, metastable He and He₂, metastable CO and high Rydberg states of atomic xenon are described as used in the work presented in this thesis. Whereas several production methods were adapted from descriptions available in the literature as referred to in the next subsections, the method of producing metastable He₂ is original and represents one of the important results of this dissertation.

2.4.1 Studies of molecular cations using seeded supersonic expansion

Direct spectroscopic investigations of molecular cations are intrinsically difficult because space-charge effects limit the concentrations of cations in the gas phase to less than about 10⁸ ions/mm³. Moreover, the total number of cations is usually distributed over many quantum states because ion samples are typically hot samples. Finally, the high reactivity of molecular cations often leads to the rapid destruction of the initial sample.

The approach followed by our group to study molecular cations is by pulsed-field-ionization zero-kinetic-energy (PFI-ZEKE) photoelectron spectroscopy, a technique that will be described in more detail in Subsection 2.5.2. The advantage of this technique is that spectra of the cations are obtained from a spectroscopic measurement on the parent neutral molecule: There are no restrictions on the number density of neutral molecules imposed by space-charge effects, and, if the neutral molecule is stable, concentrations in excess of 10¹⁴ molecules/cm³ can be obtained in a supersonic expansion. This population is distributed over only a very small number of quantum states because of the low temperatures (in the range of 1-10 K) that can be reached in supersonic expansions (see above).

The studies of the reactive species ND₃⁺, ND₄⁺, ND₂ND₄⁺, NH₃NH₄⁺, and He₂⁺ are presented in the Chapters 3, 4, and 6. For these ions the experimental task lies in the preparation of the neutral sample which is trivial in the case of ND₃⁺ because it solely consists of making an adequate mixture of ND₃ and a carrier gas such as argon. In the case of ND₄⁺ and ammoniated ammonium ions, the task is less trivial because it necessitates the creation of a suitable neutral ammonia cluster precursor in the supersonic expansion and a subsequent photolytic reaction to yield the desired radical (see Subsection 2.4.3). In the case of He₂, the task is the most challenging because it necessitates the production of metastable neutral He₂ with more than 20 eV of internal electronic energy and the formation of a supersonic expansion of these molecules (see Subsection 2.4.2)

2.4.2 Discharge source of metastable He and He₂ in supersonic expansions

To generate metastable He and He₂ (in the following we shall denote these species He* for He 1s2s ³S₁ and He₂* for He₂ a ³Σ_u⁺), we found it convenient to adapt a pulsed glow discharge source similar to those described in Refs. [38,39]. Pulsed glow discharges have distinct advantages compared with continuous glow discharges [40–42]. Indeed, because the voltage and current are applied over short periods of time, higher peak voltages and currents can be obtained for the same average power, resulting in enhanced sputtering, excitation and ionization, and therefore higher signal intensities [43–46]. Moreover, the pumping requirements are much reduced.

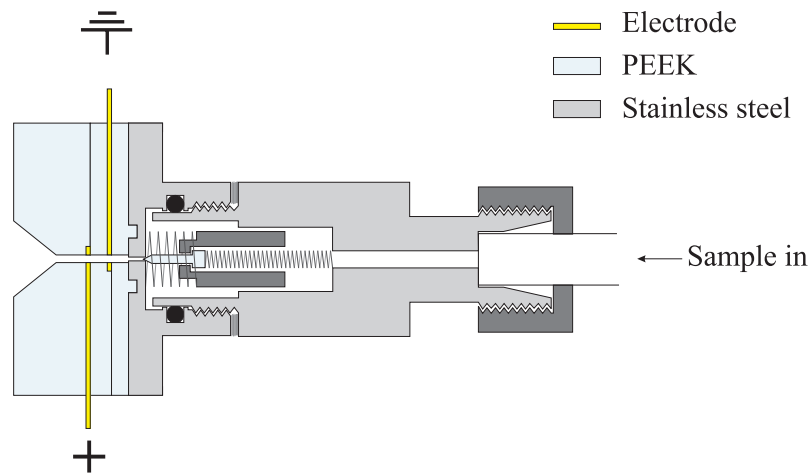


Figure 2.6: A schematic diagram of the pulsed discharge source.

One of the advantages of the discharge design used to generate metastable He and He₂ is its simplicity. By striking an intense, localized discharge behind a nozzle and by biasing the electrodes such that electrons flow against or along the gas flow, a stable, high-current discharge can be produced. In addition, the design allows the aperture to be independently biased, effectively creating a third electrode in the discharge volume. A schematic diagram of the discharge source configuration is shown in Fig. 2.6. It consists of a commercially available pulsed solenoid valve (General Valve, Series 9, with Iota One driver), several pierced extension pieces and two electrodes made of brass. The components are electrically isolated and can be biased with respect to one another. The front plate of the pulsed valve is separated from the cathode by a polyetheretherketone (PEEK) insulator. The discharge occurs through the channel of a second insulator to the anode. A high dc voltage is applied to the electrodes through an electrical circuit. The discharge takes place in a small region between the electrodes, when a high-voltage (HV) pulse is applied to one of the electrodes just after the gas is pulsed through the valve. The pulsed valve is operated at stagnation pressures ranging from 1 to 4 bar at a repetition

rate of 25 Hz for pulse durations between $170\ \mu\text{s}$ and $270\ \mu\text{s}$.

To create the discharge, the front electrode is biased positively with respect to the rear electrode by applying a high-voltage pulse. This arrangement results in electrons being accelerated in the direction of the gas flow and creates a stable and intense discharge localized upstream from the exit of the source.

The stability of the operation of the discharge unit can be verified by observing the reproducibility of the current pulses. In order to deflect charged particles so that they do not fly through the skimmer into the measurement chamber, a voltage is applied to deflecting electrodes mounted downstream of the nozzle and connected to the discharge electrodes.

The operational characteristics of the metastable source are conveniently characterized by time-of-flight (TOF) mass spectrometry. In the case of He^* and He_2^* metastables, the yield of metastable atoms and molecules can be probed following ionization with a UV laser by TOF mass spectrometry as illustrated by Fig. 2.7.

TOF spectra such as that displayed in Fig. 2.7 can be used to optimize the production of a given species by systematically changing the source conditions (nozzle stagnation pressure, discharge current and voltage, timing of the discharge pulse) so as to maximize the corresponding signal.

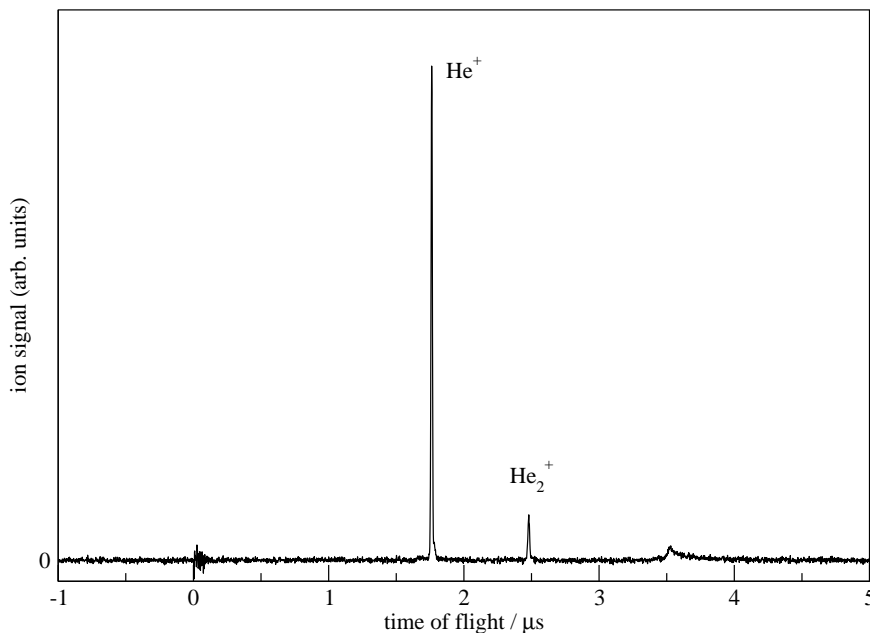
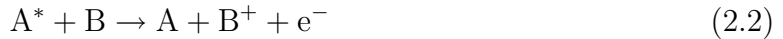


Figure 2.7: Time-of-flight mass spectrum of He^+ and He_2^+ recorded following photoionization of He^* and He_2^* with a UV laser of wave number $39\,603.96\ \text{cm}^{-1}$ and extraction of the ions with a pulsed electric field.

In our attempts to extend this method of generating metastable atoms and molecules to other rare gas samples and mixtures of rare gases, we found several important limita-

tions. Firstly, if the He sample is diluted in Ar, Kr or Xe, the formation of metastable helium atoms and molecules is entirely quenched by a process known as Penning ionization, as first described by Penning in 1927 [47]. This process, described by Eq. (2.2),



occurs very efficiently whenever the internal electronic energy of the metastable state exceeds the ionization energy of B. The only carrier gas other than helium for which reaction (2.2) cannot take place in the presence of metastable He for energetic reasons is neon. The effects of Penning ionization observed after striking a discharge in a mixture of He and Xe is demonstrated in Fig. 2.8 which shows the distribution of times of flight of the ions and the metastable species from the discharge region to the detector. The early peak corresponds to photons produced in the discharge and which reach the detector almost instantaneously. The next weak peak observed at a time-of-flight of about $40 \mu\text{s}$ can be attributed to Xe^+ ions produced by Penning ionization with metastable helium atoms and which are accelerated toward the detector. The broad peak centered around 1.1 ms corresponds to metastable Xe atoms which cannot be destroyed by Penning ionization and fly as neutral atoms all the way to the microchannel plate (MCP) detector. They are observed at the detector because their internal energy exceeds the work function of the front plate of the MCP. No He^* atoms are observed.

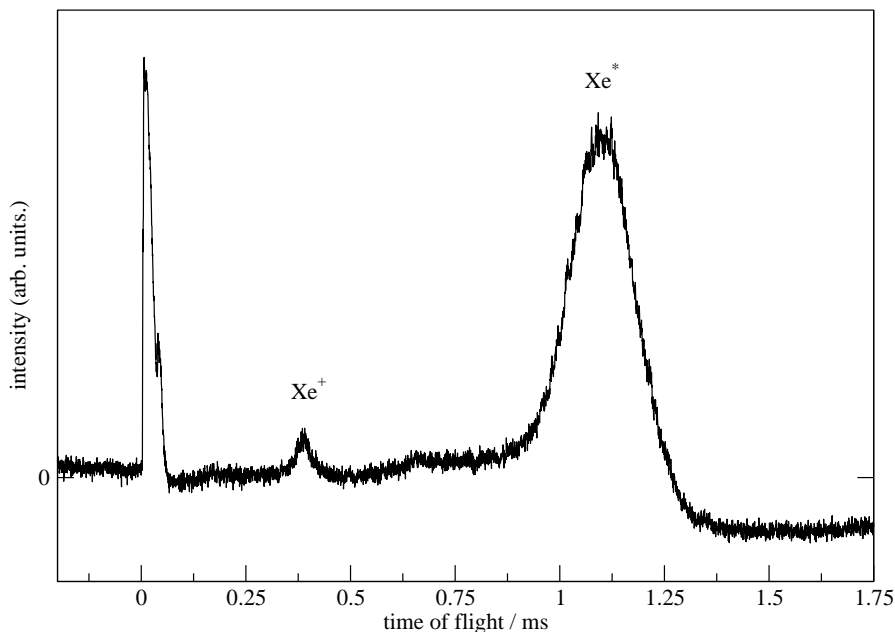


Figure 2.8: Time-of-flight of Xe^+ after collision and subsequent Penning ionisation with metastable helium. In this picture the full time-of-flight trace is shown. The peak at $t = 0$ corresponds to photons produced in the discharge.

Secondly, of all rare gas dimers, only metastable helium dimers were found to be

long-lived enough to survive the time of several tens of microseconds needed to travel from the discharge region to the photoexcitation region. This observation is compatible with the observations of Oka *et al.* [48] who found the lifetimes of the triplet states to decrease rapidly from He₂ to Xe₂ because of the growing admixture of singlet ($S = 0$) character induced by the increasing spin-orbit interaction.

2.4.3 Optical preparation of metastable states

Metastable states of atoms and molecules can also be prepared by driving forbidden transitions with intense laser fields. Two cases have been examined in this thesis: the production of metastable high Rydberg states of Xe by $(2 + 1')$ resonance-enhanced three-photon excitation for subsequent investigation of millimeter-wave transitions between high Rydberg states of Xe (see Chapter 5) and the preparation of the metastable lowest triplet state ($a^3\Pi$) of CO by single-photon excitation from the $X^1\Sigma^+$ ground state.

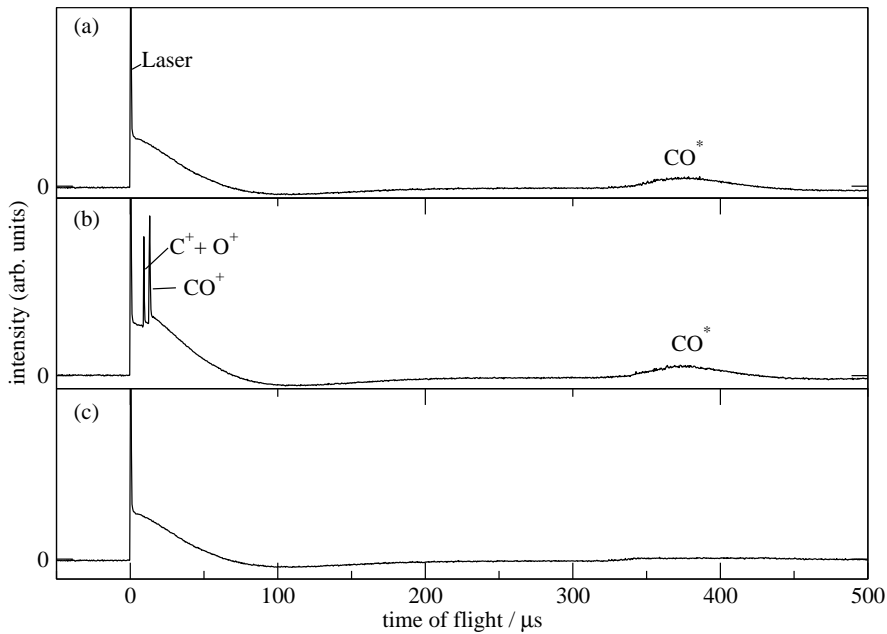


Figure 2.9: Time-of-flight spectrum illustrating the production of metastable CO* $a^3\Pi_{\Omega=1}$ molecules in a supersonic expansion. a) TOF spectrum recorded without applying any voltage on the extraction plates surrounding the photoexcitation region. b) TOF spectrum recorded with a voltage of 1 kV on the repeller plates of the extraction region. c) TOF spectrum recorded under the same conditions as b) but after detuning the UV laser.

The formation of metastable CO ($a^3\Pi_{\Omega=0-2}$, denoted below as CO*) following single-photon excitation from the CO $X^1\Sigma^+$ ground state at a wave number of $48\,486\text{ cm}^{-1}$ is illustrated by the TOF spectra depicted in Fig. 2.9. The top trace (a) was obtained by monitoring the CO* molecules arriving at the MCP detector where their internal energy (6 eV) causes ionization because it exceeds the work function of the alloy at the MCP

surface. The middle trace (b) was obtained under the same conditions as trace (a) with the only difference that a voltage was applied to the extraction plates to also accelerate ions produced by the UV laser. The ions (C^+ , O^+ and CO^+) are observed as sharp features of times of flight of $\approx 10 \mu s$. The broad peak corresponding to CO^* is unaffected by the voltage which proves that the metastables fly as long-lived neutral molecules all the way to the detector for $400 \mu s$. The bottom trace (c) was recorded under the same conditions as trace (b) but after detuning the UV laser. This trace demonstrates that CO^* is produced by optical excitation from the ground state.

Spectra of the forbidden $a^3\Pi_{\Omega=0-2} \leftarrow X^1\Sigma^+$ transition can be recorded by setting an integrating time gate at the position in the TOF spectra corresponding to the CO^* molecules and monitoring the integrated signal as a function of the wave number of the UV laser. An example illustrating the production of CO^* a $^3\Pi_{\Omega=1}$ metastables is depicted in Fig. 2.10. The spectral features observed in this spectrum correspond to the formation of low rotational levels of the $a^3\Pi_{\Omega=1}$ states from the lowest ($J'' = 0, 1$ and 2) rotational levels of the $X^1\Sigma^+$ ground state of CO. The signal-to-noise ratio in this spectrum is limited by the large width of the integrating time gate and fluctuations of the UV laser intensity.

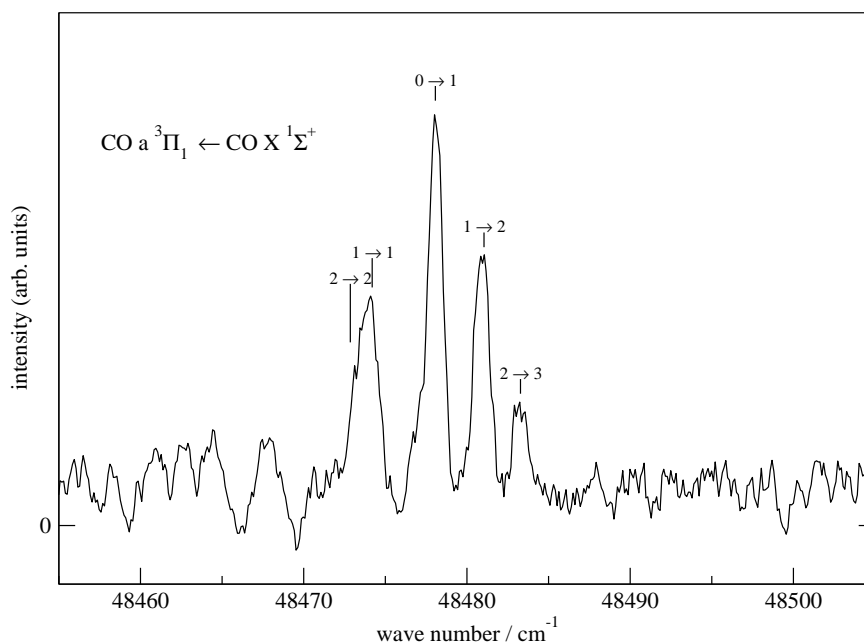


Figure 2.10: Spectrum of the "forbidden" $a^3\Pi_{\Omega=1} (v' = 0) \leftarrow X^1\Sigma^+ (v'' = 0)$ transition of CO obtained by recording the CO^* molecules at the MCP detector after a flight time of $400 \mu s$ as a function of the wave number of a UV laser.

The possibility of generating metastable $a^3\Pi_{\Omega}$ CO molecules is not only interesting in view of high-resolution spectroscopic studies of high Rydberg states of CO having $S = 1$ character but also in the context of recent experiments in our group in which

multistage Zeeman deceleration and magnetic trapping is used to generate cold molecular samples [49, 50].

2.4.4 Photolysis source of metastable radicals in supersonic expansions

Recently, Willitsch *et al.* [51] have developed a source of cold radicals in supersonic expansions that relies on the photodissociation of suitable precursor molecules in a quartz capillary mounted at the orifice of a pulsed valve. The formation of a supersonic expansion into the vacuum at the exit of the capillary led to very efficient cooling of the internal (rotational and vibrational) degrees of freedom of the radical. In combination with PFI-ZEKE photoelectron spectroscopy, this method turned out to be a powerful way to obtain spectroscopic informations on the neutral radicals and the cations formed by photoionization, as illustrated by studies of the PFI-ZEKE photoelectron spectrum of NH_2 [52], C_5H_5 [53], and CH_3 [54].

Unfortunately, when the radicals are unstable and decay by predissociation on the microsecond time scale or faster this method cannot be employed because the radicals decay during the flight from the exit of the capillary orifice to the region where the photoionization is carried out. In this case, it is more convenient to carry out the photodissociation of the precursor molecule directly in the photoionization region. An example of such an unstable radical is the ammonium radical studied by PFI-ZEKE photoelectron spectroscopy by Palm *et al.* [55] and Signorell *et al.* [56] (see also Subsection 4.3.1). The study of metastable ammoniated ammonium radicals presented in Chapter 4 relied on the same method as used in Refs. [55, 56]. The optimization of the radical cluster yield was carried out by photoionization mass spectrometry illustrated in Fig. 2.11 for ammoniated ammonium radical clusters formed by photodissociation of ammonia clusters.

The top trace in this figure displays the TOF spectrum obtained by collecting the ions produced by the 206 nm photolysis laser only, i.e., the laser producing the ammoniated ammonium clusters from ammonia clusters (The production mechanism will be discussed in more detail in Chapter 4). The middle trace (b) in Fig. 2.11 shows the TOF spectrum obtained after photoexcitation/photoionization with a second UV laser of wave number $32\,051.28\text{ cm}^{-1}$ delayed by 15 ns with respect to the photolysis laser, and the bottom trace (c) shows the same spectrum from which, however, the ionization signal from the photodissociation laser was subtracted. This trace is free from background ionization signals from the photodissociation laser and enables one 1) to determine and optimize the yield of metastable radicals produced by the photodissociation laser, and 2) to study these radicals without interfering contributions to the signals from the photodissociation laser.

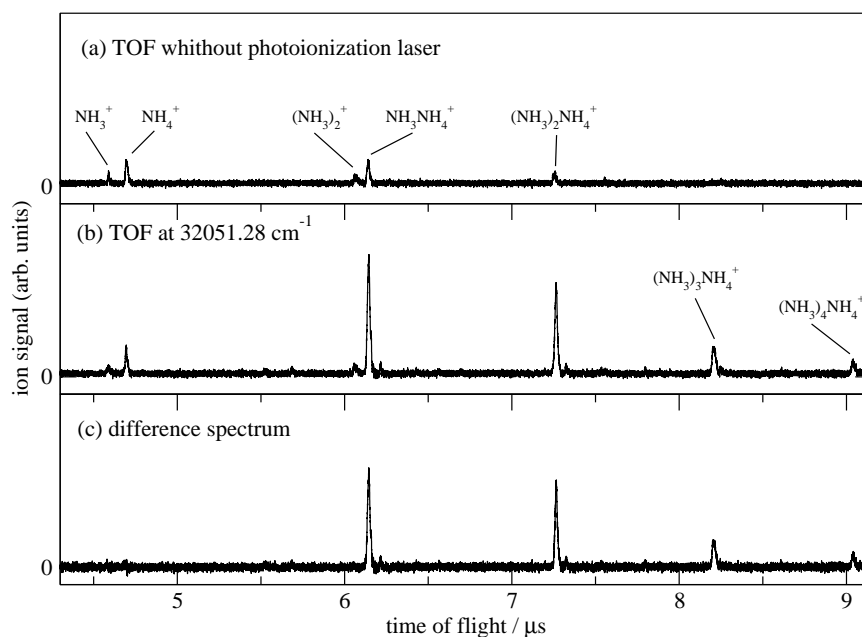


Figure 2.11: Ion TOF mass spectra of ammonia and ammoniated ammonium radical clusters. a) Background TOF mass spectrum generated by the photodissociation laser alone. b) TOF mass spectrum including background signal, obtained following photodissociation and photoionization. c) Difference spectrum obtained by subtracting trace a) from trace b). This spectrum enables one to observe the photoionization of the photodissociation products with interference from undesirable photoionization by the photodissociation laser.

2.5 Spectroscopic methods

All experiments carried out in the realm of this dissertation were performed by detecting charged particles (electrons or cations) produced either by photoionization or by the pulsed-electric-field ionization of long-lived Rydberg states. Detecting charged particles is very efficient – efficiencies of 50% or more are routinely achievable – and offers the important advantage of being background-free, i.e., the signal vanishes outside the resonances. These advantages result in a very high sensitivity which represents an essential advantage in studies of reactive or unstable species that are only formed in low concentrations. They are at the heart of the three spectroscopic methods used in this thesis and which are described in the next subsections: photoionization spectroscopy in Subsection 2.5.1, pulsed-field-ionization zero-kinetic-energy (PFI-ZEKE) photoelectron spectroscopy in Subsection 2.5.2 and millimeter-wave spectroscopy of high Rydberg states in Subsection 2.5.3.

2.5.1 Photoionization spectroscopy

In photoionization spectroscopy, the yield of charged fragments produced following photoexcitation of a molecule with a tunable light source is monitored as a function of the

frequency of the light source [57, 58]. In the most commonly used variant of photoionization spectroscopy, the fragment ions produced after photoexcitation of the parent molecule (designated here by ABC) are monitored by time-of-flight mass spectrometry which enables one to distinguish between different product channels:



⋮

Process (2.3) corresponds to the photoionization of the parent molecule, and processes (2.4) through (2.8) describe several possible dissociative ionization channels. Several continua corresponding to the energetically accessible quantum states of the charged fragments can contribute to the ion signal recorded at a given mass and, usually, the ion yield displays resonances corresponding to photoexcitation to Rydberg states of the parent molecule ABC that belong to series converging on excited states of the cation ABC^+ , as illustrated in Fig. 2.12 and described in its caption. Photoionization spectra are therefore highly structured, very complex and difficult to analyze. Usually, photoionization spectra are used to determine the appearance thresholds of the fragments, e.g. ABC^+ , AB^+ , A^+ , etc., which, in favorable cases, can be further used to derive thermochemical quantities such as the adiabatic ionization energy of ABC or the dissociation energies of ABC^+ in various fragments such as $\text{AB}^+ + \text{C}$, $\text{A}^+ + \text{BC}$, etc. In general, the presence of autoionization resonances prevents the unambiguous determination of ionization thresholds corresponding to excited states of the fragments, and renders the appearance of photoionization spectra extremely complex [16, 57, 58]. The photoionization spectra of He_2^* , presented in Chapter 6, represents an excellent example of this complexity (see, e.g., Fig 6.8).

To record a photoionization spectrum, the ions are usually extracted from the photoionization region by an electric field and directed through a field-free flight tube towards a detector, typically a microchannel plate detector. The electric field also has the effect of lowering the ionization thresholds and this effect must be corrected in the determination of ionization energies. When a dc field is used to extract the ions, the lowering of the ionization thresholds can be accurately determined using a simple classical picture by calculating the saddle point in the potential $V(r)$ resulting from the sum of the Coulomb

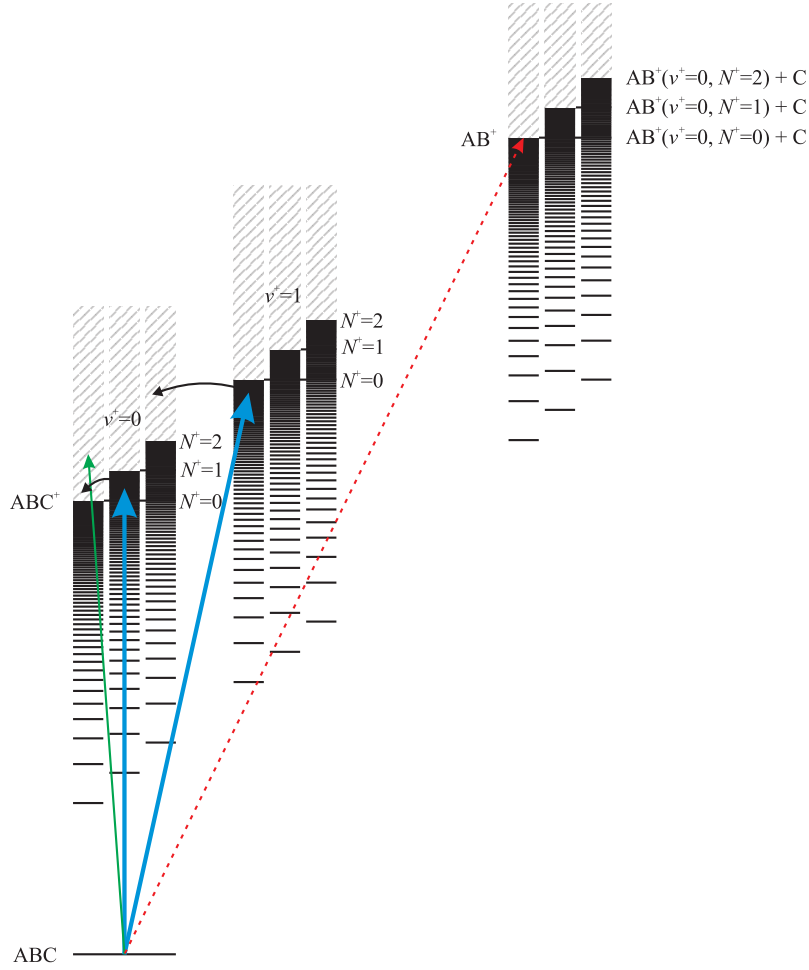


Figure 2.12: Energy level diagram illustrating the different photoionization channels of a polyatomic molecule. The ionization and dissociative ionization thresholds are marked by thick horizontal bars above which the shaded areas represent continua. These thresholds are characterized by the quantum states of the fragments. Infinite series of Rydberg states converge to each threshold. The full arrow designates direct ionization; the thick blue arrows represent ionization processes via excited states of the parent molecule, giving rise to so-called autoionization resonances in the photoionization yield; the dashed (red) arrow represents the process of dissociative ionization.

potential binding the electron to the cation $V_C(r) = -\frac{e^2}{4\pi\epsilon_0 r}$, where $r = |\vec{r}|$ and $\vec{r} = (x, y, z)$ represents the position vector of the electron relative to the center of charge of the cation, and the potential of the electron in the applied electric field ($e\mathcal{E}z$, if the field is applied in the z direction, i.e., if $\vec{\mathcal{E}} = (0, 0, \mathcal{E})$):

$$V(r) = -\frac{e^2}{4\pi\epsilon_0 r} + e\mathcal{E}z. \quad (2.9)$$

This saddle point is shifted from the field-free ionization energy E_I to lower energies by

$$\frac{\Delta E_I}{hc \text{ cm}^{-1}} = 6.12 \sqrt{\frac{\mathcal{E}}{\text{V/cm}}} \quad (2.10)$$

as can be easily determined from Eq. (2.9).

When a pulsed field is used to extract the charged fragments, the details of the field ionization dynamics must be considered in the determination of the field-induced lowering of the thresholds [14–16, 59]. In general, a reasonable approximation for the lowering of the ionization thresholds when the pulsed field does not exceed 10 V cm^{-1} and is applied with a rise time in the ns range is [15, 16]

$$\frac{\Delta E_1}{hc \text{ cm}^{-1}} = 4\sqrt{\frac{\mathcal{E}}{\text{V/cm}}}. \quad (2.11)$$

If the applied field is larger and applied with slower rise times, Eq. (2.10) represents a better approximation than Eq. (2.11).

Photoionization spectra can be recorded either directly from the ground state, or from a metastable state following single-photon excitation, or via an intermediate excited state of the parent molecule using several photons. In the latter case, one usually calls the photoionization spectra "REMPI spectra" for "resonance-enhanced multiphoton ionization spectra".

2.5.2 PFI-ZEKE photoelectron spectroscopy

Photoionization spectroscopy offers the advantage of being mass-selective but usually cannot be used to determine any ionization threshold other than the lowest one because of autoionization processes. Photoelectron spectroscopy is exactly complementary. It enables one to determine the ionization thresholds by measuring the kinetic energy of the photoelectrons but it does not provide any information on the mass of the parent molecule or the ionic products.

Photoelectron spectroscopy has a long history in studies of the electronic structure of atoms and molecules [60, 61]. In the present dissertation, a variant of photoelectron spectroscopy called pulsed-field-ionization zero-kinetic-energy (PFI-ZEKE) photoelectron spectroscopy [6, 7] has been used.

In a PFI-ZEKE photoelectron spectrum, one monitors the yield of electrons produced by the delayed pulsed-field-ionization of very high Rydberg states located just below the ionization thresholds as a function of the frequency of the photoionizing radiation (see Fig. 2.13b). This is in contrast to conventional (He I) photoelectron spectroscopy which relies on the measurement of the kinetic energy distribution of the photoelectrons produced following photoexcitation with radiation of fixed frequency (see Fig. 2.13a).

The advantage of PFI-ZEKE photoelectron spectroscopy over He I photoelectron spectroscopy results from the fact that the measurement of the electron kinetic energies, which is difficult, is bypassed (see Ref. [7] for details).

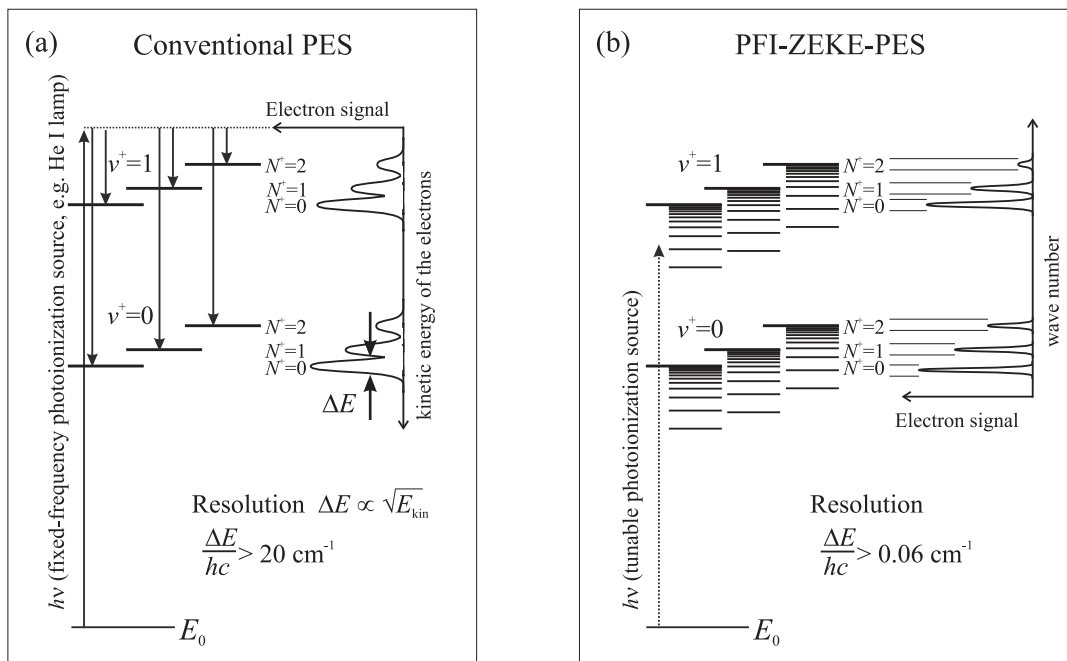


Figure 2.13: Comparison of conventional photoelectron spectroscopy (panel (a)) and PFI-ZEKE photoelectron spectroscopy (panel (b)). With the former technique the ionization energies E_I are determined by ionizing with a fixed-frequency light source (typically a He I source) and measuring the kinetic energy of E_{kin} of the photoelectrons using $E_I = h\nu - E_{\text{kin}}$. With the latter technique, they are determined by detecting the field-ionization of high Rydberg states as a function of the frequency of a tunable light source.

The electrons contributing to a PFI-ZEKE photoelectron spectrum stem exclusively from the field-ionization of long-lived high Rydberg states because electrons emitted in the ionization continua escape from the photoexcitation region before the pulsed electric field is applied. A PFI-ZEKE photoelectron spectra thus provides a map of the relative positions of the ionic energy levels with respect to those of the parent neutral molecule. Usually, small pulsed electric fields are used so that Eq. (2.11) can be used to determine the field-free ionization thresholds from the positions of the lines in the PFI-ZEKE photoelectron spectra.

The best resolution achievable by PFI-ZEKE photoelectron spectroscopy is obtained using multipulse electric field sequences [59, 62, 63]. In combination with narrow-band tunable VUV laser light sources, multipulse electric field sequences enable the recording of photoelectron spectra at a resolution of better than 0.1 cm^{-1} [59] which is sufficient to observe the full rotational structure in the spectra of polyatomic molecules such as ethylene [64], ozone [65], the cyclopentadienyl radical [66] and allene [67].

The line intensities in PFI-ZEKE photoelectron spectra do not only reflect the direct photoionization cross sections but are usually influenced by autoionization resonances of the kind depicted in Fig. 2.12 (see Refs. [16, 68] for more details). Examples will be

discussed in the Chapters 3 and 6. The analysis of the intensity distributions in PFI-ZEKE photoelectron spectra thus provide valuable information on the interactions between the different ionization channels [69, 70] and can be carried out using multichannel quantum defect theory (MQDT) [71, 72].

2.5.3 Millimeter-wave spectroscopy of high Rydberg states

By measuring transitions between neighboring high Rydberg states using millimeter waves, it is also possible to obtain spectroscopic informations on high Rydberg states and, by extrapolation of the Rydberg series, to determine the ionization thresholds [23, 73, 74]. In comparison to PFI-ZEKE photoelectron spectroscopy, a much higher resolution and a much higher precision can be achieved in the determination of ionization thresholds for several reasons: Firstly, millimeter-wave radiation sources have bandwidths of less than 1 kHz. Secondly, the Doppler width of spectral lines, which is proportional to the frequency, is extremely small in the millimeter-wave range of the electromagnetic spectrum. Thirdly, the continuous-wave nature of the millimeter-waves permits very long measurement times, which translates into a very high spectral resolution. A further advantage of millimeter-wave spectroscopy to study Rydberg states close to the ionization thresholds is that the transition moments scale as n^2 and the intensities as n^4 .

In previous studies in our group, millimeter-wave spectroscopy has been used to measure the hyperfine structure of high Rydberg states of ortho-H₂ [73], para-D₂ [75], and of ⁸³Kr [74], and to determine the hyperfine structure of the X ²Σ_g⁺ ($v^+ = 0$, $N^+ = 1$) ground state of ortho-H₂⁺ and para-D₂⁺ and of the ²P_{3/2} ground state of ⁸³Kr⁺ by extrapolation of the series using MQDT.

The very high (sub-MHz) resolution of millimeter-wave spectroscopy can only be fully exploited if both the initial and final Rydberg states of the transition have lifetimes longer than 1 μs. Such long lifetimes are not unusual in high Rydberg states because the decay rate of such states by fluorescence, predissociation or autoionization all scale as n^{-3} . High Rydberg states thus form an important class of metastable states [21].

The following procedure was followed to record millimeter-wave spectra of Rydberg states [35]: Firstly, long-lived Rydberg states are identified by recording a delayed pulsed-field-ionization spectrum of the atom or molecule of interest using tunable laser radiation and a single-photon or a multiphoton excitation scheme. The wave number of the laser is then kept fixed at the position of a transition to a long-lived Rydberg state and the excited atoms or molecules are allowed to interact with the millimeter-wave radiation for a predefined length of time (typically several microseconds to achieve sub-MHz resolution). Finally, the transitions are detected by selectively field-ionizing the final state of the millimeter-wave transition. The field-ionization signal is strongly enhanced whenever the millimeter-wave frequency corresponds to a transition between Rydberg states, and

a millimeter-wave spectrum is recorded by monitoring the field-ionization signal as a function of the millimeter-wave frequency.

To ensure that only the final state of the millimeter-wave transition is ionized by the electric field, one reduces the amplitude of the pulsed electric field in the absence of millimeter-wave irradiation until the field-ionization signal of the initial state disappears. Then one turns the millimeter-wave generator on and starts scanning its frequency. This procedure restricts the detection to transitions to Rydberg states of higher principal quantum number than the initial state.

If one chooses an initial Rydberg state with $n \geq 45$ one can always observe transitions to at least two neighboring final states of the same series within the tunable range of our millimeter wave source (240 - 380 GHz, see Section 2.3 and [36]). In a measurement series, one records millimeter-wave spectra from several different initial states which enables one to systematically reconstruct initial- and final-state combination differences on the basis of which the series can be assigned, the level positions determined and the series extrapolated to their limits.

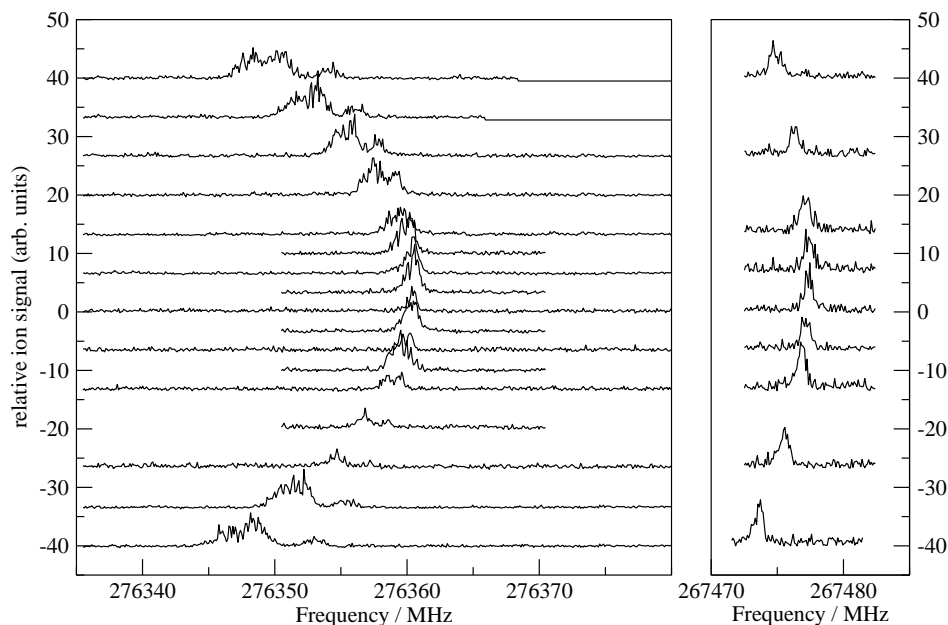


Figure 2.14: Millimeter wave transitions between Rydberg states of ^{132}Xe in the presence of different electric fields. The spectra are shifted along the vertical axis by an offset corresponding to the value of the applied field in mV cm^{-1} (from -40 mV cm^{-1} to $+40 \text{ mV cm}^{-1}$). The $57f[3/2]_2 \leftarrow 53d[1/2]_1$ transition at 276360.5 MHz (left) exhibits a stronger Stark effect than the $61p[5/2]_2 \leftarrow 55s[3/2]_1$ transition at 267477.3 MHz (right). This procedure yields the value of the compensation field necessary to minimize the stray field.

Because of the very high-resolution and precision of these measurements, great care must be taken to avoid artefacts, caused by stray electric fields and ac Stark shifts. To avoid such artefacts, the power of the millimeter-waves are attenuated until no further

level shifts is observed and the stray electric fields are carefully minimized using a method established in Refs. [17,35] and illustrated in Fig. 2.14 by a typical stray-field measurement and compensation procedure carried out as part of the studies of the hyperfine structure of high Rydberg states of Xe presented in Chapter 5. In this measurement, a selected transition, the $57f[3/2]_2 \leftarrow 53d[1/2]_1$ transition, was measured in the presence of several electric fields applied intentionally along the axis of the stack of extraction plates (see Fig. 2.2). The transition frequency shifts according to the quadratic Stark effect and form a parabolic curve, the apex of which corresponds to the applied electric field which exactly compensates the stray field. Stray field components perpendicular to this axis are usually negligible because of the cylindrical symmetry of the photoexcitation region.

By taking the measures described above to minimize dc and ac Stark shifts, millimeter-wave transition frequencies between Rydberg states can be determined with an absolute accuracy of better than 1 MHz (see also Chapter 5).

Chapter 3

The PFI-ZEKE photoelectron spectrum of ND₃: photoionization dynamics and ionization energy of ND₃ and structure of ND₃⁺

Molecular ions, though usually not metastable in their electronic ground state, are highly reactive and cannot be generated in high concentrations in the gas phase because of space charge effects. This chapter illustrates the use of pulsed-field-ionization zero-kinetic-energy (PFI-ZEKE) photoelectron spectroscopy to determine the rovibrational energy level structure of ND₃⁺ at low energies. The analysis of the intensity distributions in the PFI-ZEKE photoelectron spectra also provided insights into the photoionization dynamics of ammonia.

3.1 Introduction

Ammonia represents a prototypical polyatomic molecule. The \tilde{X} (¹A₁) neutral ground state of NH₃ and its isotopomers has been studied extensively by microwave and IR spectroscopy [76–80]. The ground state is subject to a large amplitude inversion motion along the so-called umbrella mode ν_2 and the rotational levels are split in tunneling doublets separated by 0.8 cm⁻¹ in NH₃ [78,79] and 0.0531 cm⁻¹ in ND₃ [80]. The equilibrium structure is of C_{3v} geometry, but the tunneling eigenstates are more conveniently classified in the D_{3h}(M) molecular symmetry group [81].

The electronically excited states of ammonia have been studied by REMPI spectroscopy and can be described as being of planar geometry and Rydberg character [82–86]. Most bands of the electronic spectrum are diffuse because of rapid predissociation. The \tilde{X}^+ (²A₂⁺) ground state of NH₃⁺ is also planar and has been primarily studied by He I

photoelectron spectroscopy [60,87] and IR spectroscopy [88–90].

Because of the geometry change that takes place upon ionization the photoelectron spectra of NH₃ and ND₃ consist of a very long vibrational progression in the out-of-plane bending (umbrella) mode with almost vanishing Franck-Condon factors for the origin band as illustrated by Fig. 3.1, which presents a reproduction of the He I photoelectron spectrum of NH₃ [87]. The attribution of the origin band remained controversial until the measurement of the PFI-ZEKE photoelectron spectrum following (2+1′) resonance-enhanced two-photon excitation via selected rovibrational levels of the \tilde{B} (¹E′′) Rydberg state by Müller-Dethlefs and coworkers [91]. Single-photon PFI-ZEKE photoelectron spectra of NH₃ have been reported by Niu and White [92], by Ng and coworkers [93,94], by Seiler *et al.* [95], and of NH₂D and ND₂H by Willitsch and coworkers [96]. The mass-analyzed threshold ionization spectrum of ND₃ has been recorded following (2+1′) resonance-enhanced multiphoton excitation by Dickinson *et al.* [72] who have also modeled the intensity distributions in the spectra by multichannel quantum defect theory. Finally, high-resolution photoionization spectra of NH₃, NH₂D, ND₂H, and ND₃ have been recorded in the vicinity of the adiabatic ionization threshold [95]. These spectra have an extremely complex structure, display a large number of lines of strongly differing intensities, widths and spacings. While progress in the assignment of these spectra could be made in the cases of NH₃, NH₂D, and ND₂H [95,96] for which the single-photon PFI-ZEKE photoelectron spectra have been analyzed, the large uncertainties in the positions of the low-lying rovibrational ionization thresholds of ND₃ have so far prevented progress in the analysis of the photoionization spectrum of ND₃. Determining the positions of the thresholds associated with the first three out-of-plane bending levels of ND₃ represented the main motivation for the study presented in this chapter.

A second motivation was the desire to obtain information on the photoionization dynamics and photoionization selection rules that would help to clarify contradictory statements made in the literature: Niu *et al.* [92] indeed concluded that several lines in their single-photon PFI-ZEKE photoelectron spectra could only be explained by assuming that the photoelectron is emitted as partial waves of odd- ℓ angular momentum characteristics, from which they concluded that the ionization takes place from an sp³ hybridized orbital associated with a pyramidal configuration and that rotational and orbital assignments in the photoelectron spectrum of NH₃ must be made in the C_{3v} point group, and this even for several lines in which the tunneling splitting could be partially resolved. In a reinvestigation of the first out-of-plane bending levels of the PFI-ZEKE photoelectron spectrum of NH₃ at higher resolution, Seiler *et al.* [95] could not observe a single line that could be attributed unambiguously to the emission of odd- ℓ photoelectron partial waves, and concluded that the emission of even- ℓ partial waves is dominant in the threshold ionization of ammonia. Moreover, they did not find it at all necessary to make assign-

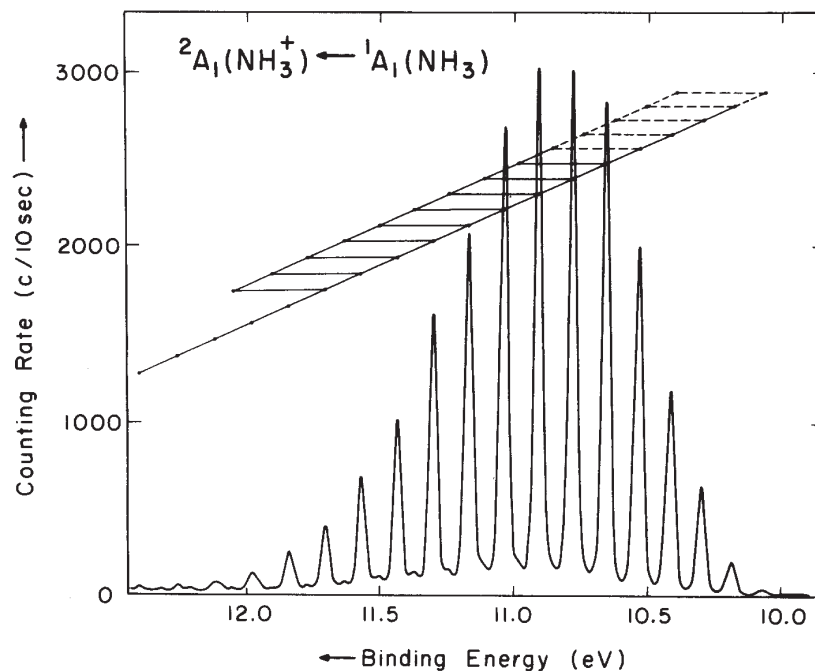


Figure 3.1: The photoelectron spectrum of the $\tilde{X}^+ 2A_1'' \text{NH}_3^+ \leftarrow \tilde{X} 1A_1' \text{NH}_3$ transition of ammonia excited by He I resonance radiation. The spectrum consists of a long progression of vibrational band starting at 10.073 eV. The spectrum is taken from Rabalais *et al.* [87] who labeled the electronic states using the C_{3v} point group.

ments in the C_{3v} point group, but used instead the D_{3h} molecular symmetry group. Ng and coworkers [93,94] measured the PFI-ZEKE photoelectron spectrum of many excited bending levels of NH_3^+ and followed the same argumentation as Niu *et al.* [92], assigning many transitions as associated with the emission of odd- ℓ photoelectron partial waves. Hollenstein *et al.* [96] finally assigned all lines in the photoelectron spectrum of NH_2D and ND_2H as arising from the emission of even- ℓ photoelectron partial waves but suggested possible rovibrational channel interactions that could, in exceptional cases, make the emission of odd- ℓ photoelectron partial wave possible in the photoionization spectrum of ammonia.

The fully resolved photoelectron spectra of ND_3 obtained in the realm of this dissertation offered another opportunity to the relative importance of even- and odd- ℓ photoelectron partial waves in the photoionization of ammonia.

This chapter is structured as follows. The rovibronic photoionization selection rules of ammonia are presented in Section 3.2. Section 3.3 provides a brief description of the experimental procedure. The main results are described in Section 3.4 and the chapter ends with a short conclusion in Section 3.5.

3.2 Rovibronic photoionization selection rules for the $\tilde{X}^+ \ ^2A_2'' \leftarrow \tilde{X} \ ^1A_1'$ photoionizing transition of ND₃

Because of the planar nature of the $\tilde{X}^+ \ (^2A_2'')$ cationic ground state, the rovibronic transitions observed in the photoelectron spectrum of ammonia are conveniently classified in the molecular symmetry group $D_{3h}(M)$ [81]. The general rovibronic selection rules for the photoionization (or for transitions to Rydberg states) of polyatomic molecules derived in Ref. [97] can be expressed as:

$$\Gamma_{\text{rve}}^+ \otimes \Gamma_{\text{rve}}'' \otimes \Gamma_{\text{e}^-} \supseteq \Gamma^*, \quad (3.1)$$

where Γ_{rve}^+ and Γ_{rve}'' represent the rovibronic symmetries of the cationic and neutral states, Γ_{e^-} the symmetry of the photoelectron wave function, and Γ^* the dipole moment representation (i.e., A_1' in $D_{3h}(M)$). For even- ℓ (odd- ℓ) partial waves Γ_{e^-} is equal to A_1' (A_1''). For ND₃ these rovibronic selection rules can be written as

$$\begin{aligned} A_1'' &\leftrightarrow A_1' \\ A_2'' &\leftrightarrow A_2' \\ E'' &\leftrightarrow E' \end{aligned} \quad (3.2)$$

for even- ℓ partial waves and

$$\begin{aligned} A_1'' &\rightarrow A_1'' \\ A_1' &\rightarrow A_1' \\ A_2'' &\rightarrow A_2'' \\ A_2' &\rightarrow A_2' \\ E'' &\rightarrow E'' \\ E' &\rightarrow E' \end{aligned} \quad (3.3)$$

for odd- ℓ partial waves.

A schematic energy level diagram of the rotational energy levels of the $\tilde{X} \ ^1A_1'$ vibronic ground state of ND₃ and of the first two out-of-plane bending levels ($2^0, 2^1$; the notation implies $v_2^{v_2^+}$) of the $\tilde{X} \ ^2A_2''$ ground state of ND₃⁺ is represented in Fig. 3.2. Because the out-of-plane bending mode of ND₃ is of a_2'' symmetry, out-of-plane bending levels with an even (odd) number of vibrational quanta transform as A_1' (A_2'') and have the same rovibronic symmetry labels as the 2^0 (2^1) levels. Distinct rovibronic selection rules and an overall different rotational structure are thus expected for transitions from the ground neutral state of ND₃ to out-of-plane bending levels of ND₃⁺ with even and odd numbers of vibrational quanta.

In ND₃ and ND₃⁺, the rovibrational energy levels can be classified in to three sets, each corresponding to one of the three possible nuclear-spin-symmetry species arising from the

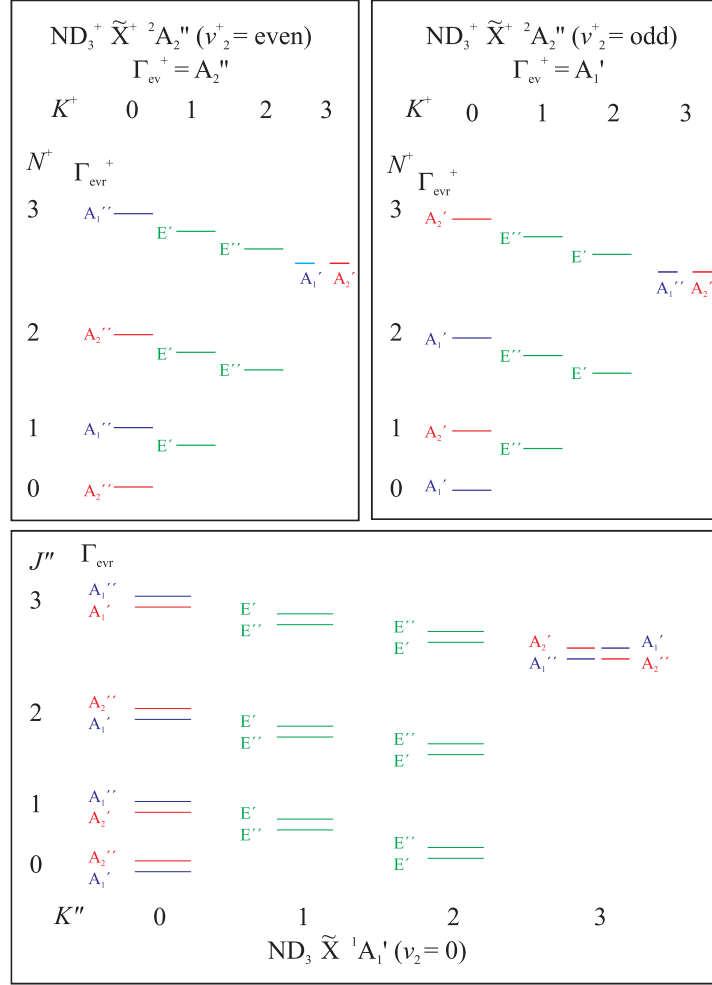


Figure 3.2: Energy level diagram showing schematically the rotational structures of the lowest vibrational level of the \tilde{X} ($^1A_1'$) ground state of ND₃ and of out-of-plane bending levels of the \tilde{X}^+ ($^2A_2''$) ground state of ND₃⁺. The rovibronic symmetry of all levels is indicated next to the levels.

three equivalent deuterons, which are bosons of nuclear spin $I = 1$. The rovibronic levels of symmetry A_1' and A_1'' have nuclear-spin statistical weights of 30, those of symmetry A_2' and A_2'' have nuclear-spin statistical weights of 3 and those of symmetry E' and E'' have nuclear-spin statistical weights of 24.

In NH₃ only levels of E' and E'' (para-NH₃, nuclear-spin statistical weights of 6) and A_2' and A_2'' (ortho-NH₃, nuclear-spin statistical weights of 12) are allowed by the generalized Pauli principle. From the possibility of observing transitions connecting rotational levels of A_1' and A_1'' rovibronic symmetries in ND₃, which do not exist in NH₃, it is thus possible to obtain more information on the odd- ℓ or even- ℓ nature of the photoelectron partial waves from the photoelectron spectrum of ND₃ than from that of NH₃.

However, consideration of the energy level diagram in Fig. 3.2 and of the rovibronic selection rules in Eqs. (3.2) and (3.3) leads to the conclusion that the unambiguous determination of the even- or odd- ℓ nature of the photoelectron partial waves is only

possible in transitions between A₁ or A₂ levels because the very small tunnel splitting of the E levels in the ground state (0.0531 cm⁻¹ [80]) cannot be resolved by PFI-ZEKE photoelectron spectroscopy and is unlikely to lead to measurable population differences between the two components of the tunneling doublet. Under these conditions, observed transitions that could only be unambiguously interpreted as arising in combination with an odd- ℓ partial wave are relatively scarce, e.g., $0_0 \leftarrow 0_0 A'_1 (A''_2)$, $2_0 \leftarrow 0_0 A'_1 (A''_2)$, $1_0 \leftarrow 1_0 A'_2 (A''_1)$, $3_0 \leftarrow 3_0 A'_2 (A''_1)$ in bands connecting the ground neutral state to cationic levels with an odd(even) number of quanta in the out-of-plane bending mode ν_2 . The same is true of transitions that could be unambiguously interpreted as arising in combination with an even- ℓ partial wave, e.g., $1_0 \leftarrow 0_0$, $0_0 \leftarrow 1_0$, $2_0 \leftarrow 1_0$, $1_0 \leftarrow 2_0$, $3_0 \leftarrow 2_0$ (see Fig. 3.2 and Eqs. (3.2) and (3.3)).

Particular attention will thus be given to transitions between $K'' = 0$ and $K^+ = 0$ levels. If such transitions are observed in combination with even (odd) values of the difference $N^+ - N''$ they unambiguously point at the odd (even) nature of the photoelectron partial waves.

In addition to the rovibronic photoionization selection rules considered above, additional selection rules result from the conservation of the total angular momentum which can be expressed as [96]

$$N^+ - N'' = 0, \pm 1, \pm 2, \pm 3, \dots, \pm(\ell + 1) \quad (3.4)$$

and

$$K^+ - K'' \leq \ell. \quad (3.5)$$

In the realm of the orbital ionization model [98], the following propensity (i.e., not strict selection) rules may also be derived if the orbital out of which ionization takes place is assumed to be a p_z orbital of the nitrogen atom

$$N^+ - N'' = 0, \pm 1 \quad (3.6)$$

$$K^+ - K'' = 0. \quad (3.7)$$

3.3 Experiment

The spectra have been recorded using a narrow bandwidth VUV laser system coupled to a photoion/photoelectron time-of-flight mass spectrometer. The main aspects of our experimental procedure have been described in detail earlier in Section 2.2.1 and are only briefly summarized here. The spectra were recorded following single-photon VUV excitation from the lowest rotation levels of the ground neutral state. Tunable VUV radiation was generated by two-photon resonance-enhanced difference-frequency mixing

($\tilde{\nu}_{\text{VUV}} = 2\tilde{\nu}_1 - \tilde{\nu}_2$) in a krypton gas beam using the $4p^5$ ($^2P_{1/2}$) $5p'[1/2]_0 \leftarrow 4p^6$ (1S_0) two-photon resonance at $2\tilde{\nu}_1 = 98\,855.071\text{ cm}^{-1}$. The tunability in the VUV was achieved by scanning the frequency $\tilde{\nu}_2$.

The gas sample was diluted in argon in a pressure ratio ND₃:argon of 1:4 and introduced into the spectrometer in a skimmed pulsed supersonic expansion. This expansion was crossed by the VUV radiation beam at a right angle in the middle of a set of six cylindrical electrodes used to apply pulsed electric fields.

High-resolution PFI-ZEKE spectra were measured using an electric field pulse sequence consisting of a discrimination pulse immediately followed by an extraction pulse. The first pulse serves the purpose of eliminating prompt electrons produced during photoexcitation from the sample volume. The electrons produced by the second pulse were monitored as a function of the laser wave number. The magnitudes chosen for these two pulses were different for the spectra of the $v_2^+ = 0, 1$ and 2 levels because of the very different intensities of the photoelectron bands. They are summarized in Table 3.1 which also lists the estimated values of the field-induced shifts of the ionization thresholds.

Table 3.1: Two pulse sequences used to record the PFI-ZEKE photoelectron spectra of the transitions of ND₃. The shifts of the ionization thresholds were estimated using the procedure described in Ref. [59].

band	2_0^0	2_0^1	2_0^2
Discrimination pulsed field / V cm^{-1}	+0.133	+0.133	+0.066
Extraction pulsed field / V cm^{-1}	-0.266	-0.133	-0.266
Shift of the ionization threshold induced by the pulse sequence / cm^{-1}	-1.7	-1.5	-1.45

The photoionization spectra were recorded by applying a 133.3 V cm^{-1} extraction pulse $1\text{ }\mu\text{s}$ after photoexcitation to accelerate the ions toward a microchannel plate detector at the end of a time-of-flight (TOF) tube.

3.4 Results

The PFI-ZEKE photoelectron spectra of the \tilde{X}^+ ($v_2^+ = 0, 1$ and 2) $\leftarrow \tilde{X}$ bands of ND₃ are displayed in Fig. 3.3a, 3.4a and 3.5a, respectively, where the transitions are assigned in the notation $N_{K^+}^+ \leftarrow N_{K''}''$. Figs. 3.3 – 3.5 consist each of four panels, the top (a) and bottom (d) panels displaying the experimental PFI-ZEKE photoelectron and photoionization spectra, respectively. The middle panels (b) and (c) represent two simulations of the spectra, the former (b) based on the orbital ionization model as described in Ref. [98] and the latter (c) calculated on the basis of less restrictive photoionization rules (see below).

The intensity distributions of the spectra displayed in panels 3.3b, 3.4b and 3.5b were

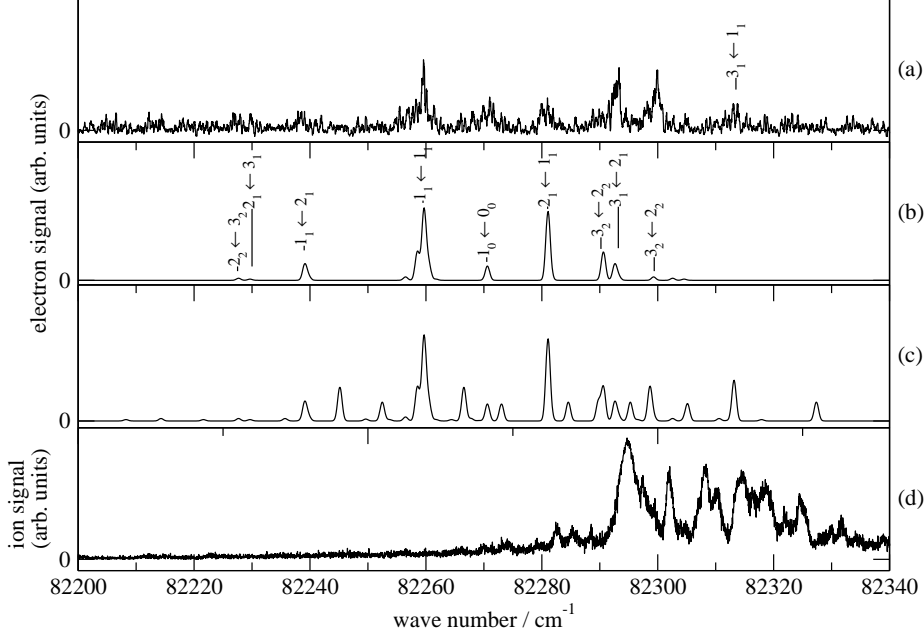


Figure 3.3: Panel (a) illustrates the experimental PFI-ZEKE photoelectron spectrum of the \tilde{X}^+ ($v_2^+ = 0$) $\leftarrow \tilde{X}$ ($v_2 = 0$) transition in ND₃. The assignment of the lines is given using the notation $N_{K^+}^+ \leftarrow N_{K''}''$. Panel (b) shows a simulation based on the orbital ionization model [98]. The simulation presented in panel (c) relies on a less restrictive photoionization model. The experimental photoionization spectrum is depicted in panel (d).

calculated using Equation (3.8) [98]

$$\begin{aligned}
 I(v^+, N^+, K^+, N'', K'') &= \rho'' C \sum_{|\lambda''| \leq \ell''} \frac{1}{2\ell'' + 1} Q(\ell'') |C_{\ell'', \lambda''}|^2 \left[\ell'' \left| F_{\ell''}^{E, \ell''-1} \right|^2 + (\ell'' + 1) \left| F_{\ell''}^{E, \ell''+1} \right|^2 \right] \\
 &= \rho'' C \sum_{|\lambda''| \leq \ell''} \frac{1}{2\ell'' + 1} Q(\ell'') B_{\ell''}
 \end{aligned} \tag{3.8}$$

In Equation (3.8) ρ'' and C represent the Boltzmann factor (including nuclear-spin statistical weight) and a proportionality constant, respectively, and ℓ'' the orbital angular momentum quantum number of the different terms of a single-center expansion with expansion coefficients $C_{\ell'', \lambda''}$ of the molecular orbital ϕ'' out of which the photoelectron is ejected

$$\phi'' = \sum_{|\lambda''| \leq \ell''} C_{\ell'', \lambda''} R_{\alpha'', \ell''}(r) Y_{\ell'', -\lambda''}(\theta, \varphi). \tag{3.9}$$

$F_{\ell''}^{E, \ell}$ is a radial integral

$$F_{\ell''}^{E, \ell} = \int R_{\ell}(r) R_{\alpha'', \ell''}(r) r^3 dr, \tag{3.10}$$

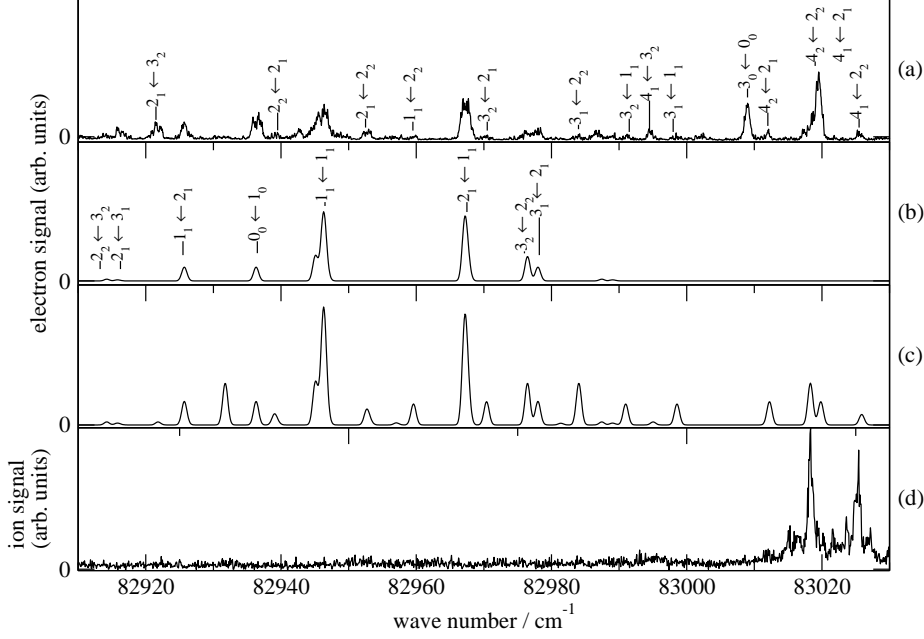


Figure 3.4: Panel (a) illustrates the experimental PFI-ZEKE photoelectron spectrum of the \tilde{X}^+ ($v_2^+ = 1$) $\leftarrow \tilde{X}$ ($v_2 = 0$) transition in ND_3 . The assignment of the lines is given using the notation $N_{K^+}^+ \leftarrow N_{K''}''$. Panel (b) shows a simulation based on the orbital ionization model [98]. The simulation presented in panel (c) relies on a less restrictive photoionization model. The experimental photoionization spectrum is depicted in panel (d).

and

$$Q(\ell'') = (2N^+ + 1) \left(\begin{array}{ccc} N^+ & \ell'' & N'' \\ -K^+ & \lambda'' & K'' \end{array} \right)^2 \quad (3.11)$$

where the term in parentheses represents a $3j$ -symbol [99].

To simulate the relative intensities of the various rotational lines of a given band, the product of the expansion coefficient $C_{\ell'', \lambda''}$ and the term in square brackets in Eq. (3.8) were treated as a single parameter $B_{\ell''}$, the value of which was adjusted to best reproduce the observed intensities. Assuming that the molecular orbital out of which the photoelectron is ejected in the $\tilde{X}^+ \leftarrow \tilde{X}$ transitions of ND_3 is a p_z orbital, (i.e., $\ell'' = 1$, $\lambda'' = 0$) reduces the sum in Eq. (3.8) to a single term

$$I(v^+, N^+, K^+, N'', K'') = C' \chi'' \exp\left(-\frac{E''}{k_B T}\right) (2N^+ + 1) g'' \left(\begin{array}{ccc} N^+ & 1 & N'' \\ -K^+ & 0 & K'' \end{array} \right)^2 \quad (3.12)$$

where $C' = C \cdot B_1$, χ'' stands for the spin statistical factors discussed in Section 3.2 and g'' is the degeneracy factor of the ground state rotational levels, i.e., $2N'' + 1$ for $K = 0$ and $2(2N'' + 1)$ for $K \neq 0$ levels. The simulations presented in the panels (b) of Figs. 3.3 – 3.5 were made using Eq. (3.12) assuming a rotational temperature of 15 K.

The line positions were calculated using a standard rigid-rotor Hamiltonian for the

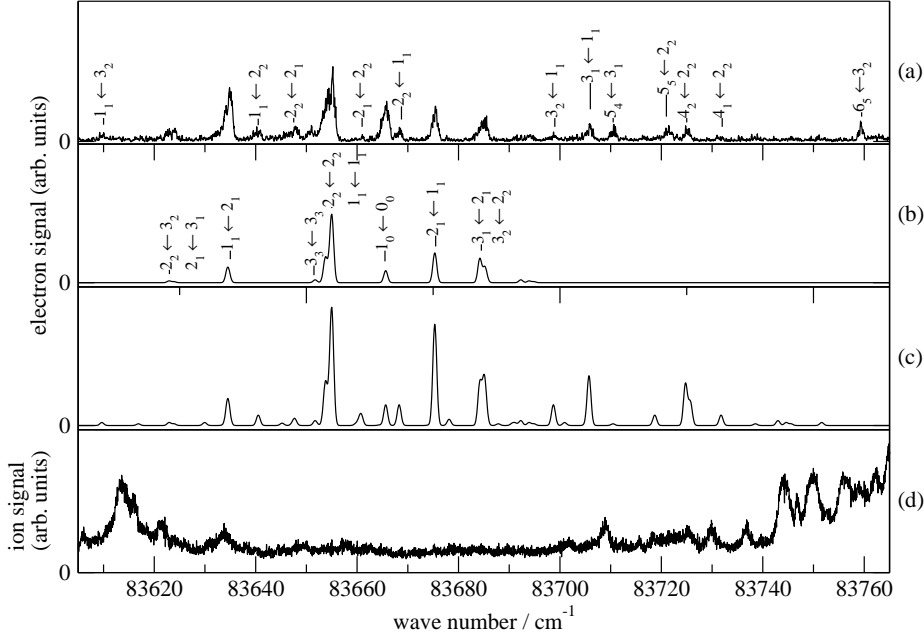


Figure 3.5: Panel (a) illustrates the experimental PFI-ZEKE photoelectron spectrum of the \tilde{X}^+ ($v_2^+ = 2$) $\leftarrow \tilde{X}$ ($v_2 = 0$) transition in ND₃. The assignment of the lines is given using the notation $N_{K^+}^+ \leftarrow N_{K''}''$. Panel (b) shows a simulation based on the orbital ionization model [98]. The simulation presented in panel (c) relies on a less restrictive photoionization model. The experimental photoionization spectrum is depicted in panel (d).

cationic rotational levels [5] and molecular constants E_{1,v_2^+} , $B_{v_2^+}^+$, and $C_{v_2^+}^+$ optimized in a least-squares fitting procedure (E_{1,v_2^+} , $B_{v_2^+}^+$, and $C_{v_2^+}^+$ represent the band origin and the oblate symmetric top rotational constants of the v_2^+ bending levels of ND₃⁺). The molecular constants of the neutral ground state of ND₃ were adopted from Ref. [80]. The second set of simulations displayed in panels (c) of Figs. 3.3 – 3.5 relied on the same molecular constants but different assumptions concerning the composition of the molecular orbital out of which the electron is ejected. These simulations, which allow transitions with $\Delta N = N^+ - N''$ and $\Delta K = K^+ - K''$ values up to 3 primarily served the purpose of identifying and assigning transitions not predicted using Eq. (3.12) nor by the propensity rules given at the end of Section 3.2.

The positions and assignments of all lines observed in the photoelectron spectra of ND₃ displayed in Figs. 3.3 – 3.5 are summarized in Tables 3.2 – 3.4, where they are compared with the positions calculated using the molecular constants determined in the least-squares fitting procedure. Table 3.5 lists the band origins E_{1,v_2^+} , corresponding to the (unobserved) $0_0 \leftarrow 0_0$ rotational transition, and the rigid-rotor rotational constants $B_{v_2^+}^+$ and $C_{v_2^+}^+$ of the ionic out-of-plane bending levels $v_2^+ = 0, 1$ and 2. From Tables 3.2 – 3.5, the positions of all ionization thresholds required to describe the photoionization spectra of ND₃ at low temperature and energy (which represented the first objective of the present work) can be determined.

Table 3.2: Observed and calculated transition wave numbers in cm^{-1} of the $N_{K^+}^+ \leftarrow N_{K''}''$ transitions of the PFI-ZEKE photoelectron spectra of ND_3 in the vicinity of the $\tilde{X}^+ (v_2^+ = 0) \leftarrow \tilde{X}$ ionization threshold. The field-free ionization thresholds can be obtained by compensating the field-induced shift. The ionization energy and rotational constants used to calculate the line positions are listed in Table 3.5.

$\tilde{\nu}_{\text{exp.}} / \text{cm}^{-1}$	$\tilde{\nu}_{\text{exp.}} - \tilde{\nu}_{\text{calc.}} / \text{cm}^{-1}$	Transition ($N_{K^+}^+ \leftarrow N_{K''}''$)
82 227.7	-0.05	$2_2 \leftarrow 3_2$
82 229.7	0.10	$2_1 \leftarrow 3_1$
82 239.0	-0.10	$1_1 \leftarrow 2_1$
82 259.6	-0.05	$1_1 \leftarrow 1_1$
82 270.4	-0.15	$1_0 \leftarrow 0_0$
82 281.0	-0.05	$2_1 \leftarrow 1_1$
82 290.5	-0.1	$3_2 \leftarrow 2_2$
82 292.8	0.15	$3_1 \leftarrow 2_1$
82 298.5	-0.1	$3_1 \leftarrow 2_2$
82 313.1	-0.05	$3_1 \leftarrow 1_1$

Table 3.3: Observed and calculated transition wave numbers in cm^{-1} of the $N_{K^+}^+ \leftarrow N_{K''}''$ transitions of the PFI-ZEKE photoelectron spectra of ND_3 in the vicinity of the $\tilde{X}^+ (v_2^+ = 1) \leftarrow \tilde{X}$ ionization threshold. The field-free ionization thresholds can be obtained by compensating the field-induced shift. The ionization energy and rotational constants used to calculate the line positions are listed in Table 3.5.

$\tilde{\nu}_{\text{exp.}} / \text{cm}^{-1}$	$\tilde{\nu}_{\text{exp.}} - \tilde{\nu}_{\text{calc.}} / \text{cm}^{-1}$	Transition ($N_{K^+}^+ \leftarrow N_{K''}''$)
82 915.8	0.05	$0_0 \leftarrow 2_0$
82 921.8	0.05	$2_1 \leftarrow 3_2$
82 925.6	-0.1	$1_1 \leftarrow 2_1$
82 936.4	-0.1	$0_0 \leftarrow 1_0$
82 939.1	-0.15	$2_2 \leftarrow 2_1$
82 946.2	-0.05	$1_1 \leftarrow 1_1$
82 952.7	0.05	$2_1 \leftarrow 2_2$
82 967.2	0.1	$2_1 \leftarrow 1_1$
82 970.4	-0.05	$3_2 \leftarrow 2_1$
82 976.2	-0.2	$3_2 \leftarrow 2_2$
82 978.0	0.05	$3_1 \leftarrow 2_1$
82 984.1	0.05	$3_1 \leftarrow 2_2$
82 991.1	-0.1	$3_2 \leftarrow 1_1$
82 994.8	-0.2	$4_1 \leftarrow 3_2$
82 998.6	0.05	$3_1 \leftarrow 1_1$
83 009.1	-0.2	$3_0 \leftarrow 0_0$
83 012.1	-0.1	$4_2 \leftarrow 2_1$
83 018.4	0.1	$4_2 \leftarrow 2_2$
83 019.6	-0.2	$4_1 \leftarrow 2_1$
83 025.7	-0.1	$4_1 \leftarrow 2_2$

From the measured intensity distributions (see Figs. 3.3 – 3.5) the following observation can be made concerning the photoionization selection rules and dynamics: 1) The

Table 3.4: Observed and calculated transition wave numbers in cm⁻¹ of the $N_{K^+}^+ \leftarrow N_{K''}''$ transitions of the PFI-ZEKE photoelectron spectra of ND₃ in the vicinity of the $\tilde{X}^+ (v_2^+ = 2) \leftarrow \tilde{X}$ ionization threshold. The field-free ionization thresholds can be obtained by compensating the field-induced shift. The ionization energy and rotational constants used to calculate the line positions are listed in Table 3.5.

$\tilde{\nu}_{\text{exp.}} / \text{cm}^{-1}$	$\tilde{\nu}_{\text{exp.}} - \tilde{\nu}_{\text{calc.}} / \text{cm}^{-1}$	Transition ($N_{K^+}^+ \leftarrow N_{K''}''$)
83 609.7	0.05	1 ₁ ← 3 ₂
83 622.9	-0.05	2 ₂ ← 3 ₂
83 624.0	0.1	2 ₁ ← 3 ₁
83 634.2	-0.1	1 ₁ ← 2 ₁
83 640.3	-0.15	1 ₁ ← 2 ₂
83 647.8	0.1	2 ₂ ← 2 ₁
83 651.6	-0.1	3 ₃ ← 3 ₃
83 653.9	0.15	2 ₂ ← 2 ₂
83 655.1	0.1	1 ₁ ← 1 ₁
83 660.9	0.1	2 ₁ ← 2 ₂
83 665.7	0.1	1 ₀ ← 0 ₀
83 668.4	0.1	2 ₂ ← 1 ₁
83 675.4	0.1	2 ₁ ← 1 ₁
83 685.0	0.1	3 ₁ ← 2 ₁
83 698.8	0.05	3 ₂ ← 1 ₁
83 705.8	0.1	3 ₁ ← 1 ₁
83 710.5	0.05	5 ₄ ← 3 ₁
83 721.1	0.1	5 ₅ ← 2 ₂
83 725.0	0.15	4 ₂ ← 2 ₂
83 731.6	-0.15	4 ₁ ← 2 ₂
83 759.1	0.15	6 ₅ ← 3 ₄

Table 3.5: Origins of $\tilde{X}^+ {}^2A_2'' (v_2^+ = 0, 1, 2) \leftarrow \tilde{X} {}^1A_1'$ bands of ND₃ and rotational constants $B_{v_2^+}$ and $C_{v_2^+}$ of the ionic levels with $v_2^+ = 0, 1$ and 2 determined from the PFI-ZEKE photoelectron spectrum in a least-squares fit. Values in parentheses represent one standard deviation in units of the digits.

	$v_2^+ = 0$	$v_2^+ = 1$	$v_2^+ = 2$
Band origin / cm ⁻¹	82 261.7(15)	82 948.2(15)	83 656.9(15)
$B_{v_2^+} / \text{cm}^{-1}$	5.389(10)	5.231(10)	5.171(10)
$C_{v_2^+} / \text{cm}^{-1}$	2.673(10)	2.714(10)	2.735(10)
vibrational energy / cm ⁻¹	0	686.5(20)	1395.2(20)

intensity of the $\tilde{X}^+ (v_2^+ = 0) \leftarrow \tilde{X}$ band is extremely weak, much weaker (the signal-to-noise ratio of the spectrum is poorer) than that of the $\tilde{X}^+ (v_2^+ = 1, 2) \leftarrow \tilde{X}$ bands. This observation can be explained by the very low Frank-Condon factor resulting from the large difference between the equilibrium structures of the ionic and neutral ground state. It is also compatible with the intensity distribution of the He I photoelectron spectrum displayed in Fig. 3.1. 2) All observed rotational transition of the $\tilde{X}^+ (v_2^+ = 0) \leftarrow \tilde{X}$ band,

except the $3_3 \leftarrow 1_1$ transition, are also present in the simulation based on Eq. (3.12), (see Figs. 3.3a and b). Whereas the relative intensities of the $2_2 \leftarrow 3_2$, $2_1 \leftarrow 3_1$, $3_3 \leftarrow 3_3$, $2_2 \leftarrow 2_2$, $1_1 \leftarrow 1_1$, $1_0 \leftarrow 0_0$, and $2_1 \leftarrow 1_1$ transitions are satisfactorily reproduced by the simulated spectrum, the measured intensities of the $3_1 \leftarrow 2_1$ and $3_2 \leftarrow 2_2$ transitions are much stronger than predicted. The positions of these transitions coincide with the positions of strong autoionizing resonances in the photoionization spectrum (panel (d) in Fig. 3.3), and one can conclude that these lines and the $3_1 \leftarrow 1_1$ line gain intensity from transitions to low autoionizing Rydberg states belonging to series converging on excited vibrational levels of the ND_3^+ ion. The calculated spectrum based on the less restrictive selection rules (Fig. 3.3c) provides a better description of the spectrum beyond $82\,295\text{ cm}^{-1}$ in the region of the strong autoionizing resonances but predicts too many lines in the low wave-number side of the spectrum. 3) Very similar conclusions can be drawn by comparing the spectra displayed in Figs. 3.4 and 3.5. In spectral regions where the photoionization spectrum is free of autoionizing resonances, i.e., the region up to $82\,990\text{ cm}^{-1}$ in Fig. 3.4 and between $83\,640\text{ cm}^{-1}$ and $83\,690\text{ cm}^{-1}$ in Fig. 3.5, the spectra calculated on the basis of Eq. (3.12) provide a qualitatively satisfactory description of the observed spectra, whereas the simulations based on the less restrictive selection rules resemble the observed spectra better in the regions of the autoionizing resonances. It thus appears that the orbital ionization model based on the assumption of photoejection of a $3p_z$ orbital is adapted to describe the direct photoionization in ND_3 and that the intensity anomalies, i.e., the lines of the photoelectron spectra poorly described by Eq. (3.12), can be explained by channel interactions. Similar observations have been made in a wide range of molecules (see Refs. [68] and [98]). 4) The dominant direct ionization channels are those associated with $\Delta N \leq 1$ and $\Delta K = 0$, as expected for the photoejection out of a molecular orbital of p_z character.

3.5 Discussion and conclusions

The molecular constants and ionization energies summarized in Tables 3.2 – 3.5 represent the first set of such parameters derived for ND_3^+ . The decrease of the value of $B_{v_2^+}^+$ and the increase of $C_{v_2^+}^+$ with increasing vibrational quantum number v_2^+ can be explained by the increasing amplitudes of the vibrational wave functions in out-of-plane regions. The slight positive anharmonicity of the ν_2^+ mode is not unusual for a bending mode. The first adiabatic ionization energy of ND_3 ($82\,261.7 \pm 1.5\text{ cm}^{-1}$) is larger than that determined for NH_3 ($82\,158.751 \pm 0.016\text{ cm}^{-1}$) [95] as a result of zero-point energy differences.

None of the observed transitions gives an unambiguous indication of the emission of odd- ℓ photoelectron partial waves, whereas the observation of the $1_0 \leftarrow 0_0$ transition of the origin and 2_0^2 bands, and of the $0_0 \leftarrow 1_0$ transition of the 2_0^1 band can only be explained

by the emission of even- ℓ photoelectron partial waves. The fact that the orbital ionization model for ionization out of a p_z -orbital provides a satisfactorily description of the intensity distributions in the photoelectron spectra in regions where the photoionization spectra are free of autoionizing resonances is also a strong evidence for the dominance of even- ℓ photoelectron partial waves in the direct photoionization of ND₃, and supports the conclusions drawn from the photoelectron spectra of NH₃ by Seiler *et al.* [95] and of NH₂D and ND₂H by Hollenstein *et al.* [96].

The observation of several transitions that are not predicted by the orbital ionization model in regions where the photoionization spectrum displays strong autoionization resonances indicates that the interactions with low Rydberg states belonging to series converging on higher-lying vibrational levels of the ND₃⁺ cation modify the photoelectron partial wave composition. Such interactions and their effects on line intensities in PFI-ZEKE photoelectron spectra have been discussed in detail in Ref. [68] and may be the reason for the observation of odd- ℓ partial waves in other studies [92–94] as already suggested by Hollenstein *et al.* [96].

The present results form the basis for future studies of the complex photoionization spectrum of ND₃⁺ by MQDT in that it enabled for the first time to precisely locate the positions of the ionization thresholds and to identify the dominant direct ionization channels. Work aiming at the complete analysis of the photoionization spectrum of ND₃ by MQDT is currently in progress in a collaboration with the group of Prof. Dr. T. P. Softley [100].

Chapter 4

Threshold photoionization of ammoniated ammonium clusters

This chapter summarizes an investigation of the photodissociation dynamics of ammonia clusters and of the threshold ionization dynamics of ammoniated ammonium radical clusters. The ammonium radical and ammoniated ammonium radical clusters represent a fascinating class of metastable molecules revealing extremely pronounced isotope effects. The emphasis of this chapter is on studies of undeuterated and perdeuterated ammoniated ammonium dimers and their singly charged ions which represent prototypical systems in which hydrogen bonds lead on the one hand to strongly bound molecular clusters and on the other hand to low barriers for proton or hydrogen transfer.

4.1 Introduction

Neutral and positively charged ammonia clusters $(\text{NH}_3)_n$ are prototypical systems to study the aggregation of molecules through hydrogen bonds and have been studied extensively both theoretically [101–105] and experimentally by multiphoton ionization [106–108], single-photon ionization [109,110], and electron impact ionization [111,112] in combination with mass spectrometry. The photophysics of these clusters is very rich and their photodissociation and photoionization dynamics have been studied in detail in pump-probe experiments using picosecond and femtosecond lasers [101,113,114]. Upon excitation of the clusters with UV radiation of about 200 nm, which corresponds to the wavelength of the transition from the \tilde{X} ground state of NH_3 to the strongly predissociative \tilde{A} state [115], the clusters rearrange and dissociate rapidly. The absorption of further UV photons during and following the rearrangement and dissociation process leads to the observation of a broad range of ionization products [113,114,116–121].

Irrespective of the method used to ionize the clusters, all mass spectra have in common that the protonated species $(\text{NH}_3)_n\text{NH}_4^+$ are more abundant than the homogeneous

$(\text{NH}_3)_m^+$ cluster ions. Theoretical investigations suggest that the equilibrium structure of $(\text{NH}_3)_n^+$ is best described by a structure of the type $(\text{NH}_3)_{n-2}\text{NH}_2\text{NH}_4^+$ which is not accessible from the neutral ground state of the clusters by virtue of the Franck-Condon principle.

Under conditions of low intensity UV irradiation, the ammonia clusters $(\text{NH}_3)_n$ fragment into NH_2 radicals and ammoniated ammonium radicals $(\text{NH}_3)_{n-2}\text{NH}_4$, and UV photolysis has proven to be a very successful method to produce such radicals for subsequent spectroscopic investigations [117]. Whereas the ammonium radical is unstable and very rapidly dissociate into NH_3 and H , the ND_4 radical is metastable and can be observed for tens of microseconds before dissociation in ND_3 and D takes place [122,123]. Ammoniated ammonium clusters $\text{NH}_4(\text{NH}_3)_n$ are not subject to fast predissociation and are either stable or metastable in their ground state. Isotopic substitution is known to have large effects on the structure and dynamics of these clusters.

Most studies of ammonia clusters have been carried out using ultrashort laser pulses and mass spectrometry, and very few high-resolution spectroscopic studies have been reported. Several high-resolution spectroscopic studies of the photolysis products of ammonia clusters have been carried out to characterize ammoniated ammonium radicals. Fuke *et al.* [117] have studied the photoionization of ammoniated ammonium clusters to determine their energetics. Signorell *et al.* [56] have obtained rotationally resolved PFI-ZEKE photoelectron spectra of ND_4 and determined accurate structural parameters for both ND_4 and ND_4^+ which complemented the information obtained in studies of the $3p \leftarrow 3s$ transition of NH_4 and ND_4 [123–125].

In recent studies of the IR spectrum of N_2H_7^+ , Asmis and coworkers [126, 127] have observed several low-lying vibrational modes involving the asymmetric proton transfer mode between the two NH_3 molecules (called ν_z) (374 cm^{-1}) and its combination with the symmetric intermolecular stretching mode (called ν_s) associated with the relative motion of the two ammonia molecules (743 cm^{-1}). Calculations predict two equivalent near- D_{3d} equilibrium structures in which the NH_3 units are eclipsed and the shared proton is slightly displaced from the symmetric position [127,128]. Because the zero-point energy of the proton transfer mode (ν_z) is predicted to be larger than the barrier separating these equilibrium structure, the structure is effectively D_{3d} . Calculated vibrational energies, however, were found to be larger than the experimental values and the fundamental band of the symmetric molecular stretching mode has not been observed yet because it is forbidden in the IR spectrum. This mode should be the dominant mode in a photoelectron spectrum because of the contraction of the N-N distance that is expected to result from photoionization.

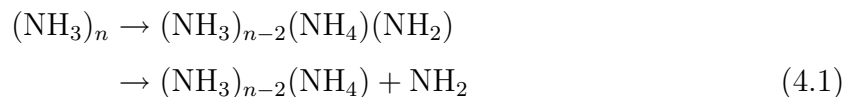
In the work described in this chapter, we attempted to measure PFI-ZEKE photoelectron spectra of ND_4ND_3 and NH_4NH_3 following the methods used by Signorell *et al.* [56]

to study ND_4 in the hope to observe low-frequency vibrations of N_2H_7^+ not observable by IR spectroscopy. Although spectral congestion prevented the recording of rotational resolved photoelectron spectra, this investigation revealed surprising differences in the behavior of deuterated and undeuterated ammonia and ammoniated ammonium clusters.

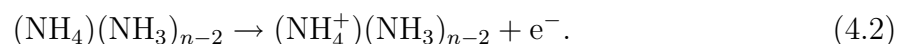
4.2 Experiment

The experimental setup used in this investigation has been described in Section 2.2.2, and the procedure used to detect the formation of ammoniated ammonium clusters has been presented in Subsection 2.4.4 (see in particular Fig. 2.11).

$(\text{NH}_3)_n$ or $(\text{ND}_3)_n$ clusters were formed in a pulsed supersonic expansion of a 4:1 Ar: NH_3 (or Ar: ND_3) gas mixture at a nozzle stagnation pressure of ≈ 2.5 bar. After selection of the coldest part of the expansion using a skimmer, the probe gas beam was intersected at right angles by the 204 nm output of a frequency-tripled dye laser operated at 612 nm without intracavity étalon at the center of the stack of extraction plates depicted in Fig. 2.2. The ammoniated ammonium clusters are thought to be formed following absorption of a UV photon in the rearrangement and dissociation process [110, 113, 114, 118, 119]



(and the analogous reaction for $(\text{ND}_3)_n$). A second tunable pulsed UV laser delayed by 28 ns with respect to the first, was then used to study the threshold photoionization of the ammoniated ammonium clusters according to Eq. (4.2)



Delaying the ionization laser pulse with respect to the photodissociation laser pulse enables one to avoid $(1 + 1')$ two-photon ionization processes as explained in Ref. [56]. Photoionization and PFI-ZEKE photoelectron spectra were observed by collecting the ions, respectively the electrons produced by pulsed field ionization of high Rydberg states as explained in Section 2.5.

Ionization processes induced by the photodissociation laser alone are unavoidable, even at low intensities, and typically lead to weak background ionization signals in the photoionization spectra recorded at the masses of the $(\text{NH}_3)_m^+$ and $\text{NH}_4^+(\text{NH}_3)_{n-2}$ ions. This undesirable background can be removed by the subtraction procedure illustrated in Fig. 2.11, and, in this chapter, we shall only present the subtracted spectra.

The experimental conditions were first optimized on the production of the ND_4 radical,

following the procedure devised by Signorell *et al.* [56], and then slightly modified to maximize the formation of the $\text{ND}_4(\text{ND}_3)_n$ and $\text{NH}_4(\text{NH}_3)_n$ radicals. In the next section, we thus first briefly summarize the results obtained for the ND_4 radical, which fully reproduced those obtained by Signorell *et al.* [56], before presenting the new results on the larger clusters.

4.3 Results and discussion

4.3.1 Formation and threshold ionization of the deuterated ammonium radical

The ND_4 radicals are produced from $(\text{ND}_3)_2$ by the photodissociation process



Consequently, their kinetic and internal (rovibrational) energy distributions are not as cold as those of other species in the supersonic expansion [56]. The PFI-ZEKE photoelectron spectrum of ND_4 recorded in the vicinity of the $\text{ND}_4^+ \tilde{X}^1\text{A}_1 \leftarrow \text{ND}_4 3\text{s } ^2\text{A}_1$ transition is depicted in Fig. 4.1 which also shows a simulation carried out using the molecular constants, the photoionization selection rules, and the effective temperature ($T = 150 \text{ K}$) derived by Signorell *et al.* [56] and summarized in Table 4.1. The spectrum presented in Fig. 4.1 corresponds almost exactly to that reported by Signorell *et al.* with the only difference that the signal-to-noise ratio of the former was better by a factor of about 2 – 3 because the distance between the nozzle and the photodissociation region was increased by 4 cm in the present experimental setup compared to that used in the earlier experiment, resulting in a lower particle density. Because the rotational structure of the PFI-ZEKE photoelectron spectrum of ND_4 was already analyzed in detail in Ref. [56], the reader is referred to that publication for further information.

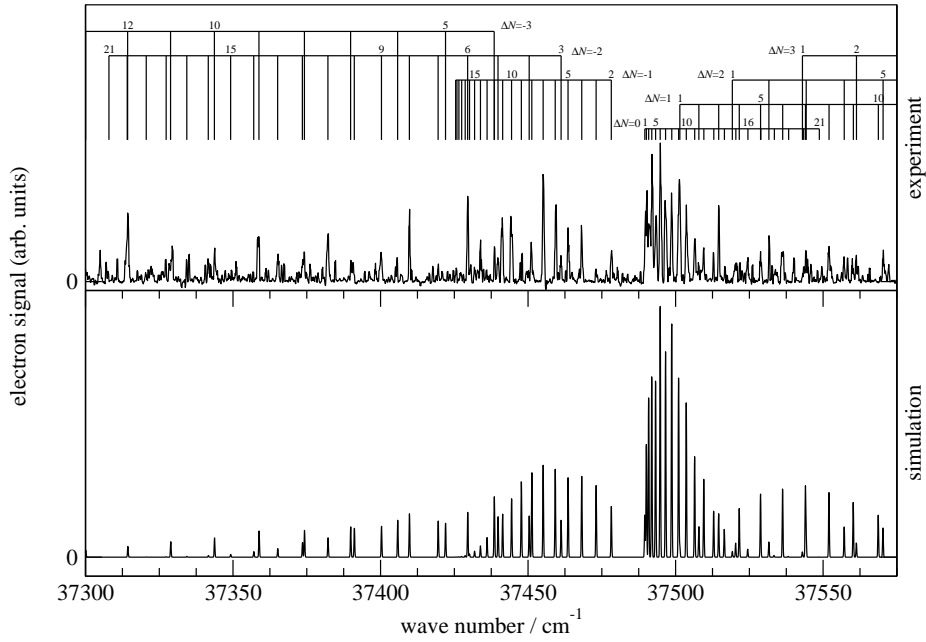
In the course of the present investigation, we also attempted to observe the PFI-ZEKE photoelectron spectrum of NH_4 and to generate the ND_4 radicals using the method developed by Willitsch *et al.* [51], which consists of producing the radicals by photolysis in a capillary mounted directly at the exit of the pulsed valve. Neither of these attempts led to any measurable signals, which confirms the current understanding of the (meta)stability of the ammonium radical: The lowest vibrational level of the $3\text{s } ^2\text{A}_1$ ground state of ND_4 and NH_4 are both located energetically above the $\text{ND}_3 + \text{D}$ and $\text{NH}_3 + \text{H}$ dissociation limits, from which they are separated by a barrier on the potential energy surface. The dissociation of NH_4



Table 4.1: Molecular constants (from Signorell [56]) used for the simulation of the PFI-ZEKE photoelectron spectrum of the $\text{ND}_4^+ \tilde{X}^1\text{A}_1 \leftarrow \text{ND}_4 3s^2\text{A}_1$ transitions.

State	Constant	Value
ND_4	E_1 / cm^{-1}	37 490.7(15)
$3s^2\text{A}_1$	B_0 / cm^{-1}	2.8560(37)
	D_0 / cm^{-1}	$4.8(14) \cdot 10^{-5}$
ND_4^+	B_0^+ / cm^{-1}	2.9855(37)
$\tilde{X}^1\text{A}_1$	D_0^+ / cm^{-1}	$4.8(15) \cdot 10^{-5}$

must thus take place by tunneling of one H atom through the barrier on the sub-ns time scale because otherwise we would have been able to observe the photoelectron spectrum of NH_4 . The heavier mass of the deuterium atom and the reduced zero-point vibrational energy greatly reduce the tunneling rate and are responsible for the metastability of ND_4 compared to NH_4 .

**Figure 4.1:** PFI-ZEKE photoelectron spectrum recorded in the vicinity of the $\text{ND}_4^+ \tilde{X}^1\text{A}_1 \leftarrow \text{ND}_4 3s^2\text{A}_1$ transition (upper trace) obtained with a pulsed electric field sequence of $+40 \text{ mV cm}^{-1}$ followed by a pulse of -100 mV cm^{-1} . The experimental spectrum is compared with a simulation (lower trace).

Unfortunately, the ND_4 radicals are not long-lived enough to survive the 12 cm flight distance (i.e., $200 \mu\text{s}$ flight time at the 600 m s^{-1} speed of the supersonic expansion using Ar as carrier gas) from the capillary where they are produced to the photodissociation region. Replacing Ar by He as carrier gas, and thus increasing the speed of the supersonic beam to $\approx 2000 \text{ m s}^{-1}$ and reducing the flight time to $\approx 60 \mu\text{s}$, did not suffice to observe any ND_4 signal and we conclude that the lifetime of the ground vibrational level of $3s^2\text{A}_1$ state of ND_4 cannot be much longer than $20 \mu\text{s}$.

4.3.2 Formation and threshold ionization of the ammoniated ammonium dimers

The dissociation of the ammonium radical is inhibited, or fully suppressed, upon formation of ammoniated ammonium clusters. Gellene, Porter and coworker have determined the lifetime of NH_3NH_4 to be $\geq 0.96 \mu\text{s}$ in experiments carried out on neutralized ion beams [122, 129, 130]. Misaizu *et al.* have estimated the lifetimes of $\text{NH}_4(\text{NH}_3)_n$ clusters with $n \geq 1$ to be longer than $1 \mu\text{s}$ [118], and Fuke *et al.* have reported lifetimes in the range of $1 \mu\text{s} < \tau < 6 \mu\text{s}$ for $n = 1$, $6 \mu\text{s} < \tau < 160 \mu\text{s}$ for $n = 2$ and $n = 3$, and $\tau > 160 \mu\text{s}$ for all clusters with $n \geq 4$ [117]. Less informations are available on the perdeuterated clusters. The reason invoked to explain the stabilization of the radicals upon cluster formation with NH_3 is that the intermolecular bond formation increases the potential energy barrier for H-atom dissociation, or even brings the ground state of the clusters energetically below the dissociation asymptote [117, 118, 122, 129–133].

Another important observation made in time-resolved studies of the dynamics of $(\text{NH}_3)_n$ is that the internal H-atom transfer in the excited state (corresponding to the $\tilde{\text{A}}$ state of NH_3) suggested by Eq. (4.1) leads to the rapid formation of a $\text{NH}_4\text{-NH}_2$ complex, which renders the observation of the photoelectron spectrum of $(\text{NH}_3)_2$ following (1+1) two-photon excitation extremely difficult [101]. This observation was explained as arising from a coupling of the $(\text{NH}_3)_2$ potential energy surface with that of the $\text{NH}_4^+\text{-NH}_2^-$ ion-pair state [101, 131]. *Ab initio* quantum chemical calculations of the relevant potential energy surfaces further confirmed the existence of a very shallow local minimum on the excited state potential energy surface corresponding to a $\text{NH}_4\text{-NH}_2$ structure which, however, is not stable with respect to dissociation (see Ref. [131] and references cited therein). If such a shallow minimum exists, one would expect the dynamics to be strongly influenced by deuteration and the prospect of observing such isotopic effects was an important motivation for the experiments that are now described.

4.3.2.1 Experiments on $(\text{NH}_3)_3$ clusters

According to Eq. (4.1) the NH_3NH_4 dimer is produced by photodissociation of $(\text{NH}_3)_3$ clusters. Fig. 4.2 displays a series of time-of-flight (TOF) traces obtained following photodissociation of $(\text{NH}_3)_n$ clusters at 204 nm followed by photoionization with a second UV laser with wave number ranging from $30\,303 \text{ cm}^{-1}$ (second trace from the top) to $32\,258 \text{ cm}^{-1}$ (bottom trace). The top trace was recorded with the photolysis laser only and represents the background ionization caused by the 204 nm radiation. This trace was subtracted from each of the other spectra shown in Fig. 4.2.

The TOF traces in Fig. 4.2 are dominated by $(\text{NH}_3)_n\text{NH}_4^+$ ionic clusters with $n = 1-3$ with almost no contribution from NH_4 , NH_3 and $(\text{NH}_3)_m$ clusters with $m = 2-4$. This

behavior is easily explained by the fact that the ionization energy of NH_4 ($\approx 37\,500\text{ cm}^{-1}$) is much lower than that of NH_3 ($\approx 80\,000\text{ cm}^{-1}$, see Chapter 3). The strong NH_3^+ signal observed at a wave number of $31\,948.9\text{ cm}^{-1}$ corresponds to an accidental resonance which facilitates a (1+1+1) doubly-resonant three-photon ionization process. Because no $(\text{NH}_3)_n^+$ ions are observed in any of the traces of Fig. 4.2, one may further conclude that the excited $(\text{NH}_3)_n^*$ clusters dissociate before they can absorb a second photon, i.e., on a time scale of less than 28 ns, a conclusion that was already drawn in earlier studies [117, 131, 134]. The peaks in the TOF spectra corresponding to $(\text{NH}_3)_2\text{NH}_4^+$ and $(\text{NH}_3)_3\text{NH}_4^+$ have intensities that are almost independent of the wave number of the photoionization laser which suggests that the adiabatic ionization energies of $\text{NH}_3(\text{NH}_3)_n$ clusters with $n > 1$ lie below $30\,303\text{ cm}^{-1}$. In contrast, the NH_3NH_4^+ mass peak shows an increase in three steps, marked A, B, and D on the right-hand side of the figure, as the wave number of the photoionization laser increases.

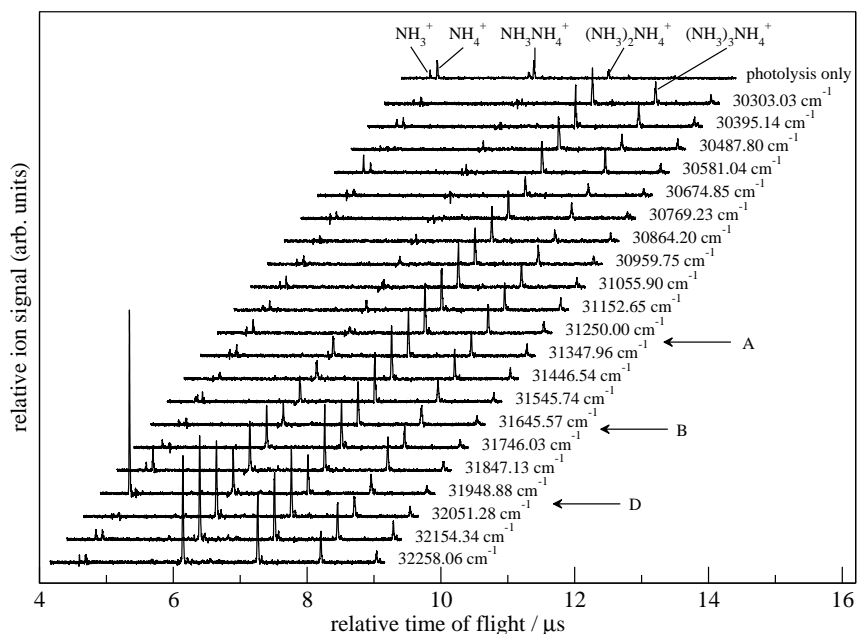


Figure 4.2: TOF mass spectra of small ammonia cluster ions produced at several ionization wave numbers in the range of $30\,303\text{ cm}^{-1} - 32\,258\text{ cm}^{-1}$ following the photolysis $(\text{NH}_3)_n$ clusters at 204 nm . The ionization efficiency of $\text{NH}_4(\text{NH}_3)_n$ ($n \geq 2$) does not change appreciably in this wave number range while that of NH_4NH_3 exhibits several thresholds indicated by arrows. The TOF spectrum at the top was recorded only with the photolysis laser and was subtracted from all other TOF spectra. The strong ion signal of NH_3^+ at $31\,948.9\text{ cm}^{-1}$ can be explained by resonance-enhanced multiphoton ionization.

These steps in the photoionization yield of NH_4NH_3 are seen more clearly in the photoionization spectrum recorded with a delayed pulsed field of 173 V cm^{-1} displayed in panel (a) of Fig. 4.3, where they are indicated by vertical arrows. Because the PFI-ZEKE photoelectron spectrum of NH_4NH_3 (4.3b) reveals bands at the positions of each step observed in the photoionization spectrum, one can conclude that they correspond

to the formation, from the NH_4NH_3 ground state, of low-lying vibrational levels of the NH_4NH_3^+ cation. The position of the ionization thresholds determined from the PFI-ZEKE photoelectron spectrum are listed in Table 4.2 where they are compared with the adiabatic ionization energy determined by Fuke *et al.* [117] and vibrational intervals determined by far-IR spectroscopy of the N_2H_7^+ ion by Yang *et al.* [127] and *ab initio* quantum chemistry [127,128]. Assuming that the lowest threshold (A in Fig. 4.3) observed in the present study corresponds to the adiabatic ionization threshold of NH_4NH_3 , we find for this quantity a slightly higher value ($31\,310(25)\text{ cm}^{-1}$) than reported by Fuke *et al.* ($31\,250(25)\text{ cm}^{-1}$ [117]). Limited informations are available in the literature on the low-frequency vibrational levels of N_2H_7^+ . The fundamental band of the asymmetric proton-transfer mode (ν_z) was recently assigned to a band centered at 374 cm^{-1} in the far-IR spectrum of N_2H_7^+ by Yang *et al.* [127] who also assigned a band at 734 cm^{-1} to the combination band ($\nu_s + \nu_z$) involving the asymmetric proton-transfer mode and the symmetric intermolecular stretching mode (ν_s) of the ammonia molecules.

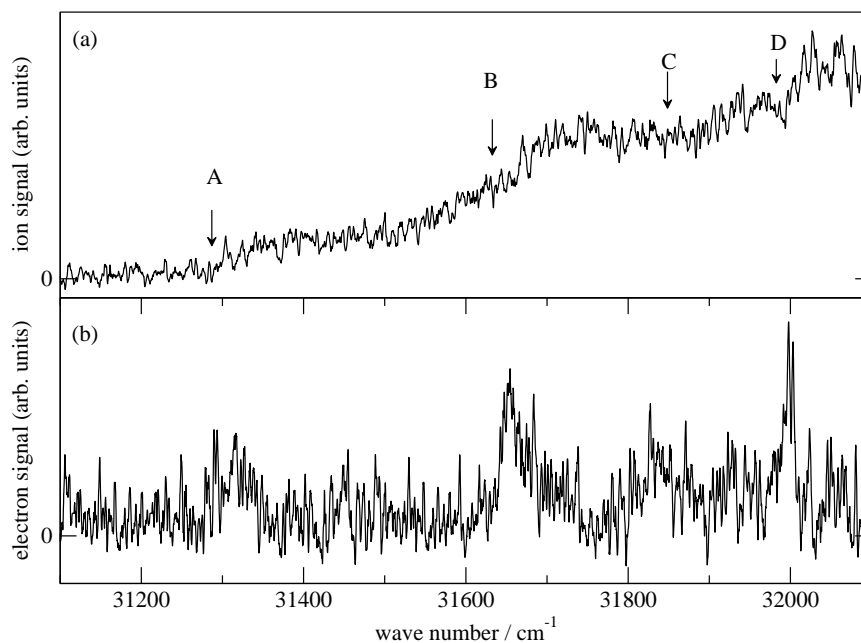


Figure 4.3: Panel (a) shows the photoionization spectrum of NH_4NH_3 recorded with a delayed pulsed electric field of 173 V cm^{-1} . Panel (b) depicts the PFI-ZEKE photoelectron spectrum recorded in the same wave number region. Ionization thresholds have been observed at $31\,310(25)\text{ cm}^{-1}$, indicated with (A), at $31\,655(25)\text{ cm}^{-1}$, indicated with (B), at $31\,830(30)\text{ cm}^{-1}$, indicated with (C), and at $32\,000(25)\text{ cm}^{-1}$, indicated with (D).

Ab initio calculations of these frequencies predict values of 464 cm^{-1} [126], 471 cm^{-1} [127] and 451 cm^{-1} [128] for the asymmetric proton-transfer mode ν_z , 765 cm^{-1} [127] and 832 cm^{-1} [128] for $\nu_s + \nu_z$ the combination band, and 434 cm^{-1} [127] and 430 cm^{-1} [128] for the symmetric stretching mode of the ammonia molecules (ν_s). The calculations thus suggest a lower fundamental wave number for ν_s than for ν_z .

Table 4.2: Positions in cm^{-1} of the vibrational bands observed in the PFI-ZEKE photoelectron spectrum of NH_3NH_4 and IR spectroscopy of NH_3NH_4^+ [126, 127].

	Position ^a / cm^{-1}	Internal vibrational energy E_v/hc / cm^{-1} of N_2H_7^+		Calculated position / cm^{-1}
Threshold A	31 310(25)	0		0
Threshold B	31 655(25)	345(25)	ν_s	434 ^b , 430 ^c
IR spectrum		373 ^b	ν_z ^b	471 ^b , 451 ^c
Threshold C	31 830(30)	520		
Threshold D	32 000(25)	690(25)	$2\nu_s$	691 ^b , 804 ^c
IR spectrum		743 ^b	$\nu_s + \nu_z$ ^b	819 ^b , 832 ^c

^aThis work^bRef. [127]^cRef. [128]

Assuming that the ionization of NH_3NH_4 leads to a contraction of the distance between the N atoms and a motion of the central proton towards the middle point between these two atoms one would expect both the asymmetric proton-transfer mode ν_z and the symmetric intermolecular stretching mode ν_s to be Franck-Condon active in the photoelectron spectrum. In particular, one would expect to be able to observe the transition to the symmetric intermolecular stretch fundamental which is forbidden in the IR spectrum. Because the vibrational structure of the photoelectron spectrum is not expected to resemble that of the IR spectrum and because none of the vibrational intervals observed by IR and PFI-ZEKE photoelectron spectroscopy are identical, only a very tentative assignment of the vibrational bands observed in the PFI-ZEKE photoelectron spectrum can be made at present on the basis of the results reported in Refs. [126–128]: The bands corresponding to thresholds B and D may correspond to transitions to the fundamental and first overtone of the symmetric stretching mode of the NH_3 molecules. High-level *ab initio* quantum chemical calculations would be desirable to test this tentative assignment.

Attempts at resolving the rotational structure of the bands in the PFI-ZEKE photoelectron spectra to gain more information have unfortunately remained unsuccessful because of the weakness of the signals and the congested nature of the spectra. The large width of the observed bands suggests a contribution from the internal rotation/torsional mode of N_2H_7^+ .

4.3.2.2 Experiments on $(\text{ND}_3)_3$ clusters

The TOF spectra observed following the 204 nm photolysis of $(\text{ND}_3)_n$ clusters and the subsequent ionization of the fragments at different wave numbers are presented in Fig 4.4, in which the top trace represents the TOF spectrum recorded without photoionization laser, which was subtracted to obtain all other spectra. The behavior of most peaks in these TOF spectra resembles that observed in the investigation of the undeuterated

ammonia clusters with two main differences: Firstly, a ND_3^+ signal is observed at all wave numbers which suggests that the initially excited $(\text{ND}_3)_2$ state does not fragment as fast as in the case of the undeuterated clusters, but survive until the second laser pulse is applied. Secondly, a strong, wave-number-dependent N_2D_6^+ signal is observed which again suggests that the excited N_2D_6 molecules do not fragment. The sharp increase of the N_2D_6^+ signal at a wave number of $\approx 30750\text{ cm}^{-1}$ marked by the A' arrow in Fig. 4.4 indicates that the ionization energy of the N_2D_6 molecule lies much lower than expected for a $(\text{ND}_3)_2$ dimer which should have an ionization threshold of more than 70000 cm^{-1} . The ND_3ND_4^+ ion peak also increases with increasing wave number as indicated by the two thresholds marked by arrows B' and C' in Fig. 4.4, but is clearly not the main ionization product.

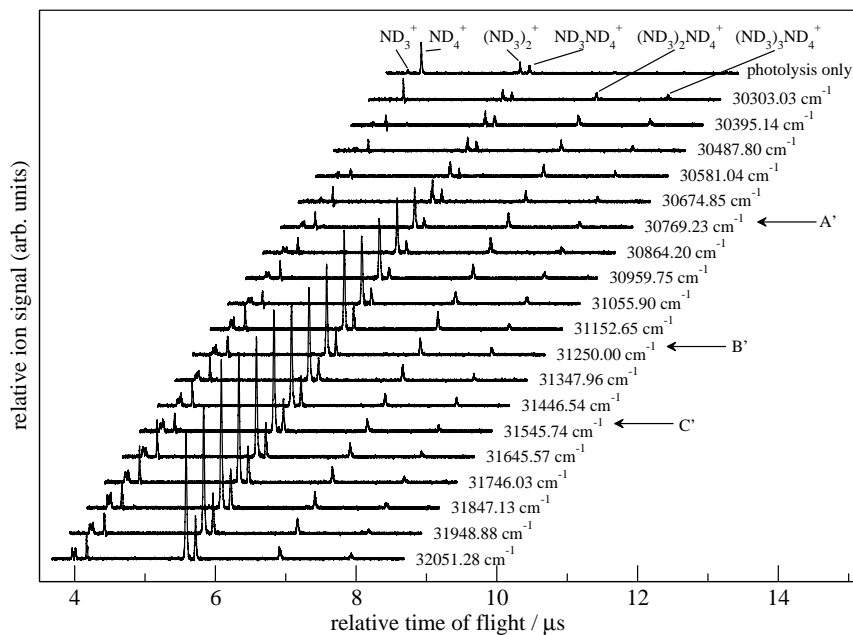


Figure 4.4: TOF mass spectra of perdeuterated ammonia cluster ions produced at several ionization wave numbers in the range $30303\text{ cm}^{-1} - 32051\text{ cm}^{-1}$ following the photolysis of $(\text{ND}_3)_n$ clusters at 204 nm. The ionization efficiency of $\text{ND}_4(\text{ND}_3)_n$ ($n \geq 2$) does not change appreciably in this wave number range while the ionization efficiency of ND_4ND_3 and $(\text{ND}_3)_2$ exhibits thresholds indicated arrows. The top TOF spectrum was recorded with only the photolysis laser on and was subtracted from all other spectra.

The photoionization spectra recorded at the masses of N_2D_6^+ and N_2D_7^+ are displayed as top and bottom traces in the upper panel of Fig. 4.5 where they can be directly compared with the PFI-ZEKE photoelectron spectrum shown in the lower panel. The broad and blue-degraded feature A' in the PFI-ZEKE photoelectron spectrum must clearly be attributed to N_2D_6 whereas the next feature labeled B' must be attributed to N_2D_7 . It is unfortunately not possible to unambiguously attribute the next broad and blue-degraded feature (C') in the PFI-ZEKE photoelectron spectrum to either N_2D_6 or N_2D_7 and it is possible that this feature comprises contributions from both molecules.

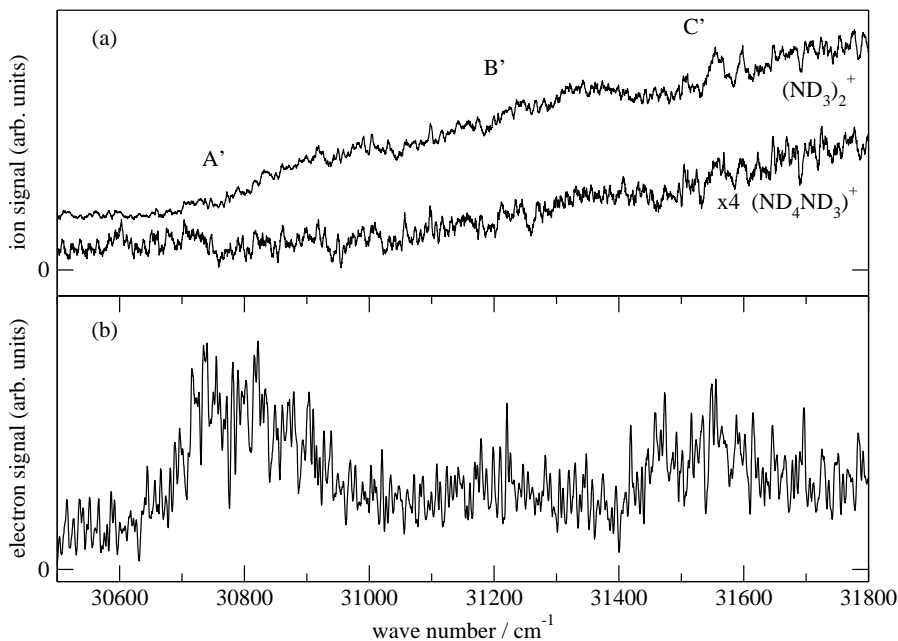


Figure 4.5: Panel (a) shows the photoionization spectrum recorded at the mass of N_2D_6^+ and N_2D_7^+ with a delayed pulsed electric field of 173 V cm^{-1} . The ionization thresholds are labeled with A', B', and C', respectively. Panel (b) depicts the PFI-ZEKE photoelectron spectrum recorded in the same wave number region.

In the light of the observations made in earlier experimental and theoretical studies and summarized at the beginning of this section, it appears likely that the N_2D_6 molecules giving rise to band A' of the photoelectron spectrum correspond to $\text{ND}_2\text{-ND}_4$ molecules produced by fragmentation of the trimer or excitation of the dimer and trapped in the shallow minimum in the potential energy surface predicted by *ab initio* quantum chemical calculations [131].

Because no such metastable $\text{NH}_2\text{-NH}_4$ structure could be observed in the experiments carried out on the ammonia clusters, one must conclude that the heavier masses and the lower zero-point vibrational energy render the $\text{ND}_2\text{-ND}_4$ species metastable, in a very similar way as deuteration renders ND_4 more stable than NH_4 . Assuming that the threshold B' ($31\,220(25) \text{ cm}^{-1}$) corresponds to the adiabatic ionization energy of ND_3ND_4 leads to the conclusion that the adiabatic ionization energy shifts towards lower wave numbers by $\approx 90 \text{ cm}^{-1}$ upon full deuteration.

4.4 Conclusions

This study of the threshold ionization of the ammonium radical and ammoniated ammonium dimers has revealed very pronounced isotopic effect on the fragmentation dynamics of ammonia clusters. Whereas photolysis of $(\text{NH}_3)_3$ by 204 nm leads predominantly to the

formation of NH_3NH_4 clusters, the photolysis of $(\text{ND}_3)_3$ and $(\text{ND}_3)_2$ at the same wavelength favors the production of $\text{ND}_4\text{-ND}_2$ clusters. The latter observation provides the first clear experimental evidence for the existence of the shallow minimum corresponding to $\text{ND}_4\text{-ND}_2$ on the excited state potential surface predicted by *ab initio* quantum chemical calculations.

The observation of several bands separated by small wave number intervals in the PFI-ZEKE photoelectron spectrum of NH_3NH_4 and the comparison with recent results on the low-lying vibrational levels of N_2H_7^+ by IR spectroscopy and quantum chemistry suggest that the vibrational mode involving the symmetric stretching motion of the two NH_3 units may be the dominant Franck-Condon active mode in the photoionization of NH_3NH_4 .

This study has revealed the unexpected richness of the photodissociation and photoionization dynamics of ammoniated ammonium clusters. In future, measurements enabling an improved signal-to-noise ratio and a better resolution would be very desirable, particularly in view of observing the rotational structure and the low frequency motions associated with the internal rotation and intramolecular modes of vibration of N_2H_7^+ , N_2D_7^+ , and N_2D_6^+ .

Chapter 5

Millimeter-wave spectroscopy and multichannel quantum-defect-theory analysis of high Rydberg states of xenon: The hyperfine structure of $^{129}\text{Xe}^+$ and $^{131}\text{Xe}^+$

Rydberg states of high principal quantum number are an important class of metastable states in atoms and molecules. Their metastability comes from the fact that the motion of the Rydberg electron is almost completely decoupled from that of the positively charged ion core in these states. Because of their long lifetimes and the very large moments of transitions connecting neighboring Rydberg states, high Rydberg states are ideally suited to be studied by high-resolution spectroscopy. This chapter illustrates how the spectroscopy of long-lived high Rydberg states can be used to extract very precise information on the energy level structure of cations and how multichannel quantum defect theory, a collision theory, can be used to analyze the observed energy level structure, including the hyperfine structure.

5.1 Introduction

The magnitude of interactions involving nuclear spins (in the absence of a strong magnetic field) is much smaller than that of the corresponding interactions involving the magnetic moment of an electron or the magnitude of the rovibrational level structure of a ground state molecule. High-resolution spectroscopy is needed to resolve the hyperfine structure of an atom or a molecule.

The effects of nuclear spins could be thought to be negligible in photoionization, and

have been neglected until recently in all theoretical treatments, which solely assume the conservation of nuclear spin symmetry. The conservation of nuclear spin symmetry lead to observable effects in molecular photoionization and photoelectron spectra, even at low resolution, as is demonstrated by the intensity of rotational transitions which are proportional to nuclear spin statistical weight factors (the photoelectron spectra of ND₃ presented in Chapter 3 represents an example). Similarly, a nonzero nuclear spin can make a “forbidden” transition “allowed” because it changes the total angular momentum, on which the selection rule for the transition depends.

Recently, effects of nuclear spins on photoionization spectra that go beyond the conservation of nuclear spin symmetry have been observed in spectra of xenon [135], krypton [136, 137], and ortho-H₂ [66]. Calculations based on high-resolution experiments have shown that hyperfine autoionization, i.e., the autoionization process by which the ionic core transfers hyperfine energy to the Rydberg electron to cause ionization, is very efficient in rare-gas atoms [135]. Whereas the hyperfine splitting of low- n Rydberg states is much smaller than the separation between two consecutive states of the same Rydberg series, the situation is different for very high- n Rydberg states, where the separation becomes smaller than the hyperfine splitting of the ionic core. As a consequence of the different n -dependence of the various interactions, different angular momentum coupling hierarchies are observed with increasing n values [66]. Because Rydberg states can be regarded as the bound part of an ionization channel, the observation of the hyperfine structure of Rydberg states, if it can be resolved, can be used to obtain information on aspects of the role of nuclear spins in photoionization that have remained unrecognized so far. It can also be used to determine, by extrapolation of the Rydberg series, the hyperfine structure of cations.

The determination of high-resolution spectroscopic information on cations represents a considerable challenge, particularly in cases where no allowed transitions lie in the infrared and visible region of the electromagnetic spectrum. In such cases, the information on the cation can be derived from Rydberg state spectroscopy and extrapolation of the Rydberg series using multichannel quantum defect theory (MQDT) [23, 138, 139]. This method has been recently used to determine the hyperfine structure of the ground state of ortho-H₂⁺ [73] and para-D₂⁺ [75] and of both spin-orbit states (²P_{3/2} and ²P_{1/2}) of the ground state of ⁸³Kr⁺ [74, 136, 137, 140]. For the two naturally occurring isotopes of xenon with nonzero nuclear spin, ¹²⁹Xe ($I = 1/2$) and ¹³¹Xe ($I = 3/2$), the hyperfine structure of the ²P_{1/2} state of the ion has been determined from the analysis of the autoionizing Rydberg series [135]. Fig. 5.1 displays schematically the hyperfine structure of the ²P_{3/2} and ²P_{1/2} states of ¹³¹Xe⁺ and ¹²⁹Xe⁺ as determined in the realm of this thesis (²P_{1/2} state) and in Ref. [135] (²P_{1/2} state).

The determination of the hyperfine structure of the ²P_{3/2} ground state of Xe⁺ from

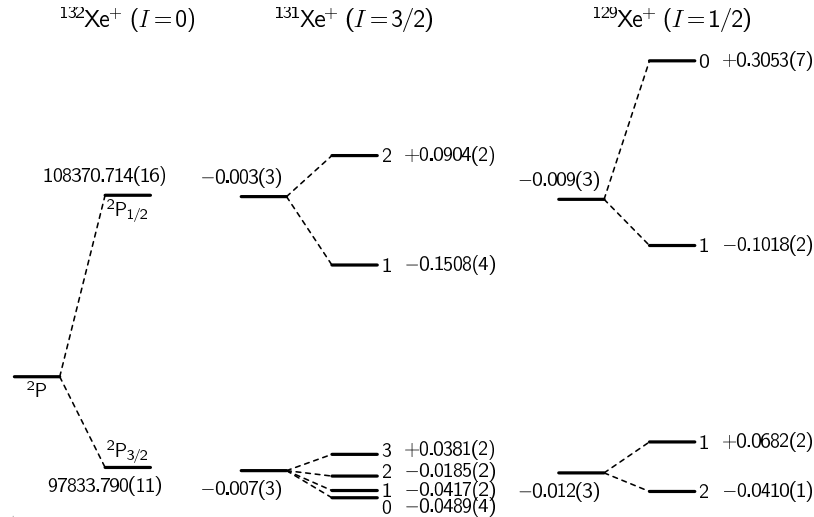


Figure 5.1: Energy level diagram (not to scale) of the $2P$ ground state of $^{132}\text{Xe}^+$, $^{131}\text{Xe}^+$, and $^{129}\text{Xe}^+$. For each spin-orbit component of the ion ($2P_{3/2}$ and $2P_{1/2}$), the wavenumbers (cm^{-1}) of the ionization energies of ^{132}Xe from the $1S_0$ ground state and the isotope shifts (cm^{-1}) for ^{131}Xe and ^{129}Xe are given. The hyperfine levels for $^{131}\text{Xe}^+$ and $^{129}\text{Xe}^+$ are labeled with the quantum number F^+ and their positions (cm^{-1}) with respect to the center of gravity of the hyperfine structure are given. The data for the $2P_{1/2}$ state are from Ref. [135], the ionization energies for the $2P_{3/2}$ state are from Ref. [141] and the hyperfine structures were determined in the present study.

high-resolution millimeter-wave spectra of high- n Rydberg states of xenon is the subject of the study presented in this chapter. The same technique, partially described in Subsection 2.5.3, was employed as was used to determine the hyperfine structure of the $2P_{3/2}$ state of $^{83}\text{Kr}^+$ [74, 142]: Millimeter-wave transitions between high- n Rydberg states of xenon were measured using selective field ionization and mass-selective detection of the ions; from the observed transition frequencies, the intervals between the Rydberg levels were derived with a precision of better than 1 MHz. The hyperfine structure of the ion was derived in a MQDT analysis of the millimeter-wave spectroscopic data and complementary experimental data from the literature [135, 141, 143–183] (see Table 5.1).¹ Even though the millimeter-wave data cover only a small range of atomic energy levels, the high-resolution makes it possible to determine accurate MQDT parameters which can be extrapolated over a substantial range of energy levels, as already shown for krypton, where the MQDT parameters of the odd-parity states determined from the bound Rydberg states [74] have been found to describe the autoionizing Rydberg states very well [136, 137]. The presence of a nonzero nuclear spin I allows access to hyperfine levels of states not accessible in $I = 0$ isotopes, and additional information is obtained from the hyperfine structure. The new high-resolution millimeter-wave data enabled us to improve the existing sets of MQDT parameters describing the photoionization of xenon [171, 183–191].

¹This analysis has been performed by Dr. Martin Schäfer.

Table 5.1: Overview of the experimental energy levels of Xe reported in the literature.

$n\ell[K]_J$	n	Refs.	$n\ell[K]_J$	n	Refs.
$nd [1/2]_0$	5–21	[147, 155, 171, 176]	$np [1/2]_0$	6–42	[147, 164, 176]
$ns' [1/2]_0$	6–7,9–15	[147, 161, 176]	$np' [1/2]_0$	6–11,13,18–31	[147, 153, 163, 169, 176, 178]
$nd [1/2]_1$	5–34	[141, 147, 155, 156, 176]	$np [1/2]_1$	6–12,15–19,28–40	[147, 153, 158, 176]
$nd [3/2]_1$	5–66	[141, 147, 155, 156, 176]	$np [3/2]_1$	6–12	[147, 176]
$ns [3/2]_1$	6–47	[147, 155, 156, 176]	$nf [3/2]_1$	4–73	[147, 153, 158, 176]
$nd' [3/2]_1$	5–78	[147, 156, 157, 161, 167, 173, 176]	$np' [3/2]_1$	6–17	[147, 153, 160, 170, 176, 178, 181]
$ns' [1/2]_1$	6–52	[141, 147, 156, 157, 161, 167, 173, 176]	$np' [1/2]_1$	6–17	[147, 153, 160, 170, 176, 178, 181]
$nd [3/2]_2$	5–25	[147, 155, 176]	$np [5/2]_2$	6–27	[147, 164, 176]
$nd [5/2]_2$	5–25	[147, 155, 176]	$np [3/2]_2$	6–27	[147, 164, 176]
$ns [3/2]_2$	6–44	[147, 155, 171, 176]	$nf [3/2]_2$	4–19 ^a	[147, 164, 171, 176]
$nd' [3/2]_2$	5,7–40	[161, 176, 177]	$nf [5/2]_2$	4–19 ^a	[147, 164, 171, 176]
$nd' [5/2]_2$	5,7–24	[161, 176, 177, 183]	$np' [3/2]_2$	6–11,13	[147, 153, 169, 176, 178, 181]
$nd [7/2]_3$	5–25	[147, 155, 176]	$nf' [5/2]_2$	4–13	[153, 169, 172, 176]
$nd [5/2]_3$	5–29	[147, 155, 171, 176]	$np [5/2]_3$	6–15	[147, 176]
$nd' [5/2]_3$	5,7–40	[147, 161, 176, 177, 183]	$nf [5/2]_3$	4–11	[147, 176]
$nd [7/2]_4$	5–44	[147, 155, 171, 176]	$nf [7/2]_3$	4–13	[147, 171, 176]
			$nf' [7/2]_3$	4–8 ^b	[176, 181]
			$nf' [5/2]_3$	4–8 ^b	[176]
			$nf [9/2]_4$	4–11	[147, 176]
			$nf [7/2]_4$	4–9	[147, 176]
			$nf' [7/2]_4$	4–8 ^b	[176, 181]
			$nf [9/2]_5$	4–11	[147, 176]

^a The $nf [3/2]_2$ and $nf [5/2]_2$ levels with $n > 19$ are not resolved in the experiments reported in Ref. [164].

^b Of the autoionizing $nf' [K]_J$ ($J = 3, 4$) Rydberg series, only the $n = 4, 5$ levels of the $K = 7/2$ ($J = 3, 4$) series reported in Ref. [181] are resolved.

Whereas the study of the hyperfine structure of the bound Rydberg states of krypton [74] covered only penetrating odd-parity states (the ns ($\ell = 0$) and nd ($\ell = 2$) Rydberg series with large quantum defects ($\delta > 1$)), the present study includes even-parity np ($\ell = 1$) and nf ($\ell = 3$) levels, of which the nf states exhibit nonpenetrating character with a qualitatively different hyperfine structure. Some p and d Rydberg states of xenon are energetically very close, even for the $I = 0$ isotopes, which enabled us to study the mixing of these states induced by small electric stray fields and to observe otherwise forbidden transitions.

5.2 Experiments

The millimeter-wave spectra of high- n Rydberg states of xenon were measured with the experimental procedure described in Section 2.5.3 and in Refs. [35, 74]. The millimeter-wave source, a phase-stabilized backward wave oscillator (BWO) operating in the frequency range 240–380 GHz, has been described in Section 2.3 and Ref. [36].

Xenon atoms were excited to high Rydberg states using ultraviolet (UV) and visible radiation from two pulsed dye lasers pumped by the tripled (355 nm) and doubled (532 nm) output of a Nd:YAG laser using the experimental setup described in Section 2.2.3. The wavenumber of the first dye laser was doubled and set to correspond to the $(5p)^5(2P_{3/2})6p[1/2]_0 \leftarrow (5p)^6\ ^1S_0$ two-photon resonance of xenon ($2\tilde{\nu}_1 = 80\,118.96\text{ cm}^{-1}$). The radiation of the second dye laser ($17\,670\text{--}17\,676\text{ cm}^{-1}$) excited the xenon atoms to high- ns and nd ($J = 1$) Rydberg states, which served as initial states for millimeter-wave transitions. In order to minimize the background ion signal (from $3\tilde{\nu}_1$ or $2\tilde{\nu}_1 + 2\tilde{\nu}_2$ photoionization), the powers of the lasers were set as low as possible, and the second laser was delayed with respect to the first one by about 15 ns using an optical delay line. Both laser beams were arranged collinearly and crossed a pulsed skimmed supersonic beam of xenon (Pangas, spectroscopic grade purity) at right angles in the middle of an array of resistively coupled cylindrical extraction plates. The millimeter-wave radiation entered the photoexcitation region perpendicularly to the xenon and the laser beams.

Because an oversized waveguide is used for the BWO, its output is distributed among different electro-magnetic modes with horizontal or vertical polarization [36]. The polarization vector of the first laser and the main polarization vector of the millimeter-wave radiation were oriented parallel to the atomic beam and the applied electric field. The polarization vector of the second laser and the secondary polarization vector of the millimeter-wave radiation were mutually perpendicular and perpendicular to the atomic beam and the applied field. This arrangement allows the observation of $\Delta M = 0, \pm 1$ transitions and does not lead to any polarization restriction of the observable millimeter-wave transitions.

The millimeter-wave transitions were detected by selective field ionization using a pulsed electric field in the range between 40 and 133 V/cm, which was applied 1–4 μs after the laser pulse and also accelerated the xenon ions towards a microchannel plate (MCP) detector. Spectra of different xenon isotopes (^{128}Xe , ^{129}Xe , ^{130}Xe , ^{131}Xe , ^{132}Xe , ^{134}Xe , and ^{136}Xe) were obtained by placing temporal gates at the corresponding positions of the time-of-flight (TOF) spectrum. Examples of such isotope-selective spectra are displayed in Figs. 5.2 and 5.3. The residual stray electric fields were reduced to values below 5 mV/cm using the procedure described in Section 2.5.3 and in Ref. [17], which consisted of measuring the Stark shift for different applied fields and determining the field for which the Stark shift was minimal. In order to avoid power broadening of the

millimeter-wave transitions (see Ref. [35]), the millimeter-wave radiation was attenuated by about -10 dB by introducing stacks of paper between the millimeter-wave source and the experimental chamber. These methods allowed an accuracy in the measured transition frequencies of better than 1 MHz.

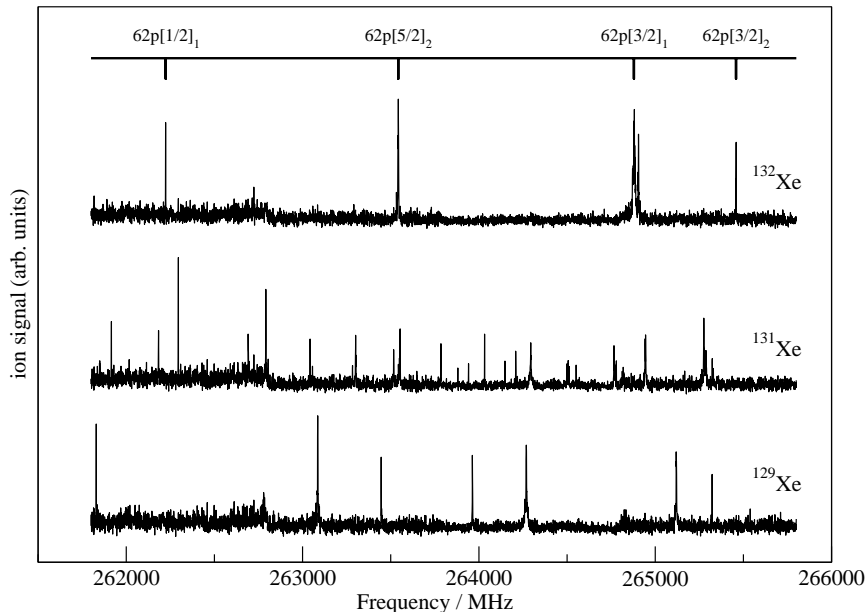


Figure 5.2: Comparison of millimeter-wave overview spectra of the $62p \leftarrow 54d [3/2]_1$ transitions for the three most abundant isotopes ^{132}Xe ($I = 0$, 26.9% nat. abundance, top trace), ^{131}Xe ($I = 3/2$, 21.2%, middle), ^{129}Xe ($I = 1/2$, 26.4%, bottom).

5.3 MQDT calculations

To analyze the Rydberg spectrum of Xe using MQDT, we follow the formalism introduced by Lu [184] and Lee and Lu [192] for the analysis of the Xe and Ar absorption spectra. This formalism was extended by Wörner *et al.* [140] for the analysis of the hyperfine structure of ^{83}Kr (in a method similar to that outlined by Sun [193]) and was used to analyze the millimeter wave spectra of ^{83}Kr [74].

In the analysis, three different angular momentum coupling schemes are used. In the close-coupling region of the electron–ion collision, the electrostatic interaction between the electron and the ion core is larger than the spin–orbit and much larger than the hyperfine interaction [192]. Therefore, the following (LS) angular momentum coupling scheme is adequate to describe the close-coupling eigenchannels:

$$\vec{L}^+ + \vec{\ell} = \vec{L}, \quad \vec{S}^+ + \vec{s} = \vec{S}, \quad \vec{L} + \vec{S} = \vec{J}, \quad \vec{J} + \vec{I} = \vec{F}, \quad (5.1)$$

where \vec{L}^+ and \vec{S}^+ represent the orbital and spin angular momenta of the ionic core, $\vec{\ell}$ and

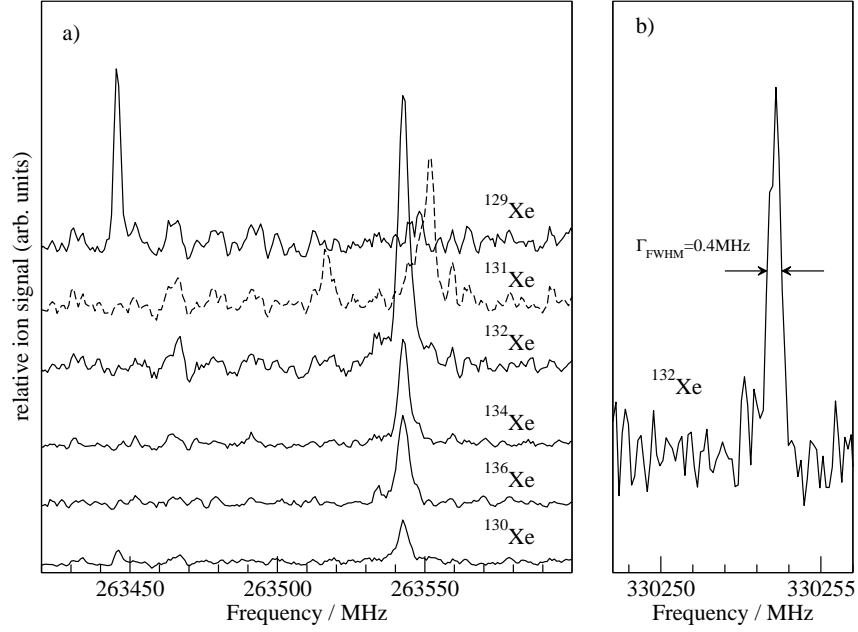


Figure 5.3: The left panel shows a section of the millimeter-wave overview spectrum of the $62p\ [5/2]_2 \leftarrow 54d\ [3/2]_1$ transition recorded in different mass channels. The spectra have been shifted along the vertical axis by an offset of 0–5 arb. units. The spectrum of the ^{131}Xe isotope is drawn with dashed line for clarity. The strong peak in the ^{129}Xe spectrum at 263 446 MHz is the $62p\ [5/2]_3(F = 5/2) \leftarrow 54d\ [3/2]_1(F = 3/2)$ transition, whereas the strong peak in the ^{131}Xe spectrum at 263 553 MHz is the $62p[5/2]_3(F = 5/2) \leftarrow 54d\ [3/2]_1(F = 5/2)$ transition. The right panel shows the millimeter-wave spectrum of the $61p\ [5/2]_2 \leftarrow 52d\ [3/2]_1$ transition of ^{132}Xe at high-resolution.

\vec{s} the corresponding angular momenta of the Rydberg electron, and \vec{I} the nuclear spin. In the long-range part of the electron–ion collision, however, the energy level structure of the Rydberg states corresponds primarily to the energy levels of the ionic core. Thus the following (J^+j or F^+j) coupling scheme is used for the dissociation channels [140]:

$$\vec{L}^+ + \vec{S}^+ = \vec{J}^+, \quad \vec{J}^+ + \vec{I} = \vec{F}^+, \quad \vec{\ell} + \vec{s} = \vec{j}, \quad \vec{F}^+ + \vec{j} = \vec{F}. \quad (5.2)$$

A summary of all possible hyperfine levels with $\ell \leq 3$ of ^{129}Xe and ^{131}Xe , below the $^2P_{3/2}$ and $^2P_{1/2}$ thresholds, is given in Table 5.2. The assignments of the Rydberg levels observed in this study are made using the notation $n\ell[K]_J$ based on the traditional Racah ($J^+\ell$) coupling scheme [194]:

$$\vec{L}^+ + \vec{S}^+ = \vec{J}^+, \quad \vec{J}^+ + \vec{\ell} = \vec{K}, \quad \vec{K} + \vec{s} = \vec{J}, \quad \vec{J} + \vec{I} = \vec{F}. \quad (5.3)$$

Table 5.1 summarizes all $n\ell[K]_J$ Rydberg series of Xe with $\ell \leq 3$ observed so far; a prime indicates, as usual, Rydberg states belonging to series converging to the $^2P_{1/2}$ ionization limit.

For atoms with a nuclear spin $I = 0$, the energies of the bound states are well de-

Table 5.2: Summary of the hyperfine Rydberg levels of Xe converging to each hyperfine state F^+ of the ion. The entries are F . The last two lines represent the case $I = 0$, where $F^+ = J^+$ and $F = J$.

F^+	$\ell = 0$		$\ell = 1$		$\ell = 2$		$\ell = 3$	
	$j = \frac{1}{2}$	$j = \frac{1}{2}$	$j = \frac{3}{2}$	$j = \frac{3}{2}$	$j = \frac{5}{2}$	$j = \frac{5}{2}$	$j = \frac{7}{2}$	
0	$\frac{1}{2}$	$\frac{1}{2}$	$\frac{3}{2}$	$\frac{3}{2}$	$\frac{5}{2}$	$\frac{5}{2}$	$\frac{7}{2}$	
1	$\frac{1}{2}, \frac{3}{2}$	$\frac{1}{2}, \frac{3}{2}$	$\frac{1}{2}, \frac{3}{2}, \frac{5}{2}$	$\frac{1}{2}, \frac{3}{2}, \frac{5}{2}$	$\frac{3}{2}, \frac{5}{2}, \frac{7}{2}$	$\frac{3}{2}, \frac{5}{2}, \frac{7}{2}$	$\frac{5}{2}, \frac{7}{2}, \frac{9}{2}$	
2	$\frac{3}{2}, \frac{5}{2}$	$\frac{3}{2}, \frac{5}{2}$	$\frac{1}{2}, \frac{3}{2}, \frac{5}{2}, \frac{7}{2}$	$\frac{1}{2}, \frac{3}{2}, \frac{5}{2}, \frac{7}{2}$	$\frac{1}{2}, \frac{3}{2}, \frac{5}{2}, \frac{7}{2}, \frac{9}{2}$	$\frac{1}{2}, \frac{3}{2}, \frac{5}{2}, \frac{7}{2}, \frac{9}{2}$	$\frac{3}{2}, \frac{5}{2}, \frac{7}{2}, \frac{9}{2}, \frac{11}{2}$	
3	$\frac{5}{2}, \frac{7}{2}$	$\frac{5}{2}, \frac{7}{2}$	$\frac{3}{2}, \frac{5}{2}, \frac{7}{2}, \frac{9}{2}$	$\frac{3}{2}, \frac{5}{2}, \frac{7}{2}, \frac{9}{2}$	$\frac{1}{2}, \frac{3}{2}, \frac{5}{2}, \frac{7}{2}, \frac{9}{2}, \frac{11}{2}$	$\frac{1}{2}, \frac{3}{2}, \frac{5}{2}, \frac{7}{2}, \frac{9}{2}, \frac{11}{2}$	$\frac{1}{2}, \frac{3}{2}, \frac{5}{2}, \frac{7}{2}, \frac{9}{2}, \frac{11}{2}, \frac{13}{2}$	
$\frac{1}{2}$	0,1	0,1	1,2	1,2	2,3	2,3	3,4	
$\frac{3}{2}$	1,2	1,2	0,1,2,3	0,1,2,3	1,2,3,4	1,2,3,4	2,3,4,5	

scribed by a set of MQDT parameters consisting of the ionization thresholds $E(^2P_{J^+})$, the eigenchannel quantum defects μ_α , their energy dependence, and the elements of the orthogonal transformation matrix $U_{i\alpha}$ connecting the close-coupling eigenchannels α to the fragmentation channels i . Each bound energy level is represented by two effective principal quantum numbers $\nu_{3/2}$ and $\nu_{1/2}$ defined by the relations

$$E = E(^2P_{3/2}) - \frac{R_M}{(\nu_{3/2})^2} = E(^2P_{1/2}) - \frac{R_M}{(\nu_{1/2})^2}, \quad (5.4)$$

where R_M is the mass-dependent Rydberg constant. The bound energy levels are the solutions satisfying the relation

$$\det |U_{i\alpha} \sin[\pi(\mu_\alpha + \nu_i)]| = 0, \quad (5.5)$$

where ν_i is $\nu_{3/2}$ or $\nu_{1/2}$ for channels associated with the $^2P_{3/2}$ or $^2P_{1/2}$ ionization limits, respectively. The elements $U_{i\alpha}$ of the $N \times N$ transformation matrix are conveniently factorized as

$$U_{i\alpha} = \sum_{\bar{\alpha}} U_{i\bar{\alpha}} V_{\bar{\alpha}\alpha}, \quad (5.6)$$

where $U_{i\bar{\alpha}} = \langle LSJ | J^+ j - LS \rangle$ represents elements of the $J^+ j - LS$ frame-transformation matrix. $V_{\bar{\alpha}\alpha}$ accounts for the typically small departure of the close-coupling channels from pure LS coupling and may be represented by $N(N-1)/2$ generalized Euler angles θ_{jk} as described by Lee and Lu [192]

$$V_{\bar{\alpha}\alpha} = \prod_j^N \prod_{k>j}^N \mathbf{R}(\theta_{jk}), \quad (5.7)$$

where $\mathbf{R}(\theta_{jk})$ are rotation matrices defined as

$$R_{mm}(\theta_{jk}) = \begin{cases} \cos \theta_{jk} & \text{if } m=j \text{ or } m=k \\ 1 & \text{otherwise} \end{cases}, \quad (5.8)$$

$$R_{mn}(\theta_{jk}) = \begin{cases} -\sin \theta_{jk} & \text{if } m=j, n=k \\ \sin \theta_{jk} & \text{if } m=k, n=j \\ 0 & \text{otherwise} \end{cases}. \quad (5.9)$$

The energy dependence of μ_α and $V_{\alpha\alpha}$ can be approximated by

$$\mu_\alpha = \mu_\alpha^0 + \epsilon \mu_\alpha^1 \quad (5.10)$$

$$\theta_{jk} = \theta_{jk}^0 + \epsilon \theta_{jk}^1 \quad (5.11)$$

where

$$\epsilon = \frac{E - E(^2P_{3/2})}{R_M} \quad \text{or} \quad \epsilon = -(\nu_{3/2})^{-2} \quad (\text{for } \epsilon < 0). \quad (5.12)$$

Because the hyperfine interaction in the ionic core is much smaller than the spin-orbit interaction, which leads to an energy splitting of $10\,536.92 \text{ cm}^{-1}$ between the $^2P_{3/2}$ and $^2P_{1/2}$ levels [135], mixing of the spin-orbit components by the hyperfine interaction is negligible. Therefore, the hyperfine structures of the two spin-orbit components (see Fig. 5.1) can be treated separately and expressed as functions of the magnetic dipole and electric quadrupole constants A_{J^+} and B_{J^+} ($B_{J^+} = 0$ for $I = 1/2$ (^{129}Xe) or $J^+ = 1/2$) as

$$E(J^+, F^+) = E(J^+) + A_{J^+} \frac{C}{2} + B_{J^+} \frac{\frac{3}{4}C(C+1) - I(I+1)J^+(J^++1)}{2I(2I-1)J^+(2J^+-1)}, \quad (5.13)$$

where $C = F^+(F^++1) - I(I+1) - J^+(J^++1)$ and $E(J^+)$ is the energy of the center of gravity of the hyperfine structure. The contribution from the octupole coupling is many orders of magnitude smaller [145, 195] and thus neglected here. In analogy to Eq. 5.5, the Rydberg levels are determined by solving the determinantal equation

$$\det |U_{i_F \alpha_F} \sin[\pi(\mu_{\alpha_F} + \nu_{i_F})]| = 0, \quad (5.14)$$

where

$$U_{i_F \alpha_F} = \sum_{\bar{\alpha}_F} U_{i_F \bar{\alpha}_F} V_{\bar{\alpha}_F \alpha_F}, \quad (5.15)$$

and ν_{i_F} is an effective principal quantum number $\nu_{J^+F^+}$ defined relative to the position of the ionization threshold of the dissociation channel i_F (i.e., the position of one of the

four or six hyperfine levels of the ion):

$$E = E(^2P_{J^+F^+}) - \frac{R_M}{(\nu_{J^+F^+})^2}. \quad (5.16)$$

The elements of the frame transformation matrix $U_{i_F\bar{\alpha}_F} = \langle LSJF|J^+F^+jF\rangle$ are calculated as [74, 140]

$$\begin{aligned} \langle LSJF|J^+F^+jF\rangle = & \\ & (2F+1)\sqrt{(2J+1)(2L+1)(2S+1)(2j+1)(2F^++1)(2J^++1)} \\ & \times \sum_{m_j, m_{J^+}, m_J, m_\ell, m_{L^+}, m_L, m_s, m_{S^+}, m_S, m_{F^+}, m_I} (-1)^{F^+-j-J^++2I-J+L-S-2s+3m_{F^+}+m_{J^+}+2m_J} \\ & \times \begin{pmatrix} I & J & F \\ m_I & m_J & -m_{F^+} \end{pmatrix} \begin{pmatrix} L & S & J \\ m_L & m_S & -m_J \end{pmatrix} \begin{pmatrix} L^+ & \ell & L \\ m_{L^+} & m_\ell & -m_L \end{pmatrix} \begin{pmatrix} S^+ & s & S \\ m_{S^+} & m_s & -m_S \end{pmatrix} \\ & \times \begin{pmatrix} F^+ & j & F \\ m_{F^+} & m_j & -m_F \end{pmatrix} \begin{pmatrix} \ell & s & j \\ m_\ell & m_s & -m_j \end{pmatrix} \begin{pmatrix} I & J^+ & F^+ \\ m_I & m_{J^+} & -m_{F^+} \end{pmatrix} \begin{pmatrix} L^+ & S^+ & J^+ \\ m_{L^+} & m_{S^+} & -m_{J^+} \end{pmatrix} \end{aligned} \quad (5.17)$$

for any value of m_F . Whereas the transformation matrix $U_{i\alpha}$ for $I = 0$ isotopes is block-diagonal in J , the transformation matrix $U_{i_F\alpha_F}$ can be separated into individual F blocks, of which the even parity $F = 5/2$ matrix of ^{131}Xe , with dimension 19×19 , is the largest. The dimensions of the $U_{i\alpha}$ and $U_{i_F\alpha_F}$ matrices can be easily derived from Table 5.2, which summarizes all s, p, d, and f Rydberg series of xenon, including hyperfine structure. Assuming that the eigenchannel quantum defects μ_α are equal for all isotopes and that the hyperfine interaction is negligible in the close-coupling region, the eigenchannel quantum defects μ_α obtained from the analysis of the Rydberg levels of any given $I = 0$ isotope and the $V_{\bar{\alpha}\alpha}$ matrix elements can also be used for the analysis of $I > 0$ isotopes, i.e., $\mu_{\alpha_F} = \mu_\alpha$ and $V_{\bar{\alpha}_F\alpha_F} = V_{\bar{\alpha}\alpha}$. The signs of the elements of the corresponding frame transformation matrices of the different J values must be consistent, which can be ensured by calculating the elements $U_{i\bar{\alpha}} = \langle LSJ|J^+jJ\rangle$ with Eq. (5.17) and setting $I = 0$ (in which case $F^+ = J^+$ and $F = J$). The resulting $U_{i\bar{\alpha}}$ matrices differ from those used by Aymar *et al.* [196] for the ns/d states of krypton and those given by Condon and Shortley [197].

5.4 Results

A typical millimeter-wave overview spectrum is shown in Fig. 5.2. Recording spectra of different isotopes simultaneously by setting several temporal gates at the corresponding positions of the TOF spectrum is very efficient. The shifts of isotopes with even mass numbers are negligible, thus the transitions between high Rydberg states occur at almost

the same frequencies for all $I = 0$ isotopes but at different frequencies for the $I \neq 0$ isotopes because of the hyperfine splittings. This observation is illustrated in Fig. 5.3a, which shows spectra of the $62p[5/2]_2 \leftarrow 54d[3/2]_1$ transition of Xe recorded for different isotopes. The quality of the mass resolution can be assessed by comparing the spectra of isotopes with mass numbers differing by one. Fig. 5.3b displays a high-resolution recording of the $61p[5/2]_2 \leftarrow 52d[3/2]_1$ transition of ^{132}Xe and shows that lines as narrow as 400 kHz can be measured.

Transitions have been assigned using combination differences and the general $\Delta F = 0, \pm 1$ selection rule ($\Delta J = 0, \pm 1$ for $I = 0$ isotopes). Electric dipole transitions are expected to occur between states with opposite parity and follow the $\Delta \ell = \pm 1$ selection rule. The latter does not strictly hold, because transitions between s and f Rydberg states could be observed for all isotopes as a result of the mixing of s and d channels. For instance, transitions to states of all np and nf Rydberg series of ^{132}Xe with $J = 1, 2$ have been observed not only from initial $nd[1/2]_1$ and $nd[3/2]_1$ Rydberg states, but also from $ns[3/2]_1$ states. The positions of all s, p, d and f Rydberg levels of ^{132}Xe determined by millimeter-wave spectroscopy are listed in Table 5.3. For convenience these positions are given relative to the position of the $52d[1/2]_1$ level.

Table 5.3: Rydberg states of ^{132}Xe observed by millimeter-wave spectroscopy.^a

$n\ell[K]_J$	n					δ
	57	58	59	60	61	
$(n+4)s[3/2]_1$		365 834		429 925		
$nf[5/2]_2$	329 949.9	364 619.5	397 540.3	428 828.5	458 589	0.030 18(12)
$nf[3/2]_2$	329 062.4	363 777.5	396 740.2	428 067.6	457 865	0.055 09(12)
$nf[3/2]_1$	328 957.8	363 677.8	396 645.6	427 977.6	457 779	0.058 04(12)
$(n+3)p[1/2]_0$			384 395	416 332	446 700	3.435 67(14)
$(n+2)d[3/2]_2$		349 416	383 100	415 101		2.475 16(13)
$(n+3)p[3/2]_2$	313 003.8	348 539.2	382 267.2	414 309.5		3.500 50(12)
$(n+2)d[1/2]_1$	312 389.4	347 956.1	381 713.6	413 783.5		2.517 34(12)
$(n+3)p[3/2]_1$	312 362.8	347 931.3	381 689.6	413 760.4		3.518 07(12)
$(n+3)p[5/2]_2$	310 876.6	346 521.0	380 351.4	412 488.7		3.558 72(12)
$(n+3)p[1/2]_1$	309 412.7	345 131.8	379 032.4	411 235.2		3.598 70(12)
$n\ell[K]_J$	50	51	52	53		δ
$(n+4)s[3/2]_1$	27 961.9	79 043.8	127 207.4			3.994 23(8)
$(n+2)d[3/2]_1$	16 267.5	68 022.6	116 809.1	162 849.0		2.215 05(8)
$(n+2)d[1/2]_1$	0.0	52 702.1	102 362.8	149 212.1		2.517 32(8)

^a Energies/ h (MHz) relative to the position of the $52d[1/2]_1$ level. The position of the $52d[1/2]_1$ level of ^{132}Xe above the 1S_0 ground state is $97\,788.976(11)\text{ cm}^{-1}$ as derived from the MQDT analysis. The last column gives the quantum defects δ of the observed Rydberg states. The number in parentheses represent one standard deviation in units of the last digit.

For ^{132}Xe , effective quantum defects $\delta = n - \nu_{3/2}$ have been obtained for the $n\ell[K]_J$

series from a fit, based on the Rydberg formula, to the spectral positions given in Table 5.3 and are given in the last column of this table. The quantum defects are almost constant for the observed levels except for the $nd[3/2]_1$ series, where the quantum defect increases with increasing energy.

These quantum defects allowed us to assign, in the spectra displayed in Fig. 5.4, several transitions located in the immediate vicinity of the (power-broadened) transitions to $np[3/2]_1$ Rydberg states to transitions to $(n-1)d[1/2]_1$ Rydberg states. These transitions are forbidden according to the $\Delta\ell = \pm 1$ and $+\leftrightarrow -$ parity selection rules for electric dipole transitions, but become allowed in the presence of residual electric fields, which mix the nearly degenerate ($\Delta\nu_{3/2} = 0.0007$) $np[3/2]_1$ and $(n-1)d[1/2]_1$ Rydberg states (see discussion below). The assignment is corroborated by the fact that the transitions disappear when the stray electric fields are minimized (see bottom trace of Fig. 5.4). "Forbidden" $n's[3/2]_1 \leftarrow nd[1/2]_1$ and $n'd[3/2]_2 \leftarrow nd[1/2]_1$ transitions have been observed and assigned as well.

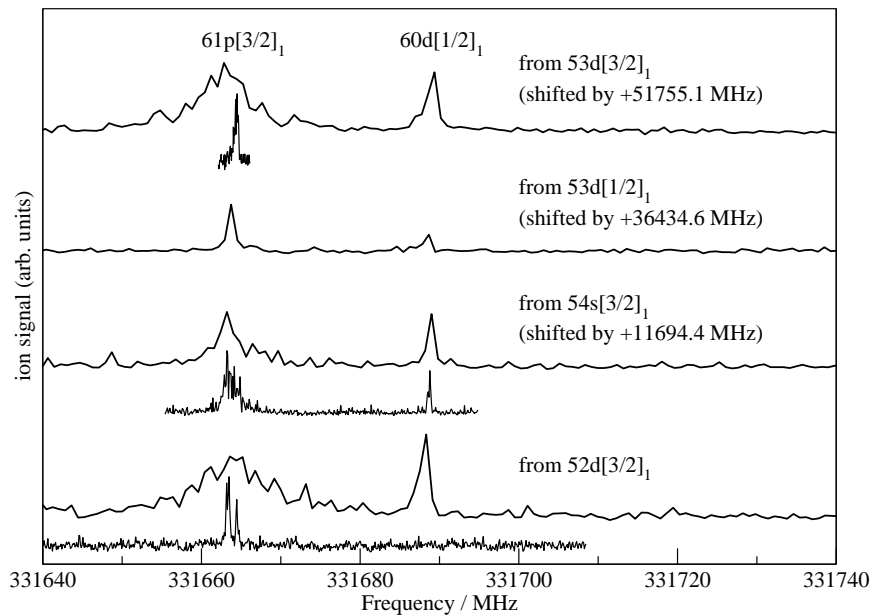


Figure 5.4: Millimeter-wave spectra exhibiting transitions to the $61p[3/2]_1$ and $60d[1/2]_1$ Rydberg states of ^{132}Xe . Transitions from d or s states to d Rydberg states are forbidden by the $\Delta\ell = \pm 1$ selection rule, but become allowed in the presence of electric fields. High-resolution spectra recorded with reduced millimeter-wave power are presented below the low-resolution overview spectra. The bottom spectrum was recorded following minimization of the stray electric field. The presence of residual electric fields result in a broadening of the transition to the $61p[3/2]_1$ state and in the observation of the transition to the $60d[1/2]_1$ state.

The positions of the observed Rydberg levels of ^{132}Xe , ^{129}Xe , and ^{131}Xe relative to the positions of the $52d[1/2]_1$, $52d[1/2]_1(F=3/2)$, and $52d[1/2]_1(F=5/2)$ levels could be determined with an accuracy better than 1 MHz and are summarized in Tables 5.3–5.5

which represent the main experimental result of this chapter. Some levels could only be observed in one or two transitions in overview scans and their positions are indicated with one digit less (their absolute accuracy is about 2 MHz). A few transitions involving np states are split and shifted by small residual electric fields, which mix these states with energetically close-lying nd states (see above and Fig. 5.4). Such cases are marked by asterisks in Table 5.5 and discussed below.

Table 5.4: Rydberg states of ^{129}Xe observed by millimeter-wave spectroscopy.^a

$n\ell[K]_J$	F	n				
		57	58	59	60	61
nf "j"	5/2			400 452	431 731	461 483
nf "g"	5/2			399 807.6	431 116	460 897
nf "f"	3/2	332 129.7	366 823	399 767.0	431 076.4	460 858
nf "e"	5/2	329 481.6	364 146.4	397 062.3	428 346	458 104
nf "d"	3/2	328 951.0	363 646.2	396 590.7	427 901.2	457 682
nf "c"	5/2	328 912.3	363 608.4	396 553.3	427 864	
nf "b"	3/2	328 484.0	363 199.8	396 163.1	427 491.2	457 290
nf "a"	1/2	328 392	363 111.6	396 079.8	427 411.6	457 214
$(n+3)p[1/2]_0$	1/2					448 224
$(n+3)p[3/2]_2$	3/2	315 457	351 000	384 736	416 786	447 260
$(n+3)p[3/2]_2$	5/2	314 571	350 160	383 938	416 029	
$(n+3)p[3/2]_1$	1/2	314 019	349 586.4	383 347.6	415 421.9	445 922
$(n+3)p[3/2]_1$	3/2	313 686.3	349 321.2	383 144.1	415 274.9	445 825
$(n+2)d[3/2]_2$	5/2		349 332.1			
$(n+2)d[1/2]_1$	3/2		347 828	381 571.6	413 628.0	
$(n+3)p[5/2]_3$	5/2	312 170.9	347 725.4	381 471.2	413 529.7	
$(n+3)p[5/2]_2$	3/2	311 772.2	347 346.4	381 110.6	413 185.4	
$(n+3)p[5/2]_2$	5/2	310 311.5	345 956.4	379 786.6	411 923.6	
$(n+2)d[1/2]_0$	1/2		346 923			
$(n+3)p[1/2]_1$	1/2	311 254.7	346 940.6	380 804.8	412 969.4	
$(n+3)p[1/2]_1$	3/2	309 062.9	344 777.2	378 671.4	410 868.7	
$n\ell[K]_J$	F	50	51	52	53	
$(n+4)s[3/2]_1$	1/2		81 723.6	129 887.2		
$(n+4)s[3/2]_1$	3/2	27 309.1	78 403.1	126 577.3		
$(n+2)d[3/2]_1$	3/2	17 461.6	69 227.2	118 024.5	164 075.5	
$(n+2)d[3/2]_1$	1/2	16 290.9	68 050.5	116 841.4	162 886.9	
$(n+2)d[1/2]_1$	1/2	1768	54 483.5	104 156.5		
$(n+2)d[1/2]_1$	3/2	0.0	52 684.7	102 328.5	149 161.5	
$(n+2)d[1/2]_0$	1/2	-1344	51 410.4	101 118.7	148 011.4	

^a Energies/ h (MHz) relative to the position of the $52d[1/2]_1(F=3/2)$ level. The position of the $52d[1/2]_1(F=3/2)$ level of ^{129}Xe above the $^1\text{S}_0(F=1/2)$ ground state is $97\,788.942(11)\text{ cm}^{-1}$.

Table 5.5: Rydberg states of ^{131}Xe observed by millimeter-wave spectroscopy.^a

$n\ell[K]_J$	F	n			
		57	58	59	60
nf "s"	7/2			398 975.8	430 258
nf "r"	5/2			398 830.2	430 117.2
nf "q"	7/2			398 780	430 070
nf "p"	3/2			398 592.5	429 889.0
nf "o"	5/2		365 583	398 516.2	429 817
nf "n"	1/2		365 386	398 329.5	429 638
nf "m"	3/2		365 273	398 222.6	429 538
nf "h"	3/2	*	364 086	*	*
nf "g"	3/2	329 230.9	363 922	396 861.7	428 167
nf "g'"	1/2				428 125
nf "f"	5/2	328 622.4	363 314.5	396 255.1	
nf "f'"	3/2		363 247		
nf "e"	7/2	328 215	362 914		
nf "d"	7/2		362 860		
nf "c"	5/2		362 768		
$(n+2)d[1/2]_1$	3/2	312 756*			
$(n+2)d[1/2]_1$	1/2			381 388	413 450.8
$(n+3)p[3/2]_2$	7/2		349 656		415 437
$(n+3)p[3/2]_2$	5/2		349 411.2	383 157	415 216.3
$(n+3)p[3/2]_2$	3/2	312 746*			
$(n+3)p[3/2]_2$	1/2	312 169.7	347 711.1	381 448.3	413 499.1
$(n+3)p[3/2]_1$	5/2	312 672.9	348 244.0		
$(n+3)p[3/2]_1$	3/2	311 719.1	347 276.2	381 024.4	413 085.6
$(n+3)p[3/2]_1$	1/2		347 035.5	380 790.0	412 856.1
$(n+3)p[5/2]_3$	7/2	312 201.0	347 845.2	381 674.6	413 811.2
$(n+3)p[5/2]_3$	5/2	310 830	346 461.3	380 283.0	412 415.2
$(n+3)p[5/2]_3$	3/2			379 794	
$(n+3)p[5/2]_2$	7/2	311 368.0	346 971.0	380 762.8	
$(n+3)p[5/2]_2$	5/2	310 606.3	346 226.8	380 032.1	412 142.7
$(n+3)p[5/2]_2$	3/2	309 945.6	345 591.1	379 423.1	411 562.0
$(n+3)p[5/2]_2$	1/2		345 260.0	379 090.0	411 228
$(n+3)p[1/2]_1$	5/2	309 960.7	345 658.2	379 535.8	411 714.4
$(n+3)p[1/2]_1$	3/2			378 496	
$(n+3)p[1/2]_1$	1/2				

Table 5.5: Rydberg states of ^{131}Xe observed by millimeter-wave spectroscopy. (*continued*)

$n\ell[K]_J$	F	n			
		50	51	52	53
$(n+4)s[3/2]_1$	5/2		80 234.7		
$(n+4)s[3/2]_1$	3/2	27 440.5	78 525.1	126 690.9	
$(n+4)s[3/2]_1$	1/2	26 801.9	77 884.7	126 049.0	
$(n+2)d[3/2]_1$	1/2	16 963.0	68 719.9	117 507.8	
$(n+2)d[3/2]_1$	3/2	16 691.3	68 450.4	117 240.5	
$(n+2)d[3/2]_1$	5/2	16 178.6	67 939.1	116 730.7	
$(n+2)d[1/2]_1$	3/2		53 101.7	102 760.2	
$(n+2)d[1/2]_1$	5/2	0.0	52 686.7	102 331.6	149 164.7

^a Energies/ h (MHz) relative to the position of the $52d[1/2]_1(F=5/2)$ level. The position of the $52d[1/2]_1(F=5/2)$ level of ^{131}Xe above the $^1\text{S}_0(F=3/2)$ ground state is $97\,788.964(11)\text{ cm}^{-1}$. The levels marked by asterisks were found to be strongly perturbed by the Stark effect caused by the stray field.

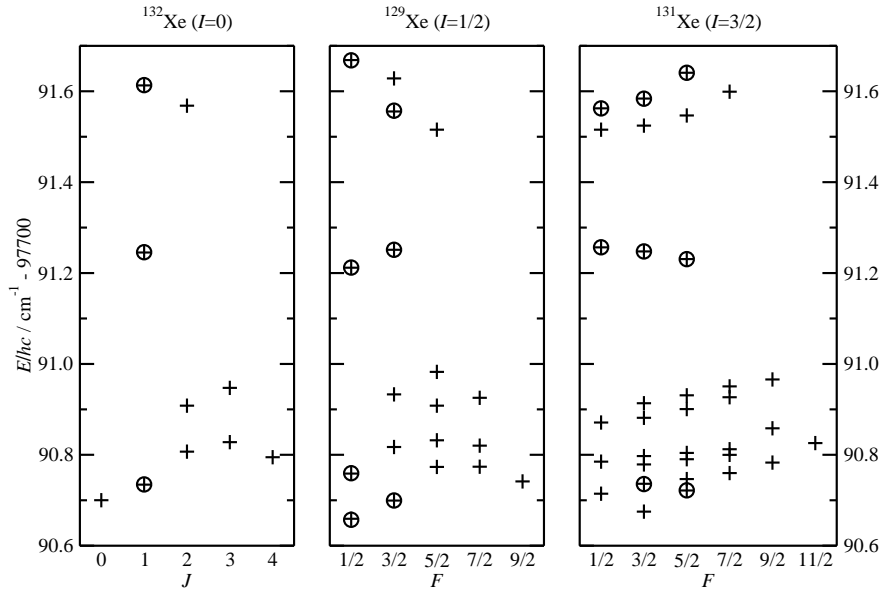


Figure 5.5: Calculated (crosses) and observed (circles) fine and hyperfine levels of the $53d$ and $55s$ Rydberg states of Xe. The sequence of the Rydberg levels of ^{132}Xe with increasing energy is $nd[1/2]_0$, $nd[1/2]_1$, $nd[7/2]_4$, $nd[3/2]_2$, $nd[7/2]_3$, $nd[5/2]_2$, $nd[5/2]_3$, $nd[3/2]_1$, $(n+2)s[3/2]_2$, $(n+2)s[3/2]_1$.

The energy level structures of the odd- and even-parity states of Xe determined experimentally are presented in Figs. 5.5 (ns and nd Rydberg states), 5.6 (np Rydberg states), and 5.7 (nf Rydberg states), where they are compared with the calculated structures (see below). The $nd[3/2]_1$ states are well separated from the other Rydberg states (see Fig. 5.5). Therefore the spectra with $nd[3/2]_1(F)$ as initial state are ideally suited to assign the hyperfine structures of the observed transitions and to extract the hyperfine structure of the ion using MQDT calculations. The assignment of the Racah-type $n\ell[K]_J$ quantum

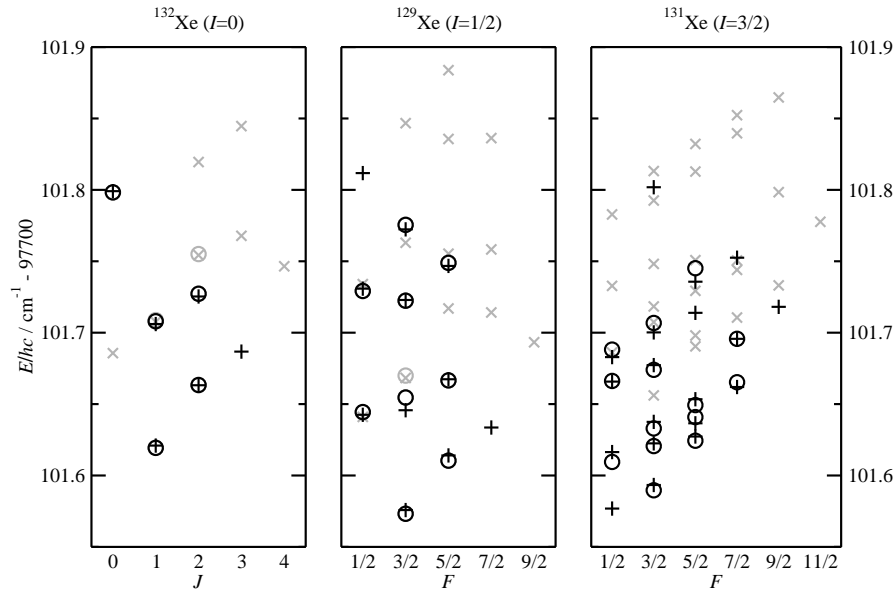


Figure 5.6: Calculated (crosses) and observed (circles) fine and hyperfine levels of the 62p Rydberg states of Xe. The sequence of the Rydberg levels of ^{132}Xe with increasing energy is $np[1/2]_1$, $np[5/2]_2$, $np[5/2]_3$, $np[3/2]_1$, $np[3/2]_2$, $np[1/2]_0$. Light gray crosses and circles indicate the calculated and observed fine and hyperfine levels of the 61d Rydberg states (see Fig. 5.5).

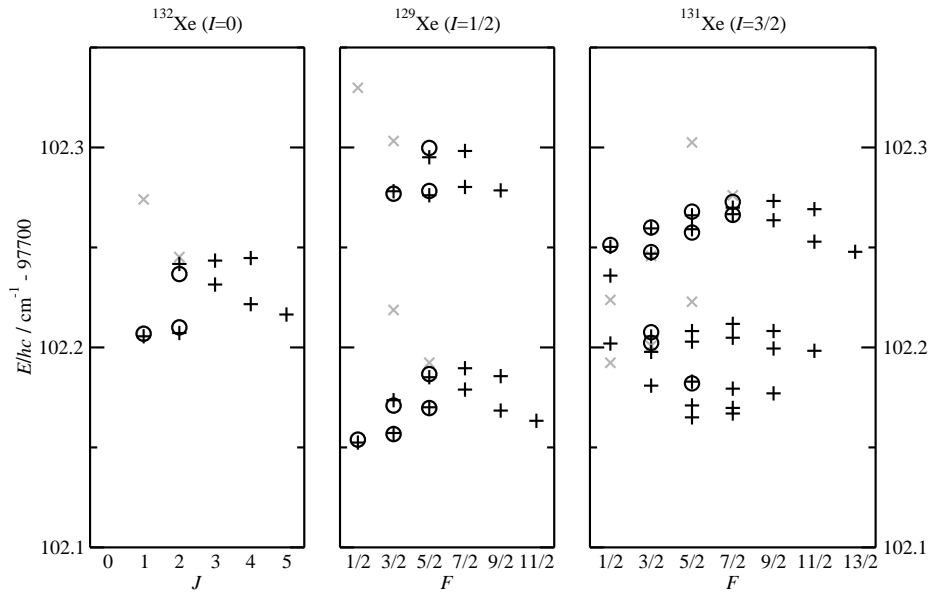


Figure 5.7: Calculated (crosses) and observed (circles) fine and hyperfine levels of the 59f Rydberg states of Xe. The sequence of the Rydberg levels of ^{132}Xe with increasing energy is $nf[3/2]_1$, $nf[3/2]_2$, $nf[9/2]_5$, $nf[9/2]_4$, $nf[5/2]_3$, $nf[5/2]_2$, $nf[7/2]_3$, $nf[7/2]_4$. Light gray crosses indicate the calculated fine and hyperfine levels of the 63s Rydberg states (see Fig. 5.5).

numbers of the Rydberg levels of ^{129}Xe and ^{131}Xe is based on the correlation diagrams, calculated by MQDT and depicted in Figs. 5.8–5.10, between hyperfine levels of high- ($n \approx 100$) and low- n states ($n \approx 30$ for $\ell < 3$), where the hyperfine splitting is smaller

than the separation between the individual $n\ell[K]_J$ levels. The assignment of the $F = 3/2$ hyperfine levels of the $(n + 2)s[3/2]_1$ and $(n + 2)s[3/2]_2$ states of ^{129}Xe has been made as if there were no avoided crossing between these states around $n \approx 40$ [see dashed line in Fig. 5.9], and is based on the assumption that states with predominantly $J = 1$ character are excited from the $6p[1/2]_0(F = I)$ intermediate state by the second laser. For the nf hyperfine states, the Racah-type $n\ell[K]_J$ quantum numbers are not assigned and replaced by a letter designating the individual hyperfine state in Tables 5.6 and 5.7.

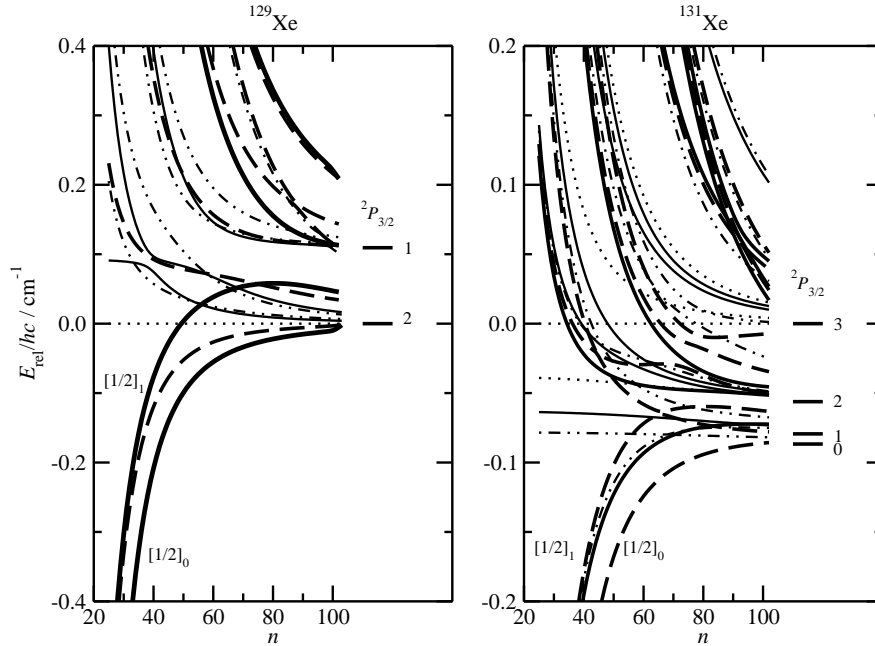


Figure 5.8: Calculated hyperfine structure of high- nd and $(n + 2)s$ Rydberg states of ^{129}Xe and ^{131}Xe relative to the hyperfine level with the highest F value ($F = 9/2$ level for ^{129}Xe and $F = 11/2$ level for ^{131}Xe) belonging to the $nd[7/2]_4$ Rydberg series. The calculated levels with $F = 1/2$ are connected by thick lines, those with $F = 3/2$ by thick dashed lines, those with $F = 5/2$ by thin dot-dashed lines, those with $F = 7/2$ by thin continuous lines, and those with $F \geq 9/2$ by thin dotted lines. On the right-hand side of each panel, the derived hyperfine structure of the cation is shown, labeled with the values of F^+ . The number of hyperfine series (and their F values) converging to each ion level can be found in Table 5.2.

The MQDT analysis of the hyperfine structure requires complete sets of MQDT parameters for the even-(p, f) and odd-parity (s, d) states. As a primary data source to determine these parameters, the compilation of energy levels of Xe by Saloman [176] has been used. This reference contains the term values of all known Rydberg states with $n \leq 20$ for a natural isotope mix. Only few isotope-selective measurements have been reported, notably the interferometric measurements on ^{136}Xe by Humphreys and Paul [147] and the VUV reference measurement by Brandi *et al.* [141]. Because the isotope shift between the mean level positions of a natural mix and the ^{132}Xe isotope is small (0.002 – 0.003 cm^{-1} [141]), i.e., smaller than the accuracy of most of the experiments and also

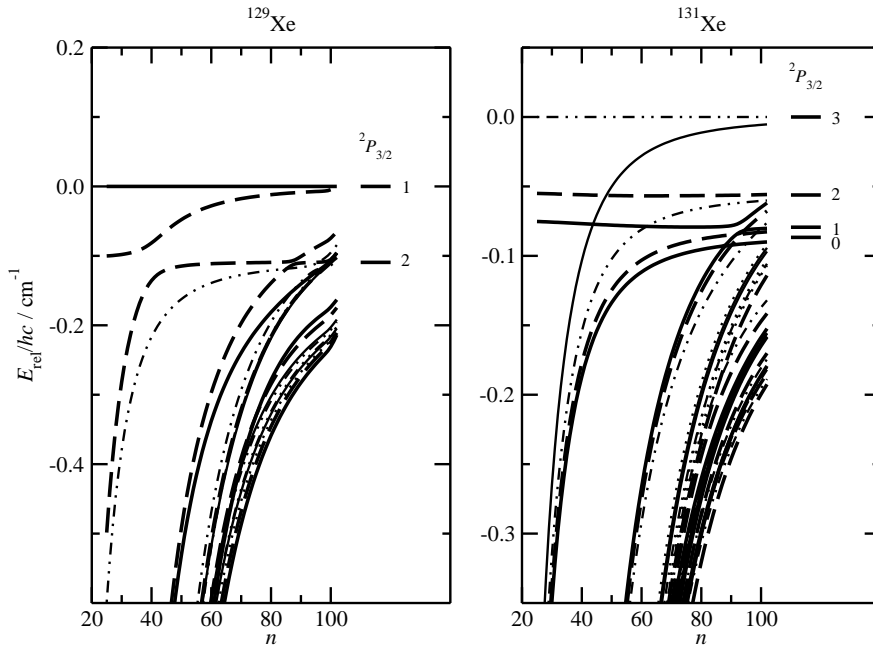


Figure 5.9: Calculated hyperfine structure of high- nd and $(n+2)s$ Rydberg states of ^{129}Xe and ^{131}Xe relative to the highest hyperfine level ($F = 1/2$ for ^{129}Xe and $F = 5/2$ for ^{131}Xe) of the $(n+2)s[3/2]_1$ state. The calculated levels with $F = 1/2$ are connected by thick lines, those with $F = 3/2$ by thick dashed lines, those with $F = 5/2$ by thin dot-dashed lines, those with $F = 7/2$ by thin continuous lines, and those with $F \geq 9/2$ by thin dotted lines. Note the avoided crossing between the $F = 3/2$ hyperfine levels of the $(n+2)s[3/2]_1$ and $(n+2)s[3/2]_2$ Rydberg states of ^{129}Xe . On the right-hand side of each panel, the derived hyperfine structure of the cation is shown, labeled with the values of F^+ .

smaller than the accuracy of the MQDT calculations at low energies, the mean values of the natural mix can be used for the ^{132}Xe isotope. In the following cases, different values than those listed in Ref. [176] have been used: 1) The term values of L'Huillier *et al.* [164] have been found to need a correction of -0.7 cm^{-1} and the corrected values have been used. 2) The values of Refs. [169, 172] for the $nf' [5/2]_2$ autoionizing Rydberg series have been adopted instead of the values of Ref. [144]. 3) The resonance positions given in Refs. [167, 173] have been used for the $nd' [3/2]_1$ autoionizing Rydberg series. For the terms missing in Ref. [176], the values from the references given in Table 5.1 have been used. The energies of the states observed in the present study relative to the $(5p)^6 \ ^1S_0$ ground state have been obtained by combining the present results with the laser spectroscopy data of the $nf[3/2]_1$ ($n \leq 73$) series [158] and the high-resolution data in Refs. [141, 147], i.e., the values on which the currently adopted ionization energy [141, 176] is based.

The autoionizing states between the $^2P_{3/2}$ and $^2P_{1/2}$ ionization limits (ns' levels with $n > 7$, np' levels with $n > 6$, nd' levels with $n > 5$, and all nf' levels) were analyzed by treating them as bound states by neglecting the coupling to the open channels; the resonance positions were adopted from the results of the line shape analyses reported

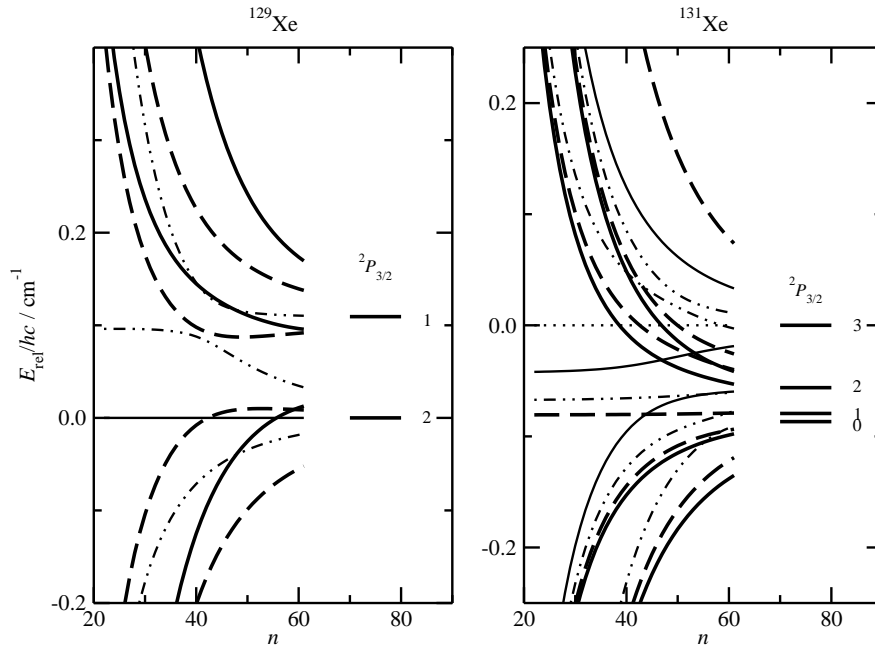


Figure 5.10: Calculated hyperfine structure of high- np Rydberg states of ^{129}Xe and ^{131}Xe relative to the hyperfine level with the highest F value ($F = 7/2$ level for ^{129}Xe and $F = 9/2$ level for ^{131}Xe) belonging to the $np[5/2]_3$ Rydberg series. The calculated levels with $F = 1/2$ are connected by thick lines, those with $F = 3/2$ by thick dashed lines, those with $F = 5/2$ by thin dot-dashed lines, those with $F = 7/2$ by thin continuous lines, and those with $F = 9/2$ by thin dotted lines. On the right-hand side of each panel, the derived hyperfine structure of the cation is shown, labeled with the values of F^+ .

in the literature without independent evaluations. The positions of the sharp $ns'[1/2]_1$ resonances (with $33 \leq \nu_{1/2} \leq 90$) of ^{129}Xe and ^{131}Xe [203] have been included to ensure that the fitted MQDT parameters describe the autoionizing states as well. Finally, the $A_{1/2}$ hyperfine constants of ^{129}Xe and ^{131}Xe and the positions of the ionization thresholds $E(^2P_{1/2})$ were fixed to the values reported in [135].

Because of the large number of parameters and correlations between parameters, some parameters, in particular the energy dependence of the quantum defects and several generalized Euler angles θ_{jk} , have been either set to zero or fixed to other values, as follows: For the interactions between the LS -coupled eigenchannels $p^5\ell^{2S+1}L_J$, only interactions between channels differing in a single quantum number (either ℓ , S , or L) were considered. The restriction $\Delta L = 0, \pm 1$ has been applied, because the spin-orbit interaction has been assumed to be the main cause of the deviation of the eigenchannels from purely LS coupled channels and because the spin-orbit interaction matrix elements $\langle L'S'J | \sum_i \xi(r_i) \vec{\ell}_i \vec{s}_i | LSJ \rangle$ vanish unless $\Delta\ell = 0$, $\Delta L = 0, \pm 1$ and $\Delta S = 0, \pm 1$ [99, 197]. The mixing of the s and d eigenchannels can be understood as an effect of short-range electrostatic interactions, i.e., quadrupole and exchange interactions, and occurs between channels with the same values of L and S [201].

The close-coupling channel parameters μ_α and $V_{\bar{\alpha}\alpha}$ (expressed in terms of the gen-

Table 5.6: MQDT parameters for odd parity states of xenon^a

	$\bar{\alpha}, i, \alpha$	1	2	3	4	5	
$J = 0$	$\bar{\alpha}$	$p^5d \ ^3P_0$	$p^5s \ ^3P_0$				
	i	$[^2P_{3/2}] d_{3/2}$	$[^2P_{1/2}] s_{1/2}$				
	μ_{α}^0	0.537 99	0.044 07				
	μ_{α}^1	-0.4314	-0.3431				
	$U_{i\alpha}$	0.9951	-0.0992				
		0.0992	0.9951				
		θ_{jk}^0		0.0993			
$J = 1$	$\bar{\alpha}$	$p^5d \ ^1P_1$	$p^5d \ ^3P_1$	$p^5d \ ^3D_1$	$p^5s \ ^1P_1$	$p^5s \ ^3P_1$	
	i	$[^2P_{3/2}] d_{5/2}$	$[^2P_{3/2}] d_{3/2}$	$[^2P_{1/2}] d_{3/2}$	$[^2P_{3/2}] s_{1/2}$	$[^2P_{1/2}] s_{1/2}$	
	μ_{α}^0	0.123 47	0.540 96	0.378 50	-0.014 78	0.039 67	
	μ_{α}^1	-0.0450	-0.3610	0.3723	-0.2817	-0.3860	
	$U_{i\alpha}$	0.7442	-0.5772	-0.3060	-0.1105	0.0845	
		0.2788	0.7070	-0.6451	-0.0637	-0.0469	
		0.5822	0.3992	0.7001	-0.1070	-0.0063	
		0.1398	0.0509	0.0000	0.9310	0.3332	
		-0.0989	0.0719	0.0000	-0.3247	0.9379	
		θ_{jk}^0		0.0342	0.0	0.1721	0.0
		θ_{jk}^1		-0.669	0.0	1.108	0.0
					0.0177	0.0	0.0882
					0.599	0.0	-0.765
						0.0	0.0
					0.0	0.0	
						0.2770	
						0.292	
$J = 2$	$\bar{\alpha}$	$p^5d \ ^3P_2$	$p^5d \ ^3D_2$	$p^5d \ ^3F_2$	$p^5d \ ^1D_2$	$p^5s \ ^3P_2$	
	i	$[^2P_{3/2}] d_{5/2}$	$[^2P_{3/2}] d_{3/2}$	$[^2P_{1/2}] d_{3/2}$	$[^2P_{1/2}] d_{5/2}$	$[^2P_{3/2}] s_{1/2}$	
	μ_{α}^0	0.532 70	0.382 40	0.496 93	0.382 54	0.017 25	
	μ_{α}^1	-0.4302	0.5615	-0.1740	0.0432	-0.3062	
	$U_{i\alpha}$	0.6500	-0.3788	-0.1844	0.6279	-0.0758	
		-0.2979	0.6301	-0.4434	0.5625	0.0348	
		-0.1447	0.1140	0.8612	0.4735	0.0169	
		0.6740	0.6682	0.1667	-0.2553	-0.0786	
		0.1159	0.0000	0.0000	0.0000	0.9933	
		θ_{jk}^0		-0.0235	0.0	0.0	0.1161
		θ_{jk}^1		0.762	0.0	0.0	-0.177
					0.0158	-0.1708	0.0
					-0.352	-5.211	0.0
						0.0	0.0
					0.0	0.0	
						0.0	
						0.0	
$J = 3$	$\bar{\alpha}$	$p^5d \ ^3D_3$	$p^5d \ ^3F_3$	$p^5d \ ^1F_3$			
	i	$[^2P_{3/2}] d_{5/2}$	$[^2P_{3/2}] d_{3/2}$	$[^2P_{1/2}] d_{5/2}$			
	μ_{α}^0	0.390 96	0.498 57	0.380 96			
	μ_{α}^1	0.4500	-0.0186	0.0567			
	$U_{i\alpha}$	0.8472	0.2486	0.4696			
		-0.4756	0.7487	0.4618			
	0.2368	0.6146	-0.7525				
	θ_{jk}^0		-0.3212	0.0			
	θ_{jk}^1		0.0	0.0			
				0.2496			
				0.0			
$J = 4$	$\bar{\alpha}$	$p^5d \ ^3F_4$					
	i	$[^2P_{3/2}] d_{5/2}$					
	μ_{α}^0	0.479 69					
	μ_{α}^1	-0.1612					

^a The $U_{i\alpha}$ frame transformation matrices are given for $E = E(^2P_{3/2})$ ($\epsilon = 0$).

Table 5.7: $s - d$ and singlet–triplet channel interaction parameters for rare gas atoms^a

	$s - d$				$^1P_1 - ^3P_1$		
	1P_1	3P_0	3P_1	3P_2	s	d	
Ne	0.032	0.0374	0.051		0	0	^b
	0.008	0.0374	0.050	0.038	0	0	^c
	0.0315		0.0489		0	0	^d
Ar	0.02		0.18		0.02	0.0	^e
	0.042		0.097		0.023	(0.006)	^f
				0.101			^g
Kr	0.485	0.154	0.142	0.128	0.037	0.016	^h
	0.495		0.148		0.125	(0.009)	^f
	(0.0)	0.172	0.102	0.12	0.038	(0.0)	ⁱ
	(0.018)		0.080		(0.002)	0.042	^j
Xe	0.172	0.099	0.088	0.116	0.277	0.034	^k
	0.099		0.109		0.245	0.038	^f
	(0.014)		0.062		0.378	0.043	^j
		0.1065					^l

^a Expressed as absolute values of the generalized Euler angles θ in rad.

^b Ref. [198].

^c Ref. [199].

^d Ref. [200].

^e *Ab initio* values from Ref. [201].

^f Derived from the $U_{i\alpha}$ matrix of Ref. [186] based on *ab initio* values.

^g Ref. [202].

^h Ref. [74].

ⁱ Derived from the $U_{i\alpha}$ matrices of Ref. [196].

^j Derived from the $U_{i\alpha}$ matrix of Ref. [185].

^k This study. Values given for $E = E(^2P_{3/2})$ ($\epsilon = 0$).

^l Ref. [187].

eralized Euler angles θ_{jk}) obtained in the fit and the transformation matrix $U_{i\alpha}$ for the $I = 0$ isotopes for the odd-parity states are listed in Table 5.6. With these parameters it is possible to reproduce the positions measured in the millimeter-wave experiments with residuals of the order of 10 MHz and the bound Rydberg states reported in the literature with residuals of less than 1 cm^{-1} except for some low- n states (especially $J = 3$ states). The corresponding MQDT parameters for the even-parity states are preliminary and not reproduced here. The agreement between calculated and observed positions can be assessed in Figs. 5.6 and 5.7. The parameters describing the hyperfine structure of the ion as determined from the MQDT analysis are summarized in Table 5.8. The quoted errors are estimated from the results of different fits and are three times the standard deviations of a single fit. The derived hyperfine structures are shown in Fig. 5.1.

Table 5.8: The fine and hyperfine structure of the 2P ground state of Xe^+ as determined from the MQDT analysis.

	^{129}Xe	^{131}Xe	^{132}Xe
R_M / cm^{-1}	109 736.8487	109 736.8558	109 736.8593
$E(^2P_{3/2}) / \text{cm}^{-1}$	97 833.778 ^a	97 833.783 ^a	97 833.790 ^a
$E(^2P_{1/2}) / \text{cm}^{-1}$	108 370.705 ^{b,c}	108 370.711 ^{b,c}	108 370.714 ^{b,c}
$E(^2P_{3/2}) - E_{\text{ref}}^d / \text{cm}^{-1}$	44.835 96(13)	44.818 91(15)	44.814 08(96)
$A_{3/2} / \text{cm}^{-1}$	-0.054 60(38)	0.015 95(21)	
$B_{3/2} / \text{cm}^{-1}$		0.008 72(85)	
$A_{1/2} / \text{cm}^{-1}$	-0.4071 ^b	0.1206 ^b	

^a Fixed to the value given in Ref. [141] (with uncertainty of 0.011 cm^{-1}).

^b Fixed to the value given in Ref. [135].

^c The uncertainty in the VUV calibration is 0.016 cm^{-1} .

^d The reference level E_{ref} is $52d[1/2]_1$ (or its $F = 3/2$ or $F = 5/2$ hyperfine level for ^{129}Xe and ^{131}Xe , respectively).

5.5 Discussion and conclusions

It has already been mentioned that the $\Delta\ell = \pm 1$ selection rule for electric dipole transitions does not strictly hold for the observed millimeter-wave transitions. The occurrence of $f \leftrightarrow s$ transitions (where the $+ \leftrightarrow -$ (or $\Delta\ell = \pm 1$) selection rule for the parity still holds) can be explained by s - d mixing resulting from the non-spherical charge distribution of the ion core. Transitions between $d[1/2]_1$ and s or d Rydberg states (see Fig. 5.4) are, in addition, forbidden according to the $+ \leftrightarrow -$ parity selection rule. Such transitions can be interpreted either as electric quadrupole transitions (selection rules $\Delta\ell = 0, \pm 2$ and $|J - J'| \leq 2 \leq J + J'$) occurring at high millimeter-wave power densities, or as arising from Stark mixing of the initial or final state with an energetically close-lying state with ℓ differing by ± 1 induced by a residual electric field. The matrix element describing the coupling mixing between two states with $\Delta\ell = \pm 1$ caused by an electric field \mathcal{E} in the $J^+\ell$ coupling scheme is [159]

$$\begin{aligned}
& \langle (\nu\ell J^+) K J M | \mathcal{E} e z | (\nu'\ell' J^+) K' J' M \rangle \\
& = (-1)^{J+J'+K+K'+\ell+J'+s-M} [(2J+1)(2J'+1)(2K+1)(2K'+1)]^{1/2} \\
& \quad \times \begin{pmatrix} J & 1 & J' \\ -M & 0 & M \end{pmatrix} \begin{Bmatrix} K & J & s \\ J' & K' & 1 \end{Bmatrix} \begin{Bmatrix} \ell & K & J^+ \\ K' & \ell' & 1 \end{Bmatrix} \langle \nu\ell || r || \nu'\ell' \rangle \mathcal{E} e
\end{aligned} \tag{5.18}$$

with

$$\begin{aligned}\langle \nu \ell || r || \nu' \ell - 1 \rangle &= \sqrt{\ell} \langle \nu \ell | r | \nu' \ell - 1 \rangle \\ \langle \nu \ell || r || \nu' \ell + 1 \rangle &= -\sqrt{\ell + 1} \langle \nu \ell | r | \nu' \ell + 1 \rangle.\end{aligned}$$

For isotopes with nonzero nuclear spin the elements of the Stark effect operator are

$$\begin{aligned}&\langle (\nu \ell J^+) K J F M | \mathcal{E} e z | (\nu' \ell' J^+) K' J' F' M \rangle \\ &= (-1)^{F+F'+J+J'+K+K'+l+J'+s+I-M} [(2F+1)(2F'+1)(2J+1)(2J'+1)(2K+1)(2K'+1)]^{1/2} \\ &\quad \times \begin{pmatrix} F & 1 & F' \\ -M & 0 & M \end{pmatrix} \begin{Bmatrix} J & F & I \\ F' & J' & 1 \end{Bmatrix} \begin{Bmatrix} K & J & s \\ J' & K' & 1 \end{Bmatrix} \begin{Bmatrix} \ell & K & J^+ \\ K' & \ell' & 1 \end{Bmatrix} \langle \nu \ell || r || \nu' \ell' \rangle \mathcal{E} e \\ &= f(M) \langle \nu \ell | r | \nu' \ell' \rangle \mathcal{E} e.\end{aligned}\tag{5.19}$$

The six- j symbols in Eqs. (5.18) and (5.19) imply the selection rules $\Delta F = 0, \pm 1$, $\Delta J = 0, \pm 1$, $\Delta K = 0, \pm 1$, and $\Delta \ell = 0, \pm 1$. For nearly degenerate high- n levels ($|\Delta \nu| \ll 1$), the radial integral can be approximated by [204, 205]

$$\langle \nu \ell | r | \nu' \ell - 1 \rangle \approx \frac{3}{2} \nu \nu' [1 - \ell^2 / (\nu \nu')]^{1/2}\tag{5.20}$$

(in atomic units [206]), where $\nu = n^*$ stands for the effective principal quantum number. In the first approximation of perturbation theory, the admixture of a state Ψ_2 in a state Ψ_1 is

$$\frac{\langle \Psi_2 | \mathcal{E} e z | \Psi_1 \rangle}{E_1 - E_2} \Psi_2.\tag{5.21}$$

Thus the matrix element of the “forbidden” transition between initial state Ψ_1 and final state Ψ_3 contains a term

$$\frac{\langle \Psi_2 | \mathcal{E} e z | \Psi_1 \rangle \langle \Psi_3 | \mu | \Psi_2 \rangle}{E_1 - E_2},\tag{5.22}$$

which is nonzero if transitions from the “intermediate” state Ψ_2 to the initial state Ψ_1 and final state Ψ_3 are allowed [207]. Significant Stark mixing occurs when the matrix element becomes as large as the energy difference between the states $\Delta E \approx 2R_M \Delta \nu / \nu^3$, i.e., at electric fields of the order of $\mathcal{E} \sim \Delta \nu / \nu^5$ (in atomic units [206]). As a consequence of this n^{-5} -scaling law, such mixing occurs easily for very high- n Rydberg states. For instance, transitions from d states to nd or ns Rydberg states with $n > 150$ have been observed in millimeter-wave spectra of krypton induced by electric fields as low as 2.5 mV/cm [36]. Because the $np[3/2]_1$ and $(n-1)d[1/2]_1$ Rydberg states are energetically very close ($\Delta \nu_{3/2} = 0.0007$), $\Delta \nu / \nu^5$ corresponds to an electric field of 10 mV/cm for $n = 55$ or 4.8 mV/cm for $n = 63$ and these states are efficiently mixed even by small stray fields.

The field-induced shift $|\Delta E|$ of the energies of two near-degenerate levels (separated by $\Delta\nu/\nu^3$) with $\Delta\ell = \pm 1$ can be estimated from the relation (expressed in atomic units):

$$\begin{aligned} |\Delta E| &= \left[|\langle \nu\ell FM | \mathcal{E} e z | \nu'\ell' F'M \rangle|^2 + \left(\frac{\Delta\nu}{2\nu^3} \right)^2 \right]^{1/2} - \frac{\Delta\nu}{2\nu^3} \\ &\approx \frac{\Delta\nu}{2\nu^3} \left(\left[\left(\frac{3f(M)\mathcal{E}\nu^5}{\Delta\nu} \right)^2 + 1 \right]^{1/2} - 1 \right). \end{aligned} \quad (5.23)$$

For weak fields or $\mathcal{E}\nu^5/\Delta\nu \ll 1$, a quadratic Stark shift

$$\begin{aligned} |\Delta E| &= \frac{\Delta\nu}{\nu^3} \left(\frac{3f(M)\mathcal{E}\nu^5}{2\Delta\nu} \right)^2 \quad \text{or} \\ |\Delta E/h| &= 5.60 \cdot 10^{-13} \text{ kHz } (f(M)(\mathcal{E}/\text{mV cm}^{-1}))^2 \frac{\nu^7}{\Delta\nu} \end{aligned} \quad (5.24)$$

results, whereas in the case $\mathcal{E}\nu^5/\Delta\nu \gg 1$, a linear Stark shift

$$\begin{aligned} |\Delta E| &= \frac{3}{2} |f(M)\mathcal{E}| \nu^2 \quad \text{or} \\ |\Delta E/h| &= 1.92 \text{ kHz } |f(M)(\mathcal{E}/\text{mV cm}^{-1})| \nu^2 \end{aligned} \quad (5.25)$$

is obtained with $|f(M)| < 0.5$ for interacting p and d states. Numerical evaluation of Eq. (5.23) yields, for a residual field of 5 mV/cm, a Stark shift of 0.29 MHz for the $M = 1$ levels of the $63p[3/2]_1$ and $62d[1/2]_1$ states ($f(1) = 0.0745$ for purely $J^+\ell$ coupled states); the magnitude of this shift is less than the frequency accuracy estimated in Section 5.2. Thus the presence of a stray electric field is marked by the presence of the “forbidden” transition to the $nd[1/2]_1$ state rather than by an obvious shift of the transition frequency. The excessive broadening of the $np[3/2]_1 \leftarrow n'd[3/2]_1$ transitions, compared to the “forbidden” $(n-1)d[1/2]_1 \leftarrow n'd[3/2]_1$ transitions and transitions to other np states (see Figs. 5.2 and 5.4), can be attributed to power broadening.

The same arguments have been used for the assignment of transitions of ^{129}Xe or ^{131}Xe . For example, the transitions to the $np[5/2]_3(F = 5/2)$ states of ^{129}Xe are broader than the transition to the neighboring $(n-1)d[1/2]_1(F = 3/2)$ states. In this case, Stark mixing occurs because the $np[5/2]_3(F = 5/2)$ state is mixed with the $np[3/2]_2(F = 5/2)$ state (note the avoided crossing in Fig. 5.10).

In some overview scans for ^{131}Xe , series of four almost equidistant lines separated by about 11 MHz were observed in the region of the $60p[3/2]_2(F = 3/2)$ final state. Such a quartet structure can be explained by two almost degenerate (separated by $\Delta E/h < 10$ MHz) np and nd levels with $F = 3/2$, split by a stray electric field. If we assume that the interacting state is a pure $59d[1/2]_1(F = 3/2)$ state, for which $f(M) = 0.069M$, the

stray field must have been of the order of $\mathcal{E} = 24$ mV/cm according to Eq. (5.25). Fig. 5.8 indicates an admixture of the $59d[3/2]_2(F = 3/2)$ state, which has a larger value for the Stark effect matrix element [$f(M) = -0.143M$], so that the magnitude of the stray field was probably less than the value calculated above. In other scans with smaller stray fields, only one line was observed indicating the position of the $60p[3/2]_2(F = 3/2)$ state.

From the preliminary results of the MQDT analysis summarized above, the following conclusions for the odd-parity $J = 0, 1$ ionization channels of Xe can be drawn. As has been observed for krypton [74], the quantum defects μ_α are almost independent of the J value, and only the generalized Euler angles θ_{jk} which correspond to the s–d interaction [$\theta(d^1P_1-s^1P_1) \approx 0.17$ and $\theta(d^3P_J-s^3P_J) \approx 0.1$] (see Table 5.7) and to the singlet–triplet interaction ($|\theta| \leq 0.3$) are significant. Comparing the results with literature values for $J = 1$, we find that the absolute values of the Euler angles (or the transformation matrix elements $U_{i\alpha}$) and the energy dependences of the eigenchannel quantum defects μ_α^1 obtained by Johnson *et al.* [186] from *ab initio* calculations and adjusted to spectra of the autoionizing Rydberg series are the ones which come closest to the values of the present study. A similar observation was made in the millimeter-wave study of Rydberg states of krypton [74].

In Table 5.7, the s–d and singlet–triplet channel interaction parameters of xenon are compared to those of other rare gases. Values in parentheses are considered not to be significant because other interaction parameters (not included in this table) are much larger. Despite significant differences between the results of different studies, the singlet–triplet interaction parameters show a tendency to increase with increasing nuclear charge. For the s–d interaction, the largest values are obtained for krypton.

This chapter has illustrated the power of the combination of high-resolution millimeter-wave spectroscopy of Rydberg states and MQDT to determine the hyperfine structure of cations. The chapter has also demonstrated the high sensitivity of high- n Rydberg states to small residual electric fields and how Stark mixing induced by weak stray fields can be exploited to obtain spectroscopic information as Rydberg states not accessible by electric-dipole selection rules under field-free conditions.

The hyperfine structure of the $^2P_{3/2}$ ground state of $^{129}\text{Xe}^+$ and $^{131}\text{Xe}^+$ could be determined experimentally for the first time.

Chapter 6

PFI-ZEKE photoelectron spectroscopy of metastable He and He₂: ionization energies and rovibrational structure of He₂⁺

The study of the electronically excited states of He and He₂ is challenging. The transitions from the ground electronic state to the first excited electronic state lies in the deep VUV below 60 nm. Moreover, the ground state of He₂ is repulsive at short range with a very shallow van der Waals well at large intermolecular distance that can only sustain a single rovibrational level. Fortunately He and He₂ each possess a very long-lived metastable state, the 1s2s ³S₁ state and the a ³Σ_u⁺ state, respectively, that can be efficiently populated in electric discharges.

In the investigations presented in this chapter a simple and efficient method of producing metastable He and He₂ in a pulsed supersonic expansion is exploited to access the high Rydberg states of He and He₂.

This chapter summarizes investigations of the Rydberg states of He and He₂ by photoionization and pulsed field ionization spectroscopy and of the PFI-ZEKE photoelectron spectrum of He₂ from which detailed information on the energy level structure of the He₂⁺ cation could be derived. The chapter is based on Ref. [208]. My main contribution to this work has been on the experimental side whereas the analysis of the Rydberg spectra by multichannel quantum defect theory was primarily carried out by M. Schäfer.

6.1 Introduction

Since the discovery of the spectrum of He₂ almost 100 years ago [209,210], the dimers of rare gas atoms and their cations have attracted large attention both from experimentalists

and theoreticians. The rare gases in their electronic ground state form weakly bound van der Waals complexes, whereas the excited states (and the cations) are strongly bound and often called excimers (*excited dimers*). In the case of the helium dimer, these excited states can be considered as Rydberg states and, hence, He₂ can be described as a Rydberg molecule — for many years it was the only known molecule fulfilling this definition [211]. Emission continua from excited rare gas dimer states to the repulsive part of the potential curve of the electronic ground state are used as sources of vacuum ultraviolet radiation [212–215].

The dimer of helium differs in certain aspects from the dimers of the heavier rare gases. Whereas the potential wells of the van der Waals complexes of the heavier rare gases are sufficiently deep to support many rotational and several vibrational states [216–225], the potential well of He₂ X ¹Σ_g⁺ is so shallow ($D_e = 7.650(3) \text{ cm}^{-1}$, $r_e = 2.968(6) \text{ \AA}$ [226–232]) that the ⁴He₂ species can exist in only one quantum state ($v = 0$, $J = 0$) with a very small binding energy ($E_b/k = 1.73 \pm 0.04 \text{ mK}$) and that the wave function $\Psi(r)$ is delocalized over an extremely large range of internuclear distances r resulting in a long mean bond length $\langle r \rangle = 45.6 \pm 0.5 \text{ \AA}$ [231, 233, 234]. For the ³He₂ isotopomer, no bound state exists in the electronic ground state. Therefore, He₂^{*} and He₂⁺ have to be produced by reaction of He atoms with He^{*} and He⁺ formed by electron impact, respectively [235, 236].

The properties of Rydberg states are governed by the properties of the ionic core. Whereas the heavier dimer cations possess six low-lying electronic states correlated with their lowest dissociation limits $np^5 \text{ } ^2\text{P}_{3/2,1/2}^{\circ} (\text{Rg}^+) + np^6 \text{ } ^1\text{S}_0 (\text{Rg})$ [224, 237–252], He₂⁺ has only two states associated with the $1s \text{ } ^2\text{S}_{1/2} (\text{He}^+) + 1s^2 \text{ } ^1\text{S}_0 (\text{He})$ dissociation limit [224, 253]. The ionic ground states ²Σ_{1/2u}⁺, or I(1/2_u⁺) in Hund’s case (c) nomenclature, are strongly bound with dissociation energies D_e ranging from 7933 cm⁻¹ for Xe₂⁺ [248] to 19 946 cm⁻¹ for He₂⁺ [254]. Whereas most of the information about the Rydberg states of He₂ has been obtained from emission spectra [235, 255–268], only little information is available from emission spectra of the heavier dimers because most of the levels above the a ³Σ_u⁺ (1_u[±], 0_u⁻) and A ¹Σ_u⁺ (0_u⁺) states are predissociated to various degrees [224]. Nevertheless, additional information can be obtained from photoexcitation from the metastable a ³Σ_u⁺ state or, for the heavier dimers, from the X ¹Σ_g⁺ ground state. The metastable a ³Σ_u⁺ state of He₂ is ideal for such experiments because of its very long lifetime of 18 s for the $v = 0$ state [269]. The lifetimes of the lowest-energy triplet molecular states in neon, argon, krypton, and xenon are much shorter, measured to be 6.6 μs, 3.2 μs, 350 ns, and about 50 ns, respectively [48]. The large difference between the lifetimes of helium and the heavier noble gases can be explained by the respective strength of the spin-orbit coupling, which increases as the nuclear charge Z increases and mixes the triplet state with singlet states which decay by fluorescence. The metastable helium atom is in an S state, while the metastable neon, argon, krypton and xenon atoms are in

P states. Therefore, the heavier noble gas molecules contain an intrinsic orbital angular momentum to contribute to the spin-orbit coupling that is lacking in helium molecules.

With only three electrons, He_2^+ represents one of the few molecular systems for which highly accurate ab initio quantum chemical calculations are possible [253, 270–273]. Non-adiabatic corrections have been determined [254, 274] and quantum electrodynamics (QED) calculations can be performed [275]. Unfortunately, the experimental determination of the energy level structure of He_2^+ is not straightforward and, to date, surprisingly little is known about this fundamental cation. Yu and Wing measured the $v^+ = 1 - 0$ fundamental vibration-rotation band of the mixed isotopomer $^3\text{He}^4\text{He}^+$ and could partially resolve the hyperfine structure [236, 276]. Carrington and coworkers observed microwave transitions from highly vibrationally excited states of $X^+ \ ^2\Sigma_u^+$ to the weakly bound $A^+ \ ^2\Sigma_g^+$ state of $^4\text{He}_2^+$ [253]. Ginter and coworkers used multichannel quantum defect theory (MQDT) to analyze Rydberg series in emission spectra of He_2 and obtained rotational term values for the $v^+ = 0, 1$ levels of $X^+ \ ^2\Sigma_u^+ \ ^4\text{He}_2^+$ [264, 277].

He_2 in the metastable $a \ ^3\Sigma_u^+$ state was produced in a pulsed electric discharge at the exit of a pulsed nozzle.

6.2 Experiment

The experimental setup used in this study has been presented in Chapter 2.2.2 (see Fig. 2.2) and the pulsed discharge with which the metastable He atoms and He_2 molecules were generated has been described in Subsection 2.4.2 (see Fig. 2.6).

The measurements relied on the single-photon ionization of jet-cooled metastable helium atoms and dimers in a PFI-ZEKE photoelectron spectrometer using a tunable ultraviolet (UV) laser system. The metastable helium atoms and dimers were formed in a pulsed skimmed supersonic beam of neat ^4He gas (PanGas, 99.996% purity) at a nozzle stagnation pressure between 2 bar and 4 bar. Spectra of $^3\text{He}_2$ were obtained by using a small sample of pure ^3He gas (Chemgas, $\geq 99.91\%$ enrichment). The discharge chamber was connected to the photoexcitation/photoionization chamber by the 1 mm diameter orifice of a skimmer. Both chambers were differentially pumped with turbomolecular pumps. The main components of the experimental setup have been described in Subsection 2.2.2 and in Refs. [22, 56]. Only a brief outline is given here. The helium dimers produced in the discharge were photoexcited with the frequency-doubled output of a Nd:YAG (532 nm)-pumped dye laser (Lambda-Physik, ScanMate 2E) operated in the wavelength range 575–590 nm with a mixture of Rhodamine 6G and Rhodamine B laser dyes yielding pulse energies of about 1 mJ.

To record PFI-ZEKE photoelectron spectra, a two-pulse electric-field sequence was used [62, 69]. The first pulse with an amplitude of +0.066 V/cm and 500 ns duration

served the purpose of eliminating free electrons produced during photoexcitation from the sample volume. This pulse was immediately followed by a -0.133 V/cm extraction pulse of $2 \mu\text{s}$ duration used to field-ionize Rydberg states with principal quantum numbers $n > 200$ and to extract the electrons. The electrons released by this second pulse were monitored as a function of the laser wave number by setting a suitable detection gate in the electron time-of-flight (TOF) spectrum. Optimal conditions were obtained using a delay time of about $1 \mu\text{s}$ between photoexcitation and the application of the electric-field pulse sequence. This pulse sequence enabled a resolution of $\Gamma_{\text{FWHM}} = 0.5 \text{ cm}^{-1}$ in the PFI-ZEKE photoelectron spectra. To determine the field-free ionization energies, the field-induced shift of the thresholds has to be taken into account. Using numerical simulations of the line shapes according to the procedure described in Ref. [59], a field shift of $-1.198(53) \text{ cm}^{-1}$ and a line width (FWHM) of 0.50 cm^{-1} were obtained for the pulse sequence used in the experiment.

The photoionization spectra of metastable He and He₂ were recorded by monitoring the total He⁺ and He₂⁺ yield as a function of the laser wave number. The ions were extracted from the photoionization region by applying a large pulsed electric field (400 V/cm) delayed by 70 ns with respect to the laser pulse. This pulse also led to the field ionization of low-lying Rydberg states located within 120 cm^{-1} of the ionization threshold.

The tunable laser radiation in the regions $33\,600 \text{ cm}^{-1} - 34\,400 \text{ cm}^{-1}$ and $38\,400 \text{ cm}^{-1} - 38\,500 \text{ cm}^{-1}$ corresponding to the positions of the lowest ionization thresholds of He₂^{*} and He^{*}, respectively, was generated by doubling the frequency of a Nd:YAG-pumped dye laser in a BBO crystal (see Chapter 2, Subsection 2.2.2).

To calibrate the spectra, a fraction ($< 4\%$) of the fundamental frequency beam was directed toward an optogalvanic cell filled with neon gas. The fundamental frequency was calibrated against tabulated transitions in neon [30]. The accuracy of the calibration procedure is estimated to be better than 0.15 cm^{-1} for the fundamental and 0.3 cm^{-1} for the doubled output of the laser. The relative positions of the ionic energy levels could be determined with an accuracy of better than 0.05 cm^{-1} .

6.3 Results

6.3.1 Performance of the pulsed discharge

The production of metastable atoms and molecules was observed by time-of-flight (TOF) mass spectrometry of the metastable species or the corresponding cations formed by photoionization using a microchannel plate (MCP) detector installed at the end of the TOF tube. Figs. 6.1 and 6.2 illustrate TOF measurements of the metastable atoms and molecules created in the discharge and of He⁺ and He₂⁺ ions produced by photoionization of the metastables, respectively.

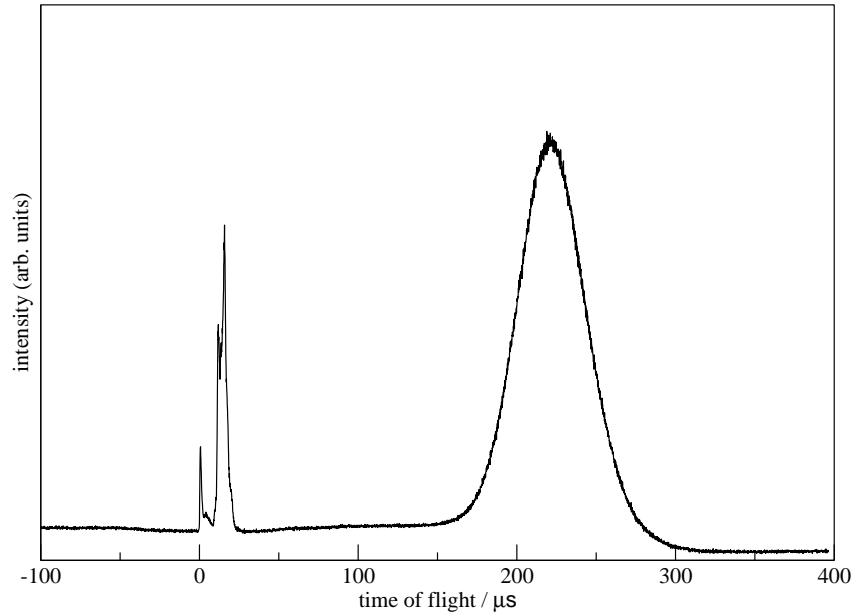


Figure 6.1: Time-of-flight mass spectrum of the metastable helium atoms and molecules. The origin of the TOF axis was set to the onset of the discharge pulse. The peaks at $t = 0$ and $15 \mu\text{s}$ correspond to photons and ions produced in the discharge.

In Fig. 6.1, the sharp peak appearing at $t = 0$ is caused by photons generated in the discharge and hitting the detector, and the shape of the peak reflects the pulsed discharge current waveform. The peak at $t = 15 \mu\text{s}$ arises from ions produced in the discharge and accelerated by the negative offset voltage at the discharge electrode. The broad peak centered around $t = 220 \mu\text{s}$ matches the times of flight of the metastable atoms or molecules. Assuming that the signal is dominated by that of the metastable atoms (as is indicated by the mass-resolved time-of-flight spectrum, see Fig. 6.2a) and that the metastable species are produced during the $10 \mu\text{s}$ long period the discharge is on, a translational temperature (in the direction of the supersonic expansion) of $T_{\parallel} \approx 10 \text{ K}$ can be estimated for the metastable helium atoms from the velocity distribution

$$f(v) \propto \exp\left(-\frac{m}{2kT_{\parallel}}(v - \bar{v})^2\right) = \exp\left(-\frac{(v - \bar{v})^2}{2\sigma_v^2}\right)$$

with mean value $\bar{v} \approx 1950 \text{ ms}^{-1}$ and half width at half maximum $\Delta v = \sqrt{2 \ln 2} \sigma_v \approx 180 \text{ ms}^{-1}$ (k is the Boltzmann constant and m the mass of the helium atoms). The mean velocity corresponds to the terminal velocity of a supersonic expansion of helium with an initial temperature of about 365 K . From the relative intensities of the rovibrational transitions in the PFI-ZEKE photoelectron spectra of $^4\text{He}_2$ (see Fig. 6.4 and text below), vibrational and rotational temperatures of about $T_{\text{vib}} \approx 1000 \text{ K}$ and $T_{\text{rot}} \approx 300 \text{ K}$, respectively, were obtained, though it must be realized that these temperatures only represent empirical parameters describing a nonequilibrium system.

Using a high-voltage discharge pulse shorter than the gas pulse significantly reduces the heating effect of the discharge, so that lower translational, vibrational and rotational temperatures are obtained. It also offers the possibility to match the discharge to different time segments of the pulsed supersonic expansion with differing mean velocities and cooling efficiencies [278, 279].

The TOF distribution of neutral metastable species displayed in Fig. 6.1 does not enable one to distinguish metastable species of different masses in the supersonic expansion because the mean velocity of all species in a supersonic expansion corresponds to that of the most abundant species (here He). Photoionization mass spectrometry can be used to obtain information on the masses of the metastable species as is illustrated by the TOF mass spectra depicted in Fig. 6.2.

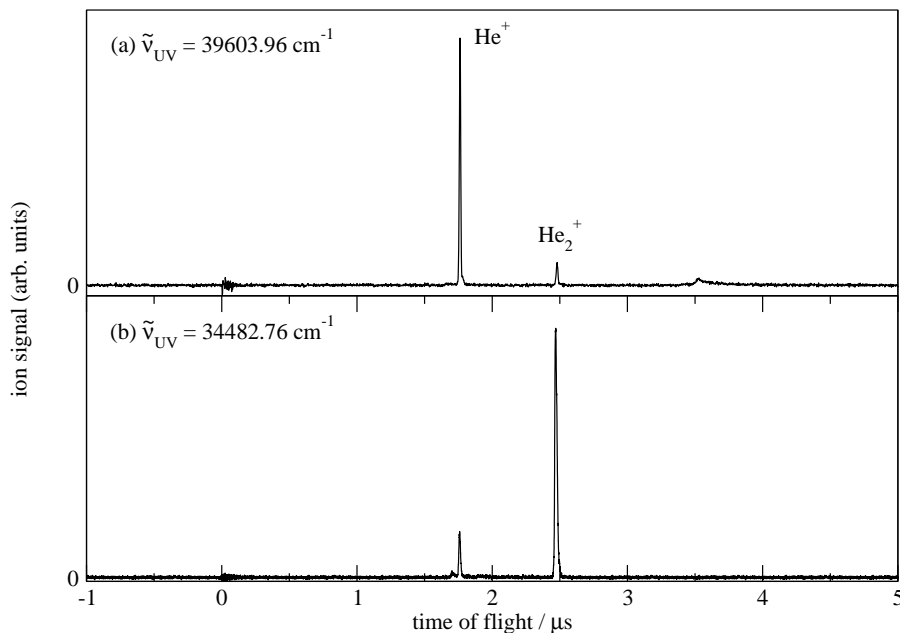


Figure 6.2: Photoionization mass spectra used to characterize the source of metastable He^* and He_2^* . a) Spectrum obtained following photoionization at $39\,603.96 \text{ cm}^{-1}$, above the ionization threshold of both He^* and He_2^* . b) Spectrum obtained following photoionization at $34\,482.76 \text{ cm}^{-1}$ above the ionization threshold of He_2^* but below that of He^* .

Choosing the laser wave number so that it lies above the ionization energy of both He^* and He_2^* ($\tilde{\nu}_{\text{UV}} = 39\,603.96 \text{ cm}^{-1}$) led to the TOF spectrum displayed in Fig. 6.2a. In this figure, the TOF peak corresponding to He^+ is much more intense than that corresponding to He_2^+ . Assuming similar photoionization cross sections for He^* and He_2^* leads to the conclusion that the former metastable species is formed more abundantly than the latter. By choosing an ionization wave number below the ionization threshold of He^* , e.g., $34\,482.76 \text{ cm}^{-1}$, enables one to greatly reduce the He^+ ion signal. The rest He^+ signal visible in this figure is present even when the ionization laser is turned off and therefore corresponds to He^+ ions that were either produced in the discharge and could

not be deflected by the transverse electric field located after the nozzle, or were generated by collisional ionization processes between the discharge zone and the photoexcitation region.

6.3.2 The photoionization and PFI-ZEKE photoelectron spectra of He*

The photoionization and PFI-ZEKE photoelectron spectra of $1s2s\ ^3S_1\ ^4\text{He}$ in the region of the lowest threshold $1s\ ^2S_{1/2} \leftarrow 1s2s\ ^3S_1$ are displayed in Figs. 6.3b and a, respectively.

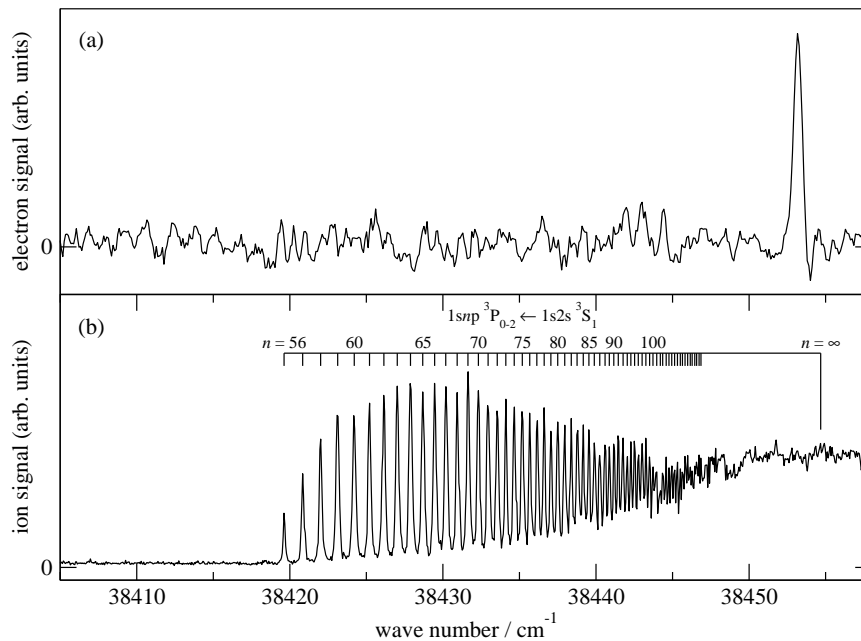


Figure 6.3: Panel a) shows the PFI-ZEKE photoelectron spectrum of the $^2S_{1/2} \leftarrow ^3S_1$ transition of ^4He . In panel b) the photoionization spectrum of the $1snp\ ^3P_{0-2} \leftarrow 1s2s\ ^3S_1$ Rydberg series is shown. The Rydberg states and the series limit are indicated by vertical lines.

The photoionization spectrum, which was recorded by collecting the He^+ ions extracted with a pulsed field of $\mathcal{E} = 133\ \text{V cm}^{-1}$ delayed by 200 ns with respect to the laser pulse, shows an extended Rydberg series assigned to the $1s2s\ ^3S_1 \rightarrow 1snp\ ^3P_{0-2}$ series with unresolved fine structure starting at $\approx 38419.5\ \text{cm}^{-1}$ and extending towards the ionization threshold (vertical line in Fig. 6.3b). The lowest observed Rydberg state ($n = 56$) is located $\approx 35.2\ \text{cm}^{-1}$ below the field-free ionization threshold which implies a value of $C = 3.1$ rather than 6.12 in Equation (2.10) (see Chapter 2)

$$\frac{\Delta E_1}{hc\ \text{cm}^{-1}} = C \sqrt{\frac{\mathcal{E}}{\text{V/cm}}} \quad (6.1)$$

and suggests that the field ionization takes place diabatically (see Refs. [14, 16]). The

Rydberg series, which can be resolved up to principal quantum number beyond $n = 100$ is free of perturbations and can be used to determine, by extrapolation using Rydberg's formula (Eq. 1.1), the ionization energy of the $1s2s\ ^3S_1$ metastable atoms. The ionization energy and quantum defects obtained from the experimentally determined spectral positions in a least-squares fitting procedure are compared with previous values in Table 6.1: The uncertainty of $\pm 0.3\text{ cm}^{-1}$ in the ionization energy is limited by the accuracy of the calibration procedure whereas the uncertainty of ± 0.03 in the value of the quantum defect is determined by the width of the spectra lines (full width at half maximum 0.3 cm^{-1}) and the fact that only Rydberg states with $n \geq 56$ were observed. The perfect agreement between the ionization energy and quantum defect determined here and the earlier, more accurate values of Refs. [280–283] demonstrates the reliability of the calibration procedure.

Table 6.1: Measured and calculated ionization Energy (E_I) and quantum defect (μ) for the np series.

	E_I / cm^{-1}	μ
This work (PFI-ZEKE photoelectron spectrum)	38 454.7(4)	
This work (photoionization spectrum)	38 454.7(3)	0.70(3)
G. W. F. Drake and W. C. Martin [281]	38 454.69464(84) ^a	
D. C. Morton <i>et al.</i> [282]	38 454.694 650(2) ^b	
W. C. Martin [283]	38 454.694 67(40) ^c	0.68

^aObtained by combining the frequency of the $2\ ^3S_1 - 3\ ^3D_1$ transition measured by Dorrer *et al.* [284] with the calculated $3\ ^3D_1$ energy.

^bValue obtained from a compilation of measured energy intervals between Rydberg states of He and the theoretical ionization energies of the of $^3D_{1-3}$, 1D_2 , 1P_1 , and 1D_2 levels.

^cObtained by combining experimental nD term values with term values calculated by Kono and Hattori [285, 286].

The PFI-ZEKE photoelectron spectrum of the $2S_{1/2} \leftarrow ^3S_1$ threshold of He depicted in Fig. 6.3a was recorded by collecting the electrons produced by field-ionization using a sequence of two electric field pulses, a discrimination pulse of $+0.133\text{ V cm}^{-1}$ immediately followed by a -0.2 V cm^{-1} field ionization and extraction pulse. Using numerical simulations of the line shape expected for this pulse sequence, according to the procedure described in Ref. [59], the observed line should be displaced by -1.54 cm^{-1} from the field-free ionization threshold and have a full width at half maximum of 0.5 cm^{-1} , slightly broader than the observed value. The position of the field-free ionization threshold is determined to be $38\,454.7(4)\text{ cm}^{-1}$, the uncertainty being caused by the uncertainty of the calibration procedure (0.3 cm^{-1} , see above) and the uncertainty in the field-induced shift of the ionization energy ($\approx 0.25\text{ cm}^{-1}$). The good agreement with earlier, more precise values of the ionization energy and with the value determined from the photoionization spectrum shows that our method of determining the field-induced shifts of the ionization thresholds is reliable.

The two spectra displayed in Fig. 6.3 nicely illustrate the complementary nature

of photoionization and PFI-ZEKE photoelectron spectra. Whereas the former provides information on an ionization channel primarily in the form of a Rydberg series and shows a smooth intensity distribution when the ionization threshold is traversed, the latter does not provide any information on individual Rydberg states but shows a single sharp line just below the field-free threshold. The reason why no electron signal is detected above the position of the ionization threshold in a PFI-ZEKE spectrum is a consequence of the low mass of the electron: Electrons emitted above the threshold are either efficiently accelerated out of the extraction region by the discrimination field pulse or have sufficient initial velocity to leave the extraction region before the detection pulsed field is applied.

Whereas in an atom like He the PFI-ZEKE photoelectron spectrum does not yield any information that is not contained in the photoionization spectrum, the situation is very different in molecules which often have several closely spaced ionization thresholds: In molecules, photoionization spectra tend to be spectrally extremely congested and difficult to assign whereas PFI-ZEKE photoelectron spectra remain simple to interpret. The complementary of photoionization and PFI-ZEKE photoelectron spectra and how it can be used to unravel the photoionization dynamics of molecules will become apparent in the next subsections describing our measurements on He_2^* .

6.3.3 The PFI-ZEKE spectra of He_2^* and their assignment

The $X^+ \ ^2\Sigma_u^+ \leftarrow a \ ^3\Sigma_u^+$ PFI-ZEKE photoelectron spectrum of $^4\text{He}_2$ is displayed in Figs. 6.4 and 6.5 and a section of that of $^3\text{He}_2$ in Fig. 6.6. The electric-field pulse sequences used to record these spectra were chosen to achieve, in each case, a satisfactory compromise between resolution and signal-to-noise ratio. The full width at half maximum (FWHM) of the spectral lines is about 0.5 cm^{-1} , which suffices to resolve the rotational structure but not the fine structures of the doublet and triplet states. We can therefore use Hund's case (b) notation and express the energy as a function of the quantum number N associated with the total angular momentum excluding spin. The spectrum consists of a dominant Q-type ($\Delta N = N^+ - N'' = 0$) branch and weaker O-type ($\Delta N = -2$) and S-type ($\Delta N = +2$) branches associated with the $v^+ = 0 \leftarrow v'' = 0$ band. Whereas the intensity distribution of the S-type branch is regular, the intensity of the O-type branch reveals pronounced irregularities. Weaker sequence bands ($v^+ = 1 \leftarrow v'' = 1$ and $v^+ = 2 \leftarrow v'' = 2$) with the same overall structure are also observed in the same spectral region.

For the interpretation of the spectra of the homonuclear isotopomers $^4\text{He}_2$ and $^3\text{He}_2$, it is necessary to consider the symmetry properties ($+/-$, s/a, $A_{g/u}$) of the molecular wavefunctions and photoionization selection rules. The labels $+$ and $-$ represent the parity, and the labels s and a indicate whether the wavefunction is symmetric or antisymmetric with respect to the permutation of the nuclei. The labels g and u indicate the symmetry of the electronic wavefunction with respect to the inversion center of the molecule, A stands

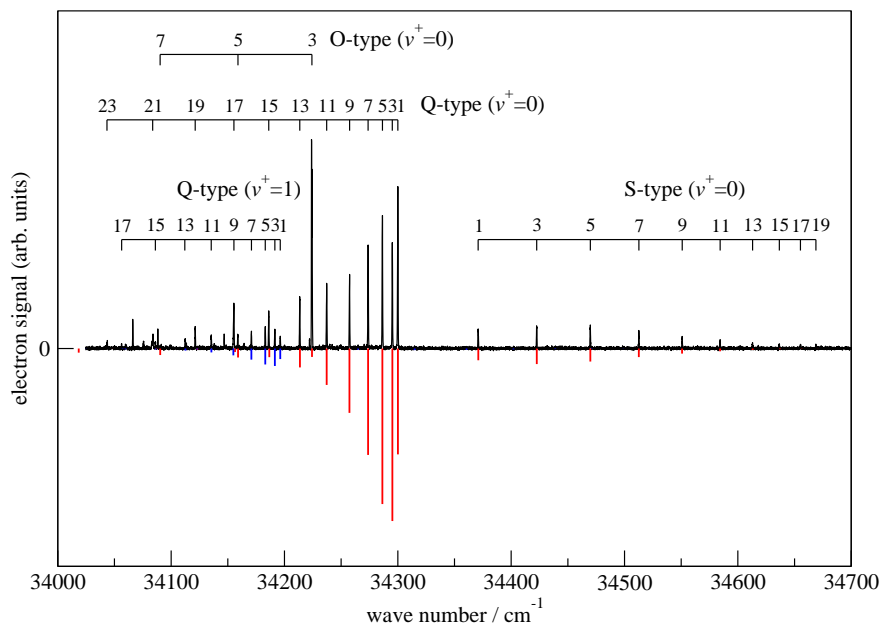


Figure 6.4: PFI-ZEKE photoelectron spectrum of the $X^+ 2\Sigma_u^+ \leftarrow a 3\Sigma_u^+$ transition of ${}^4\text{He}_2$. Below the experimental spectrum, the simulated spectra for $v^+ = v'' = 0$ and $v^+ = v'' = 1$ are shown as inverted stick spectra.

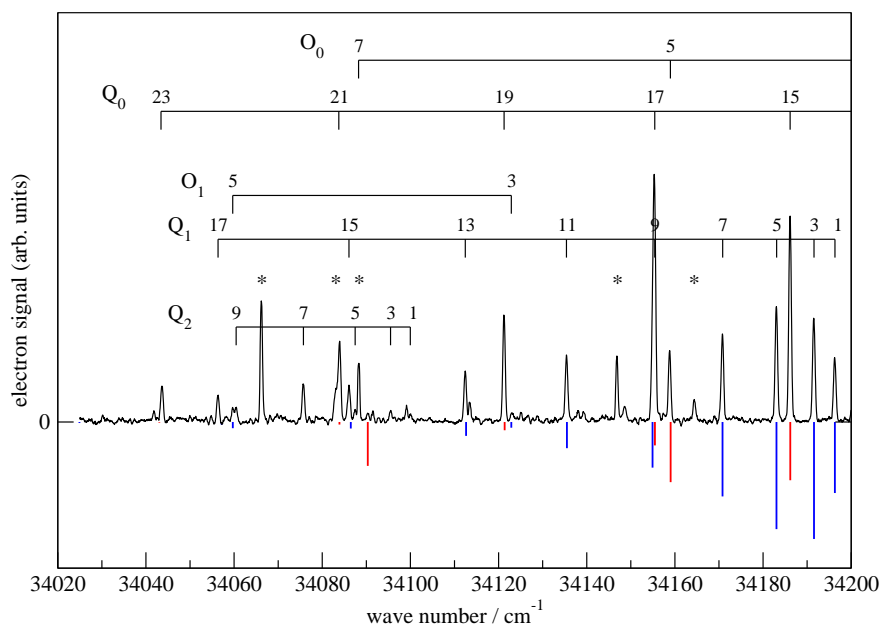


Figure 6.5: Portion of the PFI-ZEKE photoelectron spectrum of the $X^+ 2\Sigma_u^+ \leftarrow a 3\Sigma_u^+$ transition of ${}^4\text{He}_2$ in the region of the Q-type branches of the $v^+ = v'' = 1$ (Q_1) and $v^+ = v'' = 2$ (Q_2) transitions. Asterisks designate transitions which cannot be assigned to an ionization threshold but originate from channel interactions.

for the quantum number associated with the projection of the orbital angular momentum on the internuclear axis. The symmetries of the rovibronic wavefunctions are determined by the symmetries of the electronic and rotational wavefunctions $\Gamma_{\text{rve}} = \Gamma_{\text{el}} \otimes \Gamma_{\text{rot}}$, where

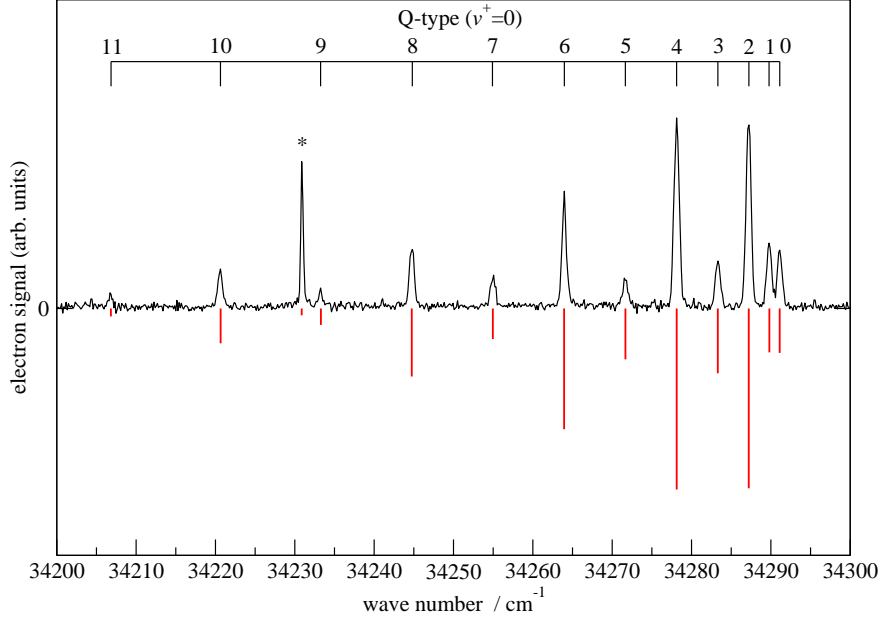


Figure 6.6: PFI-ZEKE photoelectron spectrum of the $X^+ 2\Sigma_u^+ \leftarrow a 3\Sigma_u^+$ transition of ${}^3\text{He}_2$. The asterisk marks the $N^+ = 0 \leftarrow N'' = 2$ transition. Below the experimental spectrum, the simulated spectrum is shown as inverted stick spectrum.

the symmetries Γ_{el} are $+s/a$ for $2S+1\Sigma_{g/u}^+$, $-s/a$ for $2S+1\Sigma_{u/g}^-$ and $+s/-a$ for $2S+1\Pi_g^{+/-}$ states; the symmetries of the rotational wavefunctions are $+s$ for even N and $-a$ for odd N values. The nuclear spin wavefunctions Ψ_{nspin} are either symmetric ($+s$) or antisymmetric ($+a$) with weight factors $(2I+1)(I+1)$ and $(2I+1)I$, respectively. The spin statistical weights are determined by the relation

$$\Gamma_{\text{rve}} \otimes \Gamma_{\text{nspin}} \supset \Gamma_{\text{int}}, \quad (6.2)$$

where the complete internal wavefunction Ψ_{int} must be symmetric $+/-s$ (Σ_g^+/Σ_u^-) for bosonic nuclei or antisymmetric $+/-a$ (Σ_u^+/Σ_g^-) for fermionic nuclei [3, 81]. Because only the symmetric nuclear wavefunction of the dimer of ${}^4\text{He}$ ($I = 0$) has nonzero spin statistical weight, every second line is missing in the spectra of ${}^4\text{He}_2$ [287]. Only levels with odd N occur in the $a 3\Sigma_u^+$ and $X^+ 2\Sigma_u^+$ states ($\Gamma_{\text{rve}} = -s$) and in the $np\pi 3\Pi_g^-$ Rydberg series ($\Gamma_{\text{rve}} = +s$), whereas only levels with even N occur in the $np\sigma 3\Sigma_g^+$ ($N = 0, 2, 4, \dots$) and $np\pi 3\Pi_g^+$ ($N = 2, 4, \dots$) Rydberg series ($\Gamma_{\text{rve}} = +s$). For the dimer of ${}^3\text{He}$ ($I = \frac{1}{2}$), the same levels as for ${}^4\text{He}_2$ occur with statistical weight 1, but, in addition, the levels missing in ${}^4\text{He}_2$ (e.g., the $N = 0, 2, 4, \dots$ levels of $a 3\Sigma_u^+$ and $X^+ 2\Sigma_u^+$ with symmetry $\Gamma_{\text{rve}} = +a$) occur with weight 3. Because the nuclear spin symmetry is not altered upon photoionization, $\Delta N = N^+ - N''$ must be even in the $X^+ 2\Sigma_u^+ \leftarrow a 3\Sigma_u^+$ PFI-ZEKE photoelectron spectra of ${}^4\text{He}_2$ and ${}^3\text{He}_2$ according to Eq. (6.2).

For electric dipole transitions between Rydberg states, the general rovibronic selection

rules

$$\begin{aligned}
 + &\leftrightarrow -, & + &\leftrightarrow +, & - &\leftrightarrow - \\
 s &\leftrightarrow s, & a &\leftrightarrow a, & s &\leftrightarrow a \\
 g &\leftrightarrow u, & g &\leftrightarrow g, & u &\leftrightarrow u
 \end{aligned} \tag{6.3}$$

hold [$\Gamma'_{\text{rve}} \otimes \Gamma''_{\text{rve}} \supset -s (\Sigma_{\text{u}}^-)$]. The selection rules for photoionization depend on the orbital angular momentum ℓ of the ejected photoelectron. If ℓ is even, the same rules as for the electric dipole transitions [Eq. (6.3)] are valid [$\Gamma'_{\text{rve}} \otimes \Gamma''_{\text{rve}} \supset -s (\Sigma_{\text{u}}^-)$]. If ℓ is odd, the following selection rules hold [288]:

$$\begin{aligned}
 + &\leftrightarrow +, & - &\leftrightarrow -, & + &\leftrightarrow - \\
 s &\leftrightarrow s, & a &\leftrightarrow a, & s &\leftrightarrow a \\
 g &\leftrightarrow g, & u &\leftrightarrow u, & g &\leftrightarrow u
 \end{aligned} \tag{6.4}$$

[$\Gamma'_{\text{rve}} \otimes \Gamma''_{\text{rve}} \supset +s (\Sigma_{\text{g}}^+)$]. Therefore, $np\sigma$ $^3\Sigma_{\text{g}}^+$ and $np\pi$ $^3\Pi_{\text{g}}$ Rydberg states with $\Delta N = 0, \pm 1$ are expected to be accessed by photoexcitation from the $[(1\sigma_{\text{g}})^2(1\sigma_{\text{u}})]2s\sigma_{\text{g}}$ a $^3\Sigma_{\text{u}}^+$ state according to the standard selection rules for Hund's case (b) molecules [3] and the $\Delta\ell = \pm 1$ rule for Rydberg-Rydberg transitions. Field ionization leads to the ejection of the p electron, resulting in the following selection rule for the X^+ $^2\Sigma_{\text{u}}^+ \leftarrow a$ $^3\Sigma_{\text{u}}^+$ PFI-ZEKE photoelectron spectra of $^4\text{He}_2$ and $^3\text{He}_2$:

$$\Delta N = N^+ - N'' = 0, \pm 2. \tag{6.5}$$

A qualitative interpretation of the relative intensities of the rotational lines in the PFI-ZEKE spectra can be gained from an orbital ionization model [98, 289]. Photoionization of a $^3\Sigma_{\text{u}}^+$ He₂ leaves a ($2\sigma_{\text{g}}$) hole with predominantly s character ($\ell'' = 0$) and a small d contribution ($\ell'' = 2$) in the core. Conservation of angular momentum and the assumption that the angular momentum characteristics of the photoionizing radiation is fully transferred to the photoelectron require that $\vec{\ell}'' + \vec{N}^+ = \vec{N}''$, where $\vec{\ell}''$ is the electron hole angular momentum [98]. It is therefore expected that the PFI-ZEKE photoelectron spectra show dominant Q-type branches and weaker S-type and O-type branches as observed experimentally. In Figs. 6.4–6.6, the experimental spectra are compared with simulated stick spectra (inverted traces) calculated according to the equations in Refs. [98, 290]. Overall, the calculated intensities reproduce the observed ones satisfactorily. However, the intensities of several lines in the O-type branches of the experimental spectrum (e.g., O(3) of the 0–0 band, see Fig. 6.4) appear too strong. These deviations, which are characteristic of the PFI-ZEKE photoelectron spectra of small molecules [68–70], will be discussed in more detail in Subsection 6.3.5 and Section 6.4.

In the analysis of the PFI-ZEKE photoelectron spectra, the rovibrational energy levels are expressed in standard manner [3]

$$\begin{aligned}
 T(v, N) &= T_e + G(v) + F_v(N) & (6.6) \\
 G(v) &= \omega_e(v + \frac{1}{2}) - \omega_e x_e(v + \frac{1}{2})^2 + \dots \\
 F_v(N) &= B_v N(N + 1) - D_v [N(N + 1)]^2 + H_v [N(N + 1)]^3 + \dots \\
 B_v &= B_e - \alpha_e(v + \frac{1}{2}) + \dots \\
 D_v &= D_e + \beta_e(v + \frac{1}{2}) + \dots
 \end{aligned}$$

The line positions (corrected for the field-induced shift of the ionization thresholds, see Table 6.2) were fitted using the program SPFIT [291] with the lower state (a $^3\Sigma_u^+$) constants fixed to the values reported in Ref. [268]. The corresponding values for the $^3\text{He}_2$ isotopomer were obtained according to the relation [3]

$$Y_{jk}^{(i)} = (\mu/\mu^{(i)})^{j/2+k} Y_{jk}, \quad (6.7)$$

where Y_{jk} is the coefficient for the term $(v + \frac{1}{2})^j [N(N + 1)]^k$, μ is the reduced mass and (i) indicates the isotopic form. The fitted molecular constants are listed in Table 6.3. Inclusion of the H_v term for the $v^+ = 0$ state reduced the root-mean-square of the residuals S considerably, but significantly affected the values of the B_v and D_v constants (when H_0^+ is set to zero, $T_0^+ = 34\,302.236(20)\text{ cm}^{-1}$, $B_0^+ = 7.097\,96(25)\text{ cm}^{-1}$, $D_0^+ = 5.012(5) \cdot 10^{-4}\text{ cm}^{-1}$, $S = 1.336$). For the further analysis, the parameter sets with and without H_0^+ are referred to as Set 1 and Set 2, respectively; in many cases Set 2 is preferred because it has to be compared to another set without H_v^+ constants. For comparison, the transition wave numbers of the mixed isotopomer reported in Ref. [236] were fitted using the same model. The standard errors of the weighted fits are close enough to 1 that one can conclude that Eq. (6.6) suffices to adequately describe the transition wave numbers observed experimentally. The lower half of Table 6.3 represents the most accurate set of spectroscopic constants derived so far for He_2^+ . The present results are in excellent agreement with those derived by Ginter et al. from spectroscopic measurements of the low- n Rydberg states of He_2 in a MQDT analysis [258, 264, 277] but are more precise.

Table 6.2: Observed transition wave numbers (cm^{-1}) in the $X^+ \ ^2\Sigma_u^+ \leftarrow a \ ^3\Sigma_u^+$ PFI-ZEKE photoelectron spectra of $^4\text{He}_2$ and $^3\text{He}_2$ and differences between observed and calculated line positions $\tilde{\nu}_{\text{obs}} - \tilde{\nu}_{\text{calc}}$ (cm^{-1}). The line positions have been corrected for the field-induced shift of the ionization thresholds. The number of significant figures has been adapted to the experimental accuracy of the relative line positions. The absolute uncertainty amounts to $\pm 0.3 \text{ cm}^{-1}$.

$N^+ - N''$	$^4\text{He}_2$						$^3\text{He}_2$	
	$v^+ - v''; 0 - 0$		1 - 1		2 - 2		0 - 0	
0 - 0							34292.310	0.012
1 - 1	34 301.196	0.035	34 197.457	0.017	34 101.206	0.002	34 290.983	-0.014
2 - 2							34 288.390	-0.009
3 - 3	34 296.323	0.032	34 192.709	0.009	34 096.692	-0.021	34 284.520	0.013
4 - 4							34 279.321	-0.006
5 - 5	34 287.571	0.025	34 184.217	0.022	34 088.669	0.042	34 272.856	-0.011
6 - 6							34 265.145	0.008
7 - 7	34 274.981	0.023	34 171.990	0.018	34 076.909	-0.029	34 256.171	0.020
8 - 8							34 245.942	0.021
9 - 9	34 258.594	0.016	34 156.356 ^a	0.265	34 061.637	0.007	34 234.428	-0.036
10 - 10							34 221.787	-0.013
11 - 11	34 238.436	-0.031	34 136.610	-0.017			34 207.961	0.015
13 - 13	34 214.683	-0.020	34 113.630	-0.031				
15 - 15	34 187.325	-0.052	34 087.272	0.000				
17 - 17	34 156.626 ^a	0.030	34 057.536	0.003				
19 - 19	34 122.433	-0.050						
21 - 21	34 085.154	-0.027						
23 - 23	34 044.836	-0.013						
3 - 1	34 372.095	-0.009	34 266.090	-0.019				
5 - 3	34 423.718	-0.008	34 315.939	-0.107				
7 - 5	34 471.002	-0.023	34 361.743	-0.037				
9 - 7	34 513.827	-0.012	34 403.166	0.008				
11 - 9	34 552.052	0.027	34 440.109	0.061				
13 - 11	34 585.479	0.018						
15 - 13	34 614.076	0.030						
17 - 15	34 637.734	0.031						
19 - 17	34 656.405	0.028						
21 - 19	34 670.059	0.019						
0 - 2							34232.102	0.000
1 - 3	34 225.596 ^b	0.249						
3 - 5	34 160.000	-0.110	34 060.893	0.044				
5 - 7	34 091.519	0.040						

^aThe $(v^+, N^+) \leftarrow (v'', N'') = (1, 9) \leftarrow (1, 9)$ transition is overlapped by the stronger $(0, 17) \leftarrow (0, 17)$ transition and was not included in the fit.

^bTransition not included in the fit because the determination of the line position may be affected by the presence of the transition to the $39p\pi \ ^3\Pi_g^-(N=3)$ Rydberg state.

Table 6.3: Molecular constants for the a $^3\Sigma_u^+$ state of He_2 and for the ground $X^+ \ ^2\Sigma_u^+$ state of He_2^+ .

	$^4\text{He}_2$			$^4\text{He}^3\text{He}$		$^3\text{He}_2$
	$v, v^+ = 0$	$v, v^+ = 1$	$v, v^+ = 2$	$v^+ = 0$	$v^+ = 1$	$v, v^+ = 0$
T_v / cm^{-1}	0.0	1732.1615 ^a	3386.5024 ^a			0.0
B_v / cm^{-1}	7.589 14 ^a	7.348 74 ^a	7.101 75 ^a			10.0386(95)
$D_v \cdot 10^{-4} / \text{cm}^{-1}$	5.6153 ^a	5.6538 ^a	5.7439 ^a			9.90 ^b
$H_v \cdot 10^{-8} / \text{cm}^{-1}$	3.22 ^a	2.84 ^a	3.31 ^a			
$T_v^+ - T_v / \text{cm}^{-1}$	34 302.135(24) ^c	34 198.390(24) ^c	34 102.102(46) ^c			34 292.298(27) ^c
$T_v^+ - T_0^+ / \text{cm}^{-1}$	0.0	1628.416	3186.469	0.0	1750.5569(44) ^d	0.0
B_v^+ / cm^{-1}	7.101 63(54)	6.873 94(52)	6.6528(27)	8.2515(22) ^d	7.9681(13) ^d	9.3884(91)
$D_v^+ \cdot 10^{-4} / \text{cm}^{-1}$	5.220(28)	5.094(18)	5.79(28)	7.29(25) ^d	7.22(21) ^d	9.051(94)
$H_v \cdot 10^{-8} / \text{cm}^{-1}$	2.89(37)	0.0	0.0			
S^e		0.680			0.149 ^d	0.323

^aFixed to the value of Ref. [268].

^bValue derived from the corresponding value of $^4\text{He}_2$.

^cAbsolute error estimated to be less than 0.3 cm^{-1} .

^dFit of the transition wave numbers reported in Ref. [236].

^eStandard error of the weighted fit.

6.3.4 The photoionization spectrum He_2^* and its analysis by MQDT

The different optically accessible p channels and their interactions are depicted schematically in Fig. 6.7. The dominant interactions are between channels of the same v^+ and N values but of N^+ values differing by two. These interactions lead to perturbations in the bound part of the spectrum (i.e., below the $N^+ - 2$ threshold) and to autoionization above the $N^+ - 2$ threshold. Transitions to channels with $N^+ = N''$ are strong and those to channels with $N^+ = N'' \pm 2$ are weak for the reason already used to explain why Q-type lines in the PFI-ZEKE photoelectron spectrum are stronger than O-type and S-type lines. The $N = N^+ \ n p \pi \ ^3\Pi_g^-$ channels are thus intense and free of perturbations, whereas the $N = N^+ \pm 1 \ n p \pi \ ^3\Pi_g^+$ and $n p \sigma \ ^3\Sigma_g^+$ channels are strongly perturbed. Q-type transitions from a $^3\Sigma_u^+, N''$ to $N = N'' - 1$ ($\Pi_g^+ + \Sigma_g^+$) Rydberg states converging on the $N^+ = N''$ threshold lend intensity to the O-type transitions associated with the $N^+ = N'' - 2$ channel, and can enhance the intensity of an O-type line in the PFI-ZEKE photoelectron spectrum. Above the $N^+ = N'' - 2$ ionization threshold these transitions are observed as autoionization resonances with close-to-Lorentzian line shapes. The S-type transitions from a $^3\Sigma_u^+, N''$ to $N = N'' + 1$ ($\Pi_g^+ + \Sigma_g^+$) Rydberg states are intrinsically weak but can gain intensity from the strong Q-type transitions to channels of the same N value. Above the N^+ ionization threshold, these transitions appear as so-called window resonances.

The photoionization spectrum of $^4\text{He}_2$ a $^3\Sigma_u^+$ is displayed in Fig. 6.8. The horizontal bars labeled Q(N) indicate the positions of the $(v^+ = v'', N^+ = N'') \leftarrow (v'', N'')$ thresholds for $v'' = 0, 1$. The photoionization signal increases gradually as the successive thresholds are traversed. Below these thresholds, the photoionization spectrum consists of transitions to discrete Rydberg states which are ionized by the applied electric field or by channel

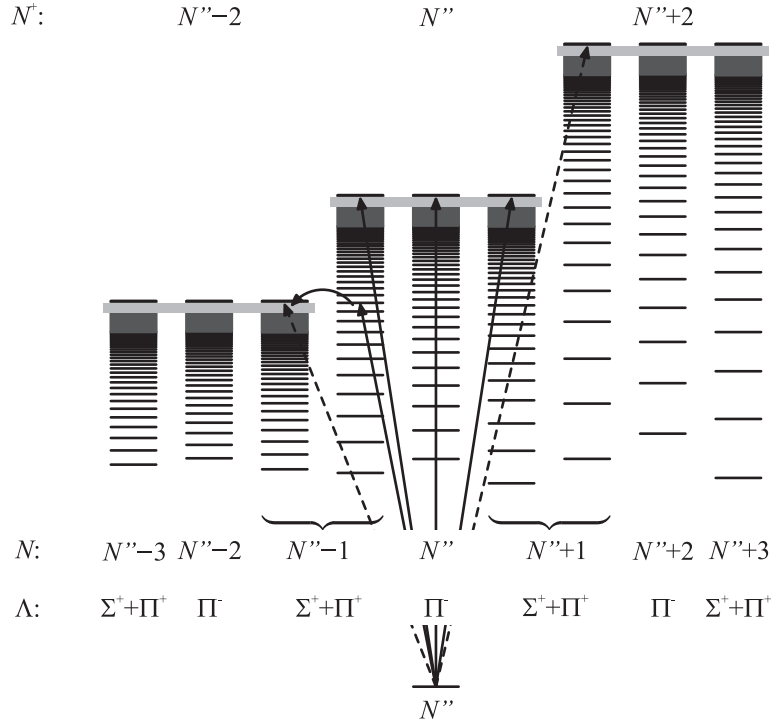


Figure 6.7: Schematic representation of the p channels optically accessible from the $a\ ^3\Sigma_u^+$ state (only levels with $v^+ = v''$ considered). The light grey areas mark the high- n Rydberg states which are field-ionized in the PFI-ZEKE experiments. Transitions to channels with $N^+ = N''$ are strong (full arrows) and those to channels with $N^+ = N'' \pm 2$ are weak (dashed arrows). Transitions to Rydberg states with $N = N'' - 1$ converging on the $N^+ = N'' - 2$ threshold gain intensity from stronger transitions to Rydberg states with the same N but converging to the $N^+ = N''$ threshold.

interactions. The electric field of the extraction pulse ($400\ \text{V cm}^{-1}$) allows field-ionization within $120\ \text{cm}^{-1}$ of the zero-field ionization thresholds. Channel interactions between discrete Rydberg series and the continua of open channels can occur and lead to rotational and vibrational autoionization, of which the former is more important in the region of interest here. In Fig. 6.8, the $(v^+ = v'', N^+ = N'' - 2) \leftarrow (v'', N'')$ rotational autoionization thresholds are indicated along the horizontal lines labeled $O(N)$. The thresholds for vibrational autoionization $(v^+ = 0, N^+ = N'') \leftarrow (v'' = 1, N'')$ lie below the low-frequency end of Fig. 6.8. Forced autoionization is also observed as a channel interaction between a Rydberg state and the pseudo-continuum of high Rydberg states which are field-ionized by the applied electric field [68].

In order to obtain the ionization energy without the uncertainty of the field shift of the PFI-ZEKE measurement, the $np\pi\ ^3\Pi_g^\pm$ and $np\sigma\ ^3\Sigma_g^+$ Rydberg series in the photoionization spectrum (Figs. 6.8 and 6.9) have been analyzed by multichannel quantum defect theory (MQDT) [292]. The model I of Ginter and coworkers [264, 277] using two channels for even N values ($\alpha, i = 1, 2$) and one channel for odd N values ($\alpha, i = 3$) has been applied (cf. Fig. 6.7). If interactions between states of different N values are considered to be

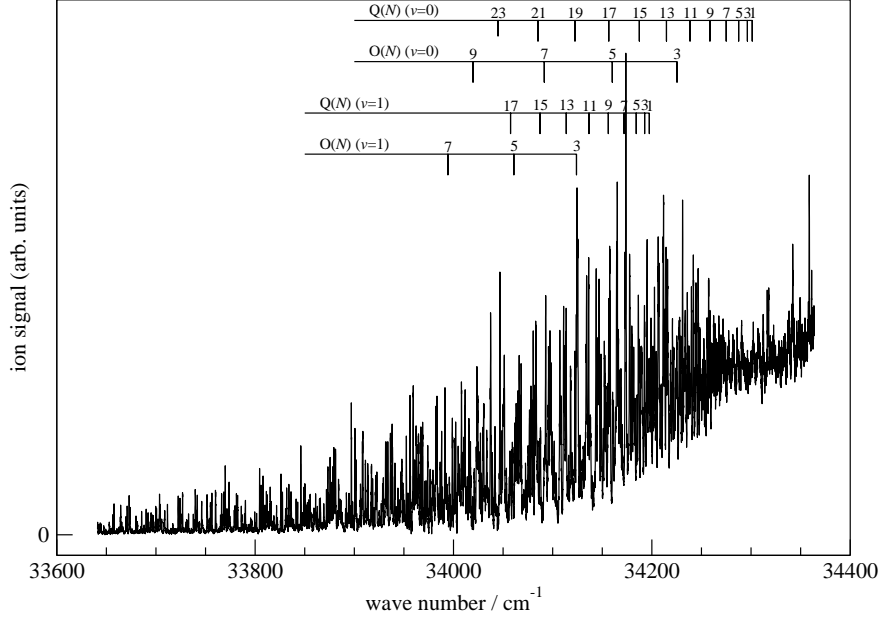


Figure 6.8: Photoionization spectrum of ${}^4\text{He}_2$ a ${}^3\Sigma_u^+$. The positions of the $(v^+ = v, N^+ = N) \leftarrow (v, N)$ or $(v^+ = v, N^+ = N - 2) \leftarrow (v, N)$ ionization thresholds are indicated along the horizontal bars by $Q(N)$ and $O(N)$, respectively.

negligible, the energy terms can be calculated separately for each N value. For each N block, the bound energy levels are the solutions of the determinantal equation

$$\det |U_{i\alpha} \sin[\pi(\mu_\alpha + \nu_i)]| = 0, \quad (6.8)$$

where μ_α are the eigenchannel quantum defects with their energy dependence expressed as

$$\mu_\alpha = \mu_\alpha^{(0)}(1 + \mu_\alpha^{(1)}\epsilon)(1 + A_\alpha N(N + 1)) \quad (6.9)$$

with

$$\epsilon = [E - E({}^2\Sigma_u^+, v^+, N^+ = 0)]/R_M. \quad (6.10)$$

The effective quantum number ν_i in Eq. (6.8) is defined by

$$\nu_i^2 = R_M/[E({}^2\Sigma_u^+, v^+, N_i^+) - E] \text{ with } \begin{cases} N_1^+ = N - 1 \\ N_2^+ = N + 1 \\ N_3^+ = N \end{cases} . \quad (6.11)$$

The Rydberg constant R_M in Eqs. (6.10) and (6.11) has the value $R_M = 109\,729.7956 \text{ cm}^{-1}$ for ${}^4\text{He}_2$. The matrix $U_{i\alpha}$ in Eq. (6.8) for even N values is the frame transformation matrix from the close-coupling Hund's case (b) to the long-range Hund's case (d) basis set and

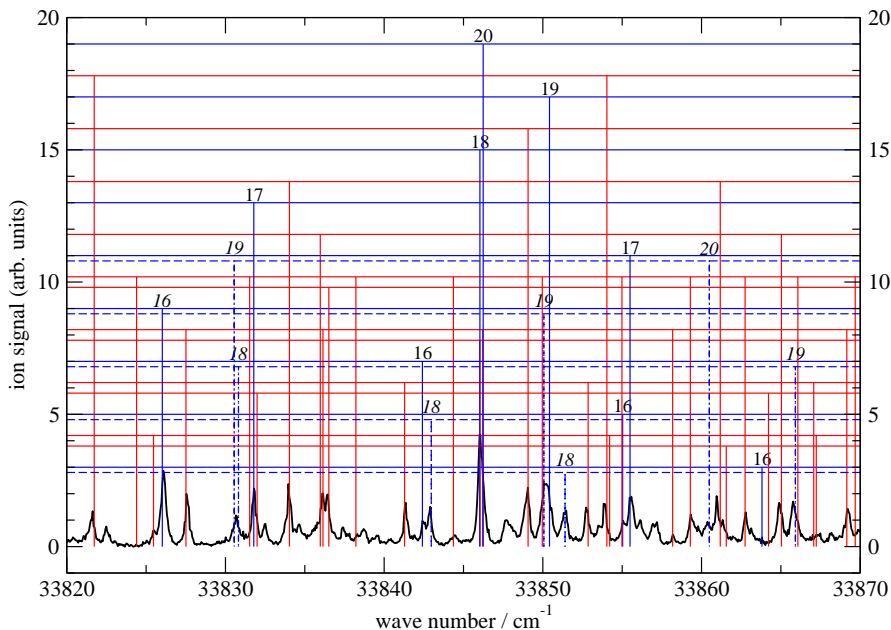


Figure 6.9: Detailed view of a selected portion of the photoionization spectrum of ${}^4\text{He}_2$ a ${}^3\Sigma_u^+$. The horizontal assignment bars for $N = 3 - 19$ have been shifted along the vertical axis so that their positions correspond to the value of N . The full (dashed) horizontal lines correspond to $v^+ = 0 \leftarrow v'' = 0$ ($v^+ = 1 \leftarrow v'' = 1$; indicated only for $N = 3, 5, \dots, 11$) series. The principal quantum number n of the $np\pi$ ${}^3\Pi_g^-$ Rydberg series, which only occur for odd N values and form Q-type progressions ($N^+ - N'' = N - N'' = 0$), are indicated above the corresponding assignment bars. The $np\pi$ ${}^3\Pi_g^+$ and $np\sigma$ ${}^3\Sigma_g^+$ Rydberg series, which only occur for even N values, are fully mixed and form P ($N - N'' = -1$) and R ($N - N'' = +1$) branches. The assignment bars of the P branches are placed above those of the R branches; for both branches, only the Rydberg levels converging to the lower ionization threshold $N^+ = N - 1$ are assigned.

has the form [138]

$$\begin{array}{rcc}
 \alpha: & 1 & 2 \\
 & np\sigma \quad {}^3\Sigma_g^+ & np\pi \quad {}^3\Pi_g^+ \\
 i: & & \\
 1 & \left[\frac{N}{2N+1} \right]^{1/2} & \left[\frac{N+1}{2N+1} \right]^{1/2} \\
 2 & - \left[\frac{N+1}{2N+1} \right]^{1/2} & \left[\frac{N}{2N+1} \right]^{1/2} .
 \end{array} \quad (6.12)$$

The eigenchannel quantum defects of the $np\pi$ ${}^3\Pi_g^+$ and $np\pi$ ${}^3\Pi_g^-$ channels were constrained to the same values, an approximation also used by Ginter and coworkers [264, 277]. No interactions between $v^+ = 0$ and $v^+ = 1$ channels were included in the model. Indeed, the density of Rydberg levels belonging to series converging on vibrationally excited levels is very low in the vicinity of the $v^+ = 0$ threshold. To minimize the effect of local perturbations by these levels, a robust fitting method has been applied [293, 294].

Initial assignments of the peaks in the photoionization spectrum relied on MQDT forward calculations based on fits of the positions of Rydberg levels (with n up to 17) compiled by Ginter and coworkers [261, 262, 264, 277] and the rovibrational energy level

structure of the ion as obtained from the PFI-ZEKE photoelectron spectrum (see Table 6.3). With increasing wave number, the density of peaks in the photoionization spectrum (Fig. 6.8) increases; for wave numbers above $34\,000\text{ cm}^{-1}$, the peaks cannot be assigned anymore because of spectral congestion. Therefore, only experimental term values of Rydberg levels associated with transitions between $33\,640\text{ cm}^{-1}$ and $34\,000\text{ cm}^{-1}$ and the data mentioned above [261, 262, 264, 277] were used in the analysis. The results of the analysis are summarized in Table 6.4 and illustrated in Fig. 6.9, which presents a section of the photoionization spectrum with the assignment of the main transitions to bound Rydberg states. The higher resolution of the present spectrum compared to the photoionization spectrum reported in Ref. [295] (see their Fig. 2) enables the identification of all dominant resonances. A table comparing the positions of all observed Rydberg levels with the results of MQDT calculations is given in the Appendix. The fitted rotational and centrifugal distortion constants of the He_2^+ ion are in good agreement with the values derived in the analysis of the PFI-ZEKE photoelectron spectrum (Set 2). The vibronic term values of $\text{He}_2^+ X^+ {}^2\Sigma_u^+ (v^+, N^+ = 0)$ with respect to the $\text{He}_2 a {}^3\Sigma_u^+ v=0, N=0$ level agree with the Set 1 parameters (see Table 6.3) within the statistical uncertainties.

Table 6.4: MQDT parameters for ${}^4\text{He}_2 [X^+ {}^2\Sigma_u^+]np\lambda ({}^3\Pi_g, {}^3\Sigma_g^+)$.

α	$v = 0$		$v = 1$	
	$np\sigma {}^3\Sigma_g^+$	$np\pi {}^3\Pi_g^\pm$	$np\sigma {}^3\Sigma_g^+$	$np\pi {}^3\Pi_g^\pm$
$\mu_\alpha^{(0)}$	0.770 882(29)	0.070 679(12)	0.780 804(186)	0.068 348(57)
$\mu_\alpha^{(1)}$	-0.394 53(20)	-0.094 76(65)	-0.332 01(257)	-0.094 76 ^a
$A_\alpha \cdot 10^4$	0.377 39(49)	-1.038 2(39)	0.364 26(302)	-1.728 2(659)
$E(v^+, N^+ = 0)/hc^b / \text{cm}^{-1}$	34 302.111(21)		35 930.579(71)	
B^+ / cm^{-1}	7.098 89(28)		6.873 93(122)	
$D^+ \cdot 10^{-4} / \text{cm}^{-1}$	5.0415(74)		5.207(46)	

^aConstrained to the value of the $v = 0$ state.

^bRelative to the (hypothetical) $v = 0, N = 0$ level of a ${}^3\Sigma_u^+$.

The MQDT parameters of Table 6.4 cannot be directly compared to those of Ginter and coworkers [277], who only have analyzed the $v^+ = 0$ Rydberg series in detail by MQDT, because these authors have used a different sign for μ_α in their version of the determinantal equation (6.8) ($\det |U_{i\alpha} \sin[\pi(\nu_i - \mu_\alpha)]| = 0$), so that their values of μ_α correspond to $1 - \mu_\alpha$ of our values. The other equations are the same (except for a proportionality factor for ϵ , Eq. (6.10)), and the parameters for the energy dependence of the eigen quantum defects ($\mu_\alpha^{(1)}$ and A_α) agree qualitatively.

6.3.5 Probing the autoionization dynamics of He₂ Rydberg states by Rydberg-state-resolved threshold-ionization

The highly congested nature of the photoionization spectrum of ${}^4\text{He}_2$ a ${}^3\Sigma_u^+$ above $34\,200\text{ cm}^{-1}$ renders the identification and assignment of spectral features in this region impossible (see Fig. 6.8). In order to nevertheless obtain information on the Rydberg states in this region, experiments were carried out that relied on the detection of the electrons, rather than the ions, produced by delayed pulsed field ionization. The spectral simplification that results and which has already been illustrated in Fig. 6.3 for He* comes from the fact that all electrons emitted either by direct ionization or by autoionization do not contribute to the measured, signal only electrons produced by the delayed pulsed field ionization of long-lived Rydberg states being detected.

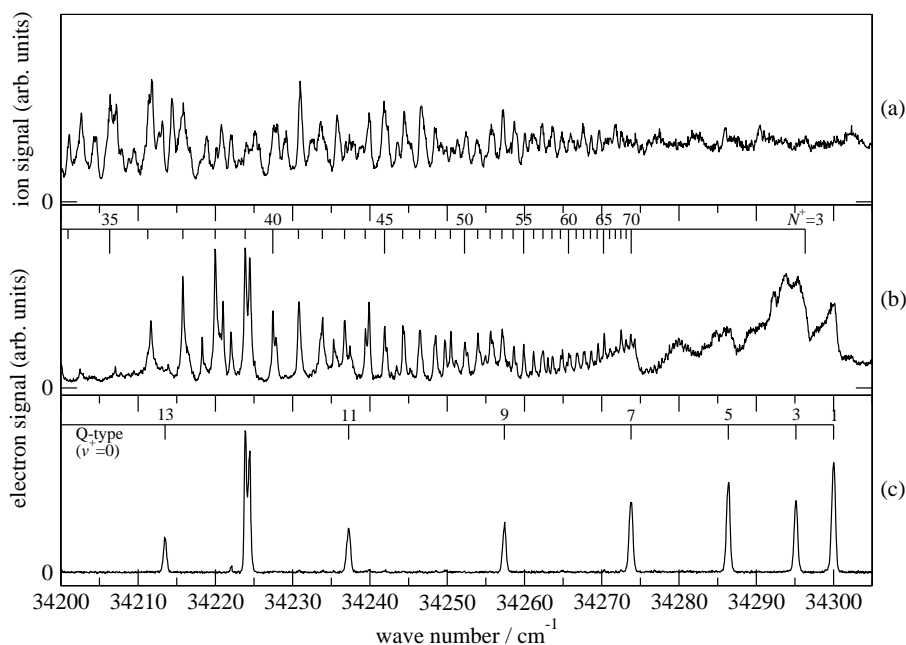


Figure 6.10: Comparison of the photoionization spectrum of ${}^4\text{He}_2$ a ${}^3\Sigma_u^+$ recorded with a pulsed electric field of $+400\text{ V cm}^{-1}$ and collecting the ${}^4\text{He}_2^+$ ions (trace (a)), the RSR-TI spectrum of ${}^4\text{He}_2$ a ${}^3\Sigma_u^+$ recorded with a pulsed electric field of -6.4 V cm^{-1} and collecting the electrons (trace (b)), and the PFI-ZEKE photoelectron spectrum of ${}^4\text{He}_2$ a ${}^3\Sigma_u^+$ measured with a pulse sequence consisting of a discrimination pulse of $+66\text{ mV cm}^{-1}$ followed by an extraction pulse of -133 mV cm^{-1} (trace (c)). The Q-type lines of the PFI-ZEKE photoelectron spectrum are labeled by the value of N^+ .

Using large pulsed electric fields in these measurements enables one to observe not only very high Rydberg states with $n \approx 300$ but, in favorable cases, also Rydberg states below $n = 100$ which can be resolved spectrally. Seiler *et al.* have exploited such large electric field pulses to obtain PFI-ZEKE photoelectron spectra in which each line, rather than consisting of only unresolved high- n Rydberg states, also revealed resolved Rydberg series [95, 296, 297], and called such spectra "Rydberg-state-resolved threshold-ionization"

(RSR-TI) spectra to distinguish them from both photoionization spectra and the usual PFI-ZEKE photoelectron spectra. The differences between these three spectra in the region between $34\,200\text{ cm}^{-1}$ and $34\,310\text{ cm}^{-1}$ can be seen in Fig. 6.10. The top (a) and bottom (c) spectra in this figure represent the photoionization spectrum already displayed in Fig. 6.8, and the PFI-ZEKE photoelectron spectrum already displayed in Fig. 6.4, respectively. The middle spectrum (b) correspond to a RSR-TI spectrum recorded with a pulsed field of -6.4 V cm^{-1} . Whereas the photoionization spectrum is too congested for assignments of Rydberg states to be made, the PFI-ZEKE photoelectron spectrum reveals perfectly resolved ionization thresholds corresponding to Q-type transitions (see assignments bars). The RSR-TI spectrum reveals well resolved series of autoionizing resonances in addition to broader unresolved structures associated with the Q-type lines.

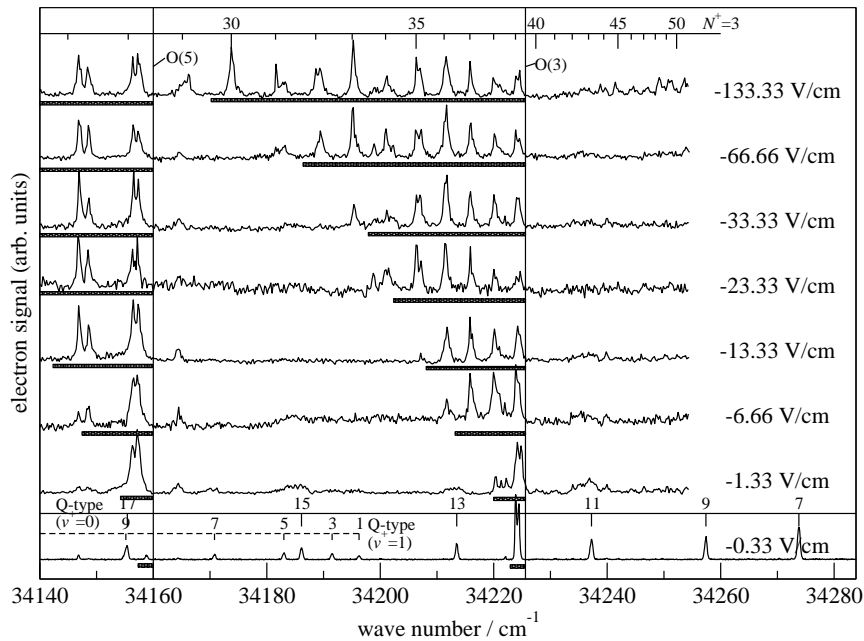


Figure 6.11: RSR-TI spectra of ${}^4\text{He}_2\ a\ 3\Sigma_u^+$ in the region of the O(5) and O(3) thresholds recorded using pulsed electric fields ranging from -0.33 V cm^{-1} (bottom) to -133.33 V cm^{-1} (top). The field ionization regions of these fields are indicated below each spectrum by the long rectangular frames. The lines of the bottom spectrum, which corresponds to the PFI-ZEKE photoelectron spectrum are assigned along the full line ($v^+ = 0$) and dashed line ($v^+ = 1$). The two vertical lines correspond to the field-free position of the O(5) and O(3) thresholds.

The use of RSR-TI spectra to unravel the photoionization dynamics of ${}^4\text{He}_2\ a\ 3\Sigma_u^+$ near the O(3) and O(5) lines of the PFI-ZEKE photoelectron spectrum near $34\,220\text{ cm}^{-1}$ is further illustrated by Figs. 6.11 and 6.12. The former figure (Fig. 6.11) displays, from bottom to top, a series of spectra obtained with a single pulsed electric field of magnitude increasing from 0.33 V cm^{-1} to 133.3 V cm^{-1} . The positions of the O(3) and O(5) ionization thresholds are marked by vertical lines and the horizontal frames below the spectra indicate the field ionization regions of the different electric field pulses assuming

that the field-induced lowering of the thresholds by the pulsed fields can be described by Eq. (2.11). The low-wave-number onset of the field ionization is well described by assuming that the pulsed field lowers the ionization thresholds by $\Delta E_1/(hc \text{ cm}^{-1}) = 4.8\sqrt{\mathcal{E}/(\text{V}/\text{cm})}$. The spectral structures observed in these spectra can be attributed to Rydberg series converging to the $N^+ = 3$ and $N^+ = 5$ thresholds. The Rydberg states are coupled to the $N^+ - 2$ pseudo continua of high Rydberg states and are field ionized when the pulsed electric fields are applied. The latter figure (Fig. 6.12) shows, from top to bottom, a series of RSR-TI spectra recorded by carrying out the photoexcitation in the presence of discrimination dc electric fields of magnitude increasing from 0 V cm^{-1} to 1.9 V cm^{-1} measured with a delayed pulsed field of -23.3 V cm^{-1} . The discrimination dc field prevents the observation, in the spectra, of Rydberg states in the regions marked by horizontal frames and located above the corresponding field-induced lowered threshold, which in the case of dc-fields is adequately described by Eq. (2.10).

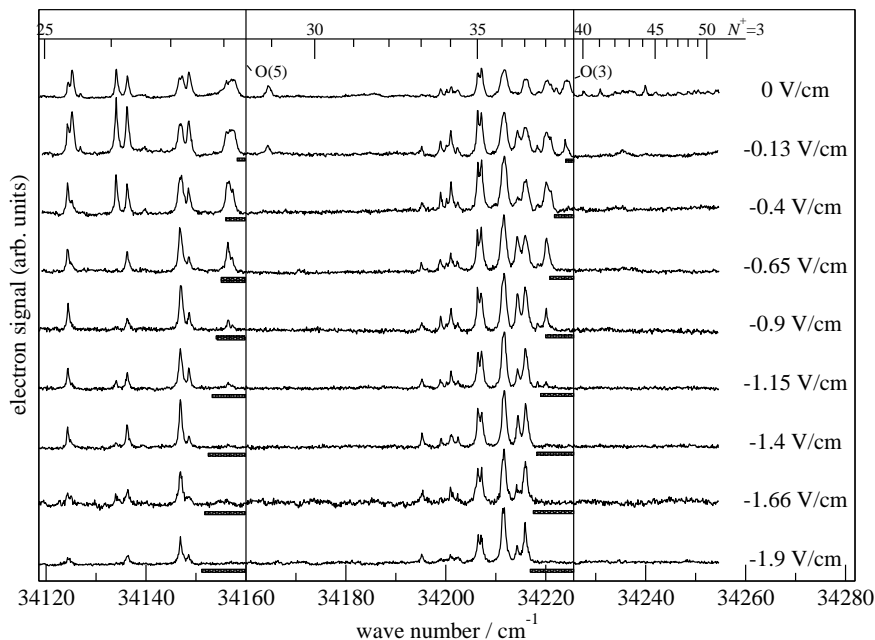


Figure 6.12: RSR-TI spectra of ${}^4\text{He}_2$ $a \ ^3\Sigma_u^+$ in the region of the O(5) and O(3) thresholds recorded using a pulsed extraction field of -23.3 V cm^{-1} and dc discrimination fields ranging from 0 V cm^{-1} (top spectrum) to -1.9 V cm^{-1} (bottom spectrum). The field free positions of the O(3) and O(5) thresholds are indicated by vertical lines and the long horizontal rectangular frames indicate the field ionization region of the dc discrimination fields.

The top spectrum in Fig. 6.12 still shows weak spectral structures above the position of the O(3) threshold that correspond to the Rydberg series converging to the $N^+ = 3$ threshold and, to a lesser extent, Rydberg series converging to the $N^+ = 5$ threshold (see also Fig. 6.13 where these series are assigned). The application of a dc field during photoexcitation, however, leads to their disappearance. This observation may be interpreted as providing evidence for long-lived np Rydberg states converging to the $N^+ = 3$ which

do not autoionize into the $N^+ = 1$ continua in the absence of electric fields but which do so when the pulsed field is applied. Because all other spectra in Fig. 6.12 do not show such structures above the $O(3)$ threshold, one may also conclude that the dc fields induce the autoionization of these states before the pulsed detection field is applied.

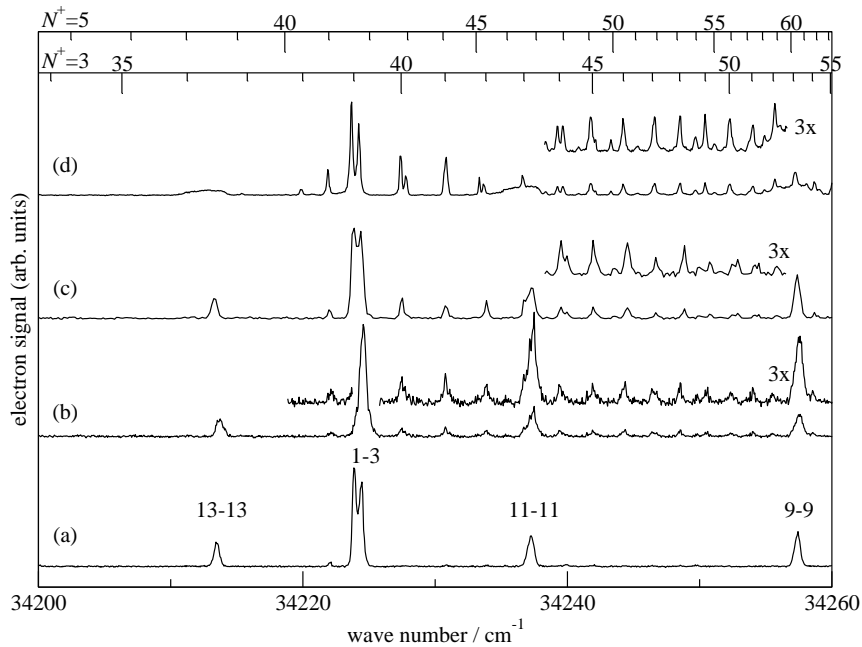


Figure 6.13: Comparison between PFI-ZEKE spectra of ${}^4\text{He}_2$ a ${}^3\Sigma_u^+$ recorded under different conditions. Spectra (a) and (c) were recorded with a discrimination pulse field of $+66$ mV/cm applied $1 \mu\text{s}$ after photoexcitation and an extraction pulse field of -133 mV/cm. Spectrum (b) was recorded with an electric field pulse sequence of $+40$ mV/cm and -133 mV/cm applied 210 ns after photoexcitation. Spectrum (d) was recorded without discrimination field pulse and an extraction field of -1.33 V/cm starting $1.5 \mu\text{s}$ after photoexcitation; the stronger extraction field caused a significant broadening of the $N^+ \leftarrow N''$ ZEKE transitions. Spectra (b) to (d) show transitions from $(v''=0, N''=3)$ to $n p \pi {}^3\Pi_g^-(N=3)$ Rydberg states located above the $N^+ = 1$ threshold for $n > 39$; the positions of the transitions are given at the top. In spectrum (d) (and also weakly in spectrum (c)), transitions from $(v''=0, N''=5)$ to $n p \pi {}^3\Pi_g^-(N=5)$ Rydberg states are observable. The $(v^+ = 0, N^+) \leftarrow (v'' = 0, N'')$ ZEKE transitions are labeled with $N^+ - N''$.

Pulsed discrimination electric fields appear to have a similar, though less pronounced effect than dc discrimination fields. Fig. 6.13 shows PFI-ZEKE photoelectron spectra recorded under several combinations of pulsed electric field sequences. The top spectrum (d) was recorded without any discrimination field and reveals, as the top trace of Fig. 6.12 the Rydberg series converging to the $N^+ = 3$ threshold above the position of the $O(3)$ threshold. Applying small pulsed field in the range of $40 - 66$ mV cm^{-1} tends to reduce the intensity of these series although this reduction also appears to depend on further, so far not identified, experimental characteristics: indeed, although traces (a) and (c) were recorded using the same discrimination and extraction pulses, the Rydberg series above the $O(3)$ ionization threshold has completely disappeared in trace (a) but only partially

in trace (c). We shall return to these observations in Subsection 6.4.2.

6.4 Discussion

6.4.1 Energy level structure of the He₂⁺ cation

Using the experimentally determined rotational constants of at least two vibrational states, it is possible to determine the equilibrium structure of He₂⁺ X⁺ ²Σ_u⁺. The equilibrium rotational constants calculated by using the approximation $B_e \approx (3B_0 - B_1)/2$ and the values obtained from the analysis of the PFI-ZEKE photoelectron spectra are listed in Table 6.5. The equilibrium bond length r_e is given by $I_e = \mu r_e^2 = h/8\pi^2 c B_e$, where the nuclear reduced masses μ are 2.000753 u, 1.507466 u and 1.719429 u for ⁴He₂, ³He₂ and ³He⁴He, respectively. The experimental values are in excellent agreement with the theoretical [253, 254, 272] and earlier experimental values [236, 258]. It should be noted that in the work of Ginter and coworkers the information about the $v^+ = 2$ level of He₂⁺ relies on the extrapolation from a few low n Rydberg states and are thus less precise [258]; the term values of the $v^+ = 0$ and 1 vibrational states of He₂⁺ X⁺ ²Σ_u⁺ given in Refs. [264, 277] are consistent with our values.

Table 6.5: Equilibrium and ground state bond length and harmonic wave numbers of He₂⁺ X⁺ ²Σ_u⁺.

		B_e / cm^{-1}	$r_e / \text{Å}$	$r_0 / \text{Å}$	$\omega_e / \text{cm}^{-1}$	$\omega_e x_e / \text{cm}^{-1}$
⁴ He ₂ ⁺	Set 1 (fit incl. H_v^+)	7.215 48(85)	1.080 61(6)	1.089 24(4)	1698.780(114)	35.182(43)
	Set 2 (fit excl. H_v^+)	7.209 97(46)	1.081 02(3)	1.089 52(2)	1698.578(106)	35.131(40)
	Ref. [258]	7.211	1.0806	1.0894	1698.6	35.25
³ He ⁴ He ⁺	this work	8.3931(33)	1.080 80(22)	1.090 04(14)	1832.273(115) ^a	40.879(47) ^a
	Ref. [236]	8.3906(40)	1.080 96(26)		1832.7598(50)	41.1 ^b
³ He ₂ ⁺	this work			1.091 39(53)	1956.854(122) ^a	46.627(53) ^a
Theory	Ref. [254]		1.0811(3)			
	Refs. [253, 272]		1.0815(5)			

^aValue derived from the corresponding value of ⁴He₂ (Set 2).

^bValue derived from the corresponding value of ⁴He₂ of Ref. [258].

Experimental harmonic wave numbers and anharmonicity constants for ⁴He₂⁺ were determined using the relations $\omega_e = 3[G(1) - G(0)] - [G(2) - G(0)]$ and $\omega_e x_e = [G(1) - G(0)] - [G(2) - G(0)]/2$. The corresponding values for ³He⁴He⁺ and ³He₂⁺ were derived according to Eq. (6.7) and are also given in Table 6.5. The calculated values for $T_1^+ - T_0^+ = 1750.614(158) \text{ cm}^{-1}$ (using the parameters of Set 1) and $1750.514(148) \text{ cm}^{-1}$ (Set 2) for ³He⁴He⁺ agree well with the experimental value $(1750.5569(44) \text{ cm}^{-1})$ in Table 6.3.

Assuming that the zero-point energies of the ³He₂ isotopomer can be derived with the same accuracy as is the case for the ³He⁴He isotopomer, one can combine these values with the ionization energy of the ³He₂ a ³Σ_u⁺ state to obtain the energy difference ΔE_{BO}

between the minima of the potential energy curves of the $X^+ \ ^2\Sigma_u^+$ and a $^3\Sigma_u^+$ states of He_2 :

$$\begin{aligned}\Delta E_{\text{BO}}/hc &= E_1(^3\text{He}_2 \text{ a } ^3\Sigma_u^+)/hc + G(0, ^3\text{He}_2 \text{ a } ^3\Sigma_u^+) - G(0, ^3\text{He}_2^+ X^+ \ ^2\Sigma_u^+) \\ &= 34\,354.64(12) \text{ cm}^{-1}.\end{aligned}$$

The comparison with the corresponding value for $^4\text{He}_2$ ($34\,356.31(8) \text{ cm}^{-1}$ for Set 1 and $34\,356.50(7) \text{ cm}^{-1}$ for Set 2) leads to the conclusion that this difference is reduced by $1.77(22) \text{ cm}^{-1}$ (errors from the calibration of the different spectra neglected here). This small deviation stems primarily from the difference in the ionization energies of the 2^3S_1 state of atomic helium [$(E_1(^4\text{He}) - E_1(^3\text{He}))/hc = 1.7978 \text{ cm}^{-1}$ [282]], the contribution from the dissociation energies being very small for the homonuclear isotopomers. Calculations of Born-Oppenheimer correction terms showed that the dissociation energy $D_e(X^+ \ ^2\Sigma_u^+)$ for $^3\text{He}_2^+$ is larger by 0.08 cm^{-1} than that of $^4\text{He}_2^+$ [254]; no literature values are available for the a $^3\Sigma_u^+$ state, but it can be assumed that the difference is similar to that of the $X^+ \ ^2\Sigma_u^+$ state.

Table 6.6 summarizes the potential parameters for $^4\text{He}_2$ and $^4\text{He}_2^+$ derived by combining the present results and with literature values. The equilibrium term energies of He_2 are given relative to the energy of two ground state He atoms. The value of T_e for the a $^3\Sigma_u^+$ state, which has a barrier towards dissociation, is derived from the adiabatic ionization energy E_i of the a $^3\Sigma_u^+$ state and the dissociation energy D_e of $\text{He}_2^+ X^+ \ ^2\Sigma_u^+$ calculated in Ref. [254]. The strength of the chemical bond can be expressed by the force constant, which is derived from the harmonic wave number according to the relation $k = (2\pi c \omega_e)^2 \mu$ [3]. The values for $\text{He}_2 \text{ a } ^3\Sigma_u^+$ and $\text{He}_2^+ X^+ \ ^2\Sigma_u^+$ are 386 N m^{-1} and 340 N m^{-1} , respectively, showing that the removal of the 2s Rydberg electron does not substantially weaken the bond, as expected. The force constant of the ground state of He_2^+ is significantly larger than those of the heavier rare gas dimer cations (Ne_2^+ 202 N m^{-1} [252], Ar_2^+ 111.1 N m^{-1} [246], Kr_2^+ 86.7 N m^{-1} [244], Xe_2^+ 58.6 N m^{-1} [248], a tendency which is also reflected by the respective dissociation energies) and that of H_2^+ (160.0 N m^{-1} [298]), and slightly larger than that of the single-bonded ground state molecule Cl_2 (323 N m^{-1} [298]).

Hardy and coworkers claimed to have observed even and odd rotational levels of $^4\text{He}_2^+$ in a dissociative recombination reaction experiment [299]. In a reply to a critical comment by van der Zande and Ubachs [287], Hardy and Wang explained the existence of even rotational states by the presence of high Rydberg states which allow even angular momentum states [300]. This argument, however, is not confirmed by our experiments, which also include high Rydberg states, and is invalid as the following symmetry consideration demonstrates. High- n Rydberg states are best described in a Hund's case (d) basis, where the orbital angular momentum of the Rydberg electron is decoupled from the ionic

Table 6.6: Molecular potential parameters for ⁴He₂ and ⁴He₂⁺ and term values of the associated states of atomic ⁴He.

	He (1s) ² 1 ¹ S ₀	He (1s)(2s) 2 ³ S ₁	He ⁺ (1s) 2 ² S _{1/2}
T / cm^{-1}	0.0	159 855.9726(15) ^a	198 310.6672(15) ^a
	He ₂ (1σ _g) ² (1σ _u) ² X 1Σ _g ⁺	He ₂ [X ⁺ 2Σ _u ⁺] _{2sσ_g} a 3Σ _u ⁺	He ₂ ⁺ (1σ _g) ² (1σ _u) X ⁺ 2Σ _u ⁺
T_e / cm^{-1} ^b	-7.650(3) ^c	144 008 ^d	178 364.85 ^e
$r_e / \text{Å}$	2.968(6) ^c	1.045 415 8(45) ^f	1.0808(2)
$G(v=0) / \text{cm}^{-1}$		894.771(46) ^f	840.595(58)
D_e / cm^{-1}	7.650(3) ^c	15 848 ^d [15 808 ^g]	19 945.82 ^e
D_0 / cm^{-1} ^h	0.001 20(3) ^c	14 953 ^d	19 105 ^e
$E_1/hc / \text{cm}^{-1}$ ^h		34 302.1(2)	

^aFrom Ref. [281].^bRelative to the level of two separate He (1s)² 1¹S₀ atoms.^cFrom Ref. [231].^dBased on the value of $D_e(X^+ 2\Sigma_u^+)$ of Ref. [254] and the present value of the adiabatic ionization energy E_i .^eBased on the value of $D_e(X^+ 2\Sigma_u^+)$ of Ref. [254].^fFrom Ref. [268].^gFrom Ref. [301]. The potential curve has a barrier of 505 cm⁻¹ at $r = 2.71$ Å [302].^hThe adiabatic ionization and dissociation energies E_1 and D_0 refer to the (hypothetical) $v = 0, N = 0$ levels of a 3Σ_u⁺ and X⁺ 2Σ_u⁺.

core. The only relevant symmetry to classify the Rydberg electron wavefunction remains the parity; the symmetry of the Rydberg electron wavefunction Γ_{Ryd} with orbital angular momentum ℓ is therefore +s for even ℓ and -s for odd ℓ . Eq. (6.2) still has to hold for the Rydberg molecule: $\Gamma_{\text{Ryd}} \otimes (\Gamma_{\text{rve}}^+ \otimes \Gamma_{\text{nspin}}) \supset \Gamma_{\text{int}}$. Therefore, the presence of the Rydberg electron does not alter the nuclear spin statistical weights of the rotational levels of the ionic core. We therefore agree with the conclusion of Ref. [287] that the experiments on He₂⁺ by Hardy and coworkers have to be reinterpreted without invoking the existence of quantum states of even rotational angular momentum N^+ .

6.4.2 The field ionization and rotational autoionization dynamics of Rydberg states of He₂

The studies by PFI-ZEKE photoelectron spectroscopy and threshold ionization of high Rydberg states of ⁴He₂ have provided information on rotational channel interactions and on how these interactions are modified by electric fields.

Because of these channel interactions, the intensities of several lines are strongly perturbed and additional lines appear in the PFI-ZEKE photoelectron spectra under specific experimental conditions. O-type transitions in the PFI-ZEKE photoelectron spectra can borrow intensity from strong Q-type transitions to Rydberg states converging to higher-lying rotational levels of ⁴He₂⁺, examples being the $(v^+ = 0, N^+ = 1) \leftarrow (v'' = 0, N'' = 3)$ transition of ⁴He₂ (see Figs. 6.4 and 6.13) and the $(v^+ = 0, N^+ = 0) \leftarrow (v'' = 0, N'' = 2)$

transition of ${}^3\text{He}_2$ (see Fig. 6.6). Such intensity perturbations are well documented in the literature on other molecular systems [68–70].

The effect of electric fields on the channel interactions are less well understood though attempts have been made at understanding how they influence the intensity distributions in the PFI-ZEKE photoelectron spectra of diatomic molecules [303].

The subtle role played by electric fields in the threshold ionization dynamics of ${}^4\text{He}_2$ a ${}^3\Sigma_u^+$ has been revealed by the spectra displayed in Figs. 6.11–6.13. In particular, series of long-lived Rydberg states converging to the $N^+ = 3$ and $N^+ = 5$ threshold were observed between the normal lines of the PFI-ZEKE photoelectron spectrum which disappeared in the presence of weak discrimination dc-electric fields, and to a lesser extent also when weak pulsed discrimination electric fields were applied (see Figs. 6.12 and 6.13).

In this section RSR-TI spectra recorded using pulsed fields of 1.33 V cm^{-1} , 6.67 V cm^{-1} , 13.3 V cm^{-1} , 26.7 V cm^{-1} , and 66 V cm^{-1} are used in combination with MQDT calculations to provide a more quantitative understanding of the observations made in Subsection 6.3.5. To facilitate the discussion, these spectra are presented in different partially overlapping regions, the first between $34\,210 \text{ cm}^{-1}$ and $34\,310 \text{ cm}^{-1}$ in the vicinity of the Q(1), Q(3), Q(5), and Q(7) field-free thresholds (Fig. 6.14); the second between $34\,160 \text{ cm}^{-1}$ and $34\,260 \text{ cm}^{-1}$ in the vicinity of the O(3) field-free threshold (Fig. 6.15); the third between $34\,100 \text{ cm}^{-1}$ and $34\,200 \text{ cm}^{-1}$ in the vicinity of the O(5) field-free threshold (Fig. 6.16); and the fourth between $34\,020 \text{ cm}^{-1}$ and $34\,120 \text{ cm}^{-1}$ in the vicinity of the O(7) and M(5), i.e., $N^+ = 1 \leftarrow N'' = 5$ thresholds (Fig. 6.17).

The energy level diagram presented in Fig. 6.18, which is an extended version of Fig. 6.7 illustrates the np photoionization channels that are accessible from the $N'' = 1, 3$ and 5 rotational levels of the a ${}^3\Sigma_1^+$ ($v'' = 0$) metastable state of He_2 . The diagram is useful as a guide to rationalize the experimental observations. To simplify the notation, the different series will be labeled npN_N^+ . As explained in Subsection 6.3.4, the $npN_{N=N^+}^+$ series has pure ${}^3\Pi_g^-$ character, and the $npN_{N=N^+\pm 1}^+$ series have mixed ${}^3\Sigma_g^+$ and ${}^3\Pi_g^+$ character. The diagram depicts the three np Rydberg series with $N = N^+, N^+ \pm 1$ converging on each of the lowest three rotational levels of the He_2^+ ion ($N^+ = 1, 3$ and 5). The colored frames indicate the energetic regions below each threshold where field ionization can take place, the color code being blue for the $N^+ = 1$ channels, red for the $N^+ = 3$ channels and green for the $N^+ = 5$ channels.

Because of the $N^+ - N'' = 0$ propensity rule for absorption discussed in Subsection 6.3.4, the only strong transitions are those marked with full blue ($N^+ = 1 \leftarrow N'' = 1$), red ($N^+ = 3 \leftarrow N'' = 3$) and green ($N^+ = 5 \leftarrow N'' = 5$) arrows. Assuming that spins can be neglected, conservation of angular momentum implies that only channels of the same total angular momentum (without spins) quantum number N can interact. Consequently, the $np3_2$ Rydberg states located above the $N^+ = 1$ threshold and the $np5_4$ Rydberg states

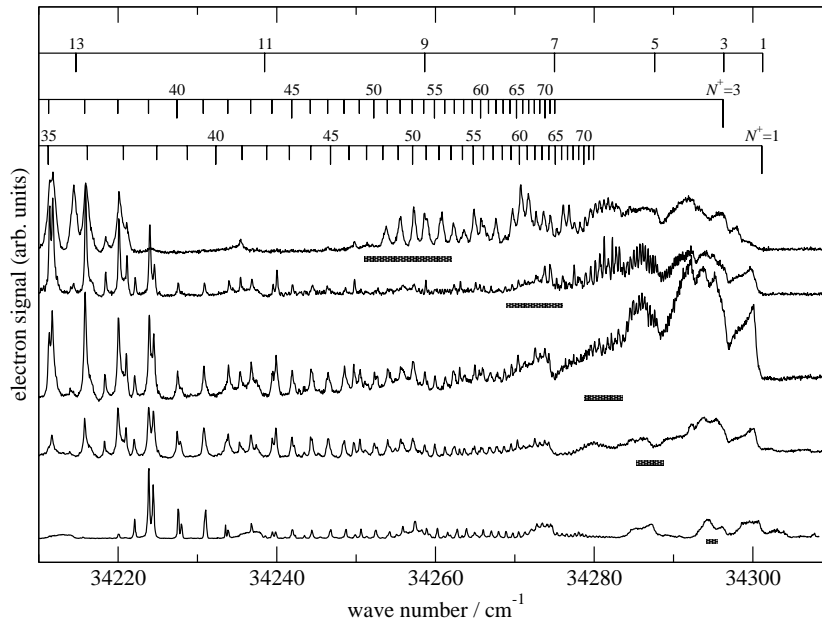


Figure 6.14: RSR-TI spectra of ${}^4\text{He}_2$ a ${}^3\Sigma_u^+$ recorded with pulsed fields of 1.33 V/cm (bottom), 6.67 V/cm, 13.3 V/cm, 26.7 V/cm, and 66.7 V/cm (top) in the vicinity of the Q(1), Q(3), Q(5) and Q(7) thresholds. The assignment bar at the top indicates the $N^+ = N'' \leftarrow N''$ ionization thresholds. The assignment bars below indicate the positions and the n quantum number of the $np(N'')_{N''} \leftarrow N''$ transitions for $N'' = 3$ and $N'' = 1$ (bottom). The broad, dark grey lines indicate the range between the $6.1 \text{ cm}^{-1} \sqrt{\mathcal{E}/(\text{V cm}^{-1})}$ and $4.8 \text{ cm}^{-1} \sqrt{\mathcal{E}/(\text{V cm}^{-1})}$ limits of the field-lowered $1 \leftarrow 1$ ionization thresholds.

located above the $N^+ = 3$ threshold undergo rapid rotational autoionization into the $N^+ = 1$ and $N^+ = 3$ p continua, respectively. The $np_{3,4}$ and $np_{5,6}$ series, on the other hand, are not subject to rapid rotational autoionization and may either decay by predissociation before the field-ionization pulse is applied or be ionized by the pulsed field. In the latter case two possible situations may be distinguished: 1) The pulsed field only ionizes the Rydberg states located within $4.8 \sqrt{\mathcal{E}/(\text{V cm}^{-1})} \text{ cm}^{-1}$ of their ionization limit (N^+), or 2) The pulsed field also induces autoionization into continua associated with the $N^+ - 2$, or even $N^+ - 4$ and $N^+ - 6$, etc. ionic states.

In the former situation (1), one expects to observe the following Rydberg series and adjacent continua in the photoionization spectrum:

1. the $np_{1,0-2}$ and the $np_{3,2}$ series from the field-lowered $N^+ = 1$ threshold up to and beyond the field-free $N^+ = 1$ threshold,
2. the $np_{3,4}$ and the $np_{5,4}$ series from the field-lowered $N^+ = 3$ threshold up to and beyond the field-free $N^+ = 3$ and 5 thresholds,
3. the $np_{5,6}$ and the $np_{7,6}$ series from the field-lowered $N^+ = 5$ threshold up to and beyond the field-free $N^+ = 5$ and 7 thresholds, etc.

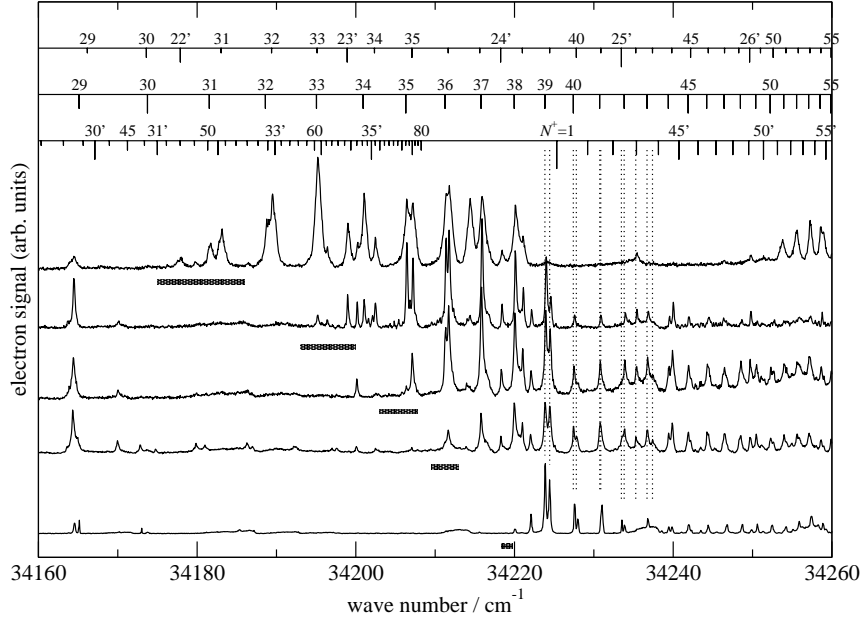


Figure 6.15: RSR-TI spectra of ${}^4\text{He}_2$ a ${}^3\Sigma_u^+$ recorded with pulsed fields of 1.33 V/cm (bottom), 6.67 V/cm, 13.3 V/cm, 26.7 V/cm, and 66.7 V/cm (top) in the vicinity of the O(3) thresholds. The assignment bars indicate the positions of the transitions starting from $N'' = 3$ and the n quantum number of the corresponding npN_N^+ Rydberg levels. The top bar shows the $np3_4$ and $np5_4$ (with primed numbers) series, the middle bar the $np3_3$ series, and the bottom bar the $np1_2$ and $np3_2$ (with primed numbers) series. The broad, dark grey lines indicate the range between the $6.1 \text{ cm}^{-1} \sqrt{\mathcal{E}/(\text{V cm}^{-1})}$ and $4.8 \text{ cm}^{-1} \sqrt{\mathcal{E}/(\text{V cm}^{-1})}$ limits of the field-lowered ionization thresholds.

This multitude of series and adjacent continua contributing to the photoionization spectrum explains its congested nature. The Rydberg series contributing to the PFI-ZEKE and RSR-TI spectra in this situation are:

1. the $np1_{0-2}$ and the $np3_2$ series only in the field ionization region below the $N^+ = 1$ threshold (i.e., located in the blue frame in Fig. 6.18),
2. the $np3_{2-4}$ and the $np5_4$ series only in the field ionization region below the $N^+ = 3$ threshold (i.e., located in the red frame in Fig. 6.18),
3. the $np5_{4-6}$ and the $np7_6$ series only in the field ionization region below the $N^+ = 5$ threshold (i.e., located in the green frame in Fig. 6.18), etc.

This explains why the PFI-ZEKE and RSR-TI spectra are much less dense spectrally than the photoionization spectrum. In the second situation (2), more series can be observed both in the photoionization and the PFI-ZEKE photoelectron spectra, in addition to the series listed above, in particular

4. the $np3_{3,4}$ series from the field-lowered $N^+ = 1$ threshold up to the field-free $N^+ = 3$ threshold,

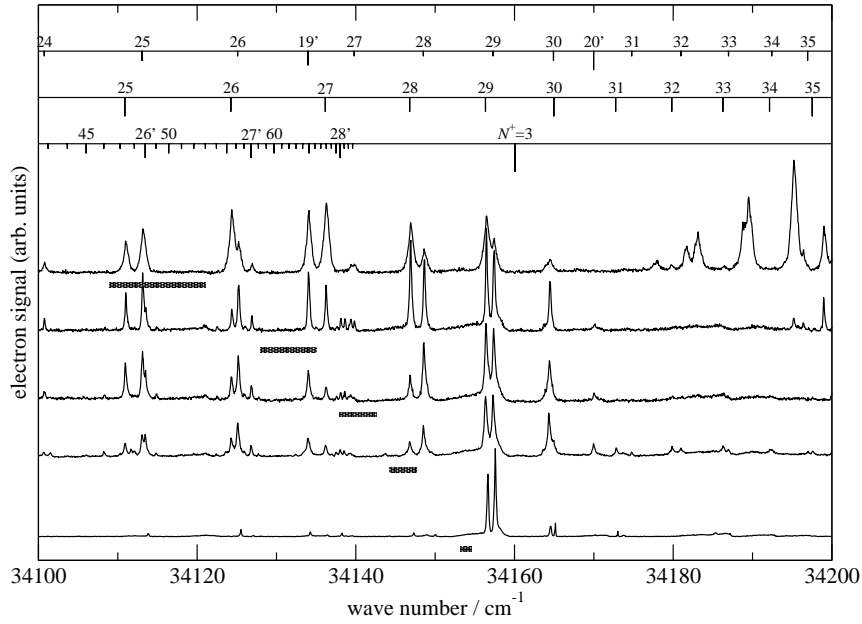


Figure 6.16: RSR-TI spectra of ${}^4\text{He}_2$ $a\ 3\Sigma_u^+$ recorded with pulsed fields of 1.33 V/cm (bottom), 6.67 V/cm, 13.3 V/cm, 26.7 V/cm, and 66.7 V/cm (top) in the vicinity of the $O(5)$ thresholds. The assignment bars indicate the positions of the transitions starting from $N'' = 5$ and the n quantum number of the corresponding npN_N^+ Rydberg levels. The top bar shows the $np5_6$ and $np7_6$ (with primed numbers) series, the middle bar the $np5_5$ series, and the bottom bar the $np3_4$ and $np5_4$ (with primed numbers) series. The broad, dark grey lines indicate the range between the $6.1\text{ cm}^{-1}\sqrt{\mathcal{E}}/(\text{V cm}^{-1})$ and $4.8\text{ cm}^{-1}\sqrt{\mathcal{E}}/(\text{V cm}^{-1})$ limits of the field-lowered ionization thresholds.

5. the $np5_{5,6}$ series from the field-lowered $N^+ = 3$ threshold up to the field-free $N^+ = 5$ threshold, etc.

This second situation can lead to the observation, in the PFI-ZEKE photoelectron spectra, of the $np3_{3,4}$ Rydberg states in the region between the $N^+ = 1$ threshold and the field-lowered $N^+ = 3$ threshold, of the $np5_{4,5}$ Rydberg states between the $N^+ = 3$ threshold and the field-lowered $N^+ = 5$ threshold, etc.

To assign the RSR-TI spectra presented in Figs. 6.14 - 6.17, the positions of all npN_{N^+} Rydberg states were calculated using MQDT as in the analysis of the photoionization spectrum in Subsection 6.3.4, i.e., using only one channel for odd- N and two channels for even- N values. For each $N'' \geq 3$ level of the $a\ 3\Sigma_u^+$ state, five Rydberg series [$np(N'' - 2)_{N''-1}$, $np(N'')_{N''-1}$, $np(N'')_{N''}$, $np(N'')_{N''+1}$, and $np(N'' + 2)_{N''+1}$] are accessible, of which only the series with $N^+ = N''$ are expected to be strong (see full lines Fig. 6.18). Because of the mixing between the two series with the same (even) N -value, it is not always clear which series ($N^+ = N + 1$ or $N^+ = N - 1$) a given Rydberg states belongs to; the assignment was made on the basis of the dominant mixing coefficient from the MQDT calculations. According to the simple MQDT model used in Subsection 6.3.4 and which corresponds to situation (1) above, npN_N^+ Rydberg states with $N = N''$ or $N'' + 1$

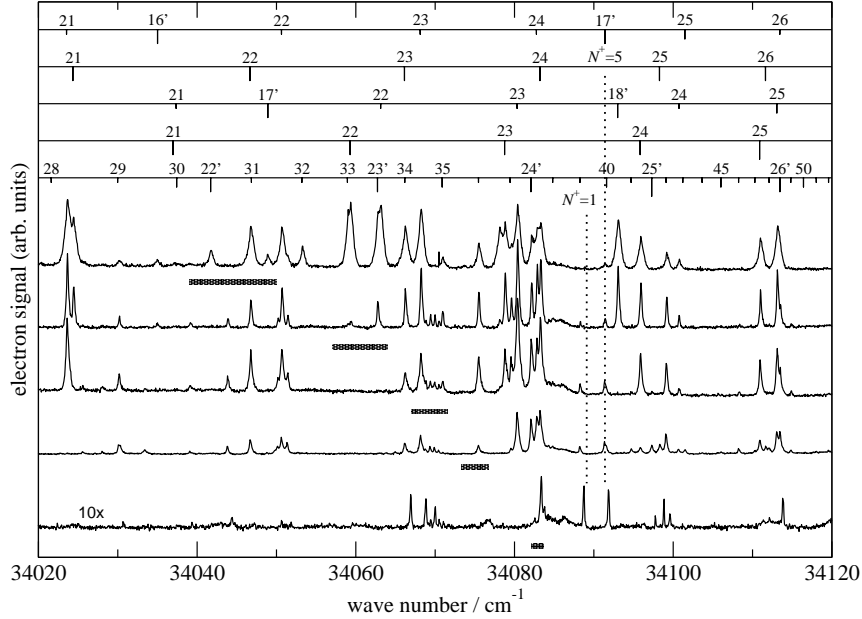


Figure 6.17: RSR-TI spectra of ${}^4\text{He}_2$ a ${}^3\Sigma_u^+$ recorded with pulsed fields of 1.33 V/cm (bottom), 6.67 V/cm, 13.3 V/cm, 26.7 V/cm, and 66.7 V/cm (top) in the vicinity of the O(7) and M(5) thresholds. The assignment bars indicate the positions and the n quantum number of the $npN_N^+ \leftarrow N''$ transitions. They refer to the following series (from bottom to top): (1) $np3_4/np5_4 \leftarrow 5$, (2) $np5_5 \leftarrow 5$, (3) $np5_6/np7_6 \leftarrow 5$, (4) $np7_7 \leftarrow 7$, and (5) $np7_8/np9_8 \leftarrow 7$. The broad, dark grey lines indicate the range between the $6.1\text{ cm}^{-1}\sqrt{\mathcal{E}/(\text{V cm}^{-1})}$ and $4.8\text{ cm}^{-1}\sqrt{\mathcal{E}/(\text{V cm}^{-1})}$ limits of the field-lowered $N^+ = 1 \leftarrow N'' = 5$ ionization thresholds. The positions of the $1 \leftarrow 5$ and $5 \leftarrow 7$ thresholds are indicated with dotted vertical lines.

should only be observable in the energetic or “detection” window between the zero-field and the field-lowered ionization threshold $N^+ = N''$, and $npN_{N''-1}^+$ Rydberg states in the corresponding detection window at $N^+ = N'' - 2$. If the applied pulsed field is small, the detection windows are small, and the typical PFI-ZEKE photoelectron spectrum results.

The experimental RSR-TI spectra in Figs. 6.14 - 6.17 are different from these expectations. The regions of the $N^+ = N''$ “Q-type” thresholds displayed in Fig. 6.14 is spectrally very dense and the overlapping Rydberg series hardly resolved. Only the $np1_N$ ($N = 1, 2$) series could be unambiguously identified in the Q(1) detection window in spectra recorded with high fields (26.7 V cm^{-1} and 67 V cm^{-1} , top two traces) in Fig. 6.14. The $np(N^+ = N'')_N$ series for $N^+ \geq 3$ are surprisingly either much weaker or not observed at all.

Transitions from the $N'' = 3$ level of the a ${}^3\Sigma_u^+$ state are observed in the vicinity of the O(3) threshold (see Fig. 6.15). The $np3_{3,4}$ and $np5_4$ series are strong in the O(3) detection window below the $N^+ = 1$ threshold. Above this threshold, these series become weaker with increasing value of the pulsed field except the $np5_4$ series which is still visible in the spectra recorded with a 67 V cm^{-1} pulse. This behavior corresponds to situation (2) described above, and it appears that the pulsed field can even induce the rotational

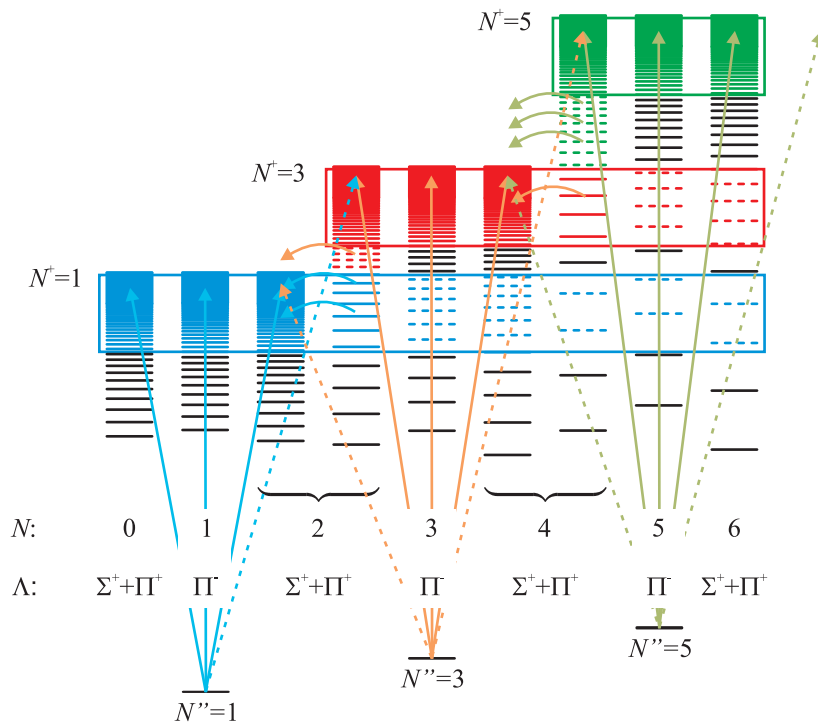


Figure 6.18: Schematic representation of the ionization channels in the photoionization of He₂* and of the rotational channel interactions expected to be dominant in the absence of electric fields.

autoionization of the $np5_4$ series into the $N^+ = 1$ continuum. The gradual decrease of the intensity of the $np3_{3,4}$ series with increasing pulsed field is attributed to an increasing stray field originating from an incomplete return to 0 V of the pulsed voltage applied to the extraction plates. This observation is consistent with that made in Subsection 6.3.5 in the description of Fig. 6.11 and 6.12 and represents another indication of field-induced rotational autoionization of the $np3_{3,4}$ series.

Strong transitions from the $N'' = 5$ level of the a $^3\Sigma_u^+$ state of $^4\text{He}_2$ to the $np5_{5,6}$ and $np7_6$ are observed from the $N^+ = 3$ threshold all the way down to the low-wave-number edge of the M(5) threshold ($N^+ = 1$) as can be seen in Figs. 6.16 and 6.17. Above the $N^+ = 3$ threshold, these series are very weak and only appear in spectra recorded with low fields (and thus low stray fields). Transitions from the $N'' = 5$ level to $np3_4$ Rydberg states are also observed in the M(5) detection window, and between the M(5) and O(3) thresholds as complex resonances [69] near the positions of the $np5_4$ states.

Similar observations are made for transitions from $N'' = 7$ and $N'' = 9$. In general $npN''_{N''}$, $npN''_{N''+1}$ and $np(N'' + 2)_{N''+1}$ levels are observed between the M(N'') and O(N''), and sometimes even below the M(N'') detection windows, which demonstrates the existence of field-induced rotational autoionization processes involving the loss of up to 6 units of rotational angular momentum induced by electric fields. The $npN''_{N''-1}$ and $np(N'' - 2)_{N''-1}$ series also contribute to the spectra below the M(N'') and O(N'')

thresholds.

Transitions from $N'' \geq 11$ levels are also observable but the initial state populations and the transition densities near the $O(N'')$ and $M(N'')$ thresholds are too low to establish specific trends.

6.5 Conclusions

A supersonic nozzle with internal discharge has been constructed and has proven to be an excellent source of metastable atoms and molecules to be studied by PFI-ZEKE photoelectron and photoionization spectroscopy. It was possible to obtain spectroscopic information about the three lowest vibrational states of ${}^4\text{He}_2^+$ and the lowest one of ${}^3\text{He}_2^+$. This study represents the first spectroscopic investigation of the metastable ${}^3\text{He}_2$ molecule and its cation. From the analysis of the rotationally resolved spectra, the equilibrium structure of He_2^+ was determined and the photoionization dynamics of the He_2 a ${}^3\Sigma_u^+$ state characterized. The adiabatic ionization energy was obtained by two different methods: directly from the analysis of the PFI-ZEKE spectra and by a MQDT analysis of high Rydberg states observed in the photoionization spectrum. The newly obtained data on the low rovibrational levels of He_2^+ , together with the data of the levels near the dissociation limit [253], can serve as a reference for high-level ab initio calculations.

The study of the threshold ionization spectra of ${}^4\text{He}_2$ presented in this chapter has not only led to the determination of the energy level structure of the ${}^4\text{He}_2^+$ and ${}^3\text{He}_2^+$ cations at low energies but also to the characterization of the rotational autoionization dynamics of the triplet np Rydberg states of ${}^4\text{He}_2$. Whereas interactions between channels differing by two units in the rotational quantum number of the ion are dominant in the absence of electric fields, stray electric fields and pulsed electric fields lead to the observation of field-induced rotational autoionization processes inducing changes of the ion rotational quantum number of up to six units. The ability to resolve the fine structure of the autoionizing levels and the use of RSR-TI spectroscopy and of MQDT to assign the complex spectra were essential elements that led to an improved understanding of rotational channel interactions in molecular photoionization.

Chapter 7

Conclusions

Rather than restating the conclusions summarized at the end of each chapter, this last chapter concludes this dissertation with a few general comments on metastability in the context of the atomic and molecular systems investigated.

The investigation of metastable states of atoms and molecules by high-resolution spectroscopy offers many opportunities. Firstly, the long observation times that are made possible by the long lifetimes of these states enables one to fully exploit the resolving power of modern radiation sources and spectroscopic and to observe the finest details of the energy level structure of atoms and molecules. Secondly, metastable states of atoms and molecules have electronic and nuclear configurations that are very different from those of the stable ground state. Metastable states therefore give access to manifolds of states that are normally not observable from the ground state. Thirdly, the metastability and its physical or chemical origins are in themselves of fundamental interest: Metastability is closely linked to symmetry selection rules and often originates from unusual, and thus interesting electronic and nuclear configurations.

The metastable states investigated in this dissertation can be grouped into three main classes: 1) States of atoms and molecules that do not decay radiatively on the microsecond timescale although they are located energetically above the ground state. Such states were observed and studied in CO, Xe, He and He₂. 2) States that do not decay by (pre)dissociation on the microsecond timescale although they are located energetically above one or more dissociation limits. Such states were observed and studied in He₂, ND₄ and ammoniated ammonium radical and ionic clusters. 3) States that do not decay by (auto)ionization on the microsecond timescale although they are located energetically above the first adiabatic ionization threshold. Such states were observed and studied in He₂.

Whereas many examples of the first class of metastability described above have been documented in the literature, particularly for atoms for which metastability is common, fewer examples of the second class have been characterized or discussed in detail. Pre-

dissociation is usually easily observable only if it is rapid, in which case line broadening is measurable and the fragments can be detected before they have moved out of the measurement region. When predissociation is not observable one usually concludes that the states are stable, which is entirely justified for all practical purposes. It is only in cases such as the ammonium radical and the ammoniated ammonium clusters discussed in Chapter 4 where the lowest observable state associated with a certain molecular configuration corresponds to a local minimum on the potential energy surface separated from the dissociation products by a barrier, that metastability becomes "observable". Strangely enough, it is the observed decay of the molecule on a very long timescale, or the observed more rapid decay of an isotopomer of the same molecule, that make one appreciate the metastability of the molecule as a meaningful concept.

The third class of metastability is by far the least common: photoionization is governed by much less restrictive selection rules than optical transitions between bound states because the photoelectron can depart as a superposition of many partial waves. If one excepts Rydberg states of very high principal quantum number ($n \gg 100$) and/or of $\ell > 3$ orbital angular momentum, for which metastability inevitably result from the fact that the Rydberg electron is completely decoupled from the ion core, only few cases of metastable states of molecules embedded in the ionization continua have been documented [1], a notable exception being H_2 [66, 304, 305]. The study of Rydberg states of He_2 presented in Chapter 6 represents a second example. From the analysis of the origin of this form of metastability by MQDT, we believe that it should also be observable in other molecular systems. For this form of metastability to be observed it is necessary that the states located energetically above the first adiabatic ionization energy are also immune to predissociation and/or internal conversion, which rules out larger molecular systems as potential molecular systems. Diatomic molecules such as N_2 , the alkali-metal dimers, BH , HeH , NeH , and triatomic molecules such as H_3 , NH_2 , and HCN may be promising examples.

Metastability with respect to ionization is more than just a curious phenomenon: The radiative and dissociative recombination of an electron and an atomic or a molecular cation can be strongly affected by very narrow (i.e., long-lived) resonances in the ionization continuum [306, 307]. The lifetimes of these resonances must be sufficiently long so as to allow the radiative stabilization of the electron-ion collision complex. The observation of metastability with respect to ionization in He_2 made in this dissertation will certainly need to be considered in the modelization of plasmas containing helium, including astrophysical plasmas.

Appendix A

Physical constants

Table A.1: Physical constants from Ref. [308].

Constant	Symbol	Value
speed of light in vacuum	c	299 792 458 m s ⁻¹ (defined)
electric constant	ϵ_0	8.854 187 817 · 10 ⁻¹² A s V ⁻¹ m ⁻¹
Planck constant	h	6.626 068 96(33) · 10 ⁻³⁴ J s
Planck constant divided by 2 π	\hbar	1.054 571 628(53) · 10 ⁻³⁴ J s
elementary charge	e	1.602 176 487(40) · 10 ⁻¹⁹ C
Rydberg constant	R_∞	10 973 731.568 527(73) m ⁻¹
Bohr radius	a_0	0.529 177 210 859(36) · 10 ⁻¹⁰ m
Hartree energy	E_h	4.359 743 94(22) · 10 ⁻¹⁸ J
electron mass	m_e	9.109 382 15(45) · 10 ⁻³¹ kg
proton mass	m_p	1.672 621 637(83) · 10 ⁻²⁷ kg
neutron mass	m_n	1.674 927 211(84) · 10 ⁻²⁷ kg
atomic mass constant	u	1.660 538 782(83) · 10 ⁻²⁷ kg
Avogadro constant	N_A	6.022 141 79(30) · 10 ²³ mol ⁻¹
molar gas constant	R	8.314 472(15) J mol ⁻¹ K ⁻¹
Boltzmann constant	k	1.380 650 4(24) · 10 ⁻²³ J K ⁻¹

Table A.2: Energy conversion factors from Ref. [308]. The last digit is given, but may be not be significant.

1 J	$\hat{=}$ 5.034 117 · 10 ²² cm ⁻¹
1 K	$\hat{=}$ 0.695 035 6 cm ⁻¹
1 eV	$\hat{=}$ 8 065.545 cm ⁻¹
1 E_h	$\hat{=}$ 219 474.6 cm ⁻¹

Appendix B

Spectral positions of the observed Rydberg levels of He₂

Table B.1: Experimental positions of $[X^+ \ ^2\Sigma_u^+] n p \lambda \ (^3\Pi_g, \ ^3\Sigma_g^+) N, v$ Rydberg levels of ⁴He₂ (relative to the position of the (hypothetical) $N = 0, v = 0$ level of a ³ Σ_u^+) and differences between observed and calculated values. # designates the number of the level within the N block of the calculation. Rydberg levels with $n \leq 17$ are taken from Ginter *et al.*, J. Chem. Phys. **81** 6013 (1984), Ginter and Ginter, J. Mol. Spectrosc. **82** 152 (1980), Orth and Ginter, J. Mol. Spectrosc. **61** 282 (1976), **64** 223 (1977).

#	Π^\pm		Σ^+		E_{obs}/hc / cm ⁻¹	$(E_{\text{obs}} - E_{\text{calc}})/hc$ / cm ⁻¹
	n	n	N	v		
1	2		1	0	4782.70	0.261
2	3		1	0	21 521.60	-0.377
3	4		1	0	27 207.12	-0.621
4	5		1	0	29 799.60	-0.268
5	6		1	0	31 194.27	-0.703
6	7		1	0	32 030.76	-0.166
7	8		1	0	32 570.92	-0.118
8	9		1	0	32 940.19	0.123
9	10		1	0	33 203.32	0.000
10	11		1	0	33 397.76	0.085
11	12		1	0	33 545.29	0.056
12	13		1	0	33 659.98	0.082
13	14		1	0	33 750.93	0.166
14	15		1	0	33 823.97	-0.020
15	16		1	0	33 883.94	0.078

Continued on next page

#	Π^\pm		Σ^+		E_{obs}/hc / cm^{-1}	$(E_{\text{obs}} - E_{\text{calc}})/hc$ / cm^{-1}
	n	n	N	v		
16	17		1	0	33 933.31	-0.132
17	18		1	0	33 975.10	0.141
1	2		2	0	4811.97	0.367
2		3	2	0	10 930.59	0.304
3	3		2	0	21 549.84	-0.317
4		4	2	0	23 639.56	0.216
5	4		2	0	27 234.64	-0.606
6		5	2	0	28 170.89	-3.603
7	5		2	0	29 826.56	0.039
8		6	2	0	30 327.35	-2.930
9	6		2	0	31 219.72	-0.774
10		7	2	0	31 523.92	-2.510
11	7		2	0	32 054.91	-0.114
12		8	2	0	32 258.30	-1.490
13	8		2	0	32 593.24	-0.244
14		9	2	0	32 741.13	-1.128
15	9		2	0	32 960.95	0.200
16		10	2	0	33 075.97	-0.812
17	10		2	0	33 222.43	0.141
18		11	2	0	33 317.96	-0.312
19	11		2	0	33 415.35	0.194
20		12	2	0	33 498.08	-0.051
21	12		2	0	33 561.68	0.029
22		13	2	0	33 635.16	-0.083
23	13		2	0	33 676.06	0.085
24		14	2	0	33 741.24	0.042
25	14		2	0	33 768.00	0.174
26		15	2	0	33 823.34	0.199
28		16	2	0	33 887.05	0.158
35	19		2	0	34 041.56	0.040
41			2	0	34 116.84	0.069
1	2		3	0	4856.02	0.220
2	3		3	0	21 593.26	-0.322
3	4		3	0	27 278.36	-0.583

Continued on next page

#	Π [±]		Σ ⁺		E_{obs}/hc / cm ⁻¹	$(E_{\text{obs}} - E_{\text{calc}})/hc$ / cm ⁻¹
	n	n	N	v		
4	5		3	0	29 870.63	-0.299
5	6		3	0	31 265.12	-0.853
6	7		3	0	32 101.74	-0.155
7	8		3	0	32 641.86	-0.130
8	9		3	0	33 011.11	0.101
9	10		3	0	33 274.30	0.044
10	11		3	0	33 468.65	0.043
11	12		3	0	33 616.17	0.007
13	14		3	0	33 821.81	0.121
14	15		3	0	33 894.99	0.077
15	16		3	0	33 955.17	0.385
16	17		3	0	34 004.46	0.096
1	2		4	0	4914.16	0.385
2		3	4	0	11 026.32	0.351
3	3		4	0	21 649.04	-0.175
4		4	4	0	23 738.67	0.223
5	4		4	0	27 332.03	-0.524
6		5	4	0	28 271.47	-3.816
7	5		4	0	29 923.38	1.557
8		6	4	0	30 430.04	-2.932
9	6		4	0	31 312.68	-0.613
10		7	4	0	31 628.92	-2.556
11	7		4	0	32 144.95	-0.014
12		8	4	0	32 366.10	-1.390
13	8		4	0	32 680.39	-0.197
14		9	4	0	32 851.53	-0.946
15	9		4	0	33 045.46	-0.056
16		10	4	0	33 188.34	-0.425
17	10		4	0	33 305.82	0.126
18		11	4	0	33 430.55	0.177
19	11		4	0	33 498.69	-0.176
20		12	4	0	33 607.10	0.260
21	12		4	0	33 648.83	-0.205
22		13	4	0	33 735.14	0.123

Continued on next page

#	Π^\pm		Σ^+		E_{obs}/hc / cm^{-1}	$(E_{\text{obs}} - E_{\text{calc}})/hc$ / cm^{-1}
	n	n	N	v		
24		14	4	0	33 830.81	0.342
25	14		4	0	33 873.79	-0.029
26		15	4	0	33 906.39	0.252
28		16	4	0	33 971.79	0.299
31	17		4	0	34 052.66	0.042
35	19		4	0	34 134.76	-0.103
44			4	0	34 236.39	-0.015
49			4	0	34 269.04	0.168
1	2		5	0	4987.69	0.096
2	3		5	0	21 721.93	-0.286
3	4		5	0	27 406.29	-0.560
4	5		5	0	29 999.56	0.975
5	6		5	0	31 392.84	-0.680
6	7		5	0	32 229.27	-0.117
7	8		5	0	32 769.27	-0.181
8	9		5	0	33 138.56	0.109
9	10		5	0	33 401.71	0.024
10	11		5	0	33 596.11	0.081
11	12		5	0	33 743.40	-0.180
12	13		5	0	33 858.86	0.623
13	14		5	0	33 949.18	0.081
14	15		5	0	34 022.54	0.219
15	16		5	0	34 082.23	0.038
16	17		5	0	34 132.29	0.521
17	18		5	0	34 173.25	-0.035
1	2		6	0	5074.26	0.326
2		3	6	0	11 176.34	0.428
3	3		6	0	21 804.54	0.048
4		4	6	0	23 894.06	0.293
5	4		6	0	27 484.00	-1.112
6		5	6	0	28 429.47	-3.763
7	5		6	0	30 073.53	2.177
8		6	6	0	30 590.82	-2.954
9	6		6	0	31 458.61	-0.693

Continued on next page

#	Π^\pm		Σ^+		E_{obs}/hc / cm^{-1}	$(E_{\text{obs}} - E_{\text{calc}})/hc$ / cm^{-1}
	n	n	N	v		
10		7	6	0	31 793.15	-2.395
11	7		6	0	32 287.78	0.313
12		8	6	0	32 533.36	-1.292
13	8		6	0	32 820.15	-0.208
14		9	6	0	33 020.72	-0.836
15	9		6	0	33 183.70	-0.344
16		10	6	0	33 356.86	-0.159
17	10		6	0	33 445.72	0.080
18		11	6	0	33 591.45	0.031
19	11		6	0	33 646.00	-0.258
20		12	6	0	33 754.06	0.253
21	12		6	0	33 809.85	-0.140
22		13	6	0	33 873.22	0.211
23	13		6	0	33 938.75	0.099
24		14	6	0	33 969.27	-0.032
25	14		6	0	34 027.88	0.562
26		15	6	0	34 059.20	0.040
28		16	6	0	34 131.88	-0.140
33	18		6	0	34 242.54	0.019
34		19	6	0	34 264.58	0.063
35	19		6	0	34 276.10	0.016
37	20		6	0	34 307.46	-0.027
38			6	0	34 320.23	0.063
44			6	0	34 375.72	0.042
46			6	0	34 392.15	0.074
47			6	0	34 397.30	0.156
52			6	0	34 424.22	0.108
53			6	0	34 427.39	0.143
57			6	0	34 442.67	0.086
1	2		7	0	5177.30	-0.082
2	3		7	0	21 907.25	-0.193
3	4		7	0	27 590.42	-0.609
4	5		7	0	30 182.21	-0.191
5	6		7	0	31 576.47	-0.707

Continued on next page

#	Π^\pm		Σ^+		E_{obs}/hc / cm^{-1}	$(E_{\text{obs}} - E_{\text{calc}})/hc$ / cm^{-1}
	n	n	N	v		
6	7		7	0	32 412.85	-0.114
7	8		7	0	32 952.83	-0.154
8	9		7	0	33 322.03	0.073
9	10		7	0	33 585.25	0.074
10	11		7	0	33 779.49	-0.017
11	12		7	0	33 927.10	0.050
12	13		7	0	34 042.02	0.318
13	14		7	0	34 132.62	0.061
14	15		7	0	34 205.99	0.211
15	16		7	0	34 265.78	0.133
16	17		7	0	34 315.49	0.268
19	20		7	0	34 422.07	0.264
20	21		7	0	34 447.71	0.135
1	2		8	0	5 291.78	0.233
2		3	8	0	11 380.04	0.481
3	3		8	0	22 015.79	0.319
4		4	8	0	24 105.19	0.439
5	4		8	0	27 692.74	0.296
6		5	8	0	28 643.92	-3.827
7	5		8	0	30 278.68	3.897
8		6	8	0	30 808.62	-3.330
9	6		8	0	31 658.05	-0.541
10		7	8	0	32 015.26	-2.211
11	7		8	0	32 484.06	0.786
12		8	8	0	32 758.11	-1.185
13	8		8	0	33 013.96	-0.334
14		9	8	0	33 245.17	-0.912
15	9		8	0	33 378.30	-0.608
16		10	8	0	33 574.25	-0.020
17	10		8	0	33 648.23	0.107
18		11	8	0	33 792.71	0.262
19	11		8	0	33 863.99	-0.307
20		12	8	0	33 946.53	0.163
21	12		8	0	34 031.17	0.007

Continued on next page

#	Π [±]		Σ ⁺		E_{obs}/hc / cm ⁻¹	$(E_{\text{obs}} - E_{\text{calc}})/hc$ / cm ⁻¹
	n	n	N	v		
22		13	8	0	34 068.72	-0.333
23	13		8	0	34 140.69	0.366
24		14	8	0	34 184.60	-0.037
25	14		8	0	34 219.25	0.244
26		15	8	0	34 269.48	0.224
29	16		8	0	34 359.69	-0.052
32		18	8	0	34 425.30	0.116
33	18		8	0	34 446.90	0.127
34		19	8	0	34 458.20	-0.050
35	19		8	0	34 473.92	0.050
36		20	8	0	34 491.47	0.120
37	20		8	0	34 506.06	0.059
38			8	0	34 514.63	-0.010
40			8	0	34 536.66	-0.015
41			8	0	34 547.73	0.083
42			8	0	34 556.77	0.067
43			8	0	34 562.58	0.018
1	2		9	0	5424.13	-0.401
2	3		9	0	22 148.53	-0.102
3	4		9	0	27 828.41	-2.439
4	5		9	0	30 421.57	-0.176
5	6		9	0	31 815.61	-0.705
6	7		9	0	32 651.91	-0.088
7	8		9	0	33 191.77	-0.190
8	9		9	0	33 560.92	0.021
9	10		9	0	33 824.11	0.015
10	11		9	0	34 018.33	-0.082
11	12		9	0	34 165.92	-0.024
12	13		9	0	34 280.85	0.262
13	14		9	0	34 371.51	0.069
14	15		9	0	34 444.58	-0.076
15	16		9	0	34 504.34	-0.181
16	17		9	0	34 554.21	0.116
17	18		9	0	34 595.76	0.153

Continued on next page

#	Π^\pm		Σ^+		E_{obs}/hc / cm^{-1}	$(E_{\text{obs}} - E_{\text{calc}})/hc$ / cm^{-1}
	n	n	N	v		
19	20		9	0	34 660.90	0.226
20	21		9	0	34 686.59	0.149
21	22		9	0	34 708.90	0.136
1	2		10	0	5 566.00	0.109
2		3	10	0	11 636.64	0.488
3	3		10	0	22 282.16	0.712
4		4	10	0	24 371.13	0.482
5	4		10	0	27 954.40	0.503
6		5	10	0	28 914.10	-3.929
7	5		10	0	30 537.72	6.089
8		6	10	0	31 083.30	-3.227
9	6		10	0	31 910.57	-0.469
10		7	10	0	32 293.66	-2.213
11	7		10	0	32 734.07	1.377
12		8	10	0	33 038.25	-1.105
13	8		10	0	33 262.76	-0.385
14		9	10	0	33 523.49	1.360
15	9		10	0	33 631.67	-0.763
16		10	10	0	33 834.13	-0.153
18		11	10	0	34 040.77	0.278
19	11		10	0	34 141.29	-0.237
21	12		10	0	34 288.77	0.271
22		13	10	0	34 337.76	-1.066
23	13		10	0	34 386.71	0.159
24		14	10	0	34 448.80	0.446
26		15	10	0	34 515.42	0.402
27	15		10	0	34 557.98	0.034
28		16	10	0	34 586.67	0.147
29	16		10	0	34 605.66	-0.028
32		18	10	0	34 677.61	0.048
33	18		10	0	34 692.41	0.085
34		19	10	0	34 711.97	0.135
35	19		10	0	34 729.74	0.143
36		20	10	0	34 743.56	0.106

Continued on next page

#	Π [±]		Σ ⁺		E_{obs}/hc / cm ⁻¹	$(E_{\text{obs}} - E_{\text{calc}})/hc$ / cm ⁻¹
	<i>n</i>	<i>n</i>	<i>N</i>	<i>v</i>		
37	20		10	0	34 752.13	0.007
38			10	0	34 764.67	1.200
40			10	0	34 786.86	0.104
41			10	0	34 796.54	0.050
42			10	0	34 804.07	0.034
43			10	0	34 809.67	0.023
47			10	0	34 836.51	0.086
48			10	0	34 842.27	0.248
49			10	0	34 847.11	0.065
50			10	0	34 851.40	0.048
51			10	0	34 854.83	0.024
57			10	0	34 875.10	0.160
1	2		11	0	5727.36	-0.850
2	3		11	0	22 444.94	-0.019
3	4		11	0	28 125.30	-0.187
4	5		11	0	30 715.64	-0.157
5	6		11	0	32 109.47	-0.642
6	7		11	0	32 945.54	-0.126
7	8		11	0	33 485.39	-0.166
8	9		11	0	33 854.68	0.228
9	10		11	0	34 117.60	-0.021
10	11		11	0	34 311.94	0.021
11	12		11	0	34 459.33	-0.109
12	13		11	0	34 574.10	0.026
13	14		11	0	34 665.02	0.100
14	15		11	0	34 738.17	0.040
15	16		11	0	34 797.84	-0.151
16	17		11	0	34 847.61	0.048
17	18		11	0	34 889.05	-0.022
18	19		11	0	34 924.37	0.191
19	20		11	0	34 954.39	0.254
1	2		12	0	5895.95	-0.099
2		3	12	0	11 945.13	0.402
3	3		12	0	22 602.70	1.170

Continued on next page

#	Π^\pm		Σ^+		E_{obs}/hc / cm^{-1}	$(E_{\text{obs}} - E_{\text{calc}})/hc$ / cm^{-1}
	n	n	N	v		
4		4	12	0	24 691.02	0.515
5	4		12	0	28 269.44	0.796
6		5	12	0	29 238.89	-4.182
7	5		12	0	30 850.20	8.956
8		6	12	0	31 413.00	-3.318
9	6		12	0	32 215.81	-0.468
10		7	12	0	32 627.00	-2.218
11	7		12	0	33 038.05	2.459
12		8	12	0	33 371.64	-0.990
13	8		12	0	33 566.67	-0.558
14		9	12	0	33 845.28	0.143
16		10	12	0	34 139.30	-0.159
18		11	12	0	34 341.97	0.119
19	11		12	0	34 461.40	0.205
21	12		12	0	34 589.40	0.218
22		13	12	0	34 663.07	0.126
23	13		12	0	34 695.98	-0.191
24		14	12	0	34 748.51	-0.003
25	14		12	0	34 800.06	0.029
26		15	12	0	34 828.19	0.155
28		16	12	0	34 893.67	0.112
29	16		12	0	34 923.56	0.133
33	18		12	0	35 003.78	0.201
34		19	12	0	35 019.24	0.056
35	19		12	0	35 029.27	-0.007
38			12	0	35 068.61	-0.004
39			12	0	35 079.81	0.103
40			12	0	35 089.03	0.042
41			12	0	35 095.68	-0.046
43			12	0	35 109.61	-0.127
48			12	0	35 140.81	0.084
49			12	0	35 145.08	-0.278
50			12	0	35 149.47	0.056
52			12	0	35 155.95	-0.002

Continued on next page

#	Π^\pm		Σ^+		E_{obs}/hc / cm^{-1}	$(E_{\text{obs}} - E_{\text{calc}})/hc$ / cm^{-1}
	n	n	N	v		
53			12	0	35 159.22	0.018
54			12	0	35 162.36	-0.103
1	2		13	0	6085.96	-1.436
2	3		13	0	22 795.50	0.093
3	4		13	0	28 473.69	-0.236
4	5		13	0	31 063.36	-0.179
5	6		13	0	32 456.78	-0.770
6	7		13	0	33 292.81	-0.142
7	8		13	0	33 832.60	-0.157
8	9		13	0	34 201.60	-0.001
9	10		13	0	34 464.75	0.013
10	11		13	0	34 659.02	0.006
11	12		13	0	34 806.46	-0.059
13	14		13	0	35 012.12	0.139
14	15		13	0	35 085.25	0.064
16	17		13	0	35 194.63	0.021
17	18		13	0	35 236.13	0.014
18	19		13	0	35 271.42	0.199
21	22		13	0	35 349.40	0.138
22	23		13	0	35 368.69	-0.037
23	24		13	0	35 385.76	-0.043
24	25		13	0	35 400.88	0.014
1	2		14	0	6280.52	-0.391
2		3	14	0	12 304.32	0.196
3	3		14	0	22 976.20	1.562
4		4	14	0	25 063.73	0.562
5	4		14	0	28 636.85	1.176
6		5	14	0	29 617.47	-4.195
7	5		14	0	31 214.72	11.943
8		6	14	0	31 796.44	-3.499
9	6		14	0	32 573.21	-0.452
10		7	14	0	33 013.71	-2.130
11	7		14	0	33 395.87	4.414
12		8	14	0	33 755.78	-0.863

Continued on next page

#	Π^\pm		Σ^+		E_{obs}/hc / cm^{-1}	$(E_{\text{obs}} - E_{\text{calc}})/hc$ / cm^{-1}
	n	n	N	v		
14		9	14	0	34 212.50	0.191
16		10	14	0	34 494.10	-0.221
18		11	14	0	34 700.05	-0.025
22		13	14	0	35 020.53	-0.032
23	13		14	0	35 074.14	-0.425
24		14	14	0	35 104.47	-0.174
25	14		14	0	35 153.00	-0.123
26		15	14	0	35 196.79	-0.060
29	16		14	0	35 276.37	0.100
30		17	14	0	35 303.76	0.110
31	17		14	0	35 325.45	-0.075
35	19		14	0	35 387.84	0.058
41			14	0	35 448.05	0.028
44			14	0	35 470.57	0.081
45			14	0	35 476.69	0.018
47			14	0	35 487.25	0.006
48			14	0	35 491.59	0.050
49			14	0	35 495.28	0.067
51			14	0	35 502.44	0.040
52			14	0	35 505.93	-0.038
53			14	0	35 509.36	-0.003
1	2		15	0	6 498.76	-2.110
2	3		15	0	23 198.95	0.188
3	4		15	0	28 874.72	-0.234
4	5		15	0	31 463.65	-0.111
5	6		15	0	32 856.54	-0.880
6	7		15	0	33 692.46	-0.185
7	8		15	0	34 232.08	-0.271
8	9		15	0	34 601.00	-0.136
9	10		15	0	34 864.13	-0.105
14	15		15	0	35 484.61	-0.002
15	16		15	0	35 544.41	-0.053
16	17		15	0	35 593.96	-0.066
17	18		15	0	35 635.54	0.010

Continued on next page

#	Π^\pm		Σ^+		E_{obs}/hc / cm^{-1}	$(E_{\text{obs}} - E_{\text{calc}})/hc$ / cm^{-1}
	n	n	N	v		
18	19		15	0	35 670.57	-0.062
19	20		15	0	35 700.65	0.065
20	21		15	0	35 726.50	0.152
23	24		15	0	35 785.26	0.053
24	25		15	0	35 800.30	0.031
1	2		16	0	6718.54	-0.633
2		3	16	0	12 712.80	-0.170
3	3		16	0	23 401.58	2.076
4		4	16	0	25 487.89	0.608
5	4		16	0	29 055.41	1.616
6		5	16	0	30 048.29	-4.102
7	5		16	0	31 630.21	15.022
8		6	16	0	32 232.14	-3.681
9	6		16	0	32 981.83	-0.442
10		7	16	0	33 451.86	-2.078
12		8	16	0	34 187.91	-0.700
23	13		16	0	35 489.28	-0.018
26		15	16	0	35 600.84	-0.124
27	15		16	0	35 638.48	-0.075
28		16	16	0	35 666.59	-0.130
29	16		16	0	35 683.77	0.011
31	17		16	0	35 729.96	0.046
33	18		16	0	35 768.66	0.151
34		19	16	0	35 781.94	-0.055
39			16	0	35 837.42	-0.006
53			16	0	35 911.82	0.065
59			16	0	35 927.07	-0.072
60			16	0	35 929.16	-0.003
61			16	0	35 931.09	0.030
62			16	0	35 932.75	-0.092
64			16	0	35 936.10	0.007
67			16	0	35 940.32	0.037
1	2		17	0	6964.34	-2.878
2	3		17	0	23 653.97	0.351

Continued on next page

#	Π^\pm		Σ^+		E_{obs}/hc / cm^{-1}	$(E_{\text{obs}} - E_{\text{calc}})/hc$ / cm^{-1}
	n	n	N	v		
3	4		17	0	29 327.03	-0.138
4	5		17	0	31 914.96	-0.098
5	6		17	0	33 307.39	-0.928
6	7		17	0	34 143.31	-0.032
14	15		17	0	35 935.01	0.005
15	16		17	0	35 994.85	0.000
16	17		17	0	36 044.29	-0.119
18	19		17	0	36 120.80	-0.209
19	20		17	0	36 150.87	-0.089
20	21		17	0	36 176.80	0.080
21	22		17	0	36 199.12	0.082
25	26		17	0	36 264.00	0.011
26	27		17	0	36 275.93	0.048
1	2		18	0	7208.35	-0.990
2		3	18	0	13 168.97	-0.726
3	3		18	0	23 877.40	2.731
4		4	18	0	25 962.01	0.715
5	4		18	0	29 523.79	2.167
6		5	18	0	30 530.47	-3.165
7	5		18	0	32 094.32	17.099
8		6	18	0	32 718.60	-3.618
9	6		18	0	33 440.50	-0.424
10		7	18	0	33 939.60	-1.963
12		8	18	0	34 665.52	-0.243
24		14	18	0	35 997.43	-0.034
27	15		18	0	36 092.21	-0.103
29	16		18	0	36 151.68	-0.058
34		19	18	0	36 237.76	0.079
37	20		18	0	36 275.33	0.050
38			18	0	36 283.68	-0.069
40			18	0	36 298.76	-0.005
1	2		19	0	7481.20	-3.631
2	3		19	0	24 159.01	0.632
3	4		19	0	29 829.01	0.040

Continued on next page

#	Π [±]		Σ ⁺		E_{obs}/hc / cm ⁻¹	$(E_{\text{obs}} - E_{\text{calc}})/hc$ / cm ⁻¹
	n	n	N	v		
4	5		19	0	32 415.82	-0.013
5	6		19	0	33 807.82	-0.826
6	7		19	0	34 643.32	-0.125
15	16		19	0	36 494.61	0.003
16	17		19	0	36 544.14	-0.020
17	18		19	0	36 585.63	-0.027
18	19		19	0	36 620.70	-0.053
20	21		19	0	36 676.39	-0.070
21	22		19	0	36 698.77	-0.006
22	23		19	0	36 718.33	0.093
26	27		19	0	36 775.79	0.176
9		6	20	0	33 947.90	-0.285
12	8		20	0	35 186.09	0.042
23	13		20	0	36 448.34	-0.062
24		14	20	0	36 501.64	0.006
25	14		20	0	36 546.14	-0.012
26		15	20	0	36 576.09	-0.080
28		16	20	0	36 626.97	-0.049
29	16		20	0	36 654.69	0.051
30		17	20	0	36 678.76	-0.028
31	17		20	0	36 699.30	-0.038
33	18		20	0	36 727.22	0.144
35	19		20	0	36 753.41	0.044
21			21	0	37 246.25	0.159
24		14	22	0	37 052.28	0.231
30		17	22	0	37 228.04	0.055
3	4		1	1	28 844.63	0.356
4	5		1	1	31 433.05	0.861
5	6		1	1	32 824.28	-1.180
6	7		1	1	33 658.39	-2.100
7	8		1	1	34 199.78	-0.307
8	9		1	1	34 568.86	0.053
9	10		1	1	34 831.84	-0.023
10	11		1	1	35 025.81	-0.277

Continued on next page

#	Π^\pm		Σ^+		E_{obs}/hc / cm^{-1}	$(E_{\text{obs}} - E_{\text{calc}})/hc$ / cm^{-1}
	n	n	N	v		
15	16		1	1	35 511.97	-0.037
17	18		1	1	35 602.99	-0.076
18	19		1	1	35 638.00	-0.166
4		4	2	1	25 228.07	0.013
5	4		2	1	28 871.35	0.397
6		5	2	1	29 779.82	0.642
7	5		2	1	31 459.02	1.041
8		6	2	1	31 945.42	1.353
9	6		2	1	32 848.95	-1.146
11	7		2	1	33 683.95	0.267
12		8	2	1	33 881.20	-0.006
13	8		2	1	34 221.34	-0.267
15	9		2	1	34 588.80	0.260
28		16	2	1	35 514.51	0.009
29	16		2	1	35 535.11	0.036
30		17	2	1	35 565.71	-0.032
33	18		2	1	35 634.52	-0.066
43			2	1	35 765.32	-0.112
3	4		3	1	28 913.63	0.246
4	5		3	1	31 501.87	0.790
5	6		3	1	32 892.89	-1.366
6	7		3	1	33 728.05	-1.187
7	8		3	1	34 268.50	-0.307
8	9		3	1	34 637.56	0.049
9	10		3	1	34 900.26	-0.297
10	11		3	1	35 094.65	-0.124
14	15		3	1	35 520.83	-0.006
16	17		3	1	35 630.19	-0.048
17	18		3	1	35 671.65	-0.087
18	19		3	1	35 706.72	-0.116
22	23		3	1	35 804.23	-0.097
4		4	4	1	25 323.72	-0.021
5	4		4	1	28 965.61	0.257
6		5	4	1	29 876.59	-0.115

Continued on next page

#	Π^\pm		Σ^+		E_{obs}/hc / cm^{-1}	$(E_{\text{obs}} - E_{\text{calc}})/hc$ / cm^{-1}
	n	n	N	v		
7	5		4	1	31 552.45	2.199
8		6	4	1	32 044.53	0.957
9	6		4	1	32 938.98	-0.820
11	7		4	1	33 770.38	-0.105
12		8	4	1	33 985.97	0.124
13	8		4	1	34 305.67	0.128
14		9	4	1	34 471.96	-0.618
15	9		4	1	34 670.31	0.214
16		10	4	1	34 811.10	1.022
28		16	4	1	35 594.70	-0.099
29	16		4	1	35 633.69	0.038
31	17		4	1	35 677.45	-0.042
32		18	4	1	35 705.77	-0.053
34		19	4	1	35 739.79	-0.077
35	19		4	1	35 758.37	-0.101
39			4	1	35 808.25	-0.070
43			4	1	35 851.15	-0.116
3	4		5	1	29 037.46	-0.060
4	5		5	1	31 626.38	1.560
5	6		5	1	33 016.52	-1.305
6	7		5	1	33 852.18	-0.539
7	8		5	1	34 391.85	-0.391
8	9		5	1	34 760.77	-0.146
9	10		5	1	35 023.87	-0.074
10	11		5	1	35 218.03	-0.118
14	15		5	1	35 644.20	0.012
15	16		5	1	35 704.03	0.000
16	17		5	1	35 753.63	0.045
17	18		5	1	35 795.01	-0.073
20	21		5	1	35 885.86	-0.029
21	22		5	1	35 908.23	0.024
4		4	6	1	25 473.63	-0.046
5	4		6	1	29 111.85	-1.474
6		5	6	1	30 028.15	-1.360

Continued on next page

#	Π^\pm		Σ^+		E_{obs}/hc / cm^{-1}	$(E_{\text{obs}} - E_{\text{calc}})/hc$ / cm^{-1}
	n	n	N	v		
7	5		6	1	31 697.37	2.365
8		6	6	1	32 199.99	0.630
9	6		6	1	33 080.25	-0.690
10		7	6	1	33 411.70	5.540
11	7		6	1	33 908.93	0.862
12		8	6	1	34 147.90	-0.289
13	8		6	1	34 440.57	0.228
14		9	6	1	34 639.71	2.692
15	9		6	1	34 803.70	0.191
16		10	6	1	34 977.24	3.054
25	14		6	1	35 647.92	-0.031
28		16	6	1	35 751.67	-0.062
30		17	6	1	35 799.82	0.090
31	17		6	1	35 826.88	0.061
32		18	6	1	35 839.69	0.155
34		19	6	1	35 884.43	-0.019
35	19		6	1	35 894.48	0.215
50			6	1	36 035.42	-0.040
3	4		7	1	29 215.70	-0.532
4	5		7	1	31 803.61	0.648
5	6		7	1	33 194.28	-1.437
6	7		7	1	34 030.13	-0.357
7	8		7	1	34 569.52	-0.419
8	9		7	1	34 938.61	0.038
9	10		7	1	35 201.55	-0.023
10	11		7	1	35 395.64	-0.120
14	15		7	1	35 821.80	0.033
15	16		7	1	35 881.58	-0.025
16	17		7	1	35 931.23	0.073
18	19		7	1	36 007.71	-0.039
19	20		7	1	36 037.66	-0.036
20	21		7	1	36 063.53	0.075
21	22		7	1	36 085.89	0.119
4		4	8	1	25 677.29	-0.006

Continued on next page

#	Π^\pm		Σ^+		E_{obs}/hc / cm^{-1}	$(E_{\text{obs}} - E_{\text{calc}})/hc$ / cm^{-1}
	n	n	N	v		
5	4		8	1	29 314.99	0.619
6		5	8	1	30 233.89	-3.102
7	5		8	1	31 895.10	3.207
8		6	8	1	32 410.07	-0.607
9	6		8	1	33 273.50	-0.069
10		7	8	1	33 620.29	-1.068
11	7		8	1	34 098.62	1.468
12		8	8	1	34 366.38	0.106
13	8		8	1	34 627.80	0.367
14		9	8	1	34 856.17	0.725
16		10	8	1	35 186.58	0.019
24		14	8	1	35 795.02	0.421
28		16	8	1	35 938.67	0.206
29	16		8	1	35 974.43	0.074
35	19		8	1	36 089.06	0.219
3	4		9	1	29 450.95	2.082
4	5		9	1	32 035.19	0.338
5	6		9	1	33 425.68	-1.604
6	7		9	1	34 261.44	-0.450
7	8		9	1	34 800.74	-0.511
8	9		9	1	35 169.30	-0.529
9	10		9	1	35 433.15	0.355
10	11		9	1	35 626.50	-0.458
14	15		9	1	36 053.07	0.146
4		4	10	1	25 933.79	-0.036
5	4		10	1	29 568.28	0.468
6		5	10	1	30 492.83	-5.504
7	5		10	1	32 144.75	4.345
8		6	10	1	32 675.42	-1.114
9	6		10	1	33 515.43	-2.112
10		7	10	1	33 890.62	-0.593
11	7		10	1	34 341.72	3.722
12		8	10	1	34 638.20	0.100
13	8		10	1	34 868.25	0.811

Continued on next page

#	Π [±]		Σ ⁺		E_{obs}/hc / cm ⁻¹	$(E_{\text{obs}} - E_{\text{calc}})/hc$ / cm ⁻¹
	n	n	N	v		
14		9	10	1	35 124.60	0.335
16		10	10	1	35 439.28	-0.887
34		19	10	1	36 319.46	0.238
36		20	10	1	36 347.47	0.475
39			10	1	36 383.40	0.203
41			10	1	36 402.54	0.131
3	4		11	1	29 733.57	-1.008
4	5		11	1	32 319.87	0.227
5	6		11	1	33 710.05	-1.624
6	7		11	1	34 545.97	-0.108
7	8		11	1	35 084.86	-0.467
8	9		11	1	35 453.61	-0.227
14	15		11	1	36 337.00	0.192
16	17		11	1	36 446.34	0.161
17	18		11	1	36 487.83	0.162
19	20		11	1	36 552.78	0.078
4		4	12	1	26 242.26	-0.027
5	4		12	1	29 873.19	0.407
6		5	12	1	30 804.23	-8.274
7	5		12	1	32 445.99	6.135
8		6	12	1	32 993.20	-2.519
9	6		12	1	33 812.05	-0.405
10		7	12	1	34 213.89	-0.296
11	7		12	1	34 633.21	2.799
12		8	12	1	34 961.35	-0.218
14		9	12	1	35 439.10	0.090
3	4		13	1	30 070.69	-1.621
4	5		13	1	32 656.29	0.007
5	6		13	1	34 046.00	-1.838
6	7		13	1	34 881.90	-0.102
16	17		13	1	36 782.04	0.311
17	18		13	1	36 823.53	0.316
18	19		13	1	36 858.56	0.259
19	20		13	1	36 888.48	0.239

Continued on next page

#	Π [±]		Σ ⁺		E_{obs}/hc / cm ⁻¹	$(E_{\text{obs}} - E_{\text{calc}})/hc$ / cm ⁻¹
	n	n	N	v		
4		4	14	1	26 601.38	-0.113
5	4		14	1	30 228.71	0.477
6		5	14	1	31 166.95	-11.308
7	5		14	1	32 796.98	7.620
8		6	14	1	33 362.05	-4.769
9	6		14	1	34 157.75	0.133
10		7	14	1	34 588.21	-0.398
11	7		14	1	34 977.65	3.844
25	14		14	1	36 739.11	0.291
26		15	14	1	36 781.53	0.262
3	4		15	1	30 458.65	-2.167
4	5		15	1	33 043.46	-0.063
5	6		15	1	34 432.72	-1.806
4		4	16	1	27 010.17	0.119
5	4		16	1	30 633.47	0.550
6		5	16	1	31 580.17	-13.973
7	5		16	1	33 197.49	9.661
8		6	16	1	33 779.61	-8.620
9	6		16	1	34 552.78	0.723
10		7	16	1	35 012.34	-0.334
36		20	16	1	37 376.38	0.123
37	20		16	1	37 388.89	-0.024
3	4		17	1	30 896.10	-2.544
4	5		17	1	33 479.92	0.008
5	6		17	1	34 868.38	-1.908
4		4	18	1	27 466.47	0.110
5	4		18	1	31 086.33	0.920
6		5	18	1	32 041.29	-17.207
7	5		18	1	33 645.82	11.863
9	6		18	1	34 999.42	4.885
3	4		19	1	31 381.35	-2.791
4	5		19	1	33 964.10	0.301
5	6		19	1	35 351.88	-1.594
4		4	20	1	27 968.75	0.136

Continued on next page

#	Π^\pm		Σ^+		E_{obs}/hc / cm^{-1}	$(E_{\text{obs}} - E_{\text{calc}})/hc$ / cm^{-1}
	n	n	N	v		
5	4		20	1	31 585.64	1.562
6		5	20	1	32 550.06	-19.392
7	5		20	1	34 140.53	14.306

List of figures

2.1	Schematic view of the experimental setup for experiments on metastable molecules, radicals and ions. The lasers with wave number $\tilde{\nu}_1$ and $\tilde{\nu}_2$ were used to generate VUV radiation of wave number $\tilde{\nu}_{\text{VUV}}$. Alternatively they could be used to induce two-color multiphoton excitation processes, in which case the four-wave mixing chamber and the monochromator were not used. The vacuum chambers where the photoexcitation and photoionization experiments were carried out are displayed on the right and the detection and measurement systems at the bottom of the figure.	8
2.2	Schematic view of the photoelectron/photoion time-of-flight mass spectrometer. Depending on the sign of the voltages applied to the set of six extraction plates (middle of the figure) and the microchannel plate detectors, either ions or electrons can be detected using the same spectrometer. The electron or ion time-of-flight tube and the photoexcitation region are surrounded by a magnetic shield consisting of two concentric mumetal cylinders.	8
2.3	Schematic view of VUV generation using resonance-enhanced four-wave mixing in rare gases.	12
2.4	Schematic view of the experimental setup used in experiments requiring a single UV laser.	12
2.5	Schematic view of the experimental setup for the xenon experiment. The photon with wave number $\tilde{\nu}_1$ was used for the two-photon resonance of $80\,118.9839\text{ cm}^{-1}$ in xenon. The photon with $\tilde{\nu}_2$ was used to prepare the Rydberg state. The millimeter-wave (mm-wave) radiation was used to induce transitions between two Rydberg states.	13
2.6	A schematic diagram of the pulsed discharge source.	17
2.7	Time-of-flight mass spectrum of He^+ and He_2^+ recorded following photoionization of He^* and He_2^* with a UV laser of wave number $39\,603.96\text{ cm}^{-1}$ and extraction of the ions with a pulsed electric field.	18

-
- 2.8 Time-of-flight of Xe^+ after collision and subsequent Penning ionisation with metastable helium. In this picture the full time-of-flight trace is shown. The peak at $t = 0$ corresponds to photons produced in the discharge. 19
- 2.9 Time-of-flight spectrum illustrating the production of metastable CO^* a $^3\Pi_{\Omega=1}$ molecules in a supersonic expansion. a) TOF spectrum recorded without applying any voltage on the extraction plates surrounding the photoexcitation region. b) TOF spectrum recorded with a voltage of 1 kV on the repeller plates of the extraction region. c) TOF spectrum recorded under the same conditions as b) but after detuning the UV laser. 20
- 2.10 Spectrum of the "forbidden" a $^3\Pi_{\Omega=1} (v' = 0) \leftarrow X \ ^1\Sigma^+ (v'' = 0)$ transition of CO obtained by recording the CO^* molecules at the MCP detector after a flight time of $400 \mu\text{s}$ as a function of the wave number of a UV laser. 21
- 2.11 Ion TOF mass spectra of ammonia and ammoniated ammonium radical clusters. a) Background TOF mass spectrum generated by the photodissociation laser alone. b) TOF mass spectrum including background signal, obtained following photodissociation and photoionization. c) Difference spectrum obtained by subtracting trace a) from trace b). This spectrum enables one to observe the photoionization of the photodissociation products with interference from undesirable photoionization by the photodissociation laser. 23
- 2.12 Energy level diagram illustrating the different photoionization channels of a polyatomic molecule. The ionization and dissociative ionization thresholds are marked by thick horizontal bars above which the shaded areas represent continua. These thresholds are characterized by the quantum states of the fragments. Infinite series of Rydberg states converge to each threshold. The full arrow designates direct ionization; the thick blue arrows represent ionization processes via excited states of the parent molecule, giving rise to so-called autoionization resonances in the photoionization yield; the dashed (red) arrow represents the process of dissociative ionization. 25
- 2.13 Comparison of conventional photoelectron spectroscopy (panel (a)) and PFI-ZEKE photoelectron spectroscopy (panel (b)). With the former technique the ionization energies E_I are determined by ionizing with a fixed-frequency light source (typically a He I source) and measuring the kinetic energy of E_{kin} of the photoelectrons using $E_I = h\nu - E_{\text{kin}}$. With the latter technique, they are determined by detecting the field-ionization of high Rydberg states as a function of the frequency of a tunable light source. 27

- 2.14 Millimeter wave transitions between Rydberg states of ^{132}Xe in the presence of different electric fields. The spectra are shifted along the vertical axis by an offset corresponding to the value of the applied field in mV cm^{-1} (from -40 mV cm^{-1} to $+40 \text{ mV cm}^{-1}$). The $57\text{f}[3/2]_2 \leftarrow 53\text{d}[1/2]_1$ transition at 276360.5 MHz (left) exhibits a stronger Stark effect than the $61\text{p}[5/2]_2 \leftarrow 55\text{s}[3/2]_1$ transition at 267477.3 MHz (right). This procedure yields the value of the compensation field necessary to minimize the stray field. 29
- 3.1 The photoelectron spectrum of the $\tilde{\text{X}}^+ \text{}^2\text{A}_2'' \text{NH}_3^+ \leftarrow \tilde{\text{X}} \text{}^1\text{A}'_1 \text{NH}_3$ transition of ammonia excited by He I resonance radiation. The spectrum consists of a long progression of vibrational band starting at 10.073 eV . The spectrum is taken from Rabalais *et al.* [87] who labeled the electronic states using the C_{3v} point group. 33
- 3.2 Energy level diagram showing schematically the rotational structures of the lowest vibrational level of the $\tilde{\text{X}}$ ($^1\text{A}'_1$) ground state of ND_3 and of out-of-plane bending levels of the $\tilde{\text{X}}^+$ ($^2\text{A}_2''$) ground state of ND_3^+ . The rovibronic symmetry of all levels is indicated next to the levels. 35
- 3.3 Panel (a) illustrates the experimental PFI-ZEKE photoelectron spectrum of the $\tilde{\text{X}}^+ (v_2^+ = 0) \leftarrow \tilde{\text{X}} (v_2 = 0)$ transition in ND_3 . The assignment of the lines is given using the notation $N_{K^+}^+ \leftarrow N_{K''}''$. Panel (b) shows a simulation based on the orbital ionization model [98]. The simulation presented in panel (c) relies on a less restrictive photoionization model. The experimental photoionization spectrum is depicted in panel (d). 38
- 3.4 Panel (a) illustrates the experimental PFI-ZEKE photoelectron spectrum of the $\tilde{\text{X}}^+ (v_2^+ = 1) \leftarrow \tilde{\text{X}} (v_2 = 0)$ transition in ND_3 . The assignment of the lines is given using the notation $N_{K^+}^+ \leftarrow N_{K''}''$. Panel (b) shows a simulation based on the orbital ionization model [98]. The simulation presented in panel (c) relies on a less restrictive photoionization model. The experimental photoionization spectrum is depicted in panel (d). 39
- 3.5 Panel (a) illustrates the experimental PFI-ZEKE photoelectron spectrum of the $\tilde{\text{X}}^+ (v_2^+ = 2) \leftarrow \tilde{\text{X}} (v_2 = 0)$ transition in ND_3 . The assignment of the lines is given using the notation $N_{K^+}^+ \leftarrow N_{K''}''$. Panel (b) shows a simulation based on the orbital ionization model [98]. The simulation presented in panel (c) relies on a less restrictive photoionization model. The experimental photoionization spectrum is depicted in panel (d). 40

-
- 4.1 PFI-ZEKE photoelectron spectrum recorded in the vicinity of the $\text{ND}_4^+ \tilde{X}^1\text{A}_1 \leftarrow \text{ND}_4 3s^2\text{A}_1$ transition (upper trace) obtained with a pulsed electric field sequence of $+40 \text{ mV cm}^{-1}$ followed by a pulse of -100 mV cm^{-1} . The experimental spectrum is compared with a simulation (lower trace). 49
- 4.2 TOF mass spectra of small ammonia cluster ions produced at several ionization wave numbers in the range of $30\,303 \text{ cm}^{-1} - 32\,258 \text{ cm}^{-1}$ following the photolysis $(\text{NH}_3)_n$ clusters at 204 nm. The ionization efficiency of $\text{NH}_4(\text{NH}_3)_n$ ($n \geq 2$) does not change appreciably in this wave number range while that of NH_4NH_3 exhibits several thresholds indicated by arrows. The TOF spectrum at the top was recorded only with the photolysis laser and was subtracted from all other TOF spectra. The strong ion signal of NH_3^+ at $31\,948.9 \text{ cm}^{-1}$ can be explained by resonance-enhanced multiphoton ionization. 51
- 4.3 Panel (a) shows the photoionization spectrum of NH_4NH_3 recorded with a delayed pulsed electric field of 173 V cm^{-1} . Panel (b) depicts the PFI-ZEKE photoelectron spectrum recorded in the same wave number region. Ionization thresholds have been observed at $31\,310(25) \text{ cm}^{-1}$, indicated with (A), at $31\,655(25) \text{ cm}^{-1}$, indicated with (B), at $31\,830(30) \text{ cm}^{-1}$, indicated with (C), and at $32\,000(25) \text{ cm}^{-1}$, indicated with (D). 52
- 4.4 TOF mass spectra of perdeuterated ammonia cluster ions produced at several ionization wave numbers in the range $30\,303 \text{ cm}^{-1} - 32\,051 \text{ cm}^{-1}$ following the photolysis of $(\text{ND}_3)_n$ clusters at 204 nm. The ionization efficiency of $\text{ND}_4(\text{ND}_3)_n$ ($n \geq 2$) does not change appreciably in this wave number range while the ionization efficiency of ND_4ND_3 and $(\text{ND}_3)_2$ exhibits thresholds indicated arrows. The top TOF spectrum was recorded with only the photolysis laser on and was subtracted from all other spectra. 54
- 4.5 Panel (a) shows the photoionization spectrum of recorded at the mass of N_2D_6^+ and N_2D_7^+ with a delayed pulsed electric field of 173 V cm^{-1} . The ionization thresholds are labeled with A', B', and C', respectively. Panel (b) depicts the PFI-ZEKE photoelectron spectrum recorded in the same wave number region. 55

- 5.1 Energy level diagram (not to scale) of the 2P ground state of $^{132}\text{Xe}^+$, $^{131}\text{Xe}^+$, and $^{129}\text{Xe}^+$. For each spin-orbit component of the ion ($^2P_{3/2}$ and $^2P_{1/2}$), the wavenumbers (cm^{-1}) of the ionization energies of ^{132}Xe from the 1S_0 ground state and the isotope shifts (cm^{-1}) for ^{131}Xe and ^{129}Xe are given. The hyperfine levels for $^{131}\text{Xe}^+$ and $^{129}\text{Xe}^+$ are labeled with the quantum number F^+ and their positions (cm^{-1}) with respect to the center of gravity of the hyperfine structure are given. The data for the $^2P_{1/2}$ state are from Ref. [135], the ionization energies for the $^2P_{3/2}$ state are from Ref. [141] and the hyperfine structures were determined in the present study. 59
- 5.2 Comparison of millimeter-wave overview spectra of the $62p \leftarrow 54d [3/2]_1$ transitions for the three most abundant isotopes ^{132}Xe ($I = 0$, 26.9% nat. abundance, top trace), ^{131}Xe ($I = 3/2$, 21.2%, middle), ^{129}Xe ($I = 1/2$, 26.4%, bottom). 62
- 5.3 The left panel shows a section of the millimeter-wave overview spectrum of the $62p [5/2]_2 \leftarrow 54d [3/2]_1$ transition recorded in different mass channels. The spectra have been shifted along the vertical axis by an offset of 0–5 arb. units. The spectrum of the ^{131}Xe isotope is drawn with dashed line for clarity. The strong peak in the ^{129}Xe spectrum at 263 446 MHz is the $62p [5/2]_3 (F = 5/2) \leftarrow 54d [3/2]_1 (F = 3/2)$ transition, whereas the strong peak in the ^{131}Xe spectrum at 263 553 MHz is the $62p [5/2]_3 (F = 5/2) \leftarrow 54d [3/2]_1 (F = 5/2)$ transition. The right panel shows the millimeter-wave spectrum of the $61p [5/2]_2 \leftarrow 52d [3/2]_1$ transition of ^{132}Xe at high-resolution. 63
- 5.4 Millimeter-wave spectra exhibiting transitions to the $61p[3/2]_1$ and $60d[1/2]_1$ Rydberg states of ^{132}Xe . Transitions from d or s states to d Rydberg states are forbidden by the $\Delta\ell = \pm 1$ selection rule, but become allowed in the presence of electric fields. High-resolution spectra recorded with reduced millimeter-wave power are presented below the low-resolution overview spectra. The bottom spectrum was recorded following minimization of the stray electric field. The presence of residual electric fields result in a broadening of the transition to the $61p[3/2]_1$ state and in the observation of the transition to the $60d[1/2]_1$ state. 68
- 5.5 Calculated (crosses) and observed (circles) fine and hyperfine levels of the $53d$ and $55s$ Rydberg states of Xe. The sequence of the Rydberg levels of ^{132}Xe with increasing energy is $nd[1/2]_0$, $nd[1/2]_1$, $nd[7/2]_4$, $nd[3/2]_2$, $nd[7/2]_3$, $nd[5/2]_2$, $nd[5/2]_3$, $nd[3/2]_1$, $(n+2)s[3/2]_2$, $(n+2)s[3/2]_1$ 71

- 5.6 Calculated (crosses) and observed (circles) fine and hyperfine levels of the 62p Rydberg states of Xe. The sequence of the Rydberg levels of ^{132}Xe with increasing energy is $np[1/2]_1$, $np[5/2]_2$, $np[5/2]_3$, $np[3/2]_1$, $np[3/2]_2$, $np[1/2]_0$. Light gray crosses and circles indicate the calculated and observed fine and hyperfine levels of the 61d Rydberg states (see Fig. 5.5). 72
- 5.7 Calculated (crosses) and observed (circles) fine and hyperfine levels of the 59f Rydberg states of Xe. The sequence of the Rydberg levels of ^{132}Xe with increasing energy is $nf[3/2]_1$, $nf[3/2]_2$, $nf[9/2]_5$, $nf[9/2]_4$, $nf[5/2]_3$, $nf[5/2]_2$, $nf[7/2]_3$, $nf[7/2]_4$. Light gray crosses indicate the calculated fine and hyperfine levels of the 63s Rydberg states (see Fig. 5.5). 72
- 5.8 Calculated hyperfine structure of high- nd and $(n+2)s$ Rydberg states of ^{129}Xe and ^{131}Xe relative to the hyperfine level with the highest F value ($F = 9/2$ level for ^{129}Xe and $F = 11/2$ level for ^{131}Xe) belonging to the $nd[7/2]_4$ Rydberg series. The calculated levels with $F = 1/2$ are connected by thick lines, those with $F = 3/2$ by thick dashed lines, those with $F = 5/2$ by thin dot-dashed lines, those with $F = 7/2$ by thin continuous lines, and those with $F \geq 9/2$ by thin dotted lines. On the right-hand side of each panel, the derived hyperfine structure of the cation is shown, labeled with the values of F^+ . The number of hyperfine series (and their F values) converging to each ion level can be found in Table 5.2. 73
- 5.9 Calculated hyperfine structure of high- nd and $(n+2)s$ Rydberg states of ^{129}Xe and ^{131}Xe relative to the highest hyperfine level ($F = 1/2$ for ^{129}Xe and $F = 5/2$ for ^{131}Xe) of the $(n+2)s[3/2]_1$ state. The calculated levels with $F = 1/2$ are connected by thick lines, those with $F = 3/2$ by thick dashed lines, those with $F = 5/2$ by thin dot-dashed lines, those with $F = 7/2$ by thin continuous lines, and those with $F \geq 9/2$ by thin dotted lines. Note the avoided crossing between the $F = 3/2$ hyperfine levels of the $(n+2)s[3/2]_1$ and $(n+2)s[3/2]_2$ Rydberg states of ^{129}Xe . On the right-hand side of each panel, the derived hyperfine structure of the cation is shown, labeled with the values of F^+ 74

- 5.10 Calculated hyperfine structure of high- np Rydberg states of ^{129}Xe and ^{131}Xe relative to the hyperfine level with the highest F value ($F = 7/2$ level for ^{129}Xe and $F = 9/2$ level for ^{131}Xe) belonging to the $np[5/2]_3$ Rydberg series. The calculated levels with $F = 1/2$ are connected by thick lines, those with $F = 3/2$ by thick dashed lines, those with $F = 5/2$ by thin dot-dashed lines, those with $F = 7/2$ by thin continuous lines, and those with $F = 9/2$ by thin dotted lines. On the right-hand side of each panel, the derived hyperfine structure of the cation is shown, labeled with the values of F^+ 75
- 6.1 Time-of-flight mass spectrum of the metastable helium atoms and molecules. The origin of the TOF axis was set to the onset of the discharge pulse. The peaks at $t = 0$ and $15 \mu\text{s}$ correspond to photons and ions produced in the discharge. 87
- 6.2 Photoionization mass spectra used to characterize the source of metastable He^* and He_2^* . a) Spectrum obtained following photoionization at $39\,603.96 \text{ cm}^{-1}$, above the ionization threshold of both He^* and He_2^* . b) Spectrum obtained following photoionization at $34\,482.76 \text{ cm}^{-1}$ above the ionization threshold of He_2^* but below that of He^* 88
- 6.3 Panel a) shows the PFI-ZEKE photoelectron spectrum of the $^2\text{S}_{1/2} \leftarrow ^3\text{S}_1$ transition of ^4He . In panel b) the photoionization spectrum of the $1snp \ ^3\text{P}_{0-2} \leftarrow 1s2s \ ^3\text{S}_1$ Rydberg series is shown. The Rydberg states and the series limit are indicated by vertical lines. 89
- 6.4 PFI-ZEKE photoelectron spectrum of the $\text{X}^+ \ ^2\Sigma_u^+ \leftarrow \text{a} \ ^3\Sigma_u^+$ transition of $^4\text{He}_2$. Below the experimental spectrum, the simulated spectra for $v^+ = v'' = 0$ and $v^+ = v'' = 1$ are shown as inverted stick spectra. 92
- 6.5 Portion of the PFI-ZEKE photoelectron spectrum of the $\text{X}^+ \ ^2\Sigma_u^+ \leftarrow \text{a} \ ^3\Sigma_u^+$ transition of $^4\text{He}_2$ in the region of the Q-type branches of the $v^+ = v'' = 1$ (Q_1) and $v^+ = v'' = 2$ transitions (Q_2). Asterisks designate transitions which cannot be assigned to an ionization threshold but originate from channel interactions. 92
- 6.6 PFI-ZEKE photoelectron spectrum of the $\text{X}^+ \ ^2\Sigma_u^+ \leftarrow \text{a} \ ^3\Sigma_u^+$ transition of $^3\text{He}_2$. The asterisk marks the $N^+ = 0 \leftarrow N'' = 2$ transition. Below the experimental spectrum, the simulated spectrum is shown as inverted stick spectrum. 93

- 6.7 Schematic representation of the p channels optically accessible from the a ${}^3\Sigma_u^+$ state (only levels with $v^+ = v''$ considered). The light grey areas mark the high- n Rydberg states which are field-ionized in the PFI-ZEKE experiments. Transitions to channels with $N^+ = N''$ are strong (full arrows) and those to channels with $N^+ = N'' \pm 2$ are weak (dashed arrows). Transitions to Rydberg states with $N = N'' - 1$ converging on the $N^+ = N'' - 2$ threshold gain intensity from stronger transitions to Rydberg states with the same N but converging to the $N^+ = N''$ threshold. 98
- 6.8 Photoionization spectrum of ${}^4\text{He}_2$ a ${}^3\Sigma_u^+$. The positions of the $(v^+ = v, N^+ = N) \leftarrow (v, N)$ or $(v^+ = v, N^+ = N - 2) \leftarrow (v, N)$ ionization thresholds are indicated along the horizontal bars by Q(N) and O(N), respectively. . . . 99
- 6.9 Detailed view of a selected portion of the photoionization spectrum of ${}^4\text{He}_2$ a ${}^3\Sigma_u^+$. The horizontal assignment bars for $N = 3 - 19$ have been shifted along the vertical axis so that their positions correspond to the value of N . The full (dashed) horizontal lines correspond to $v^+ = 0 \leftarrow v'' = 0$ ($v^+ = 1 \leftarrow v'' = 1$; indicated only for $N = 3, 5, \dots, 11$) series. The principal quantum number n of the $np\pi$ ${}^3\Pi_g^-$ Rydberg series, which only occur for odd N values and form Q-type progressions ($N^+ - N'' = N - N'' = 0$), are indicated above the corresponding assignment bars. The $np\pi$ ${}^3\Pi_g^+$ and $np\sigma$ ${}^3\Sigma_g^+$ Rydberg series, which only occur for even N values, are fully mixed and form P ($N - N'' = -1$) and R ($N - N'' = +1$) branches. The assignment bars of the P branches are placed above those of the R branches; for both branches, only the Rydberg levels converging to the lower ionization threshold $N^+ = N - 1$ are assigned. 100
- 6.10 Comparison of the photoionization spectrum of ${}^4\text{He}_2$ a ${}^3\Sigma_u^+$ recorded with a pulsed electric field of $+400 \text{ V cm}^{-1}$ and collecting the ${}^4\text{He}_2^+$ ions (trace (a)), the RSR-TI spectrum of ${}^4\text{He}_2$ a ${}^3\Sigma_u^+$ recorded with a pulsed electric field of -6.4 V cm^{-1} and collecting the electrons (trace (b)), and the PFI-ZEKE photoelectron spectrum of ${}^4\text{He}_2$ a ${}^3\Sigma_u^+$ measured with a pulse sequence consisting of a discrimination pulse of $+66 \text{ mV cm}^{-1}$ followed by an extraction pulse of -133 mV cm^{-1} (trace (c)). The Q-type lines of the PFI-ZEKE photoelectron spectrum are labeled by the value of N^+ 102

- 6.11 RSR-TI spectra of ${}^4\text{He}_2$ a ${}^3\Sigma_u^+$ in the region of the O(5) and O(3) thresholds recorded using pulsed electric fields ranging from -0.33 V cm^{-1} (bottom) to $-133.33 \text{ V cm}^{-1}$ (top). The field ionization regions of these fields are indicated below each spectrum by the long rectangular frames. The lines of the bottom spectrum, which corresponds to the PFI-ZEKE photoelectron spectrum are assigned along the full line ($v^+ = 0$) and dashed line ($v^+ = 1$). The two vertical lines correspond to the field-free position of the O(5) and O(3) thresholds. 103
- 6.12 RSR-TI spectra of ${}^4\text{He}_2$ a ${}^3\Sigma_u^+$ in the region of the O(5) and O(3) thresholds recorded using a pulsed extraction field of -23.3 V cm^{-1} and dc discrimination fields ranging from 0 V cm^{-1} (top spectrum) to -1.9 V cm^{-1} (bottom spectrum). The field free positions of the O(3) and O(5) thresholds are indicated by vertical lines and the long horizontal rectangular frames indicate the field ionization region of the dc discrimination fields. 104
- 6.13 Comparison between PFI-ZEKE spectra of ${}^4\text{He}_2$ a ${}^3\Sigma_u^+$ recorded under different conditions. Spectra (a) and (c) were recorded with a discrimination pulse field of $+66 \text{ mV/cm}$ applied $1 \mu\text{s}$ after photoexcitation and an extraction pulse field of -133 mV/cm . Spectrum (b) was recorded with an electric field pulse sequence of $+40 \text{ mV/cm}$ and -133 mV/cm applied 210 ns after photoexcitation. Spectrum (d) was recorded without discrimination field pulse and an extraction field of -1.33 V/cm starting $1.5 \mu\text{s}$ after photoexcitation; the stronger extraction field caused a significant broadening of the $N^+ \leftarrow N''$ ZEKE transitions. Spectra (b) to (d) show transitions from ($v''=0, N''=3$) to $np\pi$ ${}^3\Pi_g^-(N=3)$ Rydberg states located above the $N^+ = 1$ threshold for $n > 39$; the positions of the transitions are given at the top. In spectrum (d) (and also weakly in spectrum (c)), transitions from ($v''=0, N''=5$) to $np\pi$ ${}^3\Pi_g^-(N=5)$ Rydberg states are observable. The ($v^+=0, N^+$) \leftarrow ($v''=0, N''$) ZEKE transitions are labeled with $N^+ - N''$. 105
- 6.14 RSR-TI spectra of ${}^4\text{He}_2$ a ${}^3\Sigma_u^+$ recorded with pulsed fields of 1.33 V/cm (bottom), 6.67 V/cm , 13.3 V/cm , 26.7 V/cm , and 66.7 V/cm (top) in the vicinity of the Q(1), Q(3), Q(5) and Q(7) thresholds. The assignment bar at the top indicates the $N^+ = N'' \leftarrow N''$ ionization thresholds. The assignment bars below indicate the positions and the n quantum number of the $np(N'')_{N''} \leftarrow N''$ transitions for $N'' = 3$ and $N'' = 1$ (bottom). The broad, dark grey lines indicate the range between the $6.1 \text{ cm}^{-1} \sqrt{\mathcal{E}/(\text{V cm}^{-1})}$ and $4.8 \text{ cm}^{-1} \sqrt{\mathcal{E}/(\text{V cm}^{-1})}$ limits of the field-lowered $1 \leftarrow 1$ ionization thresholds. 110

- 6.15 RSR-TI spectra of ${}^4\text{He}_2$ a ${}^3\Sigma_u^+$ recorded with pulsed fields of 1.33 V/cm (bottom), 6.67 V/cm, 13.3 V/cm, 26.7 V/cm, and 66.7 V/cm (top) in the vicinity of the O(3) thresholds. The assignment bars indicate the positions of the transitions starting from $N'' = 3$ and the n quantum number of the corresponding npN_N^+ Rydberg levels. The top bar shows the $np3_4$ and $np5_4$ (with primed numbers) series, the middle bar the $np3_3$ series, and the bottom bar the $np1_2$ and $np3_2$ (with primed numbers) series. The broad, dark grey lines indicate the range between the $6.1 \text{ cm}^{-1} \sqrt{\mathcal{E}/(\text{V cm}^{-1})}$ and $4.8 \text{ cm}^{-1} \sqrt{\mathcal{E}/(\text{V cm}^{-1})}$ limits of the field-lowered ionization thresholds. . . 111
- 6.16 RSR-TI spectra of ${}^4\text{He}_2$ a ${}^3\Sigma_u^+$ recorded with pulsed fields of 1.33 V/cm (bottom), 6.67 V/cm, 13.3 V/cm, 26.7 V/cm, and 66.7 V/cm (top) in the vicinity of the O(5) thresholds. The assignment bars indicate the positions of the transitions starting from $N'' = 5$ and the n quantum number of the corresponding npN_N^+ Rydberg levels. The top bar shows the $np5_6$ and $np7_6$ (with primed numbers) series, the middle bar the $np5_5$ series, and the bottom bar the $np3_4$ and $np5_4$ (with primed numbers) series. The broad, dark grey lines indicate the range between the $6.1 \text{ cm}^{-1} \sqrt{\mathcal{E}/(\text{V cm}^{-1})}$ and $4.8 \text{ cm}^{-1} \sqrt{\mathcal{E}/(\text{V cm}^{-1})}$ limits of the field-lowered ionization thresholds. . . 112
- 6.17 RSR-TI spectra of ${}^4\text{He}_2$ a ${}^3\Sigma_u^+$ recorded with pulsed fields of 1.33 V/cm (bottom), 6.67 V/cm, 13.3 V/cm, 26.7 V/cm, and 66.7 V/cm (top) in the vicinity of the O(7) and M(5) thresholds. The assignment bars indicate the positions and the n quantum number of the $npN_N^+ \leftarrow N''$ transitions. They refer to the following series (from bottom to top): (1) $np3_4/np5_4 \leftarrow 5$, (2) $np5_5 \leftarrow 5$, (3) $np5_6/np7_6 \leftarrow 5$, (4) $np7_7 \leftarrow 7$, and (5) $np7_8/np9_8 \leftarrow 7$. The broad, dark grey lines indicate the range between the $6.1 \text{ cm}^{-1} \sqrt{\mathcal{E}/(\text{V cm}^{-1})}$ and $4.8 \text{ cm}^{-1} \sqrt{\mathcal{E}/(\text{V cm}^{-1})}$ limits of the field-lowered $N^+ = 1 \leftarrow N'' = 5$ ionization thresholds. The positions of the $1 \leftarrow 5$ and $5 \leftarrow 7$ thresholds are indicated with dotted vertical lines. . . . 113
- 6.18 Schematic representation of the ionization channels in the photoionization of He_2^* and of the rotational channel interactions expected to be dominant in the absence of electric fields. 114

List of tables

1.1	Properties of Rydberg states. Values are calculated for the hydrogen atom if not mentioned otherwise	5
3.1	Two pulse sequences used to record the PFI-ZEKE photoelectron spectra of the transitions of ND ₃ . The shifts of the ionization thresholds were estimated using the procedure described in Ref. [59].	37
3.2	Observed and calculated transition wave numbers in cm ⁻¹ of the N _{K⁺} ⁺ ← N _{K⁺} ^{''} transitions of the PFI-ZEKE photoelectron spectra of ND ₃ in the vicinity of the \tilde{X}^+ ($v_2^+ = 0$) ← \tilde{X} ionization threshold. The field-free ionization thresholds can be obtained by compensating the field-induced shift. The ionization energy and rotational constants used to calculate the line positions are listed in Table 3.5.	41
3.3	Observed and calculated transition wave numbers in cm ⁻¹ of the N _{K⁺} ⁺ ← N _{K⁺} ^{''} transitions of the PFI-ZEKE photoelectron spectra of ND ₃ in the vicinity of the \tilde{X}^+ ($v_2^+ = 1$) ← \tilde{X} ionization threshold. The field-free ionization thresholds can be obtained by compensating the field-induced shift. The ionization energy and rotational constants used to calculate the line positions are listed in Table 3.5.	41
3.4	Observed and calculated transition wave numbers in cm ⁻¹ of the N _{K⁺} ⁺ ← N _{K⁺} ^{''} transitions of the PFI-ZEKE photoelectron spectra of ND ₃ in the vicinity of the \tilde{X}^+ ($v_2^+ = 2$) ← \tilde{X} ionization threshold. The field-free ionization thresholds can be obtained by compensating the field-induced shift. The ionization energy and rotational constants used to calculate the line positions are listed in Table 3.5.	42
3.5	Origins of \tilde{X}^+ ² A ₂ ^{''} ($v_2^+ = 0, 1, 2$) ← \tilde{X} ¹ A ₁ ['] bands of ND ₃ and rotational constants $B_{v_2^+}$ and $C_{v_2^+}$ of the ionic levels with $v_2^+ = 0, 1$ and 2 determined from the PFI-ZEKE photoelectron spectrum in a least-squares fit. Values in parentheses represent one standard deviation in units of the digits. . . .	42
4.1	Molecular constants (from Signorell [56]) used for the simulation of the PFI-ZEKE photoelectron spectrum of the ND ₄ ⁺ \tilde{X} ¹ A ₁ ← ND ₄ 3s ² A ₁ transitions. . . .	49

4.2	Positions in cm^{-1} of the vibrational bands observed in the PFI-ZEKE photoelectron spectrum of NH_3NH_4 and IR spectroscopy of NH_3NH_4^+ [126, 127].	53
5.1	Overview of the experimental energy levels of Xe reported in the literature.	60
5.2	Summary of the hyperfine Rydberg levels of Xe converging to each hyperfine state F^+ of the ion. The entries are F . The last two lines represent the case $I = 0$, where $F^+ = J^+$ and $F = J$	64
5.3	Rydberg states of ^{132}Xe observed by millimeter-wave spectroscopy. ^a	67
5.4	Rydberg states of ^{129}Xe observed by millimeter-wave spectroscopy. ^a	69
5.5	Rydberg states of ^{131}Xe observed by millimeter-wave spectroscopy. ^a	70
5.5	Rydberg states of ^{131}Xe observed by millimeter-wave spectroscopy. (<i>continued</i>)	71
5.6	MQDT parameters for odd parity states of xenon ^a	76
5.7	s – d and singlet–triplet channel interaction parameters for rare gas atoms ^a	77
5.8	The fine and hyperfine structure of the ^2P ground state of Xe^+ as determined from the MQDT analysis.	78
6.1	Measured and calculated ionization Energy (E_I) and quantum defect (μ) for the np series.	90
6.2	Observed transition wave numbers (cm^{-1}) in the $\text{X}^+ \ ^2\Sigma_u^+ \leftarrow \text{a} \ ^3\Sigma_u^+$ PFI-ZEKE photoelectron spectra of $^4\text{He}_2$ and $^3\text{He}_2$ and differences between observed and calculated line positions $\tilde{\nu}_{\text{obs}} - \tilde{\nu}_{\text{calc}}$ (cm^{-1}). The line positions have been corrected for the field-induced shift of the ionization thresholds. The number of significant figures has been adapted to the experimental accuracy of the relative line positions. The absolute uncertainty amounts to $\pm 0.3 \text{ cm}^{-1}$	96
6.3	Molecular constants for the $\text{a} \ ^3\Sigma_u^+$ state of He_2 and for the ground $\text{X}^+ \ ^2\Sigma_u^+$ state of He_2^+	97
6.4	MQDT parameters for $^4\text{He}_2 [\text{X}^+ \ ^2\Sigma_u^+]np\lambda$ ($^3\Pi_g, ^3\Sigma_g^+$).	101
6.5	Equilibrium and ground state bond length and harmonic wave numbers of $\text{He}_2^+ \ \text{X}^+ \ ^2\Sigma_u^+$	106
6.6	Molecular potential parameters for $^4\text{He}_2$ and $^4\text{He}_2^+$ and term values of the associated states of atomic ^4He	108
A.1	Physical constants from Ref. [308].	119
A.2	Energy conversion factors from Ref. [308].	119

-
- B.1 Experimental positions of $[X^+ \ ^2\Sigma_u^+] np\lambda \ (^3\Pi_g, \ ^3\Sigma_g^+)$ N, v Rydberg levels of $^4\text{He}_2$ (relative to the position of the (hypothetical) $N = 0, v = 0$ level of a $^3\Sigma_u^+$) and differences between observed and calculated values. # designates the number of the level within the N block of the calculation. Rydberg levels with $n \leq 17$ are taken from Ginter *et al.*, J. Chem. Phys. **81** 6013 (1984), Ginter and Ginter, J. Mol. Spectrosc. **82** 152 (1980), Orth and Ginter, J. Mol. Spectrosc. **61** 282 (1976), **64** 223 (1977). 121

Bibliography

- [1] R. S. Freund, High-Rydberg molecules, in *Rydberg states of atoms and molecules*, edited by R. F. Stebbings and F. B. Duning, pages 355–392, Cambridge University Press, Cambridge, 1983.
- [2] H. Hotop, Detection of metastable atoms and molecules, in *Atomic, Molecular and Optical Physics: Atoms and Molecules – Experimental Methods in the Physical Sciences*, edited by F. B. Duning and R. G. Hulet, volume 29B, pages 191–215, Academic Press, San Diego, 1996.
- [3] G. Herzberg, *Molecular Spectra and Molecular Structure, Volume I, Spectra of Diatomic Molecules*, Krieger Publishing Company: Malabar, 2nd edition, 1989.
- [4] G. Herzberg, *Molecular Spectra and Molecular Structure, Volume II, Infrared and Raman Spectra of Polyatomic Molecules*, Krieger Publishing Company: Malabar, 1991.
- [5] G. Herzberg, *Molecular Spectra and Molecular Structure, Volume III, Electronic Spectra and Electronic Structure of Polyatomic Molecules*, Krieger Publishing Company: Malabar, 2nd edition, 1991.
- [6] G. Reiser, W. Habenicht, K. Müller-Dethlefs, and E. W. Schlag, The ionization energy of nitric oxide, *Chem. Phys. Lett.* **152**(2–3), 119–123 (1988).
- [7] K. Müller-Dethlefs and E. W. Schlag, High-Resolution Zero Kinetic Energy (ZEKE) Photoelectron Spectroscopy of Molecular Systems, *Ann. Rev. Phys. Chem.* **42**, 109–136 (1991).
- [8] L. Zhu and P. Johnson, Mass analyzed threshold ionization spectroscopy, *J. Chem. Phys.* **94**(8), 5769–5771 (1991).
- [9] J. G. Goode, J. E. LeClaire, and P. M. Johnson, Probing the photoinduced Rydberg ionization process, *Int. J. Mass Spectrom. Ion Processes* **159**(1–3), 49–64 (1996).
- [10] D. P. Taylor, J. G. Goode, J. E. LeClaire, and P. M. Johnson, Photoinduced Rydberg ionization spectroscopy, *J. Chem. Phys.* **103**(14), 6293–6295 (1995).

- [11] H. Xu, N. E. Shafer-Ray, F. Merkt, D. J. Hughes, M. Springer, R. P. Tuckett, and R. N. Zare, Measurement of the state-specific differential cross section for the $\text{H}+\text{D}_2 \rightarrow \text{HD}(v'=4, J'=3)+\text{D}$ reaction at a collision energy of 2.2 eV, *J. Chem. Phys.* **103**(12), 5157–5160 (1995).
- [12] C. Lin, M. F. Witinski, and H. F. Davis, Oxygen atom Rydberg time-of-flight spectroscopy, *J. Chem. Phys.* , 251 (2003).
- [13] B. Jones, J. Zhou, L. Yang, and C. Y. Ng, High-resolution Rydberg tagging time-of-flight measurements of atomic photofragments by single-photon vacuum ultraviolet laser excitation, *Rev. Sci. Instr.* **79**, 123106 (2008).
- [14] T. F. Gallagher, *Rydberg Atoms*, Cambridge University Press: Cambridge, 1994.
- [15] W. A. Chupka, Factors affecting lifetimes and resolution of Rydberg states observed in zero-electron-kinetic-energy spectroscopy, *J. Chem. Phys.* **98**(6), 4520–4530 (1993).
- [16] F. Merkt, Molecules in High Rydberg States, *Ann. Rev. Phys. Chem.* **48**, 675–709 (1997).
- [17] A. Osterwalder and F. Merkt, Using High Rydberg States as Electric Field Sensors, *Phys. Rev. Lett.* **82**(9), 1831–1834 (1999).
- [18] E. Vliegen, S. D. Hogan, H. Schmutz, and F. Merkt, Stark deceleration and trapping of hydrogen Rydberg atoms, *Phys. Rev. A* **76**(2), 023405 (2007).
- [19] E. Vliegen and F. Merkt, Stark deceleration of hydrogen atoms, *J. Phys. B: At. Mol. Opt. Phys.* **39**(11), L241–L247 (2006).
- [20] S. D. Hogan and F. Merkt, Demonstration of Three-Dimensional Electrostatic Trapping of State-Selected Rydberg Atoms, *Phys. Rev. Lett.* **100**(4), 043001 (2008).
- [21] F. Merkt and R. N. Zare, On the lifetimes of Rydberg states probed by delayed pulsed field ionization, *J. Chem. Phys.* **101**(5), 3495–3505 (1994).
- [22] F. Merkt, A. Osterwalder, R. Seiler, R. Signorell, H. Palm, H. Schmutz, and R. Gunzinger, High Rydberg states of argon: Stark effect and field-ionization properties, *J. Phys. B: At. Mol. Opt. Phys.* **31**(8), 1705–1724 (1998).
- [23] F. Merkt and A. Osterwalder, Millimeter wave spectroscopy of high Rydberg states, *Int. Rev. Phys. Chem.* **21**(3), 385–403 (2002).

-
- [24] R. Hilbig, G. Hilber, A. Lago, B. Wolff, and R. Wallenstein, Tunable Coherent VUV Radiation Generated by Nonlinear Optical Frequency Conversion in Gases, *Comments At. Mol. Phys.* **18**(4), 157–180 (1986).
- [25] C. R. Vidal, Four-Wave Frequency Mixing in Gases, in *Topics in Applied Physics*, edited by L. F. Mollenauer and J. C. White, volume 59: Tunable Lasers, chapter 3, pages 57–113, Springer-Verlag: Berlin, 1987.
- [26] F. Merkt, *Generation and Spectroscopic Applications of Coherent Extreme Ultraviolet (XUV) Radiation*, PhD thesis, University of Cambridge, 1992.
- [27] H. Palm and F. Merkt, Generation of tunable coherent extreme ultraviolet radiation beyond 19 eV by resonant four-wave mixing in argon, *Appl. Phys. Lett.* **73**(2), 157–159 (1998).
- [28] W. Ubachs, *Nonlinear Optics*, Lecture Notes, Vrije Universiteit Amsterdam, 2001.
- [29] U. Hollenstein, *Erzeugung und spektroskopische Anwendungen von schmalbandiger, kohärenter, vakuum-ultravioletter Strahlung*, PhD thesis, Eidgenössische Technische Hochschule Zürich, ETH Zürich, CH-8093 Zürich, Switzerland, 2003, Diss. ETH Nr. 15237.
- [30] F. M. Phelps III, editor, *M.I.T. Wavelength Tables*, volume 2, Wavelengths by Element, MIT Press: Cambridge, MA, 1982.
- [31] Y. Ralchenko, F.-C. Jou, D. E. Kelleher, A. E. Kramida, A. Musgrove, J. Reader, W. L. Wiese, and K. Olsen, NIST Atomic Spectra Database, Version 3.1.3, 2007.
- [32] S. Gerstenkorn and P. Luc, *Atlas du Spectre d’Absorption de la Molécule d’Iode: 14 800–20 000 cm^{-1}* , Laboratoire Aimé-Cotton CNRS II, Orsay, 1979, see correction in [309].
- [33] S. Gerstenkorn, J. Vergès, and J. Chevillard, *Atlas du Spectre d’Absorption de la Molécule d’Iode: 11 000–14 000 cm^{-1}* , Laboratoire Aimé-Cotton CNRS II, Orsay, 1982, see correction in [309].
- [34] S. Gerstenkorn and P. Luc, *Atlas du Spectre d’Absorption de la Molécule d’Iode: 14 000–15 600 cm^{-1}* , Laboratoire Aimé-Cotton CNRS II, Orsay, 1986, see correction in [309].
- [35] F. Merkt and H. Schmutz, Very high resolution spectroscopy of high Rydberg states of the argon atom, *J. Chem. Phys.* **108**(24), 10033–10045 (1998).

- [36] M. Schäfer, M. Andrist, H. Schmutz, F. Lewen, G. Winnewisser, and F. Merkt, A 240–380 GHz millimetre wave source for very high resolution spectroscopy of high Rydberg states, *J. Phys. B: At. Mol. Opt. Phys.* **39**(4), 831–845 (2006).
- [37] F. M. Gardner, *Phaselock Techniques*, John Wiley & Sons Ltd.: New York, New York, 1979.
- [38] Y. Ohshima and Y. Endo, Structure of C₃S studied by pulsed-discharge-nozzle Fourier-transform microwave spectroscopy, *J. Mol. Spectrosc.* **153**(1–2), 627–634 (1992).
- [39] B. Brupbacher-Gatehouse and Th. Brupbacher, The molecular geometry, harmonic force field, bonding characteristics, and nuclear shielding parameters of OPCl, as determined from high resolution microwave spectra, *J. Chem. Phys.* **111**(14), 6300–6310 (1999).
- [40] W. W. Harrison, W. Hang, X. Yan, K. Ingeneri, and C. Shilling, Temporal Considerations With a Microsecond Pulsed Glow Discharge, *J. Anal. At. Spectrom.* **12**, 891 (1997).
- [41] W. W. Harrison, Pulsed glow discharge as a solids analysis source, *J. Anal. At. Spectrom.* **13**, 1051 (1998).
- [42] W. W. Harrison, C. Yang, and E. Oxley, Peer Reviewed: Pulsed Glow Discharge: Temporal Resolution in Analytical Spectroscopy, *Anal. Chem.* **73**, 480A (2001).
- [43] X. Yan, W. Hang, B. W. Smith, J. D. Winefordner, and W. W. Harrison, Primary studies of the microsecond pulsed glow discharge as an emission source using a conventional hollow cathode lamp, *J. Anal. At. Spectrom.* **13**, 1033 (1998).
- [44] C. Yang and W. W. Harrison, Investigation of a novel hollow cathode configuration for Grimm-type glow discharge emission, *Spectrochim. Acta, Part B* **56**, 1195 (2001).
- [45] X. Yan, K. Ingeneri, W. Hang, and W. W. Harrison, Factors influencing signal profiles in microsecond pulsed glow discharge atomic emission spectrometry, *J. Anal. At. Spectrom.* **16**, 819 (2001).
- [46] S. Potapov, E. Izrailov, V. Vergizova, M. Voronov, S. Suprunovich, M. Slyadnev, and A. Ganeev, Pulsed glow discharge in thin-walled metallic hollow cathode. Analytical possibilities in atomic and mass spectrometry, *J. Anal. At. Spectrom.* **18**, 564 (2003).

-
- [47] F. M. Penning, Über Ionisation durch metastabile Atome, *Naturwissenschaften* **15**, 818 (1927).
- [48] T. Oka, K. V. S. Rama Rao, J. L. Redpath, and R. F. Firestone, Mechanism for decay and spontaneous radiative decay constants of the lowest-lying attractive excited states of Ne₂, Ar₂, and Kr₂, *J. Chem. Phys.* **61**(11), 4740–4746 (1974).
- [49] S. D. Hogan, D. Sprecher, M. Andrist, N. Vanhaecke, and F. Merkt, Zeeman deceleration of H and D, *Phys. Rev. A* **76**(2), 023412 (2007).
- [50] S. D. Hogan, A. W. Wiederkehr, H. Schmutz, and F. Merkt, Magnetic trapping of hydrogen after multistage Zeeman deceleration, *Phys. Rev. Lett.* **101**(14), 143001 (2008).
- [51] S. Willitsch, J. M. Dyke, and F. Merkt, Generation and High-Resolution Photoelectron Spectroscopy of Small Organic Radicals in Cold Supersonic Expansions, *Helv. Chim. Acta* **86**(4), 1152–1166 (2003).
- [52] S. Willitsch, J. M. Dyke, and F. Merkt, Rotationally resolved photoelectron spectrum of the lowest singlet electronic state of NH₂⁺ and ND₂⁺: photoionization dynamics and rovibrational energy level structure of the $\tilde{a}^+ \ ^1A_1$ state, *Mol. Phys.* **102**(14–15), 1543–1553 (2004).
- [53] H. J. Wörner and F. Merkt, Diradicals, antiaromaticity, and the pseudo-Jahn-Teller effect: Electronic and rovibronic structures of the cyclopentadienyl cation, *J. Chem. Phys.* **127**(3), 034303 (2007).
- [54] A. M. Schulenburg, Ch. Alcaraz, G. Grassi, and F. Merkt, Rovibrational photoionization dynamics of methyl and its isotopomers studied by high-resolution photoionization and photoelectron spectroscopy, *J. Chem. Phys.* **125**(10), 104310 (2006).
- [55] H. Palm, R. Signorell, and F. Merkt, On the Role of Ions in Pulsed Field Ionization Zero-Kinetic-Energy Photoelectron Spectroscopy, *Phil. Trans. R. Soc. London Ser. A* **355**(1729), 1551–1568 (1997).
- [56] R. Signorell, H. Palm, and F. Merkt, Structure of the ammonium radical from a rotationally resolved photoelectron spectrum, *J. Chem. Phys.* **106**(16), 6523–6533 (1997).
- [57] J. Berkowitz, *Photoabsorption, photoionization and photoelectron spectroscopy*, Academic Press: New York, 1979.
- [58] J. Berkowitz, *VUV and Soft X-Ray Photoionization*, Plenum Press: New York, 1996.

- [59] U. Hollenstein, R. Seiler, H. Schmutz, M. Andrist, and F. Merkt, Selective field ionization of high Rydberg states: Application to zero-kinetic-energy photoelectron spectroscopy, *J. Chem. Phys.* **115**(12), 5461–5469 (2001).
- [60] D. W. Turner, C. Baker, A. D. Baker, and C. R. Brundle, *Molecular Photoelectron Spectroscopy: A Handbook of He 584 Å Spectra*, John Wiley & Sons Ltd.: New York, 1970.
- [61] K. Siegbahn, C. Nordling, G. Johansson, J. Hedman, P. F. Hedén, K. Hamrin, U. Gelius, T. Bergmark, L. O. Werme, R. Manne, and Y. Baer, *ESCA, applied to free molecules*, North-Holland: Amsterdam, 1969.
- [62] H.-J. Dietrich, K. Müller-Dethlefs, and L. Y. Baranov, Fractional Stark State Selective Electric Field Ionization of Very High- n Rydberg States of Molecules, *Phys. Rev. Lett.* **76**(19), 3530–3533 (1996).
- [63] F. Merkt, H. Xu, and R. N. Zare, Preparation and characterization of long-lived molecular Rydberg states: Application to HD, *J. Chem. Phys.* **104**(3), 950–961 (1996).
- [64] S. Willitsch, U. Hollenstein, and F. Merkt, Ionization from a double bond: Rovibronic photoionization dynamics of ethylene, large amplitude torsional motion and vibronic coupling in the ground state of $C_2H_4^+$, *J. Chem. Phys.* **120**(4), 1761–1774 (2004).
- [65] S. Willitsch, F. Innocenti, J. M. Dyke, and F. Merkt, High-resolution pulsed-field-ionization zero-kinetic-energy photoelectron spectroscopic study of the two lowest electronic states of the ozone cation O_3^+ , *J. Chem. Phys.* **122**(2), 024311 (2005).
- [66] H. J. Wörner, S. Mollet, Ch. Jungen, and F. Merkt, Role of spins in molecular photoionization: Spectroscopy and dynamics of autoionizing Rydberg states of ortho- H_2 , *Phys. Rev. A* **75**(6), 062511 (2007).
- [67] A. Schulenburg and F. Merkt, accepted.
- [68] F. Merkt and T. P. Softley, Rotational Line Intensities in Zero Kinetic Energy Photoelectron Spectroscopy (ZEKE-PES), *Int. Rev. Phys. Chem.* **12**, 205–239 (1993).
- [69] F. Merkt and T. P. Softley, Final-state interactions in the zero-kinetic-energy-photoelectron spectrum of H_2 , *J. Chem. Phys.* **96**(6), 4149–4156 (1992).
- [70] F. Merkt and T. P. Softley, Rotationally resolved zero-kinetic-energy photoelectron spectrum of nitrogen, *Phys. Rev. A* **46**(1), 302–314 (1992).

-
- [71] T. P. Softley, A. J. Hudson, and R. Watson, Multichannel quantum defect theory Stark effect calculation of autoionization lifetimes in high- n Rydberg states of Ar, N₂ and H₂, *J. Chem. Phys.* **106**(3), 1041–1056 (1997).
- [72] H. Dickinson, D. Rolland, and T. P. Softley, Rotational Propensities in the State Selection of NH₃⁺ by Pulsed-Field Ionization, *Phil. Trans. R. Soc. London Ser. A* **355**(1729, Molecular Rydberg Dynamics), 1585–1607 (1997).
- [73] A. Osterwalder, A. Wüest, F. Merkt, and Ch. Jungen, High-resolution millimeter wave spectroscopy and multichannel quantum defect theory of the hyperfine structure in high Rydberg states of molecular hydrogen H₂, *J. Chem. Phys.* **121**(23), 11810–11838 (2004).
- [74] M. Schäfer and F. Merkt, Millimeter wave spectroscopy and multichannel quantum-defect-theory analysis of high Rydberg states of krypton: The hyperfine structure of ⁸³Kr⁺, *Phys. Rev. A* **74**(6), 062506 (2006).
- [75] H. A. Cruse, Ch. Jungen, and F. Merkt, Hyperfine structure of the ground state of para-D₂⁺ by high-resolution Rydberg-state spectroscopy and multichannel quantum defect theory, *Phys. Rev. A* **77**(4), 042502 (2008).
- [76] M. Snels, H. Hollenstein, and M. Quack, The NH and ND stretching fundamentals of ¹⁴ND₂H, *J. Chem. Phys.* **119**, 7893 (2003).
- [77] R. Marquardt, M. Quack, I. Thanopoulos, and D. Luckhaus, Tunneling dynamics of the NH chromophore in NHD₂ during and after coherent infrared excitation, *J. Chem. Phys.* **118**, 643 (2003).
- [78] D. Papoušek, The story of the ammonia molecule: Ten years of investigation of molecular inversion, *J. Mol. Struct.* **100**, 179 (1983).
- [79] Š. Urban, D. Papoušek, S. P. Belov, A. F. Krupnov, M. Y. Tret'yakov, K. Yamada, and G. Winnewisser, A simultaneous analysis of the microwave, submillimeter-wave, and infrared transitions between the ground and v_2 inversion-rotation levels of ¹⁵NH₃, *J. Mol. Spectrosc.* **101**(1), 16 (1983).
- [80] L. Fusina and S. N. Murzin, Inversion Spectrum and Ground State Spectroscopic Parameters of ¹⁴ND₃, *J. Mol. Spectrosc.* **167**(2), 464 (1994).
- [81] P. R. Bunker and P. Jensen, *Molecular Symmetry and Spectroscopy*, NRC Research Press: Ottawa, 2nd edition, 1998.

- [82] C. A. Coulson and H. L. Strauss, Static Jahn-Teller Distortions in the Small Molecules: CH_4^+ , CF_4^+ , NH_3^+ (excited State) and NH_3 (excited State), Proc. R. Soc. London Ser. A **269**(1339), 443–455 (1962).
- [83] J. H. Glowina, S. J. Riley, S. D. Colson, and G. C. Nieman, The MPI spectrum of expansion-cooled ammonia: Photophysics and new assignments of electronic excited states, J. Chem. Phys. **73**, 4296 (1980).
- [84] C. A. Raptis and S. T. Pratt, Rotational interactions in autoionizing Rydberg states of ammonia, Chem. Phys. Lett. **303**(3-4), 281 (1999).
- [85] W. E. Conaway, R. J. S. Morrison, and R. N. Zare, Vibrational state selection of ammonia ions using resonant $2 + 1$ multiphoton ionization, Chem. Phys. Lett. **113**(5), 429 (1985).
- [86] D. T. Cramb and S. C. Wallace, Rydberg states near the ionization continuum: Autoionization in ammonia, J. Chem. Phys. **101**, 6523 (1994).
- [87] J. W. Rabalais, L. Karlsson, L. O. Werme, T. Bergmark, and K. Siegbahn, Analysis of vibrational structure and Jahn-Teller effects in the electron spectrum of ammonia, J. Chem. Phys. **58**, 3370 (1973).
- [88] M. G. Bawendi, B. D. Rehfuss, B. M. Dinelli, M. Okumura, and T. Oka, Observation and analysis of the v_3 band of NH_3^+ , J. Chem. Phys. **90**, 5910 (1989).
- [89] S. S. Lee and T. Oka, Diode laser spectroscopy of the v_2 fundamental and hot bands of NH_3^+ , J. Chem. Phys. **94**, 1698 (1991).
- [90] T. R. Huet, Y. Kabbadj, C. M. Gabrys, and T. Oka, The $v_2 + v_3 - v_2$ Band of NH_3^+ , J. Mol. Spectrosc. **163**(1), 206 (1994).
- [91] W. Habenicht, G. Reiser, and K. Müller-Dethlefs, High-resolution zero kinetic energy electron spectroscopy of ammonia, J. Chem. Phys. **95**(7), 4809–4820 (1991).
- [92] B. Niu and M. G. White, Geometry changes in molecular photoionization: The NH_3^+ (\tilde{X}^2A_2') \leftarrow NH_3 (X^1A_1) transition, J. Chem. Phys. **104**(6), 2136–2145 (1996).
- [93] M.-K. Bahng, X. Xing, S. J. Baek, and C. Y. Ng, A two-color infrared-vacuum ultraviolet laser pulsed field ionization photoelectron study of NH_3 , J. Chem. Phys. **123**, 084311 (2005).
- [94] M.-K. Bahng, X. Xing, S. J. Baek, X. Qian, and C. Y. Ng, A Combined VUV Synchrotron Pulsed Field Ionization-Photoelectron and IR-VUV Laser Photoion Depletion Study of Ammonia, J. Phys. Chem. A **110**(27), 8488 (2006).

-
- [95] R. Seiler, U. Hollenstein, T. P. Softley, and F. Merkt, High-resolution threshold-ionization spectroscopy of NH_3 , *J. Chem. Phys.* **118**(22), 10024–10033 (2003).
- [96] U. Hollenstein, F. Merkt, L. Meyer, R. Seiler, T. P. Softley, and S. Willitsch, Rovibronic photoionization dynamics of ammonia isotopomers, *Mol. Phys.* **105**(11–12), 1711–1722 (2007).
- [97] R. Signorell and F. Merkt, General symmetry selection rules for the photoionization of polyatomic molecules, *Mol. Phys.* **92**(5), 793–804 (1997).
- [98] S. Willitsch and F. Merkt, Rovibronic photoionization dynamics of asymmetric-top molecules, *Int. J. Mass Spectrom.* **245**(1–3), 14–25 (2005).
- [99] R. N. Zare, *Angular Momentum*, John Wiley & Sons: New York, 1988.
- [100] L. Duggan, T. P. Softley, M. Raunhardt, R. Seiler, and F. Merkt, unpublished results.
- [101] P. Farmanara, W. Radloff, V. Stert, H.-H. Ritze, and I. V. Hertel, Real time observation of hydrogen transfer: Femtosecond time-resolved photoelectron spectroscopy in the excited ammonia dimer, *J. Chem. Phys.* **111**(2), 633 (1999).
- [102] J. K. Park and S. Iwata, Ab Initio Study of Photochemical Reactions of Ammonia Dimer Systems, *J. Phys. Chem. A* **101**, 3613 (1997).
- [103] S. Tomoda, Ionization of the ammonia dimer: Proton transfer in the ionic state, *Chem. Phys.* **110**, 431 (1986).
- [104] J. C. Greer, R. Ahlrichs, and I. V. Hertel, Proton transfer in ammonia cluster cations: molecular dynamics in a self consistent field, *Z. Phys. D: Atoms, Molecules and Clusters* **18**, 413 (1991).
- [105] J. C. Greer, R. Ahlrichs, and I. V. Hertel, Binding energies and structures of NH_3 clusters, *Chem. Phys.* **133**(2), 191 (1989).
- [106] O. Echt, P. D. Dao, S. Morgan, and J. A. W. Castleman, Multiphoton ionization of ammonia clusters and the dissociation dynamics of protonated cluster ions, *J. Chem. Phys.* **82**, 4076 (1985).
- [107] H. Shinohara and N. Nishi, Resonance-enhanced 2PI detection of ammonia clusters via a linear reflectron TOF mass spectrometer, *Chem. Phys. Lett.* **141**(4), 292 (1987).
- [108] S. Wei, W. B. Tzeng, and J. A. W. Castleman, Dissociation dynamics: Measurements of decay fractions of metastable ammonia cluster ions, *J. Chem. Phys.* **93**, 2506 (1990).

- [109] S. T. Ceyer, P. W. Tiedemann, B. H. Mahan, and Y. T. Lee, Energetics of gas phase proton solvation by NH_3 , *J. Chem. Phys.* **70**, 14 (1979).
- [110] E. Kaiser, J. de Vries, H. Steger, C. Menzel, W. Kamke, and I. V. Hertel, Fragmentation dynamics of ammonia cluster ions after single photon ionization, *Z. Phys. D: Atoms, Molecules and Clusters* **20**(1–4), 193–196 (1991).
- [111] K. Stephan, J. Futrell, K. Peterson, A. C. Jr., H. Wager, N. Djuric, and T. Mark, An electron-impact study of ammonia clusters in a supersonic molecular beam: appearance potentials of NH_4^+ , $(\text{NH}_3)_2^+$, $(\text{NH}_3)_2\text{H}^+$, $(\text{NH}_3)_3^+$, $(\text{NH}_3)\text{H}^+$ and $(\text{NH}_2\text{NH}_3)^+$, *Int. J. Mass Spectrom. Ion Physics* **44**, 167 (1982).
- [112] L. Posey, R. Guettler, N. Kirchner, and R. Zare, Influence of vibrational excitation and collision energy on the ion-molecule reaction $\text{NH}_3^+(\nu_2) + \text{ND}_3$, *J. Chem. Phys.* **101**, 3772 (1994).
- [113] E. M. Snyder, J. Purnell, S. Wei, S. A. Buzza, and A. W. Castleman Jr., Real-time dynamics of ammonia clusters excited through the $\tilde{\text{A}}$ state: formation of the protonated cluster ions, *Chem. Phys.* **207**(2–3), 355–366 (1996).
- [114] T. Freudenberg, W. Radloff, H.-H. Ritze, V. Stert, K. Weyers, F. Noack, and I. V. Hertel, Ultrafast fragmentation and ionisation dynamics of ammonia clusters, *Z. Phys. D: Atoms, Molecules and Clusters* **36**(3–4), 349–364 (1996).
- [115] M. N. R. Ashfold, C. L. Bennett, and R. N. Dixon, Dissociation dynamics of $\text{NH}_3(\tilde{\text{A}}^1\text{A}_2'')$. Experiment and theory, *Faraday Discuss. Chem. Soc.* **82**, 163 (1986).
- [116] W. Kamke, R. Herrmann, Z. Wang, and I. V. Hertel, On the photoionization and fragmentation of ammonia clusters using TPEPICO, *Z. Phys. D: Atoms, Molecules and Clusters* **10**, 491 (1988).
- [117] K. Fuke, R. Takasu, and F. Misaizu, Photoionization of hypervalent molecular clusters: electronic structure and stability of $\text{NH}_4(\text{NH}_3)_n$, *Chem. Phys. Lett.* **229**(6), 597–603 (1994).
- [118] F. Misaizu, P. L. Houston, N. Nishi, H. Shinohara, T. Kondow, and M. Kinoshita, Formation of protonated ammonia cluster ions: Two-color two-photon ionization study, *J. Chem. Phys.* **98**(1), 336–341 (1993).
- [119] S. Wei, J. Purnell, S. A. Buzza, and A. W. Castleman Jr., Ultrafast reaction dynamics of electronically excited $\tilde{\text{A}}$ state of ammonia clusters, *J. Chem. Phys.* **99**(1), 755–757 (1993).

- [120] P. Farmanara, H.-H. Ritze, V. Stert, W. Radloff, and I. V. Hertel, Ultrafast photodissociation dynamics and energetics of the electronically excited H atom transfer state of the ammonia dimer and trimer, *J. Chem. Phys.* **116**(4), 1443 (2002).
- [121] T. Freudenberg, W. Radloff, H.-H. Ritze, V. Stert, F. Noack, and I.V.Hertel, Ultrafast dynamics in ammonia clusters: analysis of protonated and unprotonated cluster ion signals, *Z. Phys. D: Atoms, Molecules and Clusters* **41**, 267 (1997).
- [122] G. I. Gellene, D. A. Cleary, and R. F. Porter, Stability of the ammonium and methylammonium radicals from neutralized ion-beam spectroscopy, *J. Chem. Phys.* **77**(7), 3471–3477 (1982).
- [123] G. Herzberg, Spectra of the Ammonium Radical: The Schüler Bands, *J. Astrophys. Astron.* **5**(2), 131–138 (1984).
- [124] F. Alberti, K. P. Huber, and J. K. G. Watson, Absorption spectrum and analysis of the ND₄ Schüler band, *J. Mol. Spectrosc.* **107**(1), 133–143 (1984).
- [125] J. K. G. Watson, *NBS Spec. Publ.* **716**, 650 (1986).
- [126] K. R. Asmis, Y. Yang, G. Santambrogio, M. Brümmer, J. R. Roscioli, L. R. McCunn, M. A. Johnson, and O. Kühn, Gas-Phase Infrared Spectroscopy and Multidimensional Quantum Calculations of the Protonated Ammonia Dimer N₂H₇⁺, *Angew. Chem. (int. ed. engl.)* **46**, 8691 (2007).
- [127] Y. Yang, O. Kühn, G. Santambrogio, D. J. Goebbert, and K. R. Asmis, Vibrational signatures of hydrogen bonding in the protonated ammonia clusters NH₄⁺(NH₃)_{1–4}, *J. Chem. Phys.* **129**, 224302 (2008).
- [128] P. García-Fernández, L. García-Canales, J. M. García-Lastra, J. Junquera, M. Moreno, and J. A. Aramburu, Pseudo-Jahn-Teller origin of the low barrier hydrogen bond in N₂H₇⁺, *J. Chem. Phys.* **129**, 124313 (2008).
- [129] G. I. Gellene and R. F. Porter, An experimental study of hypervalent molecular clusters by neutralized ion beam spectroscopy: ammonium-ammonia (NH₄(NH₃)_n) and deuterated ammonium-ammonia (ND₄(ND₃)_n), *J. Phys. Chem.* **88**(26), 6680 (1984).
- [130] S. J. Jeon, A. B. Raksit, G. I. Gellene, and R. F. Porter, Formation of hypervalent ammoniated radicals by neutralized ion beam techniques, *J. Am. Chem. Soc.* **107**(14), 4129 (1985).

- [131] K. Fuke and R. Takasu, Ultrafast Photochemistry of Ammonia Clusters: Formation and Decay of Hypervalent Molecular Clusters Containing the NH_4 Radical, *Bull. Chem. Soc. Jpn.* **68**, 3309 (1995).
- [132] N. Okai, A. Takahata, M. Morita, S. Nonose, and K. Fuke, Ultrafast Relaxation Process of Excited-State NH_4 Radical in Ammonia Clusters, *J. Phys. Chem. A* **108**, 727 (2004).
- [133] R. Takasu, K. Fuke, and F. Misaizu, Electronic structure and stability of $\text{NH}_4(\text{NH}_3)_n$ and $\text{NH}_4(\text{NH}_3)_m(\text{H}_2\text{O})_n$, *Surf. Rev. Lett.* **3**(1), 353 (1996).
- [134] S. Wei, J. Purnell, S. A. Buzza, R. J. Stanley, and J. A. W. Castleman, Femtosecond multiphoton ionization of ammonia clusters, *J. Chem. Phys.* **97**, 9480 (1992).
- [135] H. J. Wörner, M. Grütter, E. Vliegen, and F. Merkt, Role of nuclear spin in photoionization: Hyperfine-resolved photoionization of Xe and multichannel quantum defect theory analysis, *Phys. Rev. A* **71**(5), 052504 (2005), see erratum in *Phys. Rev. A* **73**, 059904(E) (2006).
- [136] T. Paul and F. Merkt, Isotope-resolved measurement of the high, odd parity, autoionizing Rydberg states of krypton by high-resolution XUV spectroscopy, (2008), to be published.
- [137] Th. A. Paul, J. Liu, and F. Merkt, Nuclear spin effects in the photoionization of krypton, *Phys. Rev. A* (2009), accepted.
- [138] G. Herzberg and Ch. Jungen, Rydberg series and ionization potential of the H_2 molecule, *J. Mol. Spectrosc.* **41**(3), 425–486 (1972).
- [139] M. Schäfer and F. Merkt, Structure und dynamics of high Rydberg states studied by high-resolution spectroscopy and multichannel quantum defect theory, in *Frontiers of Molecular Spectroscopy*, edited by J. Laane, Elsevier, 2008, in press.
- [140] H. J. Wörner, U. Hollenstein, and F. Merkt, Multichannel quantum defect theory of the hyperfine structure of high Rydberg states of ^{83}Kr , *Phys. Rev. A* **68**(3), 032510 (2003).
- [141] F. Brandi, I. Velchev, W. Hogervorst, and W. Ubachs, Vacuum-ultraviolet spectroscopy of Xe: Hyperfine splittings, isotope shifts, and isotope-dependent ionization energies, *Phys. Rev. A* **64**(3), 032505 (2001).
- [142] M. Schäfer and F. Merkt, Millimetre Wave Spectroscopy and MQDT Calculations of High Rydberg States, in *FUNDAMENTAL AND APPLIED SPECTROSCOPY:*

- Second International Spectroscopy Conference, ISC 2007*, edited by M. Telmini, N. T. Mliki, and E. Sediki, volume 935, pages 214–219, 2007.
- [143] C. E. Moore, *Atomic Energy Levels*, Nat. Bu. Stan. US. Circular 467/3, U.S. GPO: Washington D.C., 1958.
- [144] M. Thekaekara and G. H. Dieke, Emission Lines from Preionized Levels in Krypton and Xenon, *Phys. Rev.* **109**(6), 2029–2031 (1958).
- [145] W. L. Faust and M. N. McDermott, Hyperfine Structure of the $(5p)^5(6s) \ ^3P_2$ State of $_{54}\text{Xe}^{129}$ and $_{54}\text{Xe}^{131}$, *Phys. Rev.* **123**(1), 198–204 (1961).
- [146] C. J. Humphreys, E. Paul, Jr., R. D. Cowan, and K. L. Andrew, Spectra of the Noble Gases in the 4 Micrometer Region, *J. Opt. Soc. Am.* **57**(7), 855–864 (1967).
- [147] C. J. Humphreys and E. Paul, Jr., Interferometric Wavelength Determination in the First Spectrum of ^{136}Xe , *J. Opt. Soc. Am.* **60**(10), 1302–1310 (1970).
- [148] D. A. Jackson and M. C. Coulombe, Hyperfine Structure in the Arc Spectrum of Xenon, *Proc. R. Soc. London Ser. A* **327**(1569), 137–145 (1972).
- [149] W. Fischer, H. Hühnermann, G. Krömer, and H. J. Schäfer, Isotope shifts in the atomic spectrum of xenon and nuclear deformation effects, *Z. Phys.* **270**(2), 113–120 (1974).
- [150] D. A. Jackson and M.-C. Coulombe, Isotope Shifts in the Arc Spectrum of Xenon, *Proc. R. Soc. London Ser. A* **338**(1614), 277–298 (1974).
- [151] D. A. Jackson, M.-C. Coulombe, and J. Bauche, Interpretation of the Isotope Shifts in the Arc Spectrum of Xenon, *Proc. R. Soc. London Ser. A* **343**(1635), 443–451 (1975).
- [152] D. A. Jackson and M.-C. Coulombe, Isotope Shifts in the Arc Spectrum of Xenon. II, *Proc. R. Soc. London Ser. A* **343**(1635), 453–459 (1975).
- [153] J.-P. Grandin and X. Husson, Even-parity Rydberg and autoionising states in xenon, *J. Phys. B: At. Mol. Phys.* **14**(3), 433–440 (1981).
- [154] H. Gerhardt, F. Jeschonnek, W. Makat, E. Matthias, H. Rinneberg, F. Schneider, A. Timmermann, R. Wenz, and P. J. West, Nuclear charge radii and nuclear moments of Kr and Xe isotopes by high resolution laser spectroscopy, *Hyperfine Interactions* **9**(1–4), 175–179 (1981).
- [155] P. Labastie, F. Biraben, and E. Giacobino, Optogalvanic spectroscopy of the ns and nd Rydberg states of xenon, *J. Phys. B: At. Mol. Phys.* **15**(16), 2595–2603 (1982).

- [156] K. Yoshino and D. E. Freeman, Absorption spectrum of xenon in the vacuum-ultraviolet region, *J. Opt. Soc. Am. B* **2**(8), 1268–1274 (1985).
- [157] K. D. Bonin, T. J. McIlrath, and K. Yoshino, High-resolution laser and classical spectroscopy of xenon autoionization, *J. Opt. Soc. Am. B* **2**(8), 1275–1283 (1985).
- [158] R. D. Knight and L. guo Wang, One-photon laser spectroscopy of the np and nf Rydberg series in xenon, *J. Opt. Soc. Am. B* **2**(7), 1084–1087 (1985).
- [159] R. D. Knight and L. guo Wang, Stark structure in Rydberg states of xenon, *Phys. Rev. A* **32**(2), 896–900 (1985).
- [160] R. D. Knight and L. guo Wang, $J = 1$ even-parity autoionization in xenon, *J. Opt. Soc. Am. B* **3**(12), 1673–1677 (1986).
- [161] L. Wang and R. D. Knight, 2-Photon Laser Spectroscopy of the ns' and nd' Autoionizing Rydberg Series in Xenon, *Phys. Rev. A* **34**(5), 3902–3907 (1986).
- [162] P. R. Blazewicz, J. A. D. Stockdale, J. C. Miller, T. Efthimiopoulos, and C. Fotakis, Four-photon excitation of even-parity Rydberg states in krypton and xenon, *Phys. Rev. A* **35**(3), 1092–1098 (1987).
- [163] W. E. Ernst, T. P. Softley, and R. N. Zare, Stark-effect studies in xenon autoionizing Rydberg states using a tunable extreme-ultraviolet laser source, *Phys. Rev. A* **37**(11), 4172–4183 (1988).
- [164] A. L'Huillier, L.-A. Lompre, D. Normand, J. Morellec, M. Ferray, J. Lavancier, G. Mainfray, and C. Manus, Spectroscopy of the np and nf even-parity Rydberg series in xenon by two-photon excitation, *J. Opt. Soc. Am. B* **6**(9), 1644–1647 (1989).
- [165] J. Z. Wu, S. B. Whitfield, C. D. Caldwell, M. O. Krause, P. van der Meulen, and A. Fahlman, High-resolution photoelectron spectrometry of selected ns' and nd' autoionization resonances in Ar, Kr, and Xe, *Phys. Rev. A* **42**(3), 1350–1357 (1990).
- [166] D. Klar, K. Harth, J. Ganz, T. Kraft, M.-W. Ruf, H. Hotop, V. Tsemekhman, K. Tsemekhman, and M. Ya. Amusia, On the J -dependence of the odd (ns' , $J = 0, 1$) autoionization resonances of the rare gases Ne, Ar, Kr, and Xe, *Z. Phys. D: Atoms, Molecules and Clusters* **23**(2), 101–113 (1992).
- [167] K. Maeda, K. Ueda, and K. Ito, High-resolution measurement for photoabsorption cross sections in the autoionization regions of Ar, Kr and Xe, *J. Phys. B: At. Mol. Opt. Phys.* **26**(9), 1541–1555 (1993).

-
- [168] S. M. Koeckhoven, W. J. Buma, and C. A. de Lange, Three-photon excitation of autoionizing states of Ar, Kr, and Xe between the $^2P_{3/2}$ and $^2P_{1/2}$ ionic limits, *Phys. Rev. A* **49**(5), 3322–3332 (1994).
- [169] S. M. Koeckhoven, W. J. Buma, and C. A. de Lange, Four-photon excitation of autoionizing states of Ar, Kr, and Xe between the $^2P_{3/2}$ and $^2P_{1/2}$ ionic limits, *Phys. Rev. A* **51**(2), 1097–1109 (1995).
- [170] R. Kau, D. Klar, S. Schohl, S. Baier, and H. Hotop, Laser photoionization of metastable Xe^* ($J = 0$) atoms in the range 462–430 nm, *Z. Phys. D: Atoms, Molecules and Clusters* **36**(1), 23–30 (1996).
- [171] M. Ahmed, M. A. Baig, and B. Suleman, Laser optogalvanic spectroscopic studies of xenon, *J. Phys. B: At. Mol. Opt. Phys.* **31**(17), 4017–4028 (1998).
- [172] M. Gisselbrecht, A. Marquette, and M. Meyer, Two-photon double-resonant excitation of the $Xe^* 5p^5 nf'$ ($J = 2$) autoionization states using synchronized laser and synchrotron radiation pulses, *J. Phys. B: At. Mol. Opt. Phys.* **31**(24), L977–L984 (1998).
- [173] A. Kortyna, M. R. Darrach, P.-T. Howe, and A. Chutjian, High-resolution study of xenon autoionization using direct vacuum-ultraviolet laser excitation, *J. Opt. Soc. Am. B* **17**(11), 1934–1942 (2000).
- [174] G. D'Amico, G. Pesce, and A. Sasso, High resolution spectroscopy of stable xenon isotopes, *Hyperfine Interactions* **127**(1–4), 121–128 (2000).
- [175] M. Hanif, M. Aslam, R. Ali, A. Nadeem, M. Riaz, S. A. Bhatti, and M. A. Baig, Laser optogalvanic spectroscopy of $5p^5nf$ $J = 1 - 5$ even-parity Rydberg levels of xenon, *J. Phys. B: At. Mol. Opt. Phys.* **33**(21), 4647–4655 (2000).
- [176] E. B. Saloman, Energy Levels and Observed Spectral Lines of Xenon, Xe I through Xe LIV, *J. Phys. Chem. Ref. Data* **33**(3), 765–921 (2004).
- [177] M. Hanif, M. Aslam, R. Ali, S. A. Bhatti, M. A. Baig, D. Klar, M.-W. Ruf, I. D. Petrov, V. L. Sukhoroukov, and H. Hotop, Experimental and theoretical investigation of odd $5p(1/2)(5)nl'$ autoionizing resonances in xenon atoms: energy dependence of the reduced widths, *J. Phys. B: At. Mol. Opt. Phys.* **37**(10), 1987–2009 (2004).
- [178] S. Aloïse, P. O'Keeffe, D. Cubaynes, M. Meyer, and A. N. Grum-Grzhimailo, Photoionization of Synchrotron-Radiation-Excited Atoms: Separating Partial Cross Sections by Full Polarization Control, *Phys. Rev. Lett.* **94**(22), 223002 (2005).

- [179] T. Peters, T. Halfmann, U. Even, A. Wünnenberg, I. D. Petrov, V. L. Sukhorukov, and H. Hotop, Experimental and theoretical investigation of even $mp_{1/2}^5 np'$ autoionizing resonances of rare gas atoms, *J. Phys. B: At. Mol. Opt. Phys.* **38**(2), S51–S64 (2005).
- [180] Th. A. Paul and F. Merkt, High-resolution spectroscopy of xenon using a tunable Fourier-transform-limited all-solid-state vacuum-ultraviolet laser system, *J. Phys. B: At. Mol. Opt. Phys.* **38**(22), 4145–4154 (2005).
- [181] M. Hanif, M. Aslam, M. Riaz, S. A. Bhatti, and M. A. Baig, Laser optogalvanic measurements and line-shape analysis of $5p^5 7p$ and $5p^5 4-5f$ autoionizing resonances in xenon, *J. Phys. B: At. Mol. Opt. Phys.* **38**(2), S65–S75 (2005).
- [182] I. D. Petrov, T. Peters, T. Halfmann, S. Aloïse, P. O’Keeffe, M. Meyer, V. L. Sukhorukov, and H. Hotop, Lineshapes of the even $mp_{1/2}^5 n(p'/f')$ autoionizing resonances of Ar, Kr and Xe, *Eur. Phys. J. D* **40**(2), 181–193 (2006).
- [183] M. A. Baig, M. Hanif, M. Aslam, and S. A. Bhatti, Laser optogalvanic observations and MQDT analysis of $mp^5 nd J = 3$ autoionizing resonances in Ar, Kr and Xe, *J. Phys. B: At. Mol. Opt. Phys.* **39**(20), 4221–4229 (2006).
- [184] K. T. Lu, Spectroscopy and Collision Theory. The Xe Absorption Spectrum, *Phys. Rev. A* **4**(2), 579–596 (1971).
- [185] J. Geiger, Energy-loss spectra of xenon and krypton and their analysis by energy-dependent multichannel quantum defect theory, *Z. Phys. A* **282**(2), 129–141 (1977).
- [186] W. R. Johnson, K. T. Cheng, K.-N. Huang, and M. Le Dourneuf, Analysis of Beutler-Fano autoionizing resonances in the rare-gas atoms using the relativistic multichannel quantum-defect theory, *Phys. Rev. A* **22**(3), 989–997 (1980).
- [187] R. D. Knight, Multichannel-quantum-defect analysis of the odd-parity $J = 0$ spectra of xenon, *Phys. Rev. A* **34**(5), 3809–3812 (1986).
- [188] K. Ueda, Spectral line shapes of autoionizing Rydberg series, *Phys. Rev. A* **35**(6), 2484–2492 (1987).
- [189] K. Ueda, Spectral line shapes of autoionizing Rydberg series of xenon, *J. Opt. Soc. Am. B* **4**(3), 424–427 (1987).
- [190] A. L’Huillier, X. Tang, and P. Lambropoulos, Multiphoton ionization of rare gases using multichannel-quantum-defect theory, *Phys. Rev. A* **39**(3), 1112–1122 (1989).

-
- [191] M. J. J. Vrakking, Role of Core Interactions and External Perturbations in the Autoionization of Xe, *J. Phys. Chem. A* **101**(36), 6761–6769 (1997).
- [192] C.-M. Lee and K. T. Lu, Spectroscopy and Collision Theory. II. The Ar Absorption Spectrum, *Phys. Rev. A* **8**(3), 1241–1257 (1973).
- [193] J.-Q. Sun, Multichannel quantum defect theory of the hyperfine structure of high Rydberg states, *Phys. Rev. A* **40**(12), 7355–7355 (1989).
- [194] G. Racah, On a New Type of Vector Coupling in Complex Spectra, *Phys. Rev.* **61**(7–8), 537 (1942).
- [195] S. D. Rosner, T. D. Gaily, and R. A. Holt, Laser-Fluorescence Ion-Beam Magnetic Resonance: Xe⁺ Hyperfine Structure, *Phys. Rev. Lett.* **40**(13), 851–854 (1978).
- [196] M. Aymar, O. Robaux, and C. Thomas, Theoretical investigations on the bound odd-parity spectrum of neutral krypton, *J. Phys. B: At. Mol. Phys.* **14**(22), 4255–4270 (1981).
- [197] E. U. Condon and G. H. Shortley, *The theory of atomic spectra*, Cambridge University Press, 1953.
- [198] K. Harth, J. Ganz, M. Raab, K. T. Lu, J. Geiger, and H. Hotop, On the s–d interaction in neon, *J. Phys. B: At. Mol. Phys.* **18**(24), L825–L832 (1985).
- [199] K. Harth, M. Raab, and H. Hotop, Odd Rydberg spectrum of ²⁰NeI: High resolution laser spectroscopy and multichannel quantum defect theory analysis, *Z. Phys. D: Atoms, Molecules and Clusters* **7**(3), 213–225 (1987).
- [200] K. Ito, K. Ueda, T. Namioka, K. Yoshino, and Y. Morioka, High-resolution absorption spectrum of Ne I in the region of 565–595 Å, *J. Opt. Soc. Am. B* **5**(10), 2006–2014 (1988).
- [201] C. M. Lee, Spectroscopy and collision theory. III. Atomic eigenchannel calculation by a Hartree-Fock-Roothaan method, *Phys. Rev. A* **10**(2), 584–600 (1974).
- [202] J. M. Weber, K. Ueda, D. Klar, J. Kreil, M.-W. Ruf, and H. Hotop, Odd Rydberg spectrum of ⁴⁰Ar(I): high-resolution laser spectroscopy and multichannel quantum defect analysis of the $J = 2$ and 3 levels, *J. Phys. B: At. Mol. Opt. Phys.* **32**(10), 2381–2398 (1999).
- [203] H. J. Wörner, M. Grütter, E. Vliegen, and F. Merkt, unpublished results.

- [204] A. R. Edmonds, R. Pullen, J. Picart, and N. T. Minh, Tables for the computation of radial integrals in the Coulomb approximation, *J. Phys. B: At. Mol. Phys.* **12**(17), 2781–2787 (1979).
- [205] N. B. Delone, S. P. Goreslavsky, and V. P. Krainov, Dipole matrix elements in the quasi-classical approximation, *J. Phys. B: At. Mol. Opt. Phys.* **27**(19), 4403–4419 (1994).
- [206] Atomic units: energy $E_h = \hbar^2/m_e a_0^2 = 2R_\infty hc = 4.3597 \cdot 10^{-18}$ J; electric field $E_h/ea_0 = 5.1422 \cdot 10^{12}$ mV/cm.
- [207] V. B. Berestetskiĭ, E. M. Lifshitz, and L. P. Pitaevskiĭ, *Quantum Electrodynamics*, (L. D. Landau and E. M. Lifshitz, Course of Theoretical Physics, Vol. 4), Butterworth-Heinemann, Oxford, 2nd edition, 1982.
- [208] M. Raunhardt, M. Schäfer, N. Vanhaecke, and F. Merkt, Pulsed-field-ionization zero-kinetic-energy photoelectron spectroscopy of metastable He₂: ionization potential and rovibrational structure of He₂⁺, *J. Chem. Phys.* **128**(16), 164310 (2008).
- [209] E. Goldstein, Über ein noch nicht beschriebenes, anscheinend dem Helium angehörendes Spektrum, *Verh. Deutsch. Phys. Ges.* **15**(10), 402–412 (1913).
- [210] W. E. Curtis, A New Band Spectrum Associated with Helium, *Proc. R. Soc. London Ser. A* **89**(608), 146–149 (1913).
- [211] G. Herzberg, Rydberg Molecules, *Ann. Rev. Phys. Chem.* **38**, 27–56 (1987).
- [212] Y. Tanaka, Continuous emission spectra of the rare gases in the vacuum ultraviolet region, *J. Opt. Soc. Am.* **45**(9), 710–713 (1955).
- [213] Y. Tanaka, A. S. Jursa, and F. J. LeBlanc, Continuous emission spectra of rare gases in the vacuum ultraviolet region. II. Neon and helium, *J. Opt. Soc. Am.* **48**(5), 304–308 (1958).
- [214] R. E. Huffman, Y. Tanaka, and J. C. Larrabee, Helium continuum light source for photoelectric scanning in the 600–1100 Å region, *Appl. Opt.* **2**(6), 617–623 (1963).
- [215] R. E. Huffman, J. C. Larrabee, and Y. Tanaka, Rare Gas Continuum Light Sources for Photoelectric Scanning in the Vacuum Ultraviolet, *Appl. Opt.* **4**(12), 1581–1588 (1965).
- [216] Y. Tanaka, K. Yoshino, and D. E. Freeman, On the determination of the ground state potential energy of Ne₂ from its vacuum ultraviolet spectrum, *J. Chem. Phys.* **59**(1), 564–565 (1973).

- [217] Y. Tanaka, K. Yoshino, and D. E. Freeman, Vacuum ultraviolet absorption spectra of the van der Waals molecules Kr_2 and ArKr , *J. Chem. Phys.* **59**(9), 5160–5183 (1973).
- [218] D. E. Freeman, K. Yoshino, and Y. Tanaka, Vacuum ultraviolet absorption spectrum of the van der Waals molecule Xe_2 . I. Ground state vibrational structure, potential well depth, and shape, *J. Chem. Phys.* **61**(11), 4880–4889 (1974).
- [219] D. E. Freeman, K. Yoshino, and Y. Tanaka, Emission spectrum of rare gas dimers in the vacuum UV region. II. Rotational analysis of band system I of Ar_2 , *J. Chem. Phys.* **71**(4), 1780–1793 (1979).
- [220] P. E. LaRocque, R. H. Lipson, P. R. Herman, and B. P. Stoicheff, Vacuum ultraviolet laser spectroscopy. IV. Spectra of Kr_2 and constants of the ground and excited states, *J. Chem. Phys.* **84**(12), 6627–6641 (1986).
- [221] P. R. Herman, P. E. LaRocque, and B. P. Stoicheff, Vacuum ultraviolet laser spectroscopy. V. Rovibronic spectra of Ar_2 and constants of the ground and excited states, *J. Chem. Phys.* **89**(8), 4535–4549 (1988).
- [222] A. Wüest and F. Merkt, Determination of the interaction potential of the ground electronic state of Ne_2 by high-resolution vacuum ultraviolet laser spectroscopy, *J. Chem. Phys.* **118**(19), 8807–8812 (2003).
- [223] A. Wüest, U. Hollenstein, K. G. de Bruin, and F. Merkt, High-resolution vacuum ultraviolet laser spectroscopy of the $\text{C } 0_u^+ \leftarrow \text{X } 0_g^+$ transition of Xe_2 , *Can. J. Chem.* **82**(6), 750–761 (2004).
- [224] M. L. Ginter and J. G. Eden, Rydberg states of the rare gas dimers, *Can. J. Chem.* **82**(6), 762–778 (2004).
- [225] K. T. Tang and J. P. Toennies, The van der Waals potentials between all rare gas atoms from He to Rn, *J. Chem. Phys.* **118**(11), 4976–4983 (2003).
- [226] R. Feltgen, H. Kirst, K. A. Köhler, H. Pauly, and F. Torello, Unique determination of the He_2 ground state potential from experiment by use of a reliable potential model, *J. Chem. Phys.* **76**(5), 2360–2378 (1982).
- [227] T. van Mourik, A. K. Wilson, and T. H. Dunning Jr., Benchmark calculations with correlated molecular wavefunctions. XIII. Potential energy curves for He_2 , Ne_2 and Ar_2 using correlation consistent basis sets through augmented sextuple zeta, *Mol. Phys.* **96**(4), 529–547 (1999).

- [228] R. J. Gdanitz, Accurately solving the electronic Schrödinger equation of atoms and molecules using explicitly correlated (r_{12} -)MR-CI. VI. The helium dimer (He_2) revisited, *Mol. Phys.* **99**(11), 923–930 (2001).
- [229] J. B. Anderson, Comment on "An exact quantum Monte Carlo calculation of the helium–helium intermolecular potential" [*J. Chem. Phys.* 115, 4546 (2001)], *J. Chem. Phys.* **120**(20), 9886–9887 (2004).
- [230] K. Patkowski, W. Cencek, M. Jeziorska, B. Jeziorski, and K. Szalewicz, Accurate Pair Interaction Energies for Helium from Supermolecular Gaussian Geminal Calculations, *J. Phys. Chem. A* **111**(31), 7611–7623 (2007).
- [231] M. Jeziorska, W. Cencek, K. Patkowski, B. Jeziorski, and K. Szalewicz, Pair potential for helium from symmetry-adapted perturbation theory calculations and from supermolecular data, *J. Chem. Phys.* **127**(12), 124303 (2007).
- [232] J. J. Hurly and J. B. Mehl, ^4He Thermophysical Properties: New Ab Initio Calculations, *J. Res. Natl. Inst. Stand. Technol.* **112**(2), 75–94 (2007).
- [233] F. Luo, G. C. McBane, G. Kim, C. F. Giese, and W. R. Gentry, The weakest bond: Experimental observation of helium dimer, *J. Chem. Phys.* **98**(4), 3564–3567 (1993).
- [234] R. E. Grisenti, W. Schöllkopf, J. P. Toennies, G. C. Hegerfeldt, T. Köhler, and M. Stoll, Determination of the Bond Length and Binding Energy of the Helium Dimer by Diffraction from a Transmission Grating, *Phys. Rev. Lett.* **85**(11), 2284–2287 (2000).
- [235] M. L. Ginter, Spectrum and Structure of the He_2 Molecule. I. Characterization of the States Associated with the UAO's $3p\sigma$ and $2s$, *J. Chem. Phys.* **42**(2), 561–568 (1965).
- [236] N. Yu and W. H. Wing, Observation of the infrared spectrum of the helium molecular ion ($^3\text{He } ^4\text{He}^+$), *Phys. Rev. Lett.* **59**(18), 2055–2058 (1987), see erratum in *Phys. Rev. Lett.* 60, 2445 (1988).
- [237] R. I. Hall, Y. Lu, Y. Morioka, T. Matsui, T. Tanaka, H. Yoshii, T. Hayaishi, and K. Ito, High resolution threshold photoelectron spectroscopy of rare gas dimers, *J. Phys. B: At. Mol. Opt. Phys.* **28**(12), 2435–2451 (1995).
- [238] Y. Lu, Y. Morioka, T. Matsui, T. Tanaka, H. Yoshii, R. I. Hall, T. Hayaishi, and K. Ito, Ground and excited states of Xe_2^+ observed by high resolution threshold photoelectron spectroscopy of Xe_2 , *J. Chem. Phys.* **102**(4), 1553–1560 (1995).

- [239] A. Carrington, A. M. Shaw, and S. M. Taylor, Microwave electronic spectra of the Ar_2^+ and Ne_2^+ ions: a combined neutral/ion molecular beam technique, *Chem. Phys. Lett.* **241**(5–6), 611–617 (1995).
- [240] A. Carrington, D. I. Gammie, J. C. Page, A. M. Shaw, and S. M. Taylor, Microwave electronic spectrum of the $\text{Ne} \cdots \text{Ne}^+$ long-range complex, *Phys. Chem. Chem. Phys.* **1**(1), 29–36 (1999).
- [241] A. Carrington, D. I. Gammie, J. C. Page, A. M. Shaw, and J. M. Hutson, Microwave electronic spectrum of the $\text{Ne}-\text{Ne}^+$ long-range complex: The interaction potential, *J. Chem. Phys.* **116**(9), 3662–3669 (2002).
- [242] R. Signorell, A. Wüest, and F. Merkt, The first adiabatic ionization potential of Ar_2 , *J. Chem. Phys.* **107**(24), 10819–10822 (1997).
- [243] R. Signorell and F. Merkt, The first electronic states of Ar_2^+ studied by high resolution photoelectron spectroscopy, *J. Chem. Phys.* **109**(22), 9762–9771 (1998).
- [244] R. Signorell, U. Hollenstein, and F. Merkt, High-resolution photoelectron spectroscopic study of the first electronic state of Kr_2^+ , *J. Chem. Phys.* **114**(22), 9840–9851 (2001).
- [245] A. Wüest, P. Rupper, and F. Merkt, Experimental determination of the potential energy curves of the $I(3/2u)$ and $I(3/2g)$ states of Kr_2^+ , *Mol. Phys.* **99**(23), 1941–1958 (2001).
- [246] P. Rupper and F. Merkt, Assignment of the first five electronic states of Ar_2^+ from the rotational fine structure of PFI-ZEKE photoelectron spectra, *J. Chem. Phys.* **117**(9), 4264–4281 (2002).
- [247] P. Rupper and F. Merkt, Dissociation energies of the $I(3/2g)$ and $I(1/2g)$ states of Ar_2^+ , *Mol. Phys.* **100**(24), 3781–3784 (2002).
- [248] P. Rupper, O. Zehnder, and F. Merkt, Potential energy curves of diatomic molecular ions from high-resolution photoelectron spectra. II. The first six electronic states of Xe_2^+ , *J. Chem. Phys.* **121**(17), 8279–8290 (2004).
- [249] A. Wüest and F. Merkt, Potential energy curves of diatomic molecular ions from high-resolution photoelectron spectroscopy. I. The first six electronic states of Ar_2^+ , *J. Chem. Phys.* **120**(2), 638–646 (2004).
- [250] A. Wüest and F. Merkt, Potential energy curves of diatomic molecular ions from high-resolution photoelectron spectroscopy. III. The low-lying *ungerade* states of Kr_2^+ , *Mol. Phys.* **103**(9), 1285–1300 (2005).

- [251] I. Paidarová and F. X. Gadéa, Accurate *ab initio* calculation of potential energy curves and transition dipole moments of the Xe_2^+ molecular ion, *Chem. Phys.* **274**(1), 1–9 (2001).
- [252] T.-K. Ha, P. Rupper, A. Wüest, and F. Merkt, The lowest electronic states of Ne_2^+ , Ar_2^+ and Kr_2^+ : Comparison of theory and experiment, *Mol. Phys.* **101**(6), 827–838 (2003).
- [253] A. Carrington, C. H. Pyne, and P. J. Knowles, Microwave electronic spectrum of the He_2^+ ion, *J. Chem. Phys.* **102**(15), 5979–5988 (1995).
- [254] J. Xie, B. Poirier, and G. I. Gellene, Accurate, two-state *ab initio* study of the ground and first-excited states of He_2^+ , including exact treatment of all Born–Oppenheimer correction terms, *J. Chem. Phys.* **122**(18), 184310 (2005).
- [255] M. L. Ginter, The spectrum and structure of the He_2 molecule. Part II. Characterization of the singlet states associated with the UAO’s 3s and $2p\pi$, *J. Mol. Spectrosc.* **17**(2), 224–239 (1965).
- [256] M. L. Ginter, The spectrum and structure of the He_2 molecule. Part III. Characterization of the triplet states associated with the UAO’s 3s and $2p\pi$, *J. Mol. Spectrosc.* **18**(3), 321–343 (1965).
- [257] M. L. Ginter, Spectrum and Structure of the He_2 Molecule. IV. Characterization of the Singlet and Triplet States Associated with the UAO’s $3d\sigma$, $3d\pi$, and $3d\delta$, *J. Chem. Phys.* **45**(1), 248–262 (1966).
- [258] M. L. Ginter and D. S. Ginter, Spectrum and Structure of the He_2 Molecule. V. Characterization of the Triplet States Associated with the UAO’s $6-17p\pi$ and $7-12p\sigma$, *J. Chem. Phys.* **48**(5), 2284–2291 (1968).
- [259] C. M. Brown and M. L. Ginter, Spectrum and structure of the He_2 molecule VI. Characterization of the states associated with the UAO’s $3p\pi$ and $2s$, *J. Mol. Spectrosc.* **40**(2), 302–316 (1971).
- [260] C. M. Brown and M. L. Ginter, Spectrum and structure of the He_2 molecule. Characterization of the singlet and triplet states associated with the UAO’s $4s$, $4d\sigma$, $4d\pi$, and $4d\delta$, *J. Mol. Spectrosc.* **46**(2), 256–275 (1973).
- [261] F. B. Orth and M. L. Ginter, The spectrum and structure of the He_2 molecule. Characterization of the triplet states associated with the UAO’s $4p\sigma$, $5p\sigma$, and $6p\sigma$, *J. Mol. Spectrosc.* **61**(2), 282–288 (1976).

- [262] F. B. Orth and M. L. Ginter, The spectrum and structure of the He₂ molecule. Characterization of the triplet states associated with the UAO's $4p\pi$ and $5p\pi$, J. Mol. Spectrosc. **64**(2), 223–232 (1977).
- [263] F. B. Orth, C. M. Brown, and M. L. Ginter, The spectrum and structure of the He₂ molecule. Characterization of the singlet Π states associated with the UAO's $4p\pi-9p\pi$, J. Mol. Spectrosc. **69**(1), 53–65 (1978).
- [264] D. S. Ginter and M. L. Ginter, The spectrum and structure of the He₂ molecule. Multichannel quantum defect analyses of the triplet levels associated with $(1\sigma_g)^2(1\sigma_u)np\lambda$, J. Mol. Spectrosc. **82**(1), 152–175 (1980).
- [265] D. S. Ginter and M. L. Ginter, Spectrum and structure of the He₂ molecule: Characterization of the triplet states associated with $(1\sigma_g)^2(1\sigma_u)ns\sigma$, $nd\sigma$, $nd\pi$, and $nd\delta$ ($n = 5-12$), J. Mol. Spectrosc. **101**(1), 139–160 (1983).
- [266] D. S. Ginter and M. L. Ginter, The spectrum and structure of the He₂ molecule: Characterization of the singlet Σ states with UAOs $4p\sigma$ and $6p\sigma-9p\sigma$, J. Mol. Spectrosc. **138**(1), 29–37 (1989).
- [267] G. Herzberg and Ch. Jungen, The $4f$ states of He₂: A new spectrum of He₂ in the near infrared, J. Chem. Phys. **84**(3), 1181–1192 (1986).
- [268] C. Focsa, P. F. Bernath, and R. Colin, The Low-Lying States of He₂, J. Mol. Spectrosc. **191**(1), 209–214 (1998).
- [269] C. F. Chabalowski, J. O. Jensen, D. R. Yarkony, and B. H. Lengsfeld III, Theoretical study of the radiative lifetime for the spin-forbidden transition ${}^3\Sigma_u^+ \rightarrow X^1\Sigma_g^+$ in He₂, J. Chem. Phys. **90**(4), 2504–2512 (1989).
- [270] C. W. Bauschlicher, Jr., H. Partridge, and D. Ceperley, The dissociation energy of He₂⁺, Chem. Phys. Lett. **160**(2), 183–188 (1989).
- [271] J. Ackermann and H. Hogreve, Adiabatic calculations and properties of the He₂⁺ molecular ion, Chem. Phys. **157**(1–2), 75–87 (1991).
- [272] W. Cencek and J. Rychlewski, Many-electron explicitly correlated Gaussian functions. II. Ground state of the helium molecular ion He₂⁺, J. Chem. Phys. **102**(6), 2533–2538 (1995).
- [273] F. X. Gadéa and I. Paidarová, *Ab initio* calculations for Ar₂⁺, He₂⁺ and He₃⁺, of interest for the modelling of ionic rare-gas clusters, Chem. Phys. **209**(2–3), 281–290 (1996).

- [274] M. Stanke, D. Kędziera, S. Bubin, M. Molski, and L. Adamowicz, Lowest vibrational states of $^4\text{He}^3\text{He}^+$: Non-Born-Oppenheimer calculations, *Phys. Rev. A* **76**(5), 052506 (2007).
- [275] K. Pachucki and J. Komasa, Radiative correction to the helium dimer interaction energy, *J. Chem. Phys.* **124**(6), 064308 (2006).
- [276] N. Yu, W. H. Wing, and L. Adamowicz, Hyperfine Structure in the Infrared Spectrum of $^3\text{He}^4\text{He}^+$, *Phys. Rev. Lett.* **62**(3), 253–256 (1989).
- [277] D. S. Ginter, M. L. Ginter, and C. M. Brown, Multichannel interactions in the $(1\sigma_g)^2(1\sigma_u)np\lambda(^3\Pi_g, ^3\Sigma_g^+)$ Rydberg structures of He_2 , *J. Chem. Phys.* **81**(12), 6013–6025 (1984).
- [278] H. Lewandowski, E. R. Hudson, J. Bochinski, and J. Ye, A pulsed, low-temperature beam of supersonically cooled free radical OH molecules, *Chem. Phys. Lett.* **395**(1–3), 53–57 (2004).
- [279] M. Schäfer and A. Bauder, Vibrationally excited states in a pulsed jet observed by Fourier transform microwave spectroscopy, *Chem. Phys. Lett.* **308**(5–6), 355–362 (1999).
- [280] G. W. F. Drake and S. P. Goldman, Bethe logarithms for Ps^- , H^- , and heliumlike atoms, *Can. J. Phys.* **77**, 835 (1999).
- [281] G. W. F. Drake and W. C. Martin, Ionization energies and quantum electrodynamic effects in the lower $1sns$ and $1snp$ levels of neutral helium (^4He I), *Can. J. Phys.* **76**(9), 679–698 (1998).
- [282] D. C. Morton, Q. Wu, and G. W. F. Drake, Energy levels for the stable isotopes of atomic helium (^4He I and ^3He I), *Can. J. Phys.* **84**(2), 83–105 (2006).
- [283] W. C. Martin, Improved ^4He I $1snl$ ionization, energy levels, and Lamb shifts for $1sns$ and $1snp$ terms, *Phys. Rev. A* **36**, 3575 (1987).
- [284] C. Dorrer, F. Nez, B. de Beauvoir, L. Julien, and F. Biraben, Accurate Measurement of the $2^3\text{S}_1 - 3^3\text{D}_1$ Two-Photon Transition Frequency in Helium: New Determination of the 2^3S_1 Lamb shift, *Phys. Rev. Lett.* **78**(19), 3658 (1997).
- [285] A. Kono and S. Hattori, Variational calculations for excited states in He I: Improved estimation of the ionization energy from accurate energies for the $n^3\text{S}$, $n^1\text{D}$, $n^3\text{D}$ series, *Phys. Rev. A* **31**(2), 1199 (1985).

-
- [286] A. Kono and S. Hattori, Energy levels for S, P, and D states in He through precision variational calculations, *Phys. Rev. A* **34**(3), 1727 (1986).
- [287] W. J. van der Zande and W. Ubachs, Comment on “First Measurement of the Rotational Constants for the Homonuclear Molecular Ion He_2^+ ”, *Phys. Rev. Lett.* **84**(14), 3212 (2000).
- [288] J. Xie and R. N. Zare, Selection rules for the photoionization of diatomic molecules, *J. Chem. Phys.* **93**(5), 3033–3038 (1990).
- [289] A. D. Buckingham, B. J. Orr, and J. M. Sichel, Angular Distribution and Intensity in Molecular Photoelectron Spectroscopy I. General Theory for Diatomic Molecules, *Phil. Trans. R. Soc. London Ser. A* **268**(1184, A Discussion on Photoelectron Spectroscopy), 147–157 (1970).
- [290] J. Xie and R. N. Zare, Rotational line strengths for the photoionization of diatomic molecules, *J. Chem. Phys.* **97**(5), 2891–2899 (1992).
- [291] H. M. Pickett, The fitting and prediction of vibration-rotation spectra with spin interactions, *J. Mol. Spectrosc.* **148**(2), 371–377 (1991).
- [292] Ch. Jungen, editor, *Molecular Applications of Quantum Defect Theory*, Institute of Physics Publishing: Bristol and Philadelphia, 1996.
- [293] A. F. Ruckstuhl, W. A. Stahel, and K. Dressler, Robust Estimation of Term Values in High-Resolution Spectroscopy: Application to the $e^3\Sigma_u^+ \rightarrow a^3\Sigma_g^+$ Spectrum of T_2 , *J. Mol. Spectrosc.* **160**(2), 434–445 (1993).
- [294] J. K. G. Watson, Robust weighting in least-squares fits, *J. Mol. Spectrosc.* **219**(2), 326–328 (2003).
- [295] R. Panock, R. R. Freeman, R. H. Storz, and T. A. Miller, Observation of laser driven transitions to high Rydberg states of He_2 , *Chem. Phys. Lett.* **74**(2), 203–206 (1980).
- [296] R. Seiler, U. Hollenstein, G. M. Greetham, and F. Merkt, Rydberg-state-resolved zero-kinetic-energy photoelectron spectroscopy, *Chem. Phys. Lett.* **346**(3–4), 201–208 (2001), see also *Chem. Phys. Lett.* 350, 189 (2001).
- [297] U. Hollenstein, R. Seiler, and F. Merkt, Determination of the ionisation potential of krypton by Rydberg-state-resolved threshold-ionisation spectroscopy, *J. Phys. B: At. Mol. Opt. Phys.* **36**(5), 893–903 (2003).

- [298] K. P. Huber and G. Herzberg, *Molecular Spectra and Molecular Structure, Volume IV, Constants of Diatomic Molecules*, Van Nostrand Reinhold Company: New York, 1979.
- [299] L. Coman, M. Guna, L. Simons, and K. A. Hardy, First Measurement of the Rotational Constants for the Homonuclear Molecular Ion He_2^+ , *Phys. Rev. Lett.* **83**(14), 2715–2717 (1999).
- [300] K. Hardy and X. W. Wang, Reply to Comment on “First Measurement of the Rotational Constants for the Homonuclear Molecular Ion He_2^+ ”, *Phys. Rev. Lett.* **84**, 3212 (2000), *Phys. Rev. Lett.* **84**(14), 3213 (2000).
- [301] R. M. Jordan, H. R. Siddiqui, and P. E. Siska, Potential energy curves for the $a^3\Sigma_u^+$ and $c^3\Sigma_g^+$ states of He_2 consistent with differential scattering, *ab initio* theory, and low-temperature exchange rates, *J. Chem. Phys.* **84**(12), 6719–6727 (1986).
- [302] N. Bjerre, A. O. Mitrushenkov, P. Palmieri, and P. Rosmus, Spin-orbit and spin-spin couplings in He_2 and He_2^- , *Theor. Chem. Acc.* **100**(1–4), 51–59 (1998).
- [303] F. Merkt, H. H. Fielding, and T. P. Softley, Electric field effects on zero-kinetic-energy photoelectron spectra: An explanation of observed trends, *Chem. Phys. Lett.* **202**(1–2), 153–160 (1993).
- [304] H. Hotop and A. Niehaus, Collisional Ionization of Long-Lived Highly Excited Atoms, *J. Chem. Phys.* **47**, 2506 (1967).
- [305] H. Hotop, F. W. Lampe, and A. Niehaus, Collision Reactions of Electronically Excited Hydrogen Molecules, *J. Chem. Phys.* **51**, 593 (1969).
- [306] Y. Hahn, Electron - ion recombination processes - an overview , *Rep. Prog. Phys.* **60**, 691 (1997).
- [307] W. Yang, E. S. Shuman, and T. F. Gallagher, Spectral hole burning in the di-electronic recombination from a continuum of finite bandwidth, *Phys. Rev. A* **75**, 023411 (2007).
- [308] E. R. Cohen, T. Cvitaš, J. G. Frey, B. Holmström, K. Kuchitsu, R. Marquardt, I. Mills, F. Pavese, M. Quack, J. Stohner, H. L. Strauss, M. Takami, and A. J. Thor, *Quantities, Units and Symbols in Physical Chemistry*, RSCPublishing: Cambridge, 3rd edition, 2007.
- [309] S. Gerstenkorn and P. Luc, Absolute iodine (I_2) standards measured by means of Fourier transform spectroscopy, *Revue de Physique Appliquée* **14**, 791–794 (1979).

Publications

- M. Raunhardt, M. Schäfer, N. Vanhaecke, and F. Merkt, "Pulsed-field-ionization zero-kinetic-energy photoelectron spectroscopy of metastable He₂: ionization potential and rovibrational structure of He₂⁺", J. Chem. Phys. 128(16), 164310 (2008)
- M. Raunhardt, M. Schäfer, and F. Merkt, "PFI-ZEKE photoelectron and photoionization spectroscopy of metastable He₂: ionization potential and rovibrational structure of He₂⁺", QUASAAR (QUAntitative Spectroscopy for Atmospheric and Astrophysical Research) - Winter School, Saas Almagell, January 19 - 24, 2008
- M. Raunhardt and F. Merkt, "Spectroscopy of ammonia clusters", QUASAAR (QUAntitative Spectroscopy for Atmospheric and Astrophysical Research) - Winter School, Saas Almagell, Switzerland, January 19 - 24, 2008
- M. Raunhardt, M. Schäfer, and F. Merkt, "Fine and Hyperfine structure of high Rydberg states of xenon studied by millimeter wave spectroscopy and multichannel quantum defect theory", Latsis Symposium: Intramolecular Dynamics, Symmetry and Spectroscopy, Zurich, Switzerland, September 6 - 10, 2008
- M. Raunhardt, M. Schäfer, and F. Merkt, "Where atomic spectra are like molecular spectra: fine and hyperfine structure of high Rydberg states of xenon studied by millimeter wave spectroscopy and MQDT calculations", Swiss Chemical Society - Fall Meeting, Zurich, Switzerland, October 13, 2008
- M. Raunhardt, M. Schäfer, and F. Merkt, "Millimeter wave spectroscopy and MQDT calculations of the hyperfine structure of xenon", International Symposium on Molecular Beams, Freiburg im Breisgau, Germany, May 28 - June 1, 2007
- M. Raunhardt, M. Schäfer, and F. Merkt, "Millimeter wave spectroscopy and MQDT calculations of high Rydberg states of xenon" Swiss Chemical Society - Fall Meeting, EPF Lausanne, Switzerland, September 12, 2007
- U. Gubler, M. Raunhardt, and A. Stump, "Measurement technique for thermal conductivity of thin polymer films", Thin Solid Films 515, 1737 (2006)
- M. Raunhardt, N. Vanhaecke and F. Merkt, "Spectroscopy of metastable states of He₂", Gordon Research Conference about Electronic Spectroscopy & Dynamics, Les Diablerets, Switzerland, September 10 - 15, 2006

- M. Raunhardt, N. Vanhaecke and F. Merkt, "Study of metastable states of rare gases", Swiss Chemical Society - Fall Meeting, Zurich, Switzerland, October 13, 2006
- M. Raunhardt, M. Schäfer, F. Merkt, L. Duggan, T. P. Softley, "PFI ZEKE photoelectron spectroscopy of ND₃", 37th EGAS (European Group for Atomic Systems) Conference, Dublin, Ireland, August 3 - 6, 2005
- M. Raunhardt, M. Schäfer, F. Merkt, L. Duggan, T. P. Softley, "Rotationally resolved PFI ZEKE photoelectron spectroscopy of ND₃", Swiss Chemical Society - Fall Meeting, EPF Lausanne, Switzerland, October 13, 2005

Award

- Poster Award: QUASAAR (QUAntitative Spectroscopy for Atmospheric and Astrophysical Research) - Winter School, Saas Almagell, Switzerland, January 19 - 24, 2008

Danksagung

Ich danke allen, die zum Gelingen dieser Dissertation beigetragen haben:

Herrn Prof. Dr. Frédéric Merkt für die Möglichkeit meine Dissertation in seiner Gruppe zu machen. Ich möchte mich bei ihm auch für die Geduld und das Engagement bedanken, mit der er mir die Schönheit der Spektroskopie näher brachte. Die Gruppenausflüge ins Wallis habe ich sehr geschätzt und werde sie stets in guter Erinnerung behalten.

Herrn Prof. Dr. Alexander Wokaun danke ich für die Übernahme des Korreferats.

Martin für die gute Teamarbeit beim Xenon- und Heliumdimerprojekt.

Urs für all unsere Diskussion und seine Ratschläge in jeder Situation.

Erich für die gute Zusammenarbeit während meiner Zeit als Praktikumsassistent.

Irene für die Abnahme von administrativer Arbeit.

Hansjürg Schmutz für die Hilfe bei allen elektronischen Problemen.

Der mechanischen Werkstatt, insb. René Gunzinger und Marco Vecellio für die Hilfe bei allen Um- und Aufbauten, die für ein funktionierendes Experiment nötig waren.

Der ganzen Gruppe Merkt (Urs, Martin, Thomas, Stephen, Lorena, Daniel, Christian, Julie, Monika, Alex, Sandro, Anna, Jinjun, Konstantina, Oliver, Evgueni, Hans Jakob, Edward, Nicolas, Helen) für die gute Stimmung und die Hilfe beim Lösen aller möglichen Probleme.

Meinen Eltern und meinem Bruder. Ohne euch wäre dies nicht möglich gewesen.